UNIVERSITY OF SOUTHAMPTON

FACULTY OF PHYSICAL AND APPLIED SCIENCE

School of Electronics and Computer Science

CHARACTERISATION OF CARBON NANOTUBE VARIABILITY AND APPLICATION IN SOLAR CELLS

By

Karim M. El Shabrawy

A thesis submitted for the degree of Doctor of Philosophy

January, 2011

UNIVERSITY OF SOUTHAMPTON

ABSTRACT

FACULTY OF PHYSICAL AND APPLIED SCIENCE

SCHOOL OF ELECTRONICS AND COMPUTER SCIENCE

Doctor of Philosophy

CHARACTERISATION OF CARBON NANOTUBE VARIABILITY AND APPLICATION IN SOLAR CELLS

By Karim M. El Shabrawy

Photovoltaic solar cells (PVs) are now recognised as the world's fastest growing energy technology, yet, they only account for a mere fraction of current global renewable power capacity. It is acknowledged that this inadequate market penetration has been largely a result of the technology's excessive cost. Researchers have therefore endeavoured to find innovative, economic solutions with the aim of either cutting back on the active material quantity or improving power efficiencies to abate operating expenditure. Both approaches, however, have presented a cost vs. performance trade-off, which some believe may be surmounted by the employment of Nanotechnology. Amongst the many potential nano-materials proposed for PV conversion is the Carbon Nanotube (CNT) due to its low material utilisation, superior carrier transport properties and most notably; a tunable band-gap. This thesis investigates the theoretical performance of a range of CNT based solar cells, and in doing so, novel computational methodologies are formulated towards characterising the related electronic and optical properties with respect to the CNT structural variability.

The first part of this thesis addresses the issue concerning the differentiation of metallic and semiconducting CNTs. As an outcome, a simulation-efficient and experimentally validated analytical model is developed to distinguish the nanotubes and predict the band-gap of semiconducting CNTs. In addition, a model that approximates the semiconducting CNT's carrier effective mass is presented.

The key challenge affecting CNT's at present resides in the uncertainty of the structural characteristics realised using existing synthesis techniques. Thus, the second part of this thesis aims to statistically model the variation in band-gap and carrier effective mass as a function of typical geometric distributions. This work offers a valuable insight into the optimisation of CNT diameter related process parameters towards suppressing electronic variability.

The final part of this thesis initially focuses on modelling the optical absorption of CNTs where the photo-generated current and quantum efficiency responses are derived for various tube geometries when exposed to laser illumination. The established models are later exploited in combination with an equivalent PV circuit model to evaluate the performance metrics of a variety of isolated CNT based PV devices under solar radiation. A proposed set of multi-band-gap CNT PV devices are also analysed where the optimized CNT structures for PV conversion are outlined.

Within the confines of the assumptions made in this study, it is concluded that only specific types of CNTs may yield competitive PV conversion efficiencies compared to other nanotechnology based solar cells. However, reservations are maintained on whether CNTs could outperform bulk PV materials, even when a multiple band-gap scheme is considered.

Academic Thesis: Declaration of Authorship

I, *Karim M. El Shabrawy*, declare that this thesis entitled "*Characterisation of Carbon Nanotube Variability and Application in Solar Cells*" and the work presented in the thesis are both my own, and have been generated by me as the result of my own original research.

I confirm that:

- This work was done wholly or mainly while in candidature for a research degree at this University;
- Where any part of this thesis has previously been submitted for a degree or any other qualification at this University or any other institution, this has been clearly stated;
- Where I have consulted the published work of others, this is always clearly attributed;
- Where I have quoted from the work of others, the source is always given. With the exception of such quotations, this thesis is entirely my own work;
- I have acknowledged all main sources of help;
- Where the thesis is based on work done by myself jointly with others, I have made clear exactly what was done by others and what I have contributed myself;
- Parts of this work have been published as listed in Appendix D.

Signed:

Date:

Contents

List of Figures

List of Tables

Acknowledgements

I wish to firstly thank my supervisor, Dr. Koushik Maharatna, for his constant support throughout this PhD project and especially for always being there when I needed him. Special thanks also go to my second supervisor, Prof. Bashir M. Al-Hashimi, for his valuable feedback and guidance. I am further grateful for the studentship funding provided to me by the School of Electronics and Computer Science, University of Southampton.

This PhD project has benefited from insightful discussions with several very helpful people whom I would like to extend my gratitude. Thank you to Dr. Kees De Groot, Prof. Darren Bagnall and Prof. Peter Ashburn.

Above all, I would like to dedicate this thesis to my parents, to whom I am deeply thankful for their loving support and for truly believing in my abilities.

Chapter 1 Motivation

1.1 Energy challenge

Kindled by the industrial revolution, global energy demand has rapidly soared with the 2007 total primary energy supply recorded at a staggering 140 PWh ($x10^{15}$ Wh) [1]. Over 81% of this energy has been fulfilled by the combustion of fossil fuels (coal, oil, gas), which are envisaged to diminish in the near future due to their finite nature [1, 2]. Some countries, such as the UK for example, have already experienced a peak in fossil fuel production rates and are faced with a security-of-supply issue particularly as their ageing coal and nuclear power stations loom towards decommission [2]. As a consequence, this has intensified the dependence on foreign energy supplies adding political strain amongst nations looking to close the gap between their energy demand and supply.

Notably, it is very likely that using fossil fuels has an effect on the climate since the atmospheric concentration of CO_2, a by-product of burning fossil fuels, has grown considerably since the outset of the industrialisation period [2]. Figure 1-1 illustrates this argument. Because CO_2 is a greenhouse gas, it has a warming effect on global average temperatures and will ultimately, if not capped, alter our environment and ecosystem through the compounding of more frequent natural disasters.

The above-mentioned problems have caused worldwide concern and prompted some to seek alternative sources of energy that neither run out nor have a hazardous effect on the environment. These renewable sources of energy use natural resources such as sunlight, wind and waves to generate power, which, depending on localised weather conditions and geographical location can be undesirably intermittent. For this reason, the deployment of renewable solutions has been confined to areas with favourable conditions where they can

exhibit relatively high energy yield ratios (the ratio of energy delivered by the system over its lifetime to the energy input during the systems life cycle) [2].

Amidst the recent rise in emission cutback targets and incentivised policies for the adoption of renewable sources there has been a lack of social uptake due to the economical competitiveness of traditional fossil fuel sources. Hence, in 2008, global governments and industries invested a combined $18 billion in research and development projects to investigate solutions in reducing the overall cost of renewable technologies [3]. These initiatives ranged from cutting back on capital costs through material savings to improving system efficiencies that abate operating expenditure.

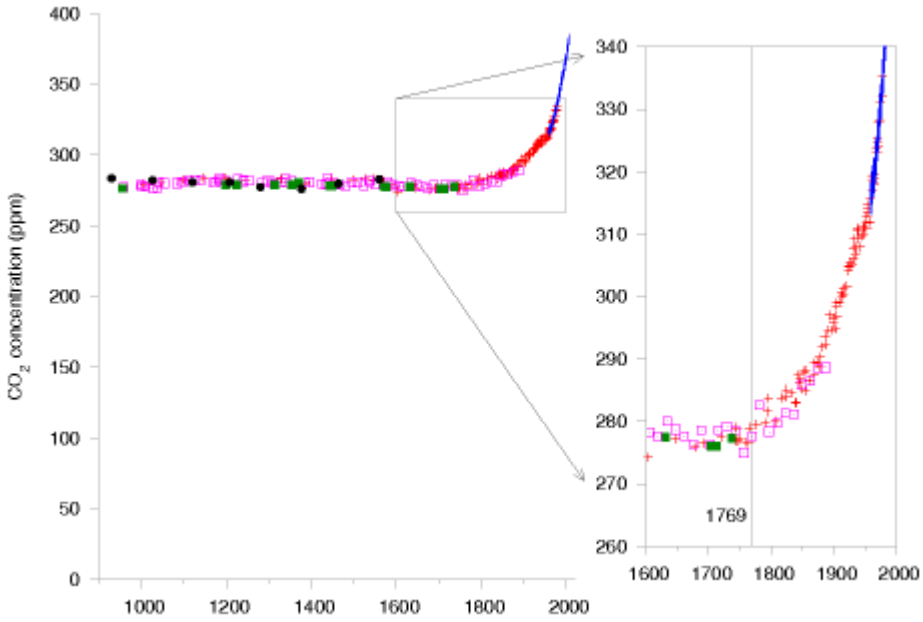

Figure 1-1: Carbon dioxide (CO_2) concentrations (in parts per million) for the last 1100 years, measured from air trapped in ice cores (up to 1977) and directly in Hawaii (from 1958 onwards) [2].

There is growing speculation that grid parity (the threshold after which the energy price of renewable sources is less than conventional grid power) will be achieved during the forthcoming decade with the expected surge in oil prices and the continuing decline in the lifetime costs of renewables. If made economical enough, it is also envisioned that off-grid renewable solutions may provide a feasible option for the 1.6 billion people situated in rural areas without access to electricity.

Given that in 1 hour the sunlight energy radiated upon our planet is equivalent to the energy consumed by humanity in 1 year, this clearly offers a great means of generating clean

energy [4]. One form of renewable technology that takes advantage of such a resource is the solar cell.

1.2 Solar cells

A solar cell converts sunlight into electricity and is often referred to as a photovoltaic (PV) - named after the discovery of the photovoltaic effect by Edmond Becquerel in 1839. Depending on the size of the PV system, power delivered can range from, typically, a few kilowatts for rooftop and grid-connected applications down to tens of milliwatts for functions such as pocket calculators and remote sensing devices. From 2004-2008, global PV capacity increased sixfold to more than 16 gigawatts peak (GW_p- the optimal power delivered under standard test conditions), becoming the world's fastest growing energy technology [5]. However, PV's only represented 6% of the total 280 GW_p renewable power capacity (excluding hydropower) owing to their high cost to performance ratio [5]. Thus, up till now, much of the PV industry and research community have been focusing on realising more cost efficient solar cells.

Silicon (Si) comprises the main constituent material of most solar cells in use today and is recognized as the 'first generation' PV technology [6]. In practice it has been shown that crystalline silicon PVs can harvest up to 25% of the incoming solar energy without any optical enhancements such as sunlight concentration [7]. This performance is not far from the nominal upper limit (31%) theoretically predicted for silicon PV's by Shockley and Queisser, which implies that standard silicon cells have almost reached their maximum achievable efficiency [8]. Incidentally, more than 50% of the total cost of a silicon cell is due to the processing of polysilicon into crystalline form [9]. As a result, any significant reduction in unit cost can only be accomplished by utilising smaller amounts of the constituent material per device or considering a lower quality material such as amorphous silicon. This strategy paved the way for the 'second generation' thin-film technology that assumes a material thickness in the order of less than a few micrometers as opposed to a hundred micrometers or more [6, 10]. Evidently, this comes at the expense of much lower operating efficiencies as revealed in Figure 1-2.

Despite silicon having a well established technology base and history owing to the rapid advances in the microelectronics industry, it is not an ideal material for photovoltaic

conversion purposes and has of late experienced extensive supply shortages [4, 9]. Consequently, other inorganic as well as organic materials have emerged as potential contenders for second generation cells [11]. Inorganic compound semiconductors such as Gallium Arsenide (GaAs) and Copper Indium-Gallium Diselenide ($Cu(In,Ga)Se_2$) are now considered mainstream thin-film technologies with efficiencies approaching that of the first generation cells [5, 6]. Organic dye-sensitized cells have also gained noteworthy attention in the flexible PV market, although their efficiencies are on average between 5-10%.

Still, a substantial increase in conversion efficiency is required if the cost over the operating lifetime of a cell is to be minimised. Since the thermodynamic Carnot limit ($1-T_{cell}/T_{sun}$) on the conversion of sunlight to electricity is 95%, this suggests that the performance of a solar cell could be improved by 2-3 times the present theoretical limit calculated for silicon cells [6]. With the evolution of new exotic materials and different device architectures, a 'third generation' of high-performance, low-cost photovoltaics has recently surfaced.

Third generation PVs generally operate under a tandem scheme where a number of solar cells bearing dissimilar solid-state characteristics, namely the band-gap, are stacked together to harness more power from the solar spectrum [4]. As pointed out in Figure 1-2, the highest recorded efficiency for a triple-junction PV device is 40.7%, which is almost double that of a single-junction silicon cell. Devices based on this optimisation technique have only just begun commercial production, finding applications predominantly in the space industry [6]. Theoretically, however, if the number of cells in the stack were to grow infinitely, a direct sunlight conversion efficiency of 68% could be obtained [12]. Approaching this performance limit using nano-structured materials has become the focus of much of present-day PV research.

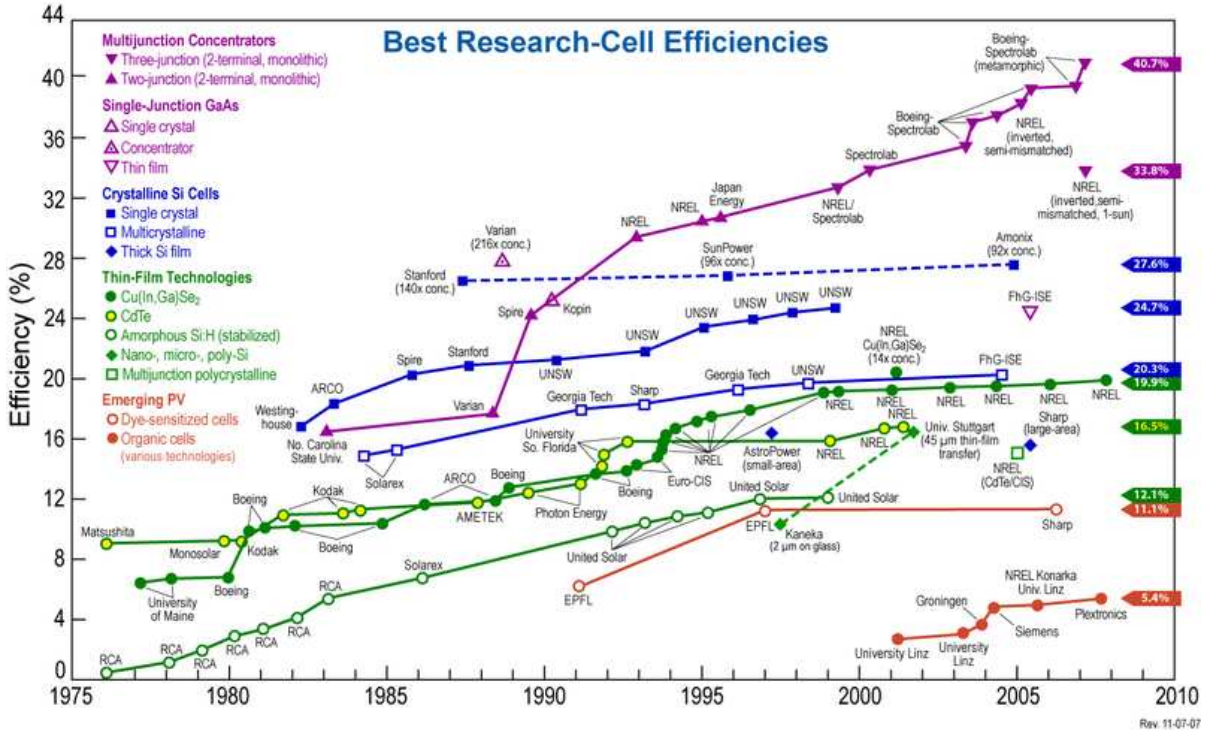

Figure 1-2: Best research solar cell efficiencies recorded from 1976 to 2008 for different PV technologies [13].

Many types of nano-materials have been studied for photovoltaic conversion, most notably, silicon nanowires, quantum dots and carbon nanotubes [4]. Although still at an early stage of research, they have yet to demonstrate similar or superior performance/cost ratios compared to first and second generation PV technologies. Owing to the low material requirements for nano-PV devices, the inexpensive fabrication processes and the high performances achieved through carrier confinement, it is anticipated that the associated costs will drop considerably with the large-scale deployment of such cells [4].

Carbon nanotubes have received least attention amongst the above mentioned nanotechnologies for PV applications given the present relative complexity in synthesising them to the desired physical dimensions that would deliver the electronic properties needed. Nevertheless, in this thesis, it is theoretically demonstrated how their geometrical structures could be optimised for the realisation of a carbon nanotube based tandem solar cell.

1.3 Carbon nanotubes

Declared as one of the greatest breakthroughs in nano-scale science, the discovery of Carbon Nanotubes (CNTs) came about in 1991 during the close inspection of a graphitic soot

produced from an arc-discharge synthesis of buckyball fullerenes (C_{60}) [14, 15]. A Single-Walled CNT (SWCNT) is composed of carbon atoms arranged in a single-layered honeycomb sheet that is self-wrapped into a cylindrical tube as depicted in Figure 1-3. With a large aspect ratio, SWCNT's typically have diameters in the order of 1-2nm and lengths ranging from hundreds of nanometers and above [16, 17].

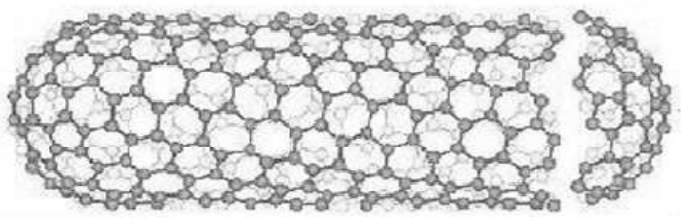

Figure 1-3: A Single-walled carbon nanotube capped with half a buckyball at each end [18].

Due to the intrinsic nature of carbon and the one-dimensional (1D) structure of SWCNTs this offers superior electronic, optical and thermal properties compared to three-dimensional (3D) bulk materials such as silicon [14]. Table 1-1 summarizes some of these distinctive properties and draws a comparison against the corresponding characteristics of Si.

	SWCNTs	**Silicon**
Band-gap (eV at 300K)	0.5-2.0 (semi. SWCNTs)	1.12
Band-gap type	Direct	Indirect
Resistivity (Ωcm at 300K)	10^{-6}	10^{3}-10^{-4} (depending on doping)
Carrier mobility (cm^2/Vs at 300K)	10^{4}	10^{2}-10^{3} (depending on doping)

Table 1-1: Comparison of SWCNT and silicon material characteristics [19, 20].

With respect to their electrical conductivity, SWCNT's can remarkably exhibit semiconducting or metallic behaviour depending on their diameter and chirality (the orientation in which the carbon honeycomb sheet is rolled with respect to its axis) [16]. Such a trait may have significant implications since the SWCNT band-gap can be effectively tuned for a desired application by varying the geometrical structure. This versatile feature has not been witnessed in any other known material [16].

The primary advantage in using semiconducting SWCNT's over conventional bulk semiconductors for devices is that they demonstrate near-ballistic carrier transport due to

their quantum confinement [17]. This results in higher carrier mobilities (almost 100x more mobile compared to silicon) with low recombination losses.

As metallic 1D conductors, where charge can only propagate backwards or forwards, SWCNTs enable carriers to flow with less scattering losses compared to bulk structures [16]. This offers lower resistivity and allows CNTs to sustain large current densities (~10^9 A/cm^2) without dissipating too much power [17]. Further, due to the strong C-C covalent bonds, the SWCNT side-walls are almost perfectly bound with very low defect densities, thus, possessing sound chemical and physical stability [17, 21].

The key challenge concerning SWCNT's at the moment rests in the uncertainty associated with the structural characteristics realised using existing synthesis techniques [14, 16, 17]. That is, even though the diameter can be controlled to some extent, the chirality cannot and hence the electronic properties may vary immensely within a single batch of SWCNT's [16]. In turn this renders irreproducible devices, which, if not rectified, could impede the widespread adoption of SWCNT's [16]. Another major challenge confronting CNTs is defining their spatial location and orientation with respect to the surface they lay upon [16, 17].

Amongst several anticipated applications, including high power-density ultracapacitors and flat-panel displays, CNTs may possibly play a role in future Integrated Circuits (ICs). For instance, there have been suggestions of replacing interconnects with metallic SWCNTs, particularly, in place of vias which interface metal lines between different layers [22]. IBM has been intensely exploring CNT based Field-Effect-Transistors (CNT-FETs) where switching characteristics have been found to outperform that of advanced silicon MOSFET devices [17]. This news has been welcomed by the microelectronics industry as they strive to find novel ways in downscaling conventional CMOS silicon circuits beyond their fundamental physical limit. However, given the impracticality of integrating CNT-FETs on a large scale using present fabrication techniques, the prospects of replacing silicon based FETs is unlikely within the foreseeable future.

Because of their direct band-gap attribute, SWCNTs have also gained a lot of attention in the optoelectronic research arena. Light emitters as well as photo-detectors have been

implemented using semiconducting SWCNT's and have shown promising light emission and absorption at different wavelengths of light [23, 24]. Proposals for an all carbon-based photovoltaic cell have even come to light with ongoing experiments investigating the potential of semiconducting SWCNT's as active materials for photovoltaic conversion [20, 21, 24-26]. In addition, there have been efforts in utilising metallic SWCNT's as transparent conductive contacts for thin-film PV technologies [20, 24].

The latest successful experimental CNT based PV device included a network of semiconducting SWCNTs as a scaffold within a hybrid CNT/Si heterojunction, which exhibited enhanced light-trapping and absorption properties [20, 24]. The resulting conversion efficiency was measured to be around 1.7% for a non-optimised cell [24]. Although this performance is relatively poor compared to conventional cells, it would be valuable to gain an insight on the maximum theoretical efficiency limit for an optimised multi-CNT based PV cell.

The primary aim of this thesis is to develop novel computational methodologies that characterise the electronic and optical properties of SWCNTs with respect to their geometrical structure variability. Further, the methodologies created will be utilised in identifying the theoretical limiting performance achieved by an isolated and tandem SWCNT based solar cell. The chief outcome of this analysis will be to define optimized nanotube geometrical properties that deliver the highest conversion efficiencies within the confines of the assumptions made. Ultimately, this study should supplement experimental efforts in the evaluation of nano-structured solar cells.

1.4 Thesis outline

Chapter 2 gives an introductory overview of present-day solar cell operation presenting standard circuit models used in evaluating their performance and subsequently highlighting the main limitations and optimisations of existing PV technologies. The second part of the chapter reviews all literature concerning the latest implementations of carbon nanotube based PV's. The strengths and shortcomings of each device are addressed, which paves the way for a newly proposed tandem CNT solar cell.

Chapter 3 provides a detailed review of single walled carbon nanotubes where an initial brief discussion is given on their structural features. The associated electronic characteristics are later studied with the development of a semi-empirical Tight-Binding with Zone Folding model that generates the SWCNT band-structure. It is confirmed that the CNT band-structure is appreciably altered with respect to its geometrical properties.

In Chapter 4, the first contribution of this thesis is made where the band-structure is calculated for a number of structurally dissimilar SWCNTs and the resulting band-gap and carrier effective mass are derived. As an outcome, a simulation-efficient and accurate analytical model is created for distinguishing metallic and semiconducting tubes. Furthermore, a band-gap model for semiconducting tubes is established. These proposed analytical models are verified against other semi-empirical and *ab-initio* approximations as well as experimental data. The chapter is concluded with the development of carrier effective mass models for achiral and chiral SWCNTs, which are also validated against previously reported results.

Chapter 5, which presents the second contribution of this thesis, deals with the uncertainty associated with the CNT geometrical properties and endeavours to statistically model the variation in band-gap and effective mass with respect to the mean diameter (d_μ) and standard deviation (d_σ). The typical distributions for CVD grown CNT structural parameters are firstly discussed and identified. Subsequently, the models derived in Chapter 4 are used in running a set of Monte Carlo simulations where the spread in band-gap and carrier effective mass are calculated for the corresponding structural parameter distribution. By establishing analytical expressions for the CNT band-gap and effective mass variability, insight is offered on optimising diameter-related process parameters in order to suppress variation.

Chapter 6 is concerned with modelling the optical absorption properties of SWCNTs using first order perturbation theory. Here, the Tight-Binding and Zone Folding method is employed once again in deriving the Transition Rate (TR) for a SWCNT when exposed to laser illumination. This technique is utilised in identifying the photo-generated current and quantum efficiency spectral responses for a range of single nanotubes giving new insights on the optimal CNT geometrical structure for optoelectronic applications. The adopted novel

approach is compared and validated against experimental as well as other theoretically simulated results.

In Chapter 7 a framework of assumptions is initially outlined with respect to the SWCNT PV devices investigated. By employing the ideal equivalent circuit model of a PV cell we determine the short-circuit current, open-circuit voltage, fill factor and conversion efficiency of various isolated SWCNT solar cells under the standard AM0 as well as AM1.5 solar irradiation spectrum. The performance of a conceptually proposed CNT based tandem cell is later calculated when exposed to solar illumination. Lastly, the optimized nanotube structural properties are analysed and defined for each photovoltaic converter in addition to the optimal number of SWCNTs required for a tandem solar cell.

Chapter 8 summarizes the key outcomes and contributions of this thesis as well as the feasibility of exploiting SWCNTs towards the development of a tandem PV device. This is followed by recommendations for future work.

The appendices include supporting material as well as a list of peer-reviewed papers that have resulted from this PhD project (see Appendix D).

Chapter 2 Introduction to Solar Cells and CNT based Photovoltaic Devices

In this chapter, firstly an overview of the operation of present-day solar cells will be discussed in Section 2.1 followed by Section 2.2 where their effectiveness and main technology limitations will be outlined. Next, an up-to-date literature review of Carbon Nanotube (CNT) based devices and photodiodes will be presented in Section 2.3 highlighting their strengths and shortcomings. In the final section, Section 2.4, a proposed hypothetical CNT based solar cell architecture will be revealed, upon which this thesis will endeavour to study and model in detail.

2.1 Basic operation of solar cells

A solar cell is an energy conversion device that generates electrical energy directly from the absorption of light energy. The source of light energy, usually typified by the sun, is generally represented by a black body radiator that emits photons (quanta of radiation) with wavelengths ranging from the ultraviolet (~0.3μm) to the infrared (~2.6μm) region of the electromagnetic spectra [19]. This is illustrated in Figure 2-1, which depicts a comparison between terrestrial measurements made of the suns' emitted power density per unit photon energy, also known as the solar irradiance, and the irradiance emitted from a black body radiator at 5800K [19]. When both graphs are compared, it can be observed that the black body approximation provides a reasonable match to the suns' measured irradiance spectrum

from earth (Air Mass AM=1.5) [27]. Notably, the solar radiation spectrum is shown to extend across a broad range of photon energies E_p= 0.48- 4.13eV.

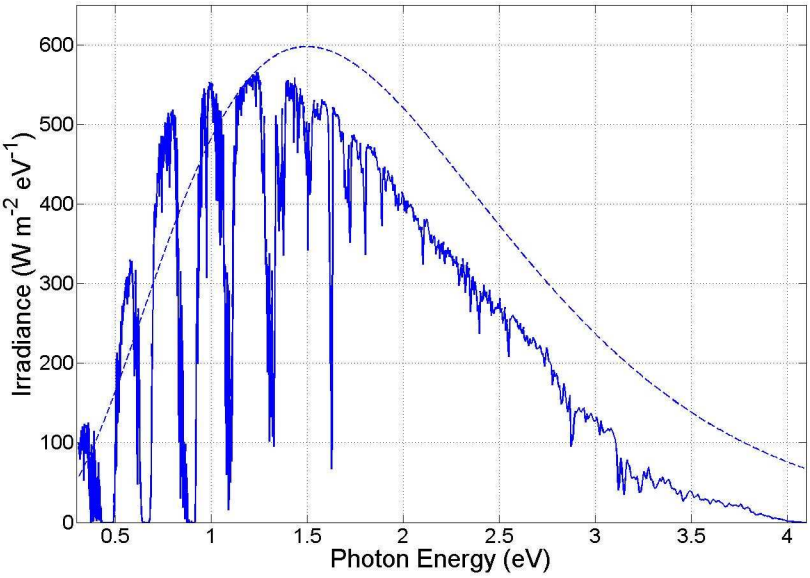

Figure 2-1: A standard terrestrial (AM=1.5) solar irradiance spectrum (—) and an approximation of a black body radiator at T_s=5800K given by Plank's Law (---).

Unlike solar thermal energy conversion where heat is exchanged from a hot body to a cool object causing a rise in the internal kinetic energy, solar cells convert the absorbed photon energy into electrochemical potential energy [28]. This process is recognised as the photovoltaic (PV) effect.

By in large, PV converters are made of semiconducting materials, which hold most of their electrons at a ground state separated entirely from a higher potential energy state by a forbidden gap E_g [11]. When a photon is absorbed in a semiconductor possessing a band-gap $E_g = E_p$, an electron transitions to the excited state leaving behind a hole (positive ion) [11]. All photons with energies $E_p < E_g$ are not absorbed and transmit through the semiconductor as if it were transparent [19]. Conversely, if $E_p > E_g$, an electron-hole pair is produced and the excess energy (E_p-E_g) is rapidly dissipated as heat, that is, the electron-hole pair undergoes 'thermalisation' to the edges of their respective bands [28].

To complete the PV conversion process, the electron-hole pairs are quickly separated from their point of creation with the support of a built-in electric field that is set-up by an asymmetric junction in the device [28]. A contact with a raised electrochemical potential

collects electrons before they relax to the ground state and, equally, the holes are collected at the other end contact with a lower electrochemical potential [28]. A photocurrent is produced as a result, which flows into an external circuit. The extra potential energy of the excited electrons establishes a potential difference, or photovoltage, across the cell terminals that drives electrons through a load where electrical work is done [28].

2.1.1 Process of photon absorption and radiative recombination

Under illumination, the photocurrent density ($J_{abs}(E_p)$) generated in a semiconducting material by the absorption of a photon with a given energy E_p is related to:

1) The incident solar photon flux density (number of photons per unit area per second per photon energy- ϕ_s),
2) The probability of photon reflection (R),
3) The absorbance (the probability of photon absorption -a).

This is denoted by Eq. 2.1 where q corresponds to the unit electron charge. Given a non-reflecting semiconductor, Eq. 2.1 assumes that if each absorbed photon generates one electron, then, the electron photocurrent density (J_{abs}) and the photon flux density are equivalent with a constant multiple of q [28].

$$J_{abs}(E_p) = q\left(1 - R(E_p)\right)a(E_p)\phi_s(E_p) \qquad 2.1$$

where:

$$a(E_p) = \begin{cases} 1 & E_p \geq E_g \\ 0 & E_p < E_g \end{cases} \qquad 2.2$$

and

$$\phi_s\left(E_p\right) = \frac{2F_s}{h^3c^2}\left(\frac{E_p^2}{e^{E_p/k_BT_s} - 1}\right) \qquad 2.3$$

The absorbance is dictated by the material properties and is commonly described as a function of the absorption coefficient $\alpha(E_p)$. However, in this introductory chapter it is sufficient to express it as a step-like function characterised by Eq. 2.2. The absorbance is also significantly influenced by the optical path length within the semiconductor [28].

The incident photon flux density per unit energy ($n_{ph}s^{-1}m^{-2}eV^{-1}$) provided by Eq. 2.3 represents the generalised form of Plank's radiation law per photon energy where k_B is the Boltzmann constant, c is the speed of light and T_s is the surface temperature of the black body radiator in Kelvins [28]. The geometrical factor F_s is a term related to the angle subtended between the incoming direction of the light and the normal to the solar cell surface and will be considered a fixed constant of $6.79\text{x}10^{-5}$ as in [28].

As well as absorbing radiation, the cell emits photons. Under thermal equilibrium (*i.e.* no exposure to illumination and no applied bias) the cell acts as a black body and emits thermal radiation characteristic of its temperature T. This emission can occur spontaneously where electrons relax from their excited state to the ground state producing a photon of light with energy equivalent to the potential energy released [28]. Due to this unavoidable spontaneous emission the performance of a photovoltaic cell will always be limited [28, 29].

Spontaneous emission can be further intensified when the cell is in a non-equilibrium state. Under illumination the electron population is raised in potential energy, which in turn causes the system to develop a finite electrochemical potential difference between the electrode terminals $\Delta\mu = qV > 0$ [28]. This potential difference facilitates more electrons in relaxing to their ground state and recombining with holes. As a result, the rate of emission is dependent upon $\Delta\mu$ [28]. Akin to Eq. 2.3, the photon flux emitted from the cell (ϕ_c) per photon energy due to $\Delta\mu$ can be expressed as follows:

$$\phi_c(E_p, \Delta\mu) = \frac{4\pi}{h^3c^2}\left(\frac{E_p^2}{e^{(E_p-\Delta\mu)/k_BT}-1}\right) \qquad 2.4$$

The geometrical factor F_s has been replaced with 2π in Eq. 2.4 since the solar cell may be considered isotropic, that is, the cell can emit photons in any direction [8]. Now if the

probability of photon emission, the emissivity (ε), is known for a given cell then the current density for radiative recombination ($J_{rad}(E_p, \Delta\mu)$) for a given E_p and $\Delta\mu$ can be defined as:

$$J_{rad}(E_p, \Delta\mu) = q(1-R(E_p))\varepsilon(E_p)\phi_c(E_p, \Delta\mu) \qquad 2.5$$

Thus, using Eq.2.1 and Eq. 2.5, the net equivalent current density for a given photon energy can be denoted by Eq. 2.6 [28].

$$\begin{aligned} J_{net}(E_p, \Delta\mu) &= J_{abs}(E_p) - J_{rad}(E_p, \Delta\mu) \\ &= q(1-R(E_p))\left[a(E_p)\phi_s(E_p) - \varepsilon(E_p)\phi_c(E_p, \Delta\mu)\right] \end{aligned} \qquad 2.6$$

Under a steady state where the concentration of electrons remains constant, the rate of photon emission by the cell must balance with the rate of photon absorption according to the theory of *detailed balance* [8, 12, 28]. That is, the absorbance and emissivity should match as denoted by:

$$a(E_p) = \varepsilon(E_p) \qquad 2.7$$

Further, in [30] it was theoretically confirmed from a generalised detailed balance argument that the cell absorbance is equal to the emissivity under a non-equilibrium bias ($\Delta\mu > 0$) operation [12, 28, 30]. This assumption holds given that $\Delta\mu$ is constant throughout the device [30].

2.1.2 Process of charge separation and collection

Given the generation of an electron-hole pair, a solar cell achieves charge separation with the aid of an intrinsically induced electrostatic field caused by an asymmetric rectifying junction. The junction can be realised by either selectively contacting a semiconducting material with metal, effectively producing a Schottky barrier, or doping a semiconductor into *n* and *p* type regions [28]. The emergence of a potential barrier at the junction provides a low resistance path for electrons to the *n* contact (blocking any positive charge flow), and for holes to the *p* contact (blocking any negative charge flow) [28].

A schematic representation of a typical silicon solar cell *pn* junction is shown in Figure 2-2 [11]. It could be seen that the *pn* junction is shallow near the exposed surface, which is

covered in anti-reflection coating to minimise $R(E_p)$ [11]. A set of ohmic contact stripes, known as finger grid contacts, are deposited on top of the *n*-doped silicon to minimise light reflection off the top surface [19]. However, the entire back surface of the p^+ type silicon is covered by a rear ohmic contact in an attempt to maximise reflection and subsequent absorption at the junction [11].

The carrier concentration gradient across the *pn* junction forms a depletion region whereby a built-in potential (V_{bi}) is established [31]. At equilibrium this prohibits the flow of the majority carriers across the junction [28, 31].

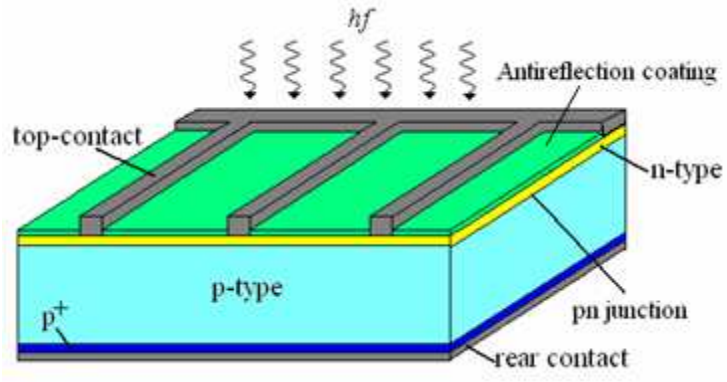

Figure 2-2: Schematic of a *pn* junction silicon solar cell [32].

When the device is subjected to a light source (*i.e.* non-equilibrium operation), the absorbed photons converted into electron-hole pairs are subsequently separated by the built-in potential where free electrons and holes are swept into the *n* side and *p* side, respectively [31].

If the contacts are located within a diffusion length (the average distance a carrier moves from point of generation until recombination) of the point of generation and material defects/impurities are low then the non-radiative recombination losses are minimised and the excess carriers collect at the electrodes [31]. In turn, these 'collected excess carriers' generate a finite current, the photocurrent (I_p), in the external circuit [31]. Assuming that the charge separation, transportation and collection in the device can all occur with a probability η_c and $a(E_p)=\varepsilon(E_p)$ using the detailed balance result, the photocurrent density is obtained by integrating J_{net} over all photon energies:

$$J_p = q\int_0^{\infty} \eta_c(E_p)\left(1-R(E_p)\right)a(E_p)\left(\phi_s(E_p)-\phi_c(E_p,\Delta\mu)\right)dE_p \qquad 2.8$$

or expressed in terms of the Quantum Efficiency, $QE(E_p)$:

$$J_p = q\int_0^{\infty} QE(E_p)\left(\phi_s(E_p)-\phi_c(E_p,\Delta\mu)\right)dE_p \qquad 2.9$$

The quantum efficiency is a good indicator of the number of electron-hole pairs generated and delivered to the external circuit per incident photon. Usually, due to factors such as incomplete photon absorption, reflection, radiative relaxation, imperfect charge separation, material-defect induced recombination and collection losses, the resulting *QE* value is less than 1 [19]. Nevertheless, if the ideal case of *QE* =1 is considered for all absorbed photon energies (*i.e.* $\eta_c(E_p)=1$, $R(E_p)=0$, $QE(E_p)=a(E_p)$) then:

$$J_{p(\max)} = q\int_{hf=E_g}^{\infty} \left(\phi_s(E_p)-\phi_c(E_p,\Delta\mu)\right)dE_p \qquad 2.10$$

Equation 2.10 offers the maximum photocurrent density for a given material band-gap provided that multiple carrier generation –the promotion of more than one electron by an absorbed photon - does not take place [28]. For a bias $\Delta\mu$ =0, this results in a photocurrent density curve as shown in Figure 2-3.

Figure 2-3 demonstrates that as the band-gap increases, less photons are absorbed generating a small photocurrent ($J_{p(max)}$) [19]. An important point to note is that the photocurrent density is predominantly a function of the semiconductor band-gap (E_g), the quantum efficiency and the incident photon radiation [19, 28].

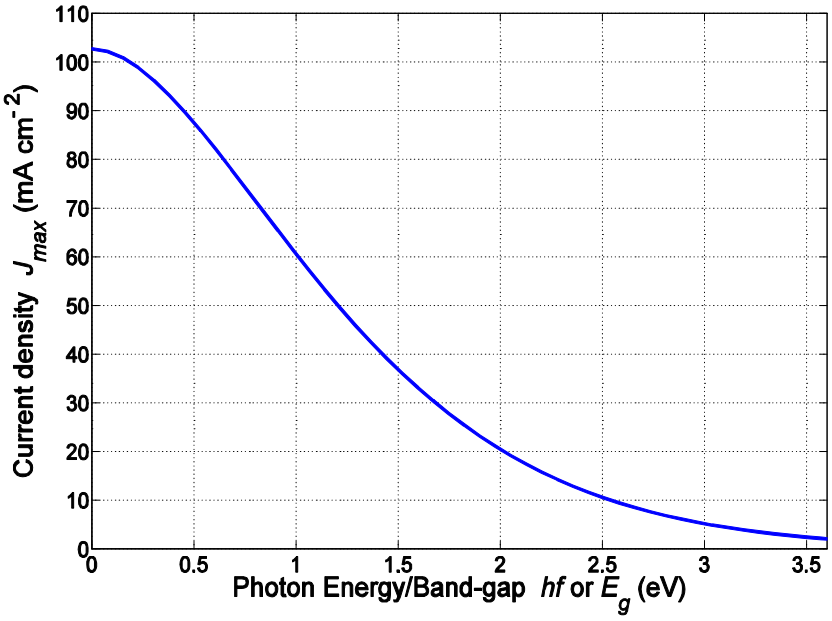

Figure 2-3: Maximum photocurrent density generated from Eq. 2.10 for an ideal solar cell with band-gap E_g.

2.1.3 Ideal equivalent circuit model and conversion efficiency

A solar cell can be considered similar to a photodiode detector, although the device designs are fundamentally different. This is because the photodiode has to only detect a narrow wavelength range centred at the optical signal wavelength, whereas, solar cells must possess a wide spectral response over a broad solar wavelength range [19].

Unlike photodiodes where the quantum efficiency is one of the key figures of merit, solar cells are evaluated based on how well they convert the incident light power (P_{in}) to power delivered to the load (R_L) [19]. This is denoted by the power conversion efficiency (η), which will be derived using the ideal equivalent circuit of the solar cell given in Figure 2-4. Figure 2-4 shows the solar cell as a current source in parallel with an asymmetric, non-linear resistive element (*i.e.* a diode) [28].

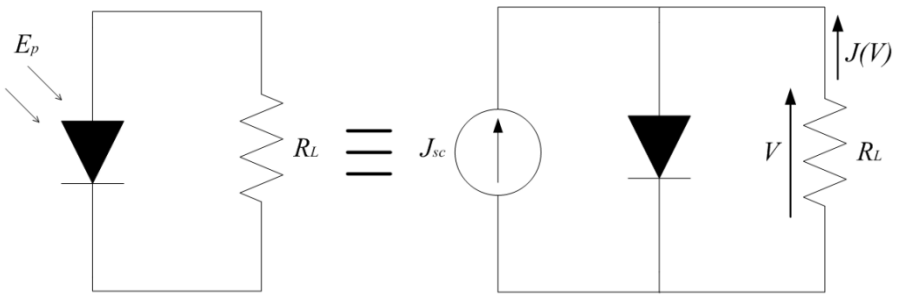

Figure 2-4: One-diode ideal equivalent circuit model for PV under illumination.

The constant current-source represents the short-circuit current density (J_{sc}) due to photo-absorption, which is equivalent to the photocurrent density (J_p denoted by Eq. 2.8) without taking account of radiative-recombination. The current flowing through the diode represents the reverse, or dark, current that arises when a bias is applied to the solar cell in the dark [28]. The generated photocurrent is divided between the variable resistance of the diode and the load (R_L) [28]. When the load resistance is higher than the operating point of the cell, more of the photocurrent flows through the diode, resulting in a high potential difference across the PV cell and a small current through the load [28]. Hence, the diode regulates the photovoltage of the cell [28].

From the equivalent circuit model, the steady-state ideal *J-V* characteristics can be derived as follows:

$$J(V) = J_{sat}(e^{qV/nk_BT} - 1) - J_{sc} \qquad 2.11$$

where the diode current is given by the Shockley equation pertaining an ideality factor characterised by n (normally 1 for an ideal diode and approaches 2 with higher defects) and J_{sat} represents the diode saturation current density given by [11]:

$$J_{sat} = q\sqrt{k_BT}N_cN_v\left(\frac{1}{N_D\sqrt{m_p^*}} + \frac{1}{N_A\sqrt{m_n^*}}\right)e^{-E_g/k_BT} \qquad 2.12$$

As can be seen the saturation current is very much dependent upon the device properties such as the effective density-of-states in the conduction and valence band, N_c and N_v, respectively [11]. N_D and N_A are the donor and acceptor dopant concentrations,

respectively. m_n^* and m_p^* are the effective masses of the electrons and holes, respectively. From Eq. 2.12 it can be reasoned that the material band-gap along with the cell temperature have an overriding influence on the saturation current, resulting in lower values with higher E_g.

Effectively, Eq. 2.11 approximates the net current as the difference between the absorbed and emitted flux densities as previously established in Eq. 2.8 with $\Delta\mu = qV$ [19, 28]. That is, as V increases the emitted flux grows owing to greater spontaneous emission and consequently the net current decreases rapidly [28]. When the net current is zero (*i.e.* the absorption current and dark current are equivalent) at a voltage point acknowledged as the open-circuit voltage (V_{oc}), the absorbed and emitted flux are precisely balanced [28].

For a device with J_{sc} = 50mA/cm^2, J_{sat} = 0.5 nA/cm^2, n = 1 and T = 300K, the J-V curve can be plotted as shown in Figure 2-5.

Since the curve is passing through the fourth quadrant this means that power is being delivered to the load R_L from the device [11]. It is therefore necessary that V never drops below 0V or exceed $V_{oc} = E_g/q$ as power will be consumed by the device acting as a photodetector or a light emitting diode, respectively [28]. A central assumption to this ideal model is that J_{sc} is constant for a given incident light intensity and is independent of the voltage V [33].

The maximum power density rectangle of Figure 2-5 corresponds to the maximum power output ($P_m = J_m V_m$) that occurs at voltage V_m with a corresponding current J_m [19]. Thus, the optimum load sheet resistance must be matched to V_m/J_m, which is achieved using an external load controller device recognised as the Maximum Power Point Tracker (MPPT) [28]. The output power density is denoted by:

$$P = VJ = VJ_{sat}\left(e^{qV/nk_BT} - 1\right) - VJ_{sc} \qquad 2.13$$

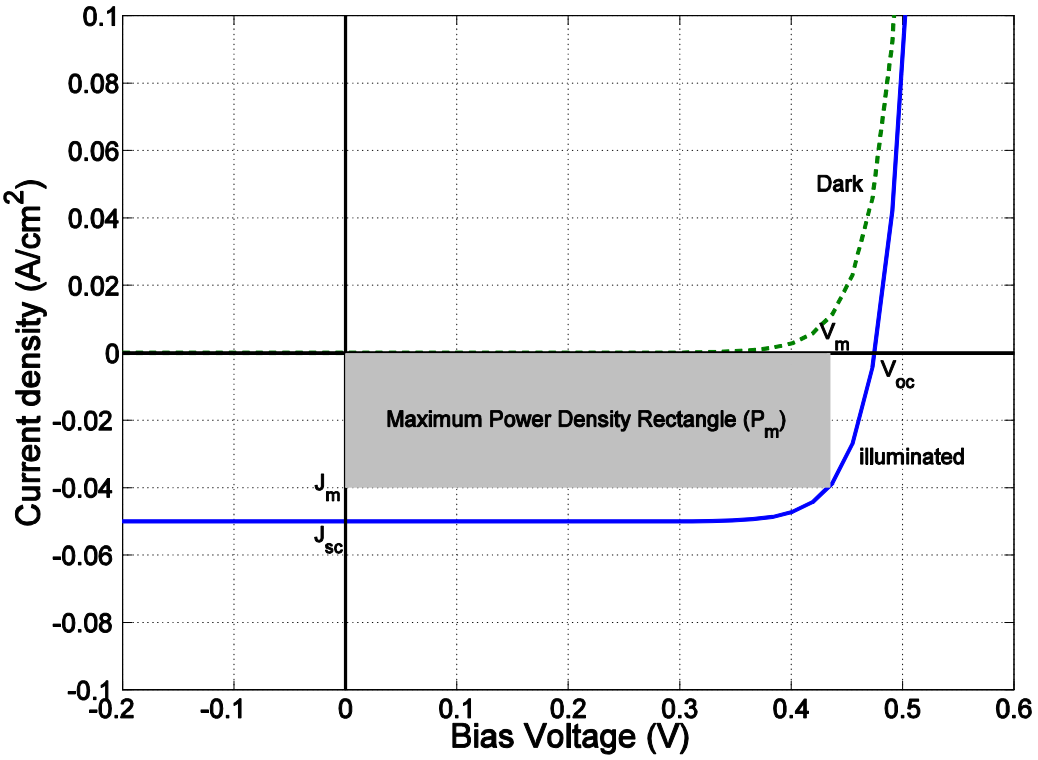

Figure 2-5: *J-V* characteristic of a solar cell device under dark (---) and illuminated (—) conditions.

To obtain the maximum power operating point one must solve for $dP/dV = 0$, which gives:

$$V_m = \frac{nk_BT}{q}\ln\left[\frac{1+(J_{sc}/J_{sat})}{1+(qV_m/nk_BT)}\right] = V_{OC} - \frac{nk_BT}{q}\ln\left(1+\frac{qV_m}{nk_BT}\right) \qquad 2.14$$

where the open-circuit voltage (V_{OC}) can be determined from Eq. 2.11 by setting $J(V) = 0$ giving:

$$V_{OC} = \frac{nk_BT}{q}\ln\left(\frac{J_{sc}}{J_{sat}}+1\right) \approx \frac{nk_BT}{q}\ln\left(\frac{J_{sc}}{J_{sat}}\right) \qquad 2.15$$

The open-circuit voltage (V_{OC}) is characteristic of the built-in potential of the *pn* junction and according to Eq. 2.15 is shown to increase logarithmically with the ratio J_{sc}/J_{sat} [28]. As mentioned above, V_{OC} can also be estimated by the semiconductor band-gap since the quantity E_g/q represents the upper voltage limit for photovoltaic conversion [19]. This, however, is not perfectly accurate because of the unavoidable radiative recombination conveyed by J_{sat}, which effectively forces the upper voltage limit downwards. Take for

example silicon (E_g=1.1eV), where it would be expected to have an open-circuit voltage of 1.1V, but in reality V_{OC}~0.7V.

The corresponding current density at V_m is:

$$J_m = J_{sat}\left(\frac{qV_m}{nk_BT}\right)e^{qV_m/nk_BT} \approx J_{sc}\left(1-\frac{1}{qV_m/nk_BT}\right) \qquad 2.16$$

Therefore, the maximum power output density P_m is:

$$P_m = J_mV_m = J_{sc}\left[V_{OC} - \frac{nk_BT}{q}\ln\left(1+\frac{qV_m}{nk_BT}\right) - \frac{nk_BT}{q}\right] \qquad 2.17$$

The power conversion efficiency of a solar cell, which is the ratio of the maximum power output density (P_m) to the incident power density (P_{in}) is given by Eq. 2.18 [11].

$$\eta = \frac{J_mV_m}{P_{in}} = \frac{V_m^2J_{sat}(q/nk_BT)e^{qV_m/nk_BT}}{P_{in}} \qquad 2.18$$

P_{in} can be obtained by integrating the photon irradiance (power per unit area per unit photon energy) over the complete solar spectrum [11]. Another method to ascertain this would be by integrating the product of the incident photon energy and flux density of Eq.2.3 as given in Eq. 2.19.

$$P_{in} = \int_0^\infty E_p\phi_s(E_p)dE_p \qquad 2.19$$

Another common representation of the conversion efficiency is with respect to the Fill Factor (FF):

$$\eta = \frac{FF.J_{sc}V_{OC}}{P_{in}} \qquad 2.20$$

where FF is defined as:

$$FF = \frac{J_m V_m}{J_{sc} V_{OC}} = 1 - \frac{nk_B T}{qV_{OC}} \ln\left(1 + \frac{qV_m}{nk_B T}\right) - \frac{nk_B T}{qV_{OC}} \qquad 2.21$$

The fill factor is a ratio of the maximum power density rectangle to the product $J_{sc}V_{OC}$ [19]. This quality parameter is a measure of the 'squareness' of a *J-V* curve and is always less than 1 due to the roundness of the exponential *J-V* curve [34]. The closer FF is to unity, the more the PV will resemble a constant current source and the higher the delivered power. In practice FF tends to be around 0.8 [19].

In order to optimise the conversion efficiency of Eq. 2.20, the quantities: FF, J_{sc} and V_{OC} have to be maximised [11]. Intuitively, to obtain a large V_{OC}, a large band-gap is required [19]. On the other hand, it was shown in Figure 2-3 that the photocurrent (J_p or J_{sc}) decreases with higher band-gap [19]. So there exists a compromise between photocurrent and open-circuit voltage, which are both strongly dictated by the material band-gap [19].

Assuming that the fill factor of Eq. 2.20 is unity and the open-circuit voltage is only related to the band-gap (*i.e.* $V_{OC} = E_g/q$), the ideal efficiency of a single band-gap solar cell operating under an AM =1.5 condition is calculated and shown in Figure 2-6 as a function of the band-gap energy [19].

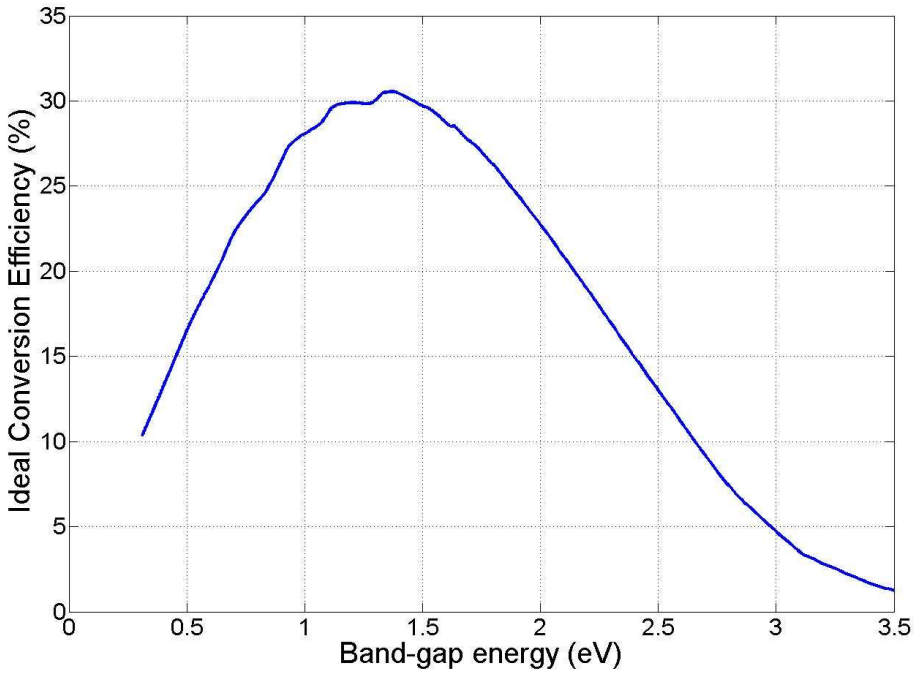

Figure 2-6: Ideal solar-cell conversion efficiency under AM=1.5 solar radiation vs. band-gap energy E_g.

From Figure 2-6 it can be deduced that the peak conversion efficiency achieved is 31% (at E_g=1.4eV), which is in agreement with the well-known Shockley-Queisser limit [6, 8]. Crucially, it can be observed that under an AM=1.5 illumination the ideal PV efficiency curve is fairly broad, where a sizable range of semiconductor band-gaps, 0.7-2.1eV, can provide efficiencies above 20% [4, 19]. Figure 2-6 additionally reinforces what was mentioned earlier, that low band-gaps demote V_{OC} and hence suppress performance whilst high band-gaps lead to small magnitudes of photocurrent (J_{sc}) also resulting in poor operation. Hence, from this argument, one could infer that optimising PV efficiency boils down to choosing the appropriate material for a given incident spectrum [28].

The curve of Figure 2-6 presumes no potential energy loss to the carriers caused by resistances anywhere in the circuit [28]. In practice, this is not the case because the current-voltage characteristic is not perfectly rectangular and a voltage drop exists at the cell junction and contacts, which shall be addressed in the following section [6, 8].

2.1.4 Non-ideal PV equivalent circuit model

Apart from the unavoidable radiative-recombination, additional factors that degrade the conversion efficiency of any PV converter can be characterised by resistive components as shown in the non-ideal one-diode equivalent circuit model of Figure 2-7.

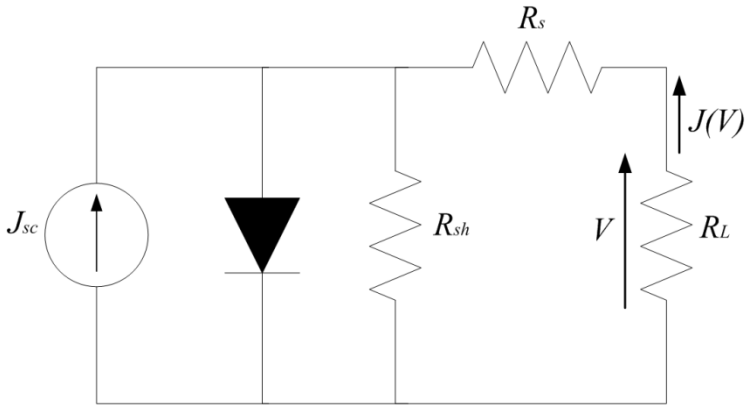

Figure 2-7: One-diode non-ideal equivalent circuit model under illumination.

The parasitic series resistance, R_s, arises mainly from the resistance of the metal contacts as well as the resistance experienced by carrier flow in the *n*-type and *p*-type regions due to impurity concentrations [11]. The series resistance is also augmented by thicker

junction depths where charge is required to travel longer distances. R_s can be a major impediment to solar cell performance particularly when operating at high photocurrents [28].

The shunt resistance R_{sh} is used to model leakage currents caused mainly by non-radiative recombination of electron-hole pairs [19]. This can usually arise across a *pn* junction owing to the presence of incomplete bonds at sites with extrinsic and intrinsic defects. The incomplete dangling bonds effectively introduce energy states in the forbidden gap (traps), which act as recombination centres that provide shunting paths for current flow across the junction [31]. It is important to note that non-radiative recombination occurs over a shorter time-scale compared to its radiative counterpart.

The *J-V* characteristic of the non-ideal equivalent circuit model can be described by Eq. 2.22:

$$f(J(V),V) = J(V) + J_{sc} - J_{sat}\left(e^{\frac{q(V-J(V)R_s)}{nk_BT}} - 1\right) - \frac{V - J(V)R_s}{R_{sh}} = 0 \qquad 2.22$$

which can be rewritten as:

$$J(V) = \frac{1}{\left(1+\frac{R_s}{R_{sh}}\right)}\left[J_{sat}\left(e^{\frac{q(V-J(V)R_s)}{nk_BT}} - 1\right) - J_{sc} + \frac{V}{R_{sh}}\right] \qquad 2.23$$

In the ideal case where R_s= 0 and R_{sh}= ∞, Eq. 2.23 reduces to the ideal form given by Eq. 2.11 in the previous section. Since Eq. 2.22 is an implicit equation, it can be solved using numerical methods. Here, the Newton-Raphson approach is employed as detailed in Appendix A given its good accuracy and quadratic rate of convergence [35].

2.1.5 Analysing the effects of series and shunt resistance on the J-V characteristics

To obtain the open-circuit voltage due to the resistive components of the non-ideal circuit *J(V)* is considered as zero in Eq. 2.23, yielding the following expression:

$$V_{oc} = \frac{nk_BT}{q}\ln\left(\frac{J_{sc} - V_{oc}/R_{sh}}{J_{sat}} + 1\right) \qquad 2.24$$

Equation 2.24 confirms that V_{oc} still depends on the ratio J_{sc}/J_{sat} but is equally influenced by an additional factor associated with the leakage through R_{sh}. Examining the equation further, it could be established that the open-circuit voltage falls considerably as the shunt resistance is reduced, thereby undermining the fill factor of the PV cell. The effects of a decreasing R_{sh} on the *J-V* characteristic can be illustrated in Figure 2-8 where all other variables remain constant. With lower shunt resistances, the slope of the *J-V* curve can be seen to get significantly steeper tending towards a linear ohmic profile that relates to $1/R_{sh}$. It is worth pointing out that the series resistance has no impact on the open-circuit voltage because no net output current is flowing in the external circuit.

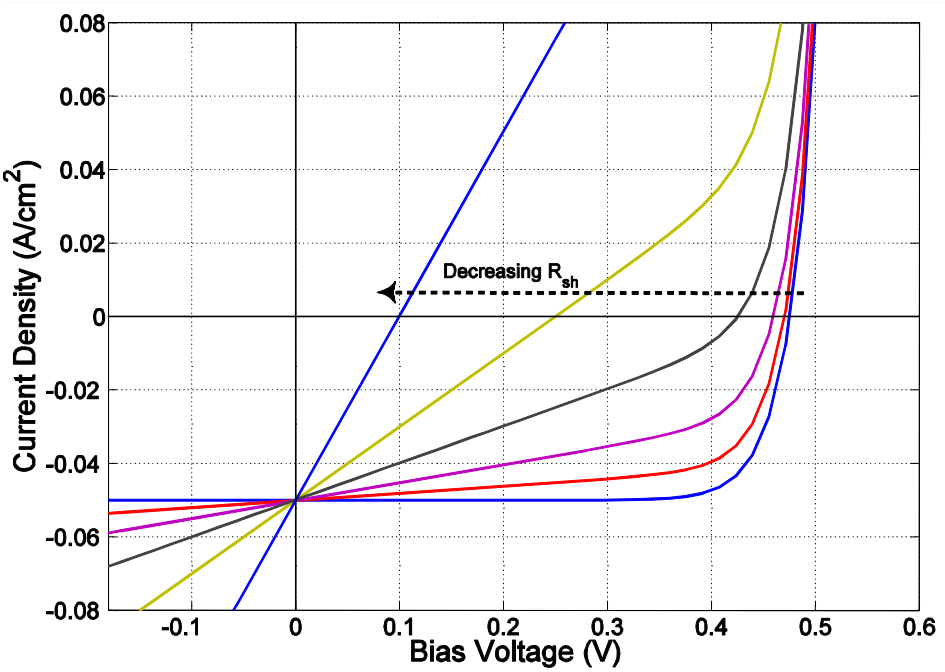

Figure 2-8: *J-V* characteristic for example PV cell with R_s=0Ω and R_{sh}=∞,50,20,10,5,2Ω.

Conversely, when no load is present (*i.e.* R_L=0 and V= 0), the output current is:

$$J(0) = \frac{1}{\left(1 + \frac{R_s}{R_{sh}}\right)}\left[J_{sat}\left(e^{\frac{q(J(0)R_s)}{nk_BT}} - 1\right) - J_{sc}\right] \qquad 2.25$$

Assuming that R_{sh}>>R_s, this leads to a negligible R_s/R_{sh} ratio and therefore it can be deduced from Eq. 2.25 that R_s has a dominant effect on the output current at 0V. Figure 2-9

shows a considerable decrease in the net output current when the series resistance is increased, in turn diminishing the Fill Factor. Moreover, for the highest series resistance a 'linearization' effect is once again observed in the *J-V* curve, exhibiting a gradient equal to $1/R_s$. The *J-V* characteristics additionally confirm that the open-circuit voltage is unchanged with a varying series resistance.

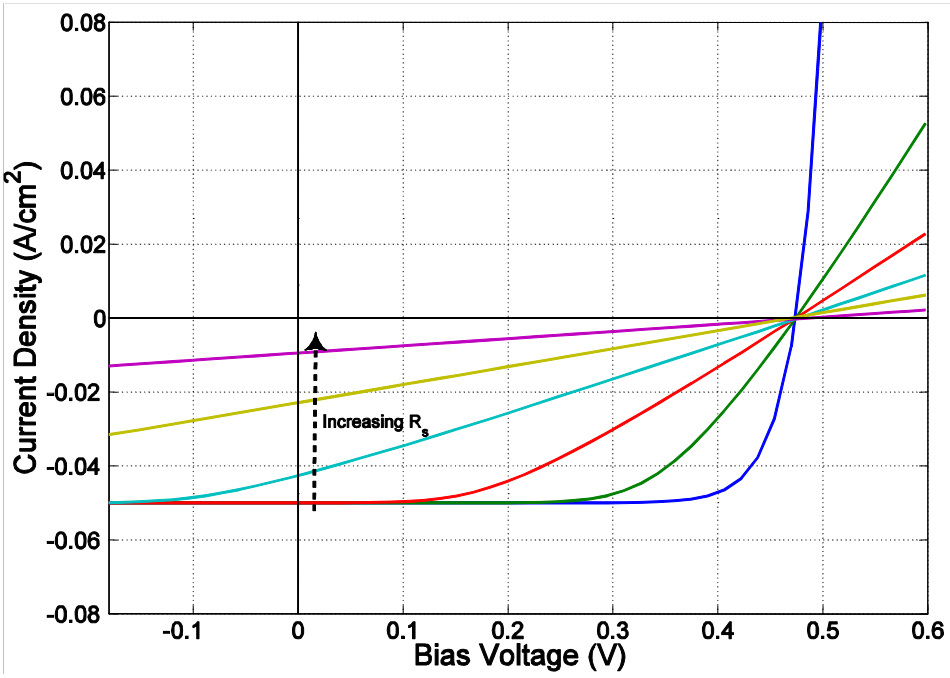

Figure 2-9: *J-V* characteristic for example PV cell with $R_{sh}=\infty\Omega$ and $R_s=0,2,5,10,20,50\Omega$.

2.2 Conventional photovoltaic design issues and optimisations

To-date, a rich variety of solar cell designs have emerged with the aim of improving light absorption, charge separation, transport and collection [28]. The following sub-sections discuss PV design considerations and the most widely-used solar cell architectures at present.

2.2.1 Single-junction solar cells

As previously mentioned, charge separation in PVs is achieved at a junction, which can either be between two different materials – a heterojunction – or between two layers of the same semiconductor that are doped differently – a homojunction [28]. Homojunctions have an advantage over heterojunctions as they do not suffer from recombination losses that arise at the defect tainted metallurgical interfaces [28]. Also, preparing a homojunction from a

single crystal semiconductor wafer alleviates the fabrication process compared to a heterojunction. Thus, the majority of solar cells today are based on a single *pn* homojunction as shown in Figure 2-2.

Silicon is the most commonly used material for present-day homojunction based PVs given that it possesses a single band-gap (1.1eV) which is reasonably optimised for the AM1.5 solar spectrum (see Figure 2-6) [9, 28]. This means that only photon energies above 1.1eV can be absorbed resulting in poor absorption within the infra-red (IR) region, which approximately covers a 20% portion of the solar spectrum [4]. Moreover, generated electron-hole pairs with energies in excess of 1.1eV must thermalise to the fundamental band-gap and in the process dissipate kinetic energy to the silicon lattice. In turn, this causes a temperature rise that exacerbates the saturation current and brings down V_{OC} considerably [28].

The most notable disadvantage with using silicon is that it has an indirect band-gap, which demands the assistance of phonons – lattice vibrations – during the photon absorption process in generating an electron-hole pair [28]. Consequently, this leads to weaker optical absorption compared with a direct band-gap semiconductor [9, 28]. For this reason, thicker silicon is needed in order to surpass the long absorption depths (10^4 cm^{-1} for a 500nm wavelength light-source) required, which ultimately results in more costly PV cells [9].

There have been solutions in minimising the cost of silicon solar cells such as the use of thin-film layers of polycrystalline and amorphous silicon. These semiconducting layers can be readily deposited on an inexpensive foreign substrate (e.g. glass, plastic, metal or ceramic) by relatively low-cost methods such as Chemical Vapour Deposition (CVD) [19]. Although thin-film solar cells have delivered the lowest manufacturing cost, they have a low efficiency of only 5% primarily as a result of the poor material quality. It is widely accepted that utilising polycrystalline or amorphous materials gives rise to the grain-boundary effect where the carrier diffusion lengths are too short compared to the absorption depth. This entails considerable collection inefficiencies [11, 28].

Hence, it is clear that silicon PVs are currently locked in a cost vs. efficiency trade-off. Another important compromise pertains to the doping level of the *pn* junction.

It was mentioned earlier that V_{OC} is related to the built-in potential (V_{bi}) of the *pn* junction, which is defined as:

$$V_{bi} = \frac{k_B T}{q} \ln\left(\frac{N_A N_D}{n_i^2} \right) \qquad 2.26$$

where n_i is the intrinsic carrier density at thermal equilibrium [11]. Therefore, in order to achieve a high V_{OC}, or a high V_{bi}, this implies that the acceptor and donor doping concentrations must be intensified. Moreover, as denoted by Eq. 2.12, higher doping concentrations lead to lower saturation current densities (J_{sat}). On the other hand, the width of the depletion region across the *pn* junction (which facilitates carrier collection) is narrowed down with higher doping concentrations [28]. This is conveyed by Eq. 2.27 where ε_s is the semiconductor permittivity [11, 28].

$$W = \sqrt{\frac{2\varepsilon_s}{q}\left(\frac{1}{N_A} + \frac{1}{N_D} \right) V_{bi}} \qquad 2.27$$

Consequently, the doping level must be controlled to provide the best compromise between cell voltage and recombination losses from the reduced depletion width [28]. This necessitates accurate, high temperature thermal diffusion techniques that can be very energy intensive.

Other design considerations that must be taken into account when fabricating a *pn* junction cell include:

1) The junction should be shallow, as shown in Figure 2-2, to ensure that it is within a diffusion length from the top contact and avoid high-energy photons from being susceptible to surface recombination [28].
2) The top semiconducting layer should be heavily doped compared to the bottom layer in order to reduce the series resistance with the front contact and maximise V_{bi}, which in turn increases V_{OC} [28]. This also thickens the depletion width within the bottom layer facilitating better collection (*i.e.* longer diffusion lengths) at the back contact without limiting V_{OC} [28].

3) Light reflection *R(E)* should be minimised by treating the semiconductor with an anti-reflective coating as depicted in Figure 2-2 [28]. This is a material with a refractive index between the semiconductor and air that enables optical impedance matching [28].

The development of compound-semiconductor heterojunction solar cells has witnessed high growth in recent years. For example, III-V crystalline materials such as GaAs and InP have become commonplace in satellite and space vehicle solar cell applications due to their strong optical absorption [11, 28]. Additionally, II-VI and I-III-V semiconductors with suitable band-gaps, such as CdTe and $CuInSe_2$, have also become commercially available PV devices although some of these materials are known to be toxic and scarce [28].

2.2.2 Multi-junction solar cells

A solution which has received much interest in the research community is the adoption of a multiple-junction regime. Multi-band-gap photovoltaics, widely known as tandem cells, have been proposed as very efficient systems because they are better matched to the sun's spectrum than a single gap system [12]. Fundamentally, these work by employing "spectrum splitting" techniques. That is, the sunlight is split into narrow wavelength bands and each band is directed to a semiconducting material with a corresponding band-gap [11]. Since the band-gap energy is tuned to the photon energy, almost no kinetic energy is lost through carrier thermalisation and the electrochemical potential extracted is close to the photon energy [28].

In a stacked multi-gap PV, N cells are ordered with the lowest gap at the bottom of the stack and the highest at the top as shown in Figure 2-10 [12]. The incoming sunlight is exposed through the top surface and a perfect back reflector is placed at the rear side [12].

Considering cell n+1 for the moment, photons with energies lower than the cell's gap (*i.e.* $E_p < E_g^{n+1}$) will transmit with a forward flux ϕ_f^n towards cell n, where they can be absorbed if the photon energy lies within the range $E_g^n < E_p < E_g^{n+1}$ [12]. Otherwise, the photons are transmitted through to the lower gap cell in the stack, n-1, with a flux ϕ_f^{n-1}. Due

to radiative recombination and reflection losses, cell *n* may also emit photons that can be collected by cell *n*+1 or *n*-1. This effect is called *radiative coupling* between the cells [12].

The maximum efficiency for a stacked device is achieved when the band-gaps for each cell and operating voltages are optimised. In [12] it was theoretically shown using the detailed balance argument that an infinite number of cells provides the best possible PV performance with a conversion efficiency of 68% for the sun assumed as a blackbody at 6000K [6, 12]. This optimisation is currently in a state where triple junction cells based on GaInP/GaAs/Ge have been fabricated recording a world leading conversion efficiency of 40.7% under a 240 sun illumination [4].

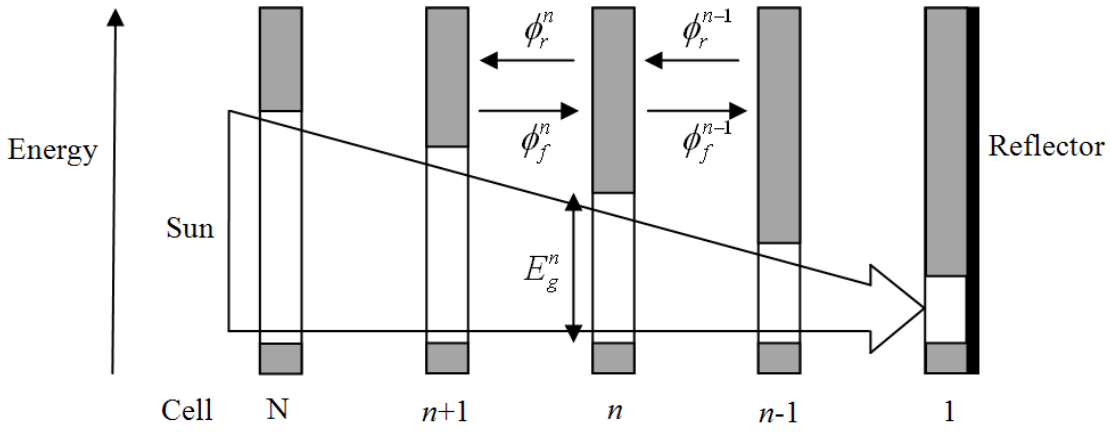

Figure 2-10: Schematic diagram of a stacked multi-band-gap PV cell [12].

Ideally, the operation of each sub-cell within a tandem device could be independently optimised by including separate electrical contacts [28]. However, in practice, this is difficult to realise [28]. Therefore, tandem cells tend to have their sub-cells electrically connected in series or parallel as discussed in [36]. The series configuration, which is the most widely used today, consists of connecting the *n*-type material of one device with the *p*-type material of the adjacent device [36]. This results in the conduction band of the former device being connected to the valence band of the latter device [36]. On the other hand, parallel configurations connect the conduction bands of all the individual sub-cells together via a common electrode [36].

Unfortunately, both these configurations exhibit a compromise that requires some form of electrical matching, which adds further complexity as well as further losses to the tandem device performance [36]. For instance, in a series-connected system, current matching is

needed since the total current is constrained by the sub-cell with the lowest producing photo-current [28]. In contrast, voltage-matching is required for a parallel configuration since the minimum band-gap material used in the tandem structure limits the open-circuit voltage of the overall system [36].

The manufacturing cost of producing multi-junction cells is relatively excessive (>\$7W^{-1}) compared to the mentioned single-junction technologies [4]. Due to the stacking of multiple layers, extra process steps are required in addition to the already energy intensive procedures needed for bulk material preparation and cell fabrication.

While the multi-band-gap strategy has demonstrated noteworthy success using bulk materials, it is also apparent that the use of low-dimensional nano-sized structures may ultimately play a key role in its realisation for future ultra-efficient low-cost solar cells [4, 6].

2.2.3 Nano-structured solar cells

It is believed that molecular assemblies sized between 1-100nm in any one dimension, commonly defined as nano-structures, could present significant cost and performance benefits over bulk technologies given their superior material utilisation and advanced optoelectronic properties [4].

Nano-structures are generally distinguished for possessing quantised energy-levels in their electronic band-structure, which invoke physical phenomena's that could be profoundly exploited towards the actualisation of ultra-high efficiency solar cells [4, 28, 37]. One such phenomena is quantum confinement that boosts carrier transport causing less charge to be lost through recombination [37]. Another effect is the generation of multiple electron-hole pairs per incident photon, which opens a new possibility of delivering power conversion efficiencies in excess of the Shockley-Queisser limit [26, 37].

From a cost standpoint, the key attraction for employing nano-structures is that, since they are solution processable, they could potentially permit solar cells to be manufactured on low-cost, flexible substrates using scalable roll-to-roll processes with room-temperature coating and continuous printing techniques [4, 38].

The nano-materials that have been explored for photovoltaic applications to-date may be classified into four categories depending on the number of dimensions the carriers are allowed to travel [4]:

- 3-Dimensional (3D) nano-pores crystalline films
- 2-Dimensional (2D) quantum wells
- 1-Dimensional (1D) nanowires and nanotubes
- 0-Dimensional (0D) quantum dots

3D nano-crystalline films, normally around 10 μm thick, are already very much in use within Dye-Sensitised (or Grätzel) Solar Cells (DSSC) [4, 39]. These PVs contain an electrochemical junction that consists of a semiconducting nano-pores surface, such as a titania (TiO_2) film, interfaced with a photosensitive organic dye [4, 28]. When an incident photon is absorbed in the dye this generates an exciton (bound electron-hole pair), which is subsequently split at the junction [28]. The electron is injected into the conduction band of the nano-film and transported to an adjoining electrode where it is collected and supplied to the external circuit [39]. Simultaneously, the corresponding hole is extracted from the dye by a surrounding liquid electrolyte typically composed of an iodine solution [4, 39].

In [39] it was demonstrated that the nano-crystalline titania layer along with a newly developed dye contributed strongly to the improved performance of the DSSC, resulting in a conversion efficiency as high as 7.9% and a FF=0.76. Even though DSSCs are cheaply manufactured and the materials used are relatively inexpensive compared to silicon, they suffer from degradation issues caused by thermal instability of the electrolyte that prompts their seal to rupture. This, in turn, inspired the development of the liquid-free polymer based solar cells that also incorporate a variety of nano-structured materials [4].

2D Quantum Wells (QWs) have been exploited in PVs by embedding them within the intrinsic region of a *p-i-n* heterojunction device like GaAs and related alloys (*e.g.* AlGaAs and InGaAs) [4, 28, 40, 41]. The fabrication of such a structure relies upon using precise, atomic level control of the thickness between adjacent layers in order to create multiple potential barriers, or multiple QWs [4]. In essence, these introduce quantum-confined states

near the band edges of the host material enabling photons of lower energy to be efficiently absorbed whilst the high energy photons still interact with the bulk band-gap [28, 40].

Over the past decade there has been an on-going debate regarding the expected efficiency enhancement of QW solar cells, particularly whether they could surpass that of the optimum single-gap cell [4, 40]. That said, it is accepted that QW PVs yield marginally higher short-circuit current densities, and thus conversion efficiencies, compared to corresponding devices devoid of QWs as a result of the extended photo-absorption and quantum confinement [40, 41]. Notably, owing to their relatively complex fabrication process, it is anticipated that QW solar cells will be principally limited to space and concentrator applications [4].

1D nanowires and nanotubes are elongated solid nanostructures that act as direct pathways for the transport of charge, exhibiting carrier mobilities as high as two orders of magnitude compared to bulk materials [4]. These nanostructures may be composed of many classes of functional materials including group IV, III-V, and II-VI semiconductors as well as metals and dielectrics [4]. They are synthesised by a variety of means, most commonly used are CVD, laser ablation and low-cost solution-based chemical synthesis [4].

Within the PV research arena, nanowires were originally introduced as an alternative semiconductor to titaina films for DSSCs as well as polymer-based solar cells [4, 42, 43]. The first realisable device of such was a ZnO nanowire array based DSSC (see Figure 2-11) that showed promising potential for the following reasons:

1. When measured, the electron diffusivity ($D_n=k_BT\mu/q$ where μ is the electron mobility) of a single dry ZnO nanowire was found to range between 0.05-0.5 cm^2s^{-1} [43]. This is several hundred times higher than that observed for a 3D nano-film ($D_n \leq 10^{-4}$ cm^2s^{-1}), which could ultimately lead to rapid carrier collection [43].
2. The use of a highly-dense nanowire array meant that the dye can be adsorped over a significantly large surface area relative to a film and therefore enhance light harvesting [43].

The nanowire-based DSSC was evaluated to deliver a short-circuit current density (J_{sc} =5.85 mA/cm^2) comparable to that of a similar sized titania film although the conversion efficiency (η=1.5%) was not as good due to a shunting resistance of unknown origin [43].

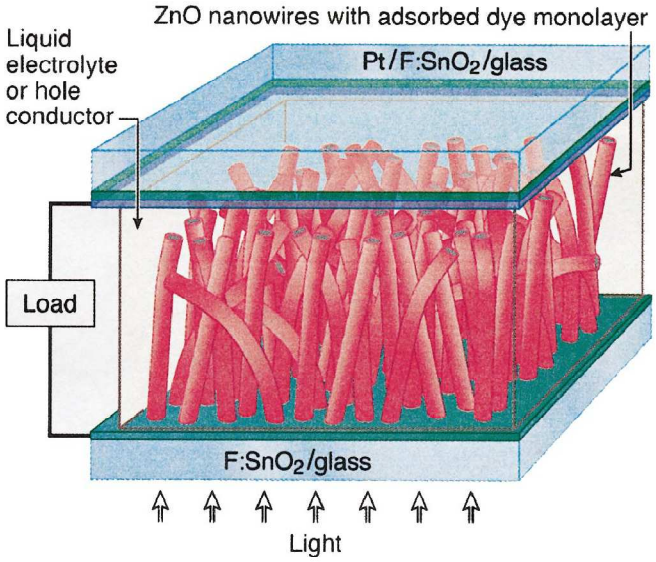

Figure 2-11: A schematic of a nanowire-based DSSC implemented by [42].

Another major breakthrough for nanowires came about when it was discovered that an array of Si-based nanowires beared superior optical properties in comparison to a similar thickness solid Si film, presenting a reflectance R<1% across the entire solar spectrum [4, 44]. It was argued that this was mainly a result of the strong scattering from individual nanowires leading to light being trapped within the nanowire ensemble [4, 44]. Although the corresponding recorded efficiencies were at a mere 1.3% owing to a high series contact resistance, it was advocated that since a lower material consumption is required using the CVD grown nanowires (only gases are used for fabricating the active material), this may yield solar cells with an improved cost benefit ($/W) compared to bulk PVs [4, 44]. However, comparable efficiencies with bulk crystalline Si will still be needed for this to materialise [4].

Nonetheless, Si nanowires still possess an indirect band-gap that is inefficient at absorbing sub-band-gap photons (<1.1eV) as has been theoretically simulated in [45]. This has recently led to the proposed use of another 1D nano-structure – the carbon nanotube.

In addition to the stated merits of 1D nano-structures, semiconducting carbon nanotubes exhibit a direct band-gap that can be tuned according to their geometrical properties, which is an ideal feature for the realisation of a nano-structured multi-bandgap PV

device [46]. Moreover, it was experimentally observed that individual CNTs exposed to light could achieve carrier multiplication due to impact excitation [26]. This may have important implications, particularly in overcoming a quantum yields of 100% [28]. The construction of vertically aligned carbon nanotube arrays has also just been reported, where the lowest-ever optical reflectance measurement relative to any other material has been reported, winning claim for being the darkest man-made material to-date [47]. For the above reasons, as well as others that will be further discussed in the following section, we shall focus our studies on this remarkable material for PV conversion.

0D Quantum Dots (QDs) are nanometre sized semiconducting crystals that have been employed in solar cells with the aim of addressing two key loss mechanisms; sub-band-gap photon energy losses and thermalisation losses [28].

By growing a regular array (super-lattice) of identical QDs within another wider band-gap semiconductor material, a cluster of discrete energy levels (mini-band) arise within the band-gap of the host semiconductor [28]. In controlling the size and spacing of the dots, the energy and width of the mini-bands can be tuned to form an Intermediate Band (IB) [28]. Hence, in theory, by engineering an IB in a PV absorber this should enable the capture and use of low energy photons. A practical demonstration of a QD-IB solar cell confirmed a slight broadening in the spectral response below the band-gap although the photocurrent contribution was relatively negligible [48]. Further, the conversion efficiency of the PV weakened due to a degradation of the open-circuit voltage (by ~20%) as a result of a higher density of defect states [48].

It has been proposed that thermalisation losses can be addressed in QD by two ways [48]. Firstly, by slowing down electron-phonon interactions (the source of kinetic energy dissipation) so that the photo-generated carriers can be collected while they are still ‘hot’ [28, 48]. The second approach is by allowing the hot photo-generated carriers to produce multiple electron-hole pairs via a process known as impact ionisation or Auger generation [28, 48]. Theoretically, the former and latter routes should enhance the conversion efficiency by increasing the photovoltage and photocurrent, respectively [48]. Unfortunately, no group has yet reported an enhanced photocurrent with quantum yields greater than 100% in any QD-

based PV device [48]. This has been attributed to challenges associated with charge separation within QD layers as well as carrier transport to the contacts [4].

2.3 Carbon nanotube photovoltaic devices

The implementation and operation of carbon nanotube based photovoltaics is different from conventional bulk solar cells. Therefore, it is necessary to distinguish how these aspects affect optical absorption, photo-generation of carriers, charge separation and collection in CNT devices. The following sub-sections start by reviewing the basic fabrication and functionality of a CNT device. Next, the photoconductivity of CNTs is detailed as well as the various CNT-based photovoltaics that have been realised in the latest literature.

2.3.1 Single-walled carbon nanotube device overview

The growth of SWCNTs for devices is essentially achieved by combining a source of carbon with a catalytic nano-particle material at elevated temperatures [16]. This has been carried out using one of three synthesis techniques: Arc-discharge, Laser Ablation and Chemical Vapour Deposition (CVD) [49]. Currently, the CVD approach offers the highest CNT yield with minimum defects and is regarded to be the most promising method to scale up [50]. Figure 2-12 illustrates the key components of the CVD process.

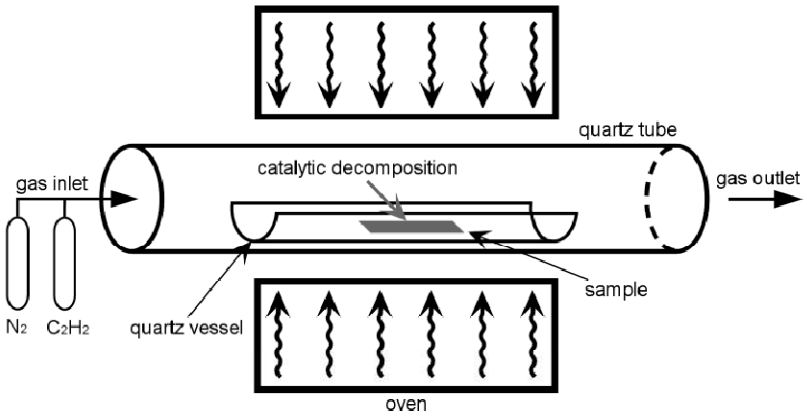

Figure 2-12: Diagram of flow reactor used in Chemical Vapour Deposition (CVD) process [51].

The CVD growth process involves heating a catalyst seed such as iron or cobalt placed on a wafer surface inside a furnace (700^0C-1000^0C) while flowing a hydrocarbon gas (*e.g.* methane mixed with a hydrogen carrier gas) through the reactor for a time scale typically within minutes to hours [50, 52]. In turn, the hydrocarbon gas decomposes on the catalyst

metal and diffuses through the particle where carbon atoms precipitate on the cooler trailing end [49, 52]. This causes a tube-like structure to grow as shown in Figure 2-13, raising the catalyst particle upwards until it is 'poisoned', bringing the growth process of the CNT to an end [49, 52].

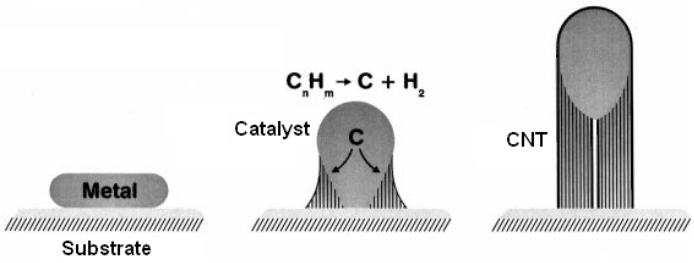

Figure 2-13: Schematic of CNT tip-growth mechanism [53].

As previously mentioned, since the electronic properties of a SWCNT are very much dictated by the geometrical structure, especially whether it is metallic or semiconducting, this necessitates precise control of the CVD growth conditions [16]. Furthermore, as there is a strong correlation between SWCNT diameter and catalyst nano-particle size, this parameter too is of paramount importance in controlling CNT properties [16, 54]. Unfortunately, so far the controllability of the CVD process has been limited, threatening to deliver unreliable and irreproducible CNT devices [16]. Once the SWCNTs have been grown, there is also the added challenge of aligning and orienting the tubes exactly as required in order to have them integrated with electrodes and gates on the wafer [16, 50].

At present, in order to fabricate a SWCNT device, first, the synthesised semiconducting tubes have to be deposited relatively close to a pre-defined alignment mark using the end tip of an Atomic Force Microscope (AFM) [16]. Subsequently, Polymethylmethacrylate (PMMA) resist is coated over the tubes so that metal electrodes could be patterned via electron beam lithography [16]. This results in a number of tubes bridging a pair of source and drain leads as shown in Figure 2-14. After a Si back-gate has been attached under the oxidised wafer (SiO_2) this completes the basic structure of a CNT-Field Effect Transistor (CNT-FET) - the most studied CNT device to date [16].

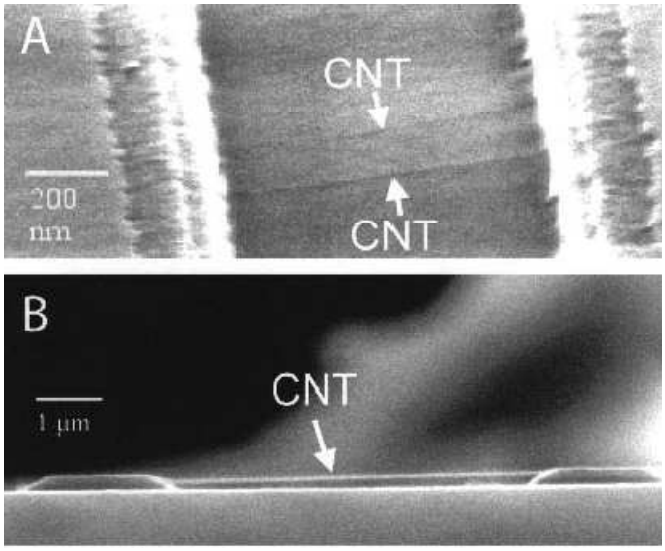

Figure 2-14: Electron microscope images (top (A) and side (B) views) showing locally grown CNTs bridging two electrodes [17].

On many occasions it has been confirmed that the conductance of the semiconducting tube is increased by several orders of magnitude when a negative voltage is applied at the gate [16, 55]. This is analogous in behaviour to a p-channel Metal-Oxide-Semiconductor FET (MOSFET) with the nanotube replacing silicon as the channel [16, 17]. The reason behind the nanotube acting as a p-type semiconductor under ambient conditions is because the interaction with chemical species in the surrounding air, particularly oxygen, adsorb to the nanotube and behave as a weak p-type dopant [16, 17]. Consequently, experiments have followed in investigating the sensitivity of the tube's doping level and hence the shift in threshold-voltage to the chemical environment of the SWCNT [16]. Again, this vulnerability can pose a significant challenge in gaining CNT devices with reproducible behaviour [16].

However, that said, controlled chemical doping of tubes, both p- and n- type have been reported [16, 56]. For example, n-type doping of SWCNTs has been accomplished by adding alkali metals that donate electrons to the nanotube [16, 56]. Further, in [17] it was shown that a CNT-FET could exhibit n-type characteristics after annealing under vacuum conditions. There has also been some work on the realisation of SWCNT *pn* junctions and *p-n-p* devices using modulated chemical doping [56].

Another source for variation arises from the contact resistance between the nanotube and metal electrodes, which can dominate electronic transport in the CNT device [17, 55]. Contact resistances are profoundly dependent upon the techniques used in coupling the CNT

to the leads as well as the types of metals employed [16, 17, 55]. In fact, the interface between the semiconducting SWCNT and the electrodes establish Schottky Barriers (SB) due to the different workfunctions between the two materials causing energy band bending in the semiconductor side. Thus, for any CNT device to operate, carriers must overcome the interface SBs by tunnelling across, which is also highly dependent on temperature in addition to defects located at the CNT-metal junction [17].

Figure 2-15 depicts the operation of both a p- and n- type ambipolar CNT-FET as the gate voltage is varied to modulate the carrier polarity and density in the CNT [17]. A corresponding qualitative band-diagram is jointly presented. For a p-type CNT-FET it could be seen that as the gate voltage is reduced below 0V, the metal Fermi level at the source-CNT junction lines-up with the valence band edge of the nanotube [17]. In turn, hole injection into the tube is instigated, tunnelling across the SB where the drain current (I_D) increases considerably. Conversely, when the gate voltage is increased above 0V for an n-type CNT-FET, the source Fermi level lines-up with the conduction band of the CNT allowing electrons to tunnel through the SB. Again, this comes with an observable increase in I_D [17].

Since the SB height is approximately linearly proportional to the SWCNT band-gap, this parameter can be used to adjust the saturation on-current of the CNT device, which further reinforces the need for controllable growth techniques as the CNT band-gap is very much dependent on the geometrical properties of the tube [57].

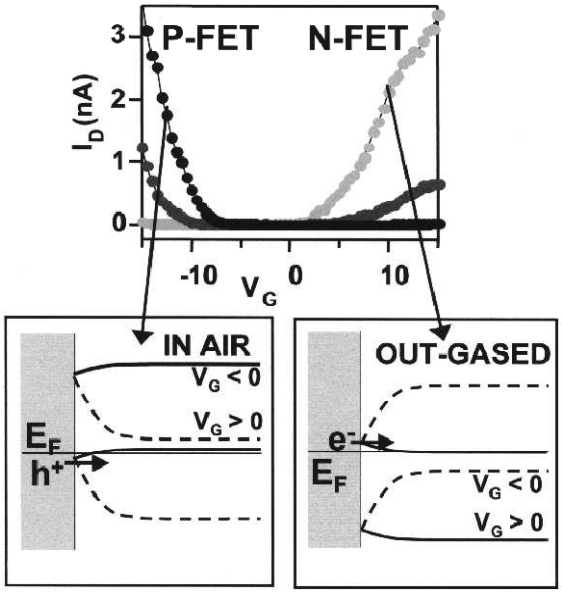

Figure 2-15: Operation of both a p- and n- type ambipolar CNT-FET as the gate voltage is varied. A corresponding qualitative band-diagram is included [17].

2.3.2 Photoconductivity of Carbon Nanotubes

The first experimental observation of carbon nanotubes responding electronically to light was in [58]. The measurements indicated that an electric current flow was generated by a filament of nanotube bundles upon light illumination, even though, it was difficult to ascertain whether this was caused by the photovoltaic or thermoelectric effect [58, 59]. Later, in [59], a CNT-FET device was exposed to a laser light source and it was established that the mechanism of photocurrent generation in the SWCNT involved the resonant excitation of the energy states belonging to the nanotube [59]. This is because when the photocurrent spectra was measured it was found to peak at photon energies matching those of the band-to-band transitions associated with the utilised nanotube as shown in Figure 2-16(left).

It was proposed that the incident light excited the second transition states (E_{22}~1.35eV) of the semiconducting SWCNT which generated e-h pairs that diffused within the channel [59]. Additionally, a moderate drain bias of -1V was applied in order to establish an electric field that would assist carrier separation and drift across the channel (see inset energy band diagram in Figure 2-16(left)) [23, 59]. Unlike the operation of the CNT-FET discussed earlier where the SB limited carrier injection from the contacts into the channel, in this case, the SBs permitted the photo-generated carriers to leave the channel and collect at the electrodes [23, 59]. This could be considered beneficial for photoexcited CNTs since the SBs reduce the

interference between the inflow of injected carriers into the SWCNT and the outflow of photocurrent [23].

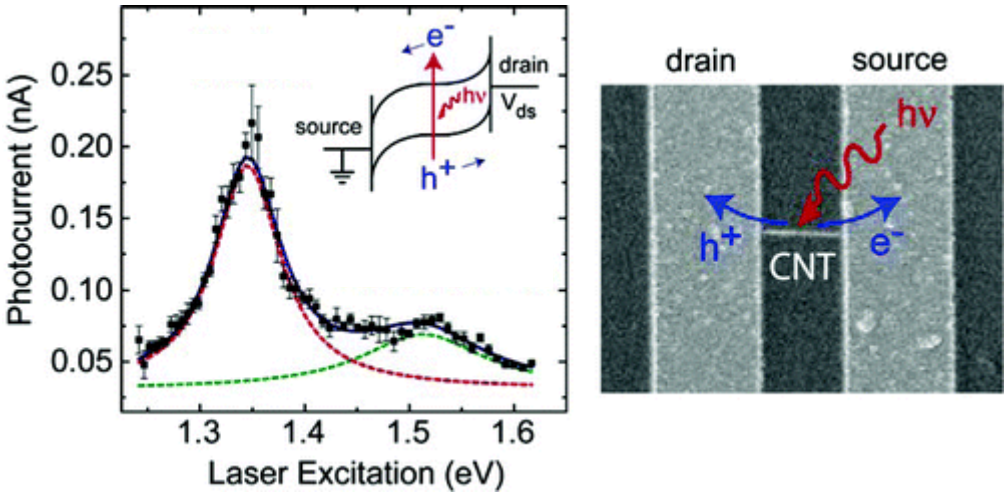

Figure 2-16: (left) Photocurrent spectra for a CNT-FET with a drain bias of -1V, a gate voltage of 2.5V (off-state of p-type device) and an incident laser power of 0.5kW/cm^2. (right) A representative electron microscope image of the device [60].

Interestingly, in the same experiment it was discovered that the measured photocurrent varied considerably with the polarisation angle of the incident light, further reconfirming its resonant origins [59]. Specifically, it was found that the photocurrent magnitude more than doubled when the light was polarised in the direction of the nanotube axis relative to perpendicular polarisation [59]. A similar behaviour was identified with different CNT samples [59].

Although the above mentioned findings provoked extensive attention towards this new nano-scaled photo-detector, the device structure, however, was far from ideal for photovoltaic applications. The main reason for this was due to the high radiative and non-radiative recombination caused by the very weak electric field at the middle of the CNT channel where the semiconductors' energy bands were flat and only curved slightly near the contacts [59]. Moreover, a larger than expected dark current was detected as a result of carrier leakage tunnelling across the SBs into the CNT [59]. This was attributed to the thinning down of the SBs with a large drain bias.

2.3.3 Experimental solar cells based on SWCNT films

When SWCNTs were first introduced into photovoltaic applications they appeared mainly in organic solar cells as embedded nano-structures within polymers yielding CNT-conjugate polymeric composites [21, 24, 61]. It was discovered that by doping polymers with SWCNTs the outcome led to substantial increases in carrier transport as well as photoresponsivity, which in turn facilitated better performing polymer based cells [21, 61].

CNT-polymer PV cells operate by absorbing most of the photons in the conjugated polymer chains, which subsequently generate excitons [21]. Once the excitons reach the SWCNT-polymer interface they dissociate and create free holes that travel into the nanotube (Acceptor) leaving behind free electrons in the polymer (Donor) [21]. Since an electric field is sustained through the difference in electrode work functions, the free carriers are swept across to their respective contacts where they collect.

Under AM1.5 solar illumination, a gradual rise in short-circuit current was observed with higher concentrations of SWCNTs (up to 1 wt.%) in the polymer due to the enhanced effective hole mobility in the SWCNTs [21]. In fact, the measured I_{sc} was found to be two orders of magnitude higher at a 1 wt.% concentration level compared to 0 wt.%, which suggests that the photoresponse was additionally augmented through improved exciton dissociations [21]. Above a 1 wt.% SWCNT concentration the photocurrent decreased as a result of a higher proportion of metallic SWCNTs within the composite material. These metallic SWCNTs behaved as traps and recombination centres in the band-gap of the composite semiconductor medium ultimately reducing the efficiency of the PV cell [21]. As a result, the maximum conversion efficiency was established to occur at a critical 1 wt.% SWCNT concentration [21].

In another similar work, the blending of different CNTs in organic solar cells was investigated where the conversion efficiency was measured to increase by three orders of magnitude at 5 wt.% concentration levels compared to devices without any nanotubes [61]. It was also revealed that the nanotube diameter distributions as well as the semiconducting/metallic ratios of the dopant played a significant role in the PV conversion performance [61].

Most recently, a hybrid PV cell based on a SWCNT/*n*-type Si heterojunction was explored [24]. It was demonstrated that the SWCNTs not only contributed to the photoconversion process as a charge separator/transporter/collector but also as an active light absorbing material [24]. In [24] it was advocated that since semiconducting nanotubes are strong light absorbers in the IR and visible range (photon energies less than 1.1eV), they could bring additional performance advantages when integrated with Si (an absorber of photon energies higher than 1.1eV) over other organic PV materials.

Because semiconducting SWCNTs are naturally *p*-type as previously mentioned, when interfaced with *n*-type Si they form *pn* heterojunctions, which typically exhibit *J*-*V* characteristics similar to that of a diode [24]. Once photogenerated carriers are produced in the semiconducting SWCNTs they separate at the heterojunction followed by hole transport and collection at the SWCNT contact [24]. In parallel, photoelectrons generated at the Si side diffuse from the depletion region into the negative electrode [24].

When the SWCNT/Si solar cell was fabricated by spraying a SWCNT film on top of an *n*-type Si surface with ohmic contacts deposited on each side, the *J*-*V* characteristics were measured under an illumination intensity of 100mWcm^{-2} (AM1.5 conditions) [24]. The recorded J_{sc}, V_{oc} and *FF* were 14.6mAcm^{-2}, 0.37V, and 0.3 respectively, yielding a conversion efficiency of ~1.7%. The poor efficiency was attributed to the high series resistance (~150Ω) established by the SWCNT film, the interface resistance between the SWCNT film and the Si substrate and the contact resistance between the SWCNT and the electrode [24].

Comparisons between the photocurrent and absorption spectra further reinforced the contribution of the SWCNTs towards light absorption since the measured photocurrent peak matched perfectly with the first inter-band transitions corresponding to the mean band-gap (E_{11}) of the semiconducting nanotubes [24].

2.3.4 Experimental photovoltaics based on nanotube photodiodes

Amongst the already mentioned realisations for an individual SWCNT *pn* junction, the most successful to date has been based on electrostatic doping [25, 26, 34].

In [34] a suspended SWCNT based *pn* junction diode was developed using electrostatic doping as depicted in Figure 2-17. Electrostatic doping was achieved by biasing a pair of split gates- VG1 and VG2- with opposite polarities [25]. VG1 was set to a positive potential to allow only electrons to flow into the CNT from the source contact whilst VG2 was set to a negative potential to allow holes to flow in from the drain electrode. The overlap regions between the gate electrodes and the SWCNT essentially defined the doped region [25].

With the source electrode connected to ground, the device of Figure 2-17 was found to resemble a rectifier at room temperature where a high conducting state was observed under forward bias ($V_{DS}>0$) and a low conductance under reverse bias ($V_{DS}<0$) [25]. In fact, the energy band diagram of the *pn* SWCNT diode could be very much likened to a planar bulk *pn* diode [25].

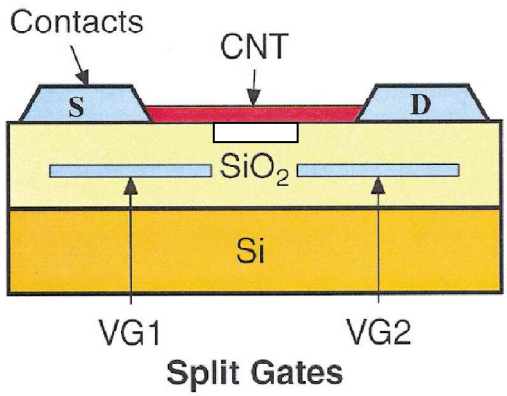

Figure 2-17: Schematic cross section of a suspended SWCNT *pn* junction diode. The split gates (VG1 =+10V, VG2=-10V) are spaced about 1μm apart and are used to electrostatically dope the SWCNT [25].

When the SWCNT diode was brought under a continuous-wave laser source (0.8eV) with a variable output power of up to 10 mW, the *I-V* characteristics were measured for a set of different illumination intensities [34]. The results are plotted in Figure 2-18 where the arrow indicates increasing illumination intensity [34].

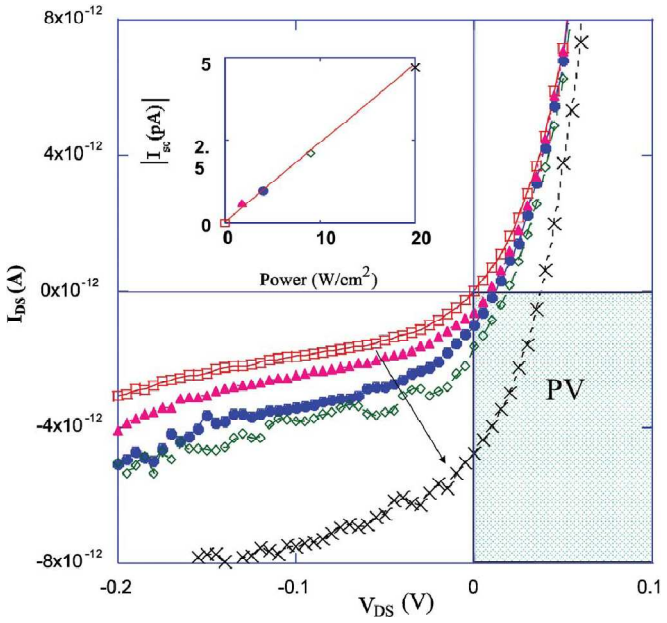

Figure 2-18: *I-V* characteristic under increased illumination intensity demonstrating a progressive shift into the fourth quadrant where the diode generates power. The inset depicts a linear increase in the short-circuit current I_{sc} (at V_{DS} =0) with illuminated power [34].

Under no applied illumination power the SWCNT diode I-V characteristics were compared to the universally recognised dark-current diode equation:

$$I = I_{sat}(e^{q(V_{DS}-IR_s)/nk_BT}-1) \qquad 2.28$$

By curve fitting the data points to Eq. 2.28 it was established that the diode exhibited ideal rectification at T=300K with an ideality factor n=1, a saturation current I_{sat}=0.8pA and a series contact resistance R_s=18MΩ [34]. It was postulated that such a behaviour was an outcome of the defect-free suspended SWCNT as it had minimal interaction with the surface it lay upon and accordingly no undesirable defect-states were introduced in the band-gap [34].

As the illumination intensity was strengthened the *I-V* curve of the SWCNT diode moved deeper into the PV region highlighted in Figure 2-18 [34]. Further, the inset of Figure 2-18 reveals that a linear increase in photocurrent I_p (I_{SC}) ensued with illumination power density for a zero bias [34]. Crucially, it was acknowledged that the photocurrent demonstrated no dependence on increased levels of doping (VG1 and VG2), consistent with the band-to-band generation of e-h pairs [34].

At forward bias, the operation of the SWCNT PV diode can be best explained by the *pn* junction energy-band diagram of Figure 2-19(a) [34]. The doped regions have been represented by the capacitive coupling of the split gate where the source and drain Fermi levels are aligned with the conduction and valence bands of the SWCNT, respectively [34]. It can also be seen that the photocurrent (I_{SC}) is created in the middle of the device where photogenerated e-h pairs are separated by the built-in potential and accelerated along the nanotube to the device contacts [26, 34]. The forward-bias dark current that depends on the SB characteristics is additionally shown flowing in the opposite direction to I_{SC} [34].

In order to determine the conversion efficiency of this PV device the peak power output ($P_m = I_m V_m$) was calculated from Figure 2-19(b) by locating the bias point (V_m, I_m) at which a maxima for the power generated ($P = I_{DS}V_{DS}$) occurred [34]. Using this, the FF was calculated to range between 0.33-0.52 [34]. The typical responsivity for the device was measured to be J_{sc}/P_{in} = 30 mA/W, where J_{sc} was estimated over the illuminated area of the SWCNT [34]. Hence, the maximum conversion efficiency ($\eta = (J_{sc}/P_{in}) \text{x} V_{OC} \text{x} FF$) for the SWCNT PV diode valued at 0.2% [34]. It was suggested that this was a result of poor optical absorption by the nanotube since the light source was circularly polarized and the geometrical structure of the SWCNT was not optimised for PV conversion [34].

A much later work used an identical device structure (see Figure 2-17) to re-examine another electrostatically doped, suspended SWCNT PV diode with different tube geometries [26].

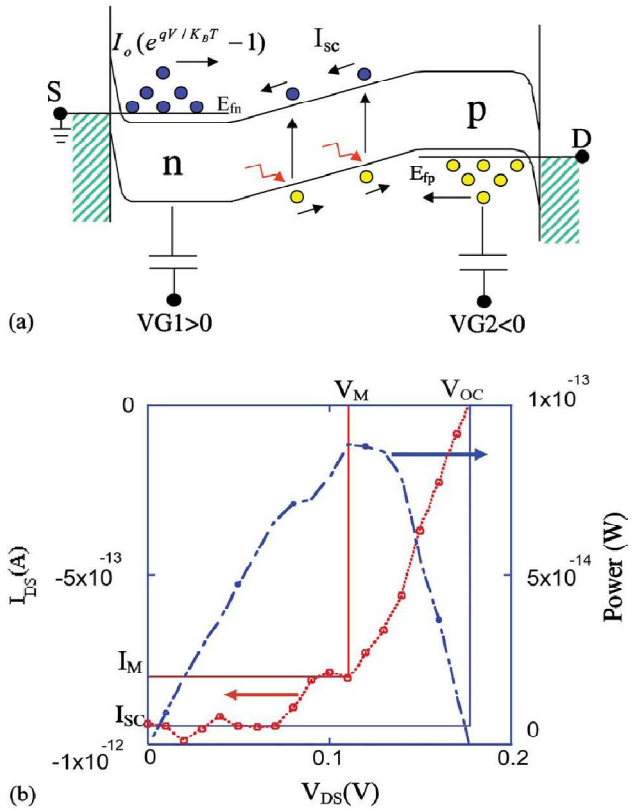

Figure 2-19: (a) The energy band-diagram of an electrostatically doped SWCNT diode showing currents from the photogenerated electron-hole pairs and the forward-bias dark current. (b) The fourth quadrant I-V curve (red) and corresponding power ($P=I_{DS}xV_{DS}$) curve (blue) [34].

The I-V_{SD} characteristics were measured under an ambient temperature of T=60K for a SWCNT with a diameter of 1.4nm at various photon energies as shown in Figure 2-20(A). Initially, it can be observed from the graph that for all I-V_{SD} curves the open-circuit voltage (V_{OC}=0.43V) remains constant at a prescribed value dictated by the SWCNT band-gap ($E_g \approx qV_{OC}$) [26]. When illuminated with low photon energies (E_p=0.75eV, E_p=0.85eV, E_p=0.95eV), the I-V_{SD} curves exhibit a standard *pn* junction photoresponse with a photocurrent of approximately 15pA at a bias voltage of V_{SD}=0V [26]. At higher photo-energies (*i.e.* E_p=1.24eV), a step-like increase in photocurrent was observed at V_{SD}=0V, which is consistent with optical absorption into the second interband transition $E_{22}=2E_{11}$ when $E_p \geq 2E_g$ [26]. In reverse-bias, this step response is more amplified with greater applied photon energies [26].

The photocurrent steps were partially attributed to extremely efficient e-h pair creation by 'hot' carriers in the second SWCNT subbands [26]. When these hot carriers undergo impact excitation events, they could generate multiple e-h pairs per incident photon as

previously mentioned that can potentially allow the device to overcome the Shockley-Queisser limit [26].

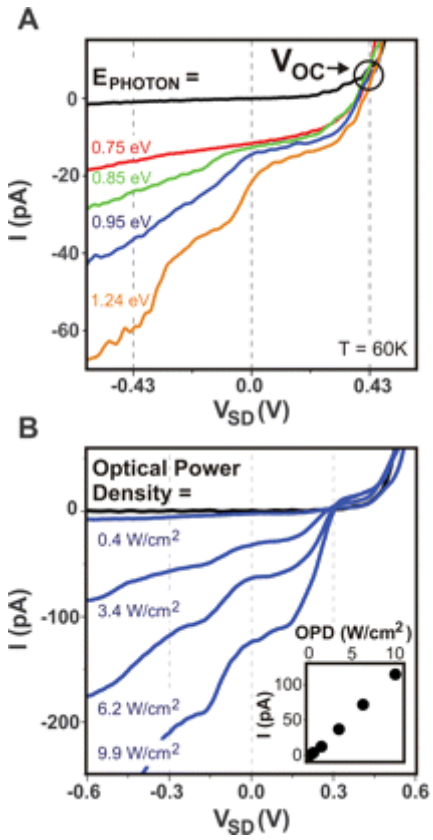

Figure 2-20: I-V_{SD} photocurrent characteristics for a SWCNT *pn* junction diode (A) at various photon energies with a fixed incident optical power density at 25W/cm^2, T=60K and tube diameter is 1.4nm (B) at several optical power densities with a fixed E_p at 0.79eV, T=10K and tube diameter is 2.0nm. (Inset) Photocurrent at V_{SD}=0V versus optical power density [26].

In the same investigation a different nanotube (E_g~0.3eV) was examined at T=10K with respect to Optical Power Density (OPD) variation as depicted in Figure 2-20(B). Again, a linear increase in photocurrent with OPD was confirmed (see inset) [26].

Most recently, a microcell consisting of a network of semiconducting SWCNT PV diodes was experimentally studied in [62]. By ultrasonically nanowelding a monolayer of SWCNTs across two asymmetric metal electrodes, Pd and Al, with high and low work functions, respectively, this produced a Schottky diode at each metal/nanotube interface creating a built-in electric field along the length of the tubes [62]. Figure 2-21 offers a schematic (a) and image (b) representation of the device.

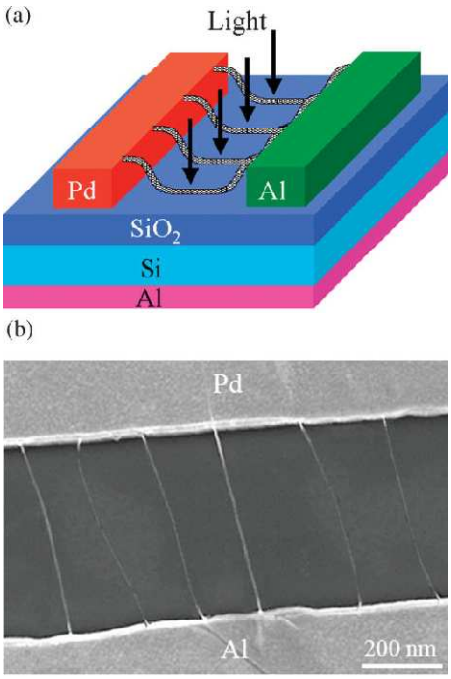

Figure 2-21: (a) Schematic diagram of the multiple SWCNT PV microcell based on nanowelded metal(Pd)/nanotube/metal(Al) junctions. (b) An electron microscope image of the SWCNT array PV device [62].

Optical measurements of the microcell were carried out under a solar-simulated light (AM1.5) source and the I-V characteristics clearly showed a rectification behaviour with PV conversion at higher illumination intensities [62]. It was claimed that this observation was a consequence of the strongly established built-in electric field that facilitated photogenerated e-h pair separation and collection [62]. Yet, the conversion efficiency of the device was reported to be just beneath 0.8%, with a FF ranging from 0.42-0.56 [62].

Despite the substantial gains in conversion efficiency compared with the previously mentioned experimental devices, performance was undermined because the full band-gap of the semiconducting tubes was not sufficiently utilised, resulting in poor device operation with a low photovoltage and high saturation current (I_{sat}=5pA) [34, 62]. Also, the introduction of undesirable defect states from interactions with the substrate surface produced high recombination losses and non-ideal diode behaviour (n=1.9) [25, 34, 62]. Most importantly, it was found that major improvements to efficiency could ensue with the selection of SWCNTs having band-gaps appropriately matched with the solar spectrum [62].

2.4 Proposed hypothetical multi-band-gap CNT based PV cell

Many researchers have reported that because of their reduced dimensionality and unique electronic properties, SWCNTs could potentially become a prospective material for photovoltaics [34, 63]. The motives behind such an expectation are summarised in the following points:

1. All semiconducting SWCNTs exhibit direct band-gap properties, which allow optical transitions to proceed without any phonon intervention [23, 64, 65]. This enables strong photo-absorption characteristics.
2. Because of their low-dimensionality they are believed to have low defect densities, reducing non-radiative transitions [34, 64].
3. SWCNTs can potentially offer ideal *pn* junction behaviour as reported in [34], which is fundamental in achieving high-quality PV conversion.
4. As a result of their high aspect ratio they include a relatively large surface area to capture incoming light- a highly desirable feature for boosting photoresponsivity.
5. By facilitating the reduced scattering of charge, hot carrier transport is sustained, where multiple e-h pairs can be generated per incident photon as reported in [26].
6. Most importantly, due to the tunable nature of the SWCNT band-gap (typically varies between 0.4-2eV), they can cater for a broad range of photon energies, which is ideal for solar absorption [34, 46]. In fact, it is believed that by combining multiple CNTs of different band-gaps, it should be possible to obtain a continuous response over a broad spectral range [65].

In [34] and [62] it was advocated that much needed improvements in SWCNT PV performance may be brought about by employing a network of tubes where electromagnetic coupling and scattering amongst the nanotubes could lead to higher responsivity. Indeed, latest experimental results indicate that vertically aligned SWCNTs possess unparalleled photoabsorption properties within a wide spectral range [47, 66]. This is because, akin to a tandem PV cell, when a photon is not absorbed by a given nanotube it is likely to either be reflected or transmitted towards another nearby tube possibly retaining an alternative band-gap to the first. This ‘photon recycling’ process may proceed from one layer of tubes to

another until the photon ultimately interacts with a CNT having a corresponding band-gap energy or lower. As an outcome, the reflectance of a sample of vertically aligned SWCNTs was measured to be R=0.07% over the visible range λ=457-633 nm [47]. However, it was conveyed that the photoresponsitivity and carrier collection were significantly hampered with the entanglement of tubes [67]. Therefore, it is necessary to ensure sufficient separation and adequate alignment amongst SWCNTs when building a nanotube array for PV purposes.

Due to the complexities associated with the precise fabrication and accurate probing of such a device, computational simulations may be performed to gain valuable insights on the number of nanotubes as well as the tube geometries needed for optimal operation.

In Figure 2-22, a hypothetical PV device is proposed comprising a large number of vertically aligned semiconducting SWCNTs with dissimilar structural geometries bridging a common drain and source metal electrode. This corresponds to a limiting scenario structure that may arise, where it is presumed that all SWCNT *pn* junctions are ideally doped and exhibit ultimate rectification behaviour. The direction of the incoming solar radiation is fixed as depicted and is polarised parallel to the tube axis (E-field is along z-axis) in order to optimise absorption. All SWCNTs are ordered, with that possessing the highest band-gap nearest to the light source and the lowest located at the furthest end. Similarly, the tube lengths (L) are fixed and are assumed to be optimised to guarantee collection of all generated electron-hole pairs. The period (a) between the centres of each tube will be regular and, again, is assumed to be optimised to maximise radiative coupling between the tubes and ensure no reflection losses.

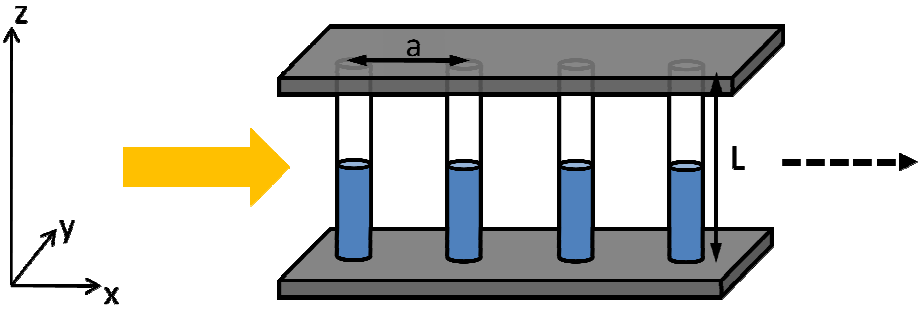

Figure 2-22: Schematic diagram of proposed multi-band-gap SWCNT solar cell.

In principle, when this device is subjected to illumination the tubes will absorb photons of various wavelengths according to the multi band-gap distribution. In turn, photogenerated

electron-hole pairs in each semiconducting tube will be effectively separated by a built-in potential produced at the *pn* junction. As a result the photocurrents generated by the individual SWCNTs will contribute towards the global cell short-circuit current. Furthermore, when the semiconducting tubes are generating power they will bias each other affecting the saturation currents produced and this must be taken into consideration when modelling the device characteristics as a whole.

This process of operation is typical of a parallel configured tandem solar cell, which, as previously mentioned, will reduce the overall photo-voltage to the lowest CNT band-gap unless the voltages of each SWCNT sub-cell are matched. In this case, voltage-matching would be impractical to implement posing a limitation on the proposed design. However, the authors believe that this compromise outweighs the added complexity associated with developing a series configured CNT based tandem solar cell since the bonding of CNTs with different structures would be much more difficult to physically realise.

The processing of such a PV device may potentially be accomplished by the CVD growth of vertically-aligned SWCNTs where catalyst nano-particles of specific geometries are regularly spaced apart on a substrate. However, this approach lacks the precision needed for our application. Thus, post-synthesis alignment and chemical attachment of pre-selected SWCNTs on a conductive surface may be a better option. This has been achieved in [68] where vertically-aligned SWCNTs have been created and attached to an optically transparent conductive electrode using a self-assembly process. Also in [69], researchers were able to vertically attach SWCNTs to a substrate using a thioester linkage. These methodologies could potentially be used for realising our proposed PV device, although, one would first need to investigate the effects of the linkage upon the CNT/contact interface to ensure that the contact resistance is minimised.

Although, currently there exists no reliable, rapid and reproducible approach to creating such a highly-specified array of nanotube devices, it is anticipated that a solution may possibly emerge with the vigorous advancement in integrating carbon nanotubes within microelectronic circuits [16].

It is envisioned that if the proposed PV device could be cascaded then a potential application may possibly be to power ultra-low-energy microcontrollers that are envisaged to operate in the nano-watt scale in the near future.

2.5 Summary

This chapter has focused on reviewing the operation of present-day solar cells and where their main technology limitations lie as well as potential solutions. An up-to-date account has also been offered of experimental SWCNT based devices and photodiodes highlighting their strengths and shortcomings. In the final section a proposed hypothetical CNT based solar cell architecture was revealed.

The following chapter will investigate the carbon nanotube in more detail and specify the chosen computational technique employed in reproducing the CNT band-structure. This will represent the underlying method upon which a more simulation efficient analytical model will be built for evaluating key nanotube parameters such as the band-gap, electronic transport and optical absorption properties in the subsequent chapters.

Chapter 3 Carbon Nanotube Band Structure Theory

This chapter details the method used in realising the band-structure of single-walled carbon nanotubes with various geometrical properties. The first section briefly discusses the structural features of carbon nanotubes. Next, the associated electronic characteristics are studied with the development of a semi-empirical nearest-neighbour Tight-Binding (TB) model. This approximation is further improved by employing the third-nearest neighbour TB approach. The SWCNT band-structure is later generated by applying the Zone Folding (ZF) technique to the established graphene band-structure. It is finally confirmed that the CNT band-structure is appreciably altered with respect to its geometrical structure.

3.1 Carbon nanotube structural characteristics

A carbon nanotube is a self-assembled hollow cylinder constructed from a rolled-up sheet of graphene [70]. Graphene is essentially a single atomic layer of Graphite- a naturally occurring crystalline material purely made of carbon atoms. A carbon atom has 6 electrons that occupy the $1s^2$, $2s^2$ and $2p^2$ orbitals [71]. The $1s^2$ orbital contains two strongly attached core electrons that are not involved in any bonding whilst the remaining four are weakly bound to the nucleus and therefore play a major role in creating covalent bonds [71]. These four valence electrons have the orbitals $2s$, $2p_x$, $2p_y$ and $2p_z$ in the crystalline phase. When carbon atoms combine together to form a material such as graphene, graphite or diamond, these electron orbitals constructively interact with each other to form new hybrid orbitals that strengthen the binding energy between the atoms.

The mixing of a single 2*s* electron with 1, 2 or 3 2*p* electrons is called sp^n hybridization where n = 1, 2 or 3 [71]. For example in graphene, sp^2-hybridiztion is observed when the 2s orbital is mixed with only 2 out of the 3 available 2*p* orbitals yielding the following new orbitals: sp^2, sp^2, sp^2 and $2p_z$ [71]. The three sp^2 orbitals are equal in strength and are separated by a 120^0 angle over the same molecular plane whereas the single $2p_z$ orbital is perpendicular to the molecular plane and is associated with a weak π-bond as indicated in Figure 3-1. In fact, the $2p_z$ orbital acts as a delocalized electron that is fully responsible for carrier transport in CNTs. Thus, it is additionally termed as the conduction π-electron.

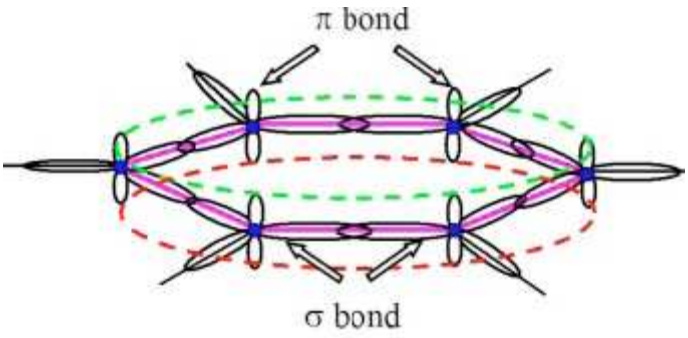

Figure 3-1: A single hexagonal bonding array of a graphene sheet. Carbon nuclei are shown as filled blue circles, σ -bonds connect the carbon nuclei in-plane (solid line) and out-of-plane (dotted lines) π –bonds contribute to attaching layers to each other [72].

When two sp^2 orbitals from different carbon atoms overlap a σ-bond is established. This is effectively a covalent bond with a strong binding energy that generates high stiffness and strength along the graphene plane [71]. On the other hand, since the weakly bound π-bonds contribute to the interlayer interaction of graphite, little strength is needed to detach the graphene planes.

Graphene sheets are composed of carbon atoms that are σ-bonded to 3 neighbouring carbon atoms over the 2-dimensional plane. This produces a bonding arrangement as shown in Figure 3-2 where hexagonal arrays of carbon atoms are tessellated throughout the molecular plane. Isolated sheets of graphene are liable to being energetically unstable due to the abundance of dangling bonds emanating from the edge atoms [71]. The dangling bonds correspond to high energy states, which are, by nature, undesirable. As a consequence, the formation of CNTs is a direct result of the tendency for the edge atoms of the graphene sheet to self-cluster together eliminating any dangling bonds. In turn, this reduces the surface energy of a graphene sheet at a cost of straining the bonds between the carbon atoms.

The curvature of a nanotube causes the 3 mentioned σ-bonds to become slightly out of plane, which introduces a small amount of sp^3 bonds. This is referred to as the σ-π rehybridization effect and can be directly related to the observation of higher electrical and thermal conductivities for a tube due to the extended delocalization of the π-electrons.

Defects of a CNT can include topological, substitutional or chemical defects. These increase the likelihood of electron scattering that result in shorter carrier mean-free paths and a consequential drop in conductivity. A defect-free CNT exhibits a pure hexagonal bonding structure with no foreign species incorporated, which will be assumed throughout this thesis.

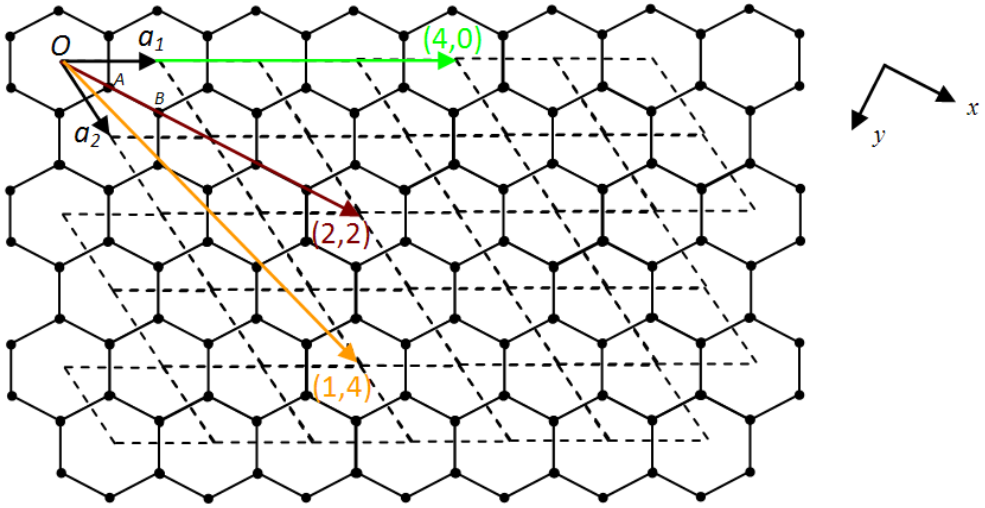

Figure 3-2: Graphene sheet (solid) showing tessellated hexagonal arrays of carbon atoms. Crystal lattice is shown (dotted) with its primitive lattice vectors a_1 and a_2 and unit cell containing 2 carbon atoms (A & B). Three different chiral vectors (4,0), (2,2) and (1,4) are depicted to represent different nanotube chiralities.

The geometrical structure of a SWCNT is based on two main parameters: the diameter (d) and chiral angle (θ), which is associated with the tilt of the hexagonal rings [73]. Before formulating expressions for these parameters, first, it is essential to define the crystal lattice of a graphene sheet and establish its coordinate axes.

3.1.1 Crystal lattice of a graphene sheet

In order to define the crystal lattice of graphene one must identify all positions within the crystal that are identical to the origin, O, as indicated in Figure 3-2 [74]. In other words, if

an observer is situated at a particular position on the sheet and the view in all directions is found to be exactly equivalent to the view observed from the origin, then that position may be deemed identical to the origin. Clearly, for this to occur one should imagine that the graphene sheet is infinitely large [74]. The set of identical points identified in this way outlines the crystal lattice and is depicted in Figure 3-2 by the points joined by the dotted lines. Notice that the crystal lattice does not have the same structure as graphene. By joining the lattice point at the origin to two of its neighbours, the primitive lattice vectors $\mathbf{a_1}$ and $\mathbf{a_2}$ emerge as the coordinate axes, which are different to the orthogonal *x-y* cartesian coordinates [74]. The reason this choice of axes is made is to reflect the hexagonal symmetry inherent in the graphene structure. Moreover, the primitive vectors allow us to define the unit cell of the crystal, which is outlined by the dotted parallelogram containing the two carbon atoms A and B in Figure 3-2. The unit cell of graphene is a building block that can be repeated indefinitely to generate the entire lattice space.

The crystal lattice can be completely defined by the lengths of $\mathbf{a_1}$ and $\mathbf{a_2}$ and the angle between them [74]. It can be clearly seen from Figure 3-2 that the angle between $\mathbf{a_1}$ and $\mathbf{a_2}$ is 60^0. Furthermore, if the C-C bond length is measured to be a_{cc} (0.142 nm) then the magnitude of the vectors $\mathbf{a_1}$ and $\mathbf{a_2}$ in terms of a_{cc} can be derived as $\sqrt{3}a_{cc}$, which is commonly referred to as the lattice constant (a) of graphene [49]. The vectors $\mathbf{a}_1$ and $\mathbf{a_2}$ can be described with respect to the cartesian *x-y* coordinate space as:

$$a_1 = \frac{\sqrt{3}}{2} a_{cc}(\hat{x} + \sqrt{3}\hat{y}) \qquad 3.1$$

$$a_2 = -\frac{\sqrt{3}}{2} a_{cc}(\hat{x} - \sqrt{3}\hat{y}) \qquad 3.2$$

In Figure 3-2, any lattice point in the crystal structure can be defined from the origin by translating these two primitive vectors by any integer value including positive, negative and zero. Here, it will be assumed that vectors $\mathbf{a_1}$ and $\mathbf{a_2}$ can be scaled by the integers m and n, respectively, to produce any translational or chiral vector such as the examples given in Figure 3-2.

3.1.2 Expressions for the diameter and chiral angle of a SWCNT

By rolling a graphene sheet into a cylinder so that the beginning and end of a *(m,n)* chiral vector join together, one obtains an *(m,n)* nanotube [50]. Mathematically, the chiral vector ($\mathbf{C_h}$) can be expressed in terms of the vectors $\mathbf{a_1}$ and $\mathbf{a_2}$ as follows [49]:

$$C_h = ma_1 + na_2 \tag{3.3}$$

substituting Eq. 3.1 and 3.2 into Eq. 3.3 the chiral vector becomes:

$$C_h = \frac{\sqrt{3}}{2} a_{cc}\left[(m-n)\hat{x} + \sqrt{3}(m+n)\hat{y}\right] \tag{3.4}$$

The magnitude of the chiral vector, $\mathbf{C_h}$, corresponds to the circumference of the nanotube. This can be used to determine the diameter (*d*) of the tube as denoted by Eq. 3.5.

$$d = \frac{\sqrt{3}}{\pi} a_{cc}\sqrt{m^2 + nm + n^2} \tag{3.5}$$

The chiral angle (θ) is defined as the angle between $\mathbf{C_h}$ and $\mathbf{a_1}$, which can be obtained by taking the scalar product of the two vectors, giving:

$$\theta = Cos^{-1}\left(\frac{2m+n}{2\sqrt{n^2+m^2+nm}}\right) \tag{3.6}$$

The chiral angle (θ) range is defined between $0^0 \le |\theta| \le 30^0$ due to the hexagonal symmetry. Another representation of the chiral angle can be in terms of the arctangent as denoted by Eq. 3.7.

$$\theta = \tan^{-1}\left(\frac{\sqrt{3}n}{2m+n}\right) \tag{3.7}$$

Three types of CNT structures exist with distinct *(m,n)* chiralities that are of critical importance when dealing with nanotubes. These three structures include the armchair, zigzag and helical or chiral nanotube.

3.1.3 Armchair, Zigzag and Chiral nanotubes

In an armchair tube the carbon atoms around the circumference trace an arm-chair pattern as shown in Figure 3-3(a) [50]. This corresponds to rolling-up the graphene sheet of Figure 3-2 along the chiral vector *(2,2)* or in general any vector *(m, n)* where *m = n*. Hence, when the integers *m* and *n* are equivalent, Eq. 3.7 reduces to:

$$\theta = \tan^{-1}\left(\frac{\sqrt{3}}{3}\right) = 30^0 \qquad 3.8$$

Similarly, if *m = 2p* and *n = -p* where *p* is any integer, this will provide a chiral angle of -30^0, which corresponds to having an angle of 30^0 due to hexagonal symmetry [49].

The zigzag tube has its carbon atoms arranged in a zig-zag fashion along the circumference as illustrated in Figure 3-3(b) and (c). In this case, this corresponds to rolling-up the graphene sheet of Figure 3-2 along the chiral vector *(4,0)* or in general any vector *(m,n)* where *n = 0*. Therefore, if *n* is zero and *m* is any integer *p* then the chiral angle according to Eq. 3.7 is 0^0. In addition, if *m =0* and *n* is any integer *p* then this will also result in a zigzag tube because from Eq. 3.7 $\theta=60^0$ and again owing to the hexagonal symmetry this is equivalent to having a chiral angle of 0^0.

All other nanotubes with a chiral angle in the range $0^0 < |\theta| < 30^0$ are chiral. This may correspond to rolling-up the graphene sheet of Figure 3-2 along the chiral vector *(1,4)*. Chiral CNTs tend to have their rows of hexagons spiralling along the nanotube axis as shown in Figure 3-3(d) [50].

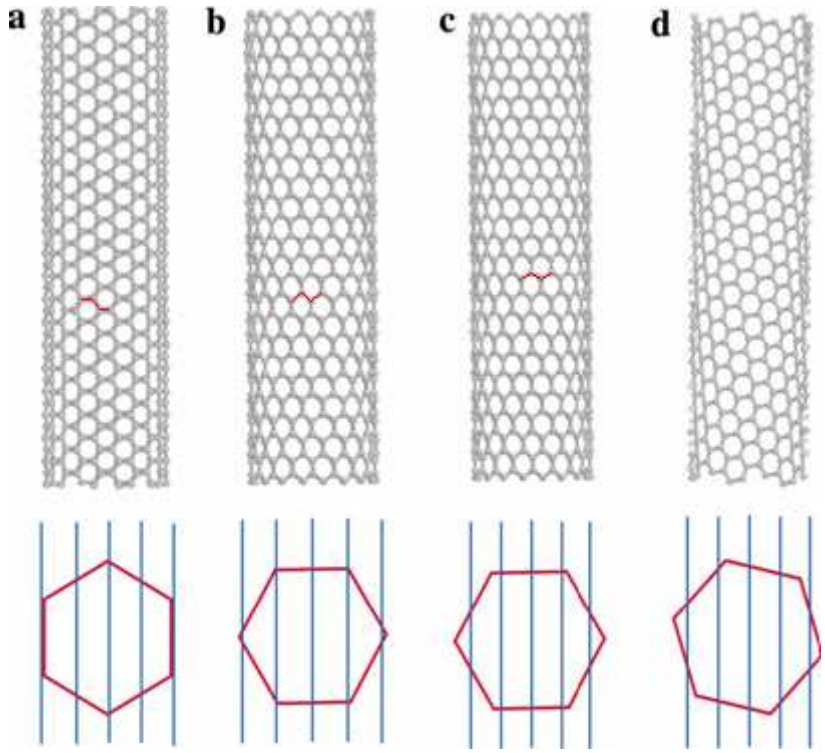

Figure 3-3: Top panel: Nanotube types. Bottom panel: The vertical blue lines illustrate the allowed electron states of the nanotube and the red hexagonal background depicts the first Brillouin zone in the reciprocal space of graphene. (a) An armchair SWCNT. The blue lines intersect with the corners of the hexagon, resulting in a metallic nanotube. (b) A zigzag nanotube. The electronic states cross the hexagon corners, but a small band gap can develop due to the curvature of the nanotube. (c) The zigzag tube is semiconducting because the allowed electron states miss the corner points of the hexagon. (d) A chiral semiconducting tube [50].

To ascertain the electronic band characteristics of the above mentioned SWCNTs, a detailed study of the band-structure pertaining to graphene will be initially addressed.

3.2 Graphene band structure

The band structure of any crystal is always defined within the reciprocal lattice space. Therefore, this section commences by defining the reciprocal lattice and first Brillouin zone of a graphene sheet.

3.2.1 Reciprocal lattice and first Brillouin zone of graphene

The reciprocal lattice is a lattice in Fourier space associated with the crystal and is commonly referred to as the **k**-space [75]. It differs from the real-space lattice by taking the

reciprocal of the dimensions defined for a given vector. Quantitatively, the reciprocal lattice can be described as follows.

Given a 3-dimensional crystal where the axes are defined by the three vectors $\mathbf{a_1}$, $\mathbf{a_2}$ and $\mathbf{a_3}$, any real-space lattice point, **r**, can be expressed from the origin, *O*, as:

$$r = r' + ma_1 + na_2 + sa_3 \qquad 3.9$$

where **r'** is another given point in the lattice and *m*, *n* and *s* are arbitrary integers. Since the lattice is composed of a regular periodic array of points in space, this suggests that the electron density, ***n(r)***, is a periodic function of **r** with periods $\mathbf{a_1}$, $\mathbf{a_2}$ and $\mathbf{a_3}$ [75]. This also implies that the vector $\mathbf{T} = m\mathbf{a_1} + n\mathbf{a_2} + s\mathbf{a_3}$ is a period of ***n(r)*** as denoted by Eq. 3.10.

$$n(r+T) = n(r) \qquad 3.10$$

Such periodicity provides an ideal situation for Fourier analysis [75]. Considering only one dimension of the electron density function, that is in the *x*-direction, with a period *a*, the Fourier series expansion can be stated as follows:

$$n(x) = b_0 + \sum_{p=1}^{\infty} \left(b_p \cos(\omega_p x) + c_p \sin(\omega_p x) \right) \qquad 3.11$$

where

$$\omega_p = \frac{2\pi}{a} p \qquad 3.12$$

b_p and c_p are the Fourier coefficients. The discrete values of ω_p define the points along the one-dimensional Fourier domain [75]. This periodic set of points corresponds to the reciprocal lattice points of a linear crystal. To extend this space to 3-dimensions the integers *p* must be replaced by a set of vectors **G** producing an electron density function:

$$n(r) = \sum_{G} h_G e^{jGr} \qquad 3.13$$

where h_G represents the complex Fourier coefficient. There is an abstract procedure for establishing the set of vectors **G** in Eq. 3.13. Any vector **G** can be expressed in terms of the three axis vectors $\mathbf{b_1}$, $\mathbf{b_2}$ and $\mathbf{b_3}$ of the reciprocal lattice as articulated by Eqs. 3.14, 3.15 and 3.16 [75]:

$$b_1 = 2\pi \frac{a_2 \times a_3}{a_1 \cdot (a_2 \times a_3)} \qquad 3.14$$

$$b_2 = 2\pi \frac{a_3 \times a_1}{a_2 \cdot (a_3 \times a_1)} \qquad 3.15$$

$$b_3 = 2\pi \frac{a_1 \times a_2}{a_3 \cdot (a_1 \times a_2)} \qquad 3.16$$

If $\mathbf{a_1}$, $\mathbf{a_2}$ and $\mathbf{a_3}$ are the primitive vectors of the crystal lattice, then the axis vectors $\mathbf{b_1}$, $\mathbf{b_2}$ and $\mathbf{b_3}$ are the primitive vectors of the reciprocal lattice [75]. The set of reciprocal lattice vectors **G** can be stated as:

$$G = hb_1 + kb_2 + lb_3 \qquad 3.17$$

where *h*, *k* and *l* are any arbitrary integers frequently labelled as the Miller indices *hkl* [75]. Any reciprocal lattice vector G constitutes the normal to a set of parallel planes in the direct lattice where the dot product G**.**T= $2\pi w$ (*w* is another integer).

The first Brillouin zone is fundamental in the analysis of any crystal's electronic energy-band structure. Usually expressed just as the Brillouin zone, it is a Wigner-Seitz primitive unit cell in the reciprocal lattice [75]. The Brillouin cell is the smallest volume enclosed by planes that are perpendicular bisectors of the reciprocal lattice vectors drawn from the origin [75].

For example, given the graphene sheet shown in Figure 3-2 with the primitive lattice vectors $\mathbf{a_1}$ and $\mathbf{a_2}$, the corresponding reciprocal lattice vectors $\mathbf{b_1}$ and $\mathbf{b_2}$ can be calculated using Eqs. 3.14 and 3.15 by substituting $\mathbf{a_3}$ with the unit normal vector ($\hat{n}$) to the plane.

$$a_1 = \begin{pmatrix} a_{1x} \\ a_{1y} \\ 0 \end{pmatrix} \qquad a_2 = \begin{pmatrix} a_{2x} \\ a_{2y} \\ 0 \end{pmatrix} \qquad a_3 = \hat{n} = \begin{pmatrix} 0 \\ 0 \\ 1 \end{pmatrix} \tag{3.18}$$

$$b_1 = \frac{2\pi}{a_{1x}a_{2y} - a_{1y}a_{2x}} \begin{pmatrix} a_{2y} \\ -a_{2x} \\ 0 \end{pmatrix} = \frac{2\pi}{\sqrt{3}a_{cc}} \left(\hat{x} + \frac{1}{\sqrt{3}} \hat{y} \right) \tag{3.19}$$

$$b_2 = \frac{2\pi}{a_{1x}a_{2y} - a_{1y}a_{2x}} \begin{pmatrix} -a_{1y} \\ a_{1x} \\ 0 \end{pmatrix} = \frac{2\pi}{\sqrt{3}a_{cc}} \left(-\hat{x} + \frac{1}{\sqrt{3}} \hat{y} \right) \tag{3.20}$$

From Eqs. 3.19 and 3.20 the magnitudes of $\mathbf{b_1}$ and $\mathbf{b_2}$ are calculated to be $4\pi/3a_{cc}$. It can be clearly observed that the real lattice vectors $\mathbf{a_1}$ and $\mathbf{a_2}$ are perpendicular to the reciprocal lattice vectors $\mathbf{b_2}$ and $\mathbf{b_1}$ respectively.

In Figure 3-4 the 2D Brillouin zone of graphene (shaded region) is enclosed by the perpendicular bisectors of the vectors pointing to the reciprocal lattice points. It can be seen that these perpendicular bisectors are positioned mid-way between the origin (Γ) and the reciprocal lattice points. Hence, a length of $2\pi/3a_{cc}$ is covered between the origin Γ and point M. The points K, K' and M are marked in Figure 3-4 to represent sites of high symmetry. It can be readily shown that the distance from the origin (Γ) to the K or K' points is $4\pi/3a$ where a is the lattice constant mentioned earlier.

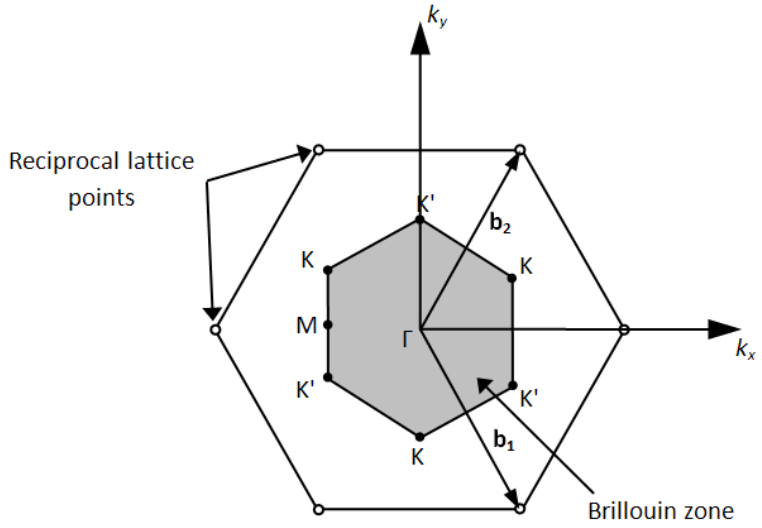

Figure 3-4: Brillouin zone (shaded) in the reciprocal lattice of graphene.

3.2.2 Electron confinement in graphene

When electrons are confined within a small space that is comparable to a lattice spacing along any given dimension, such as in graphene along its one atom thickness, they can be treated like travelling plane waves with a momentum of $p=\hbar\mathbf{k}$. The **k** term is referred to as the wavevector, which indicates the direction of wave propagation and has a magnitude related to the wavelength λ by $\mathbf{k} = 2\pi/\lambda$ [75]. Thus, an electron can be represented by a wavefunction $\psi_k(\mathbf{r})$ as conveyed by Eq. 3.21. Eq. 3.21 simply describes the wavefunction as a plane wave in space with a wavevector **k**.

$$\psi_k(r) = e^{jk\cdot r} \qquad 3.21$$

The above wavefunction is a solution to Schrödinger's equation so long as it satisfies a set of boundary conditions, which will be discussed in more detail in the following sub-section. A solution to Schrödinger's equation corresponds to an 'orbital', which is a term given to specify an exact quantum state that can be occupied by at most one electron to obey the Pauli exclusion principle [75]. Thus, any allowed point in the **k**-space can be used to represent a state in which an electron can occupy.

The crystal's band structure illustrates how the energy (E) of an electron can vary for different allowed pairs of states (k_x, k_y). This relationship (commonly referred to as the dispersion relation) is periodic over the whole **k**-space. Therefore, it is sufficient enough to solve only for the lowest energy band, which lies within the first Brillouin zone ($-2\pi/3a_{cc} \leq k_x \leq 2\pi/3a_{cc}$, $-4\pi/3a \leq k_y \leq 4\pi/3a$) defined above [75]. In the case that more than one orbital has the same energy, this is referred to as degeneracy [75].

If an electron is injected into a crystal with an infinite linear lattice in the x direction, the periodic potential **V(x)** of each ion core will set a perturbation to the motion of the electron wave. This perturbation will generate a reflected wave. When the incident and reflected waves interact to form a standing wave (which has a group velocity of zero *i.e.* $d\omega/dk = (1/\hbar)(dE/dk) = 0$) the electron is captured at an ion core site.

Energy gaps can occur in the crystal band structure when the electron waves are in synchronism with the periodicity of the lattice potential [74]. This gap denotes the amount of

energy required by a valence electron captured at the ion core site to penetrate the potential perturbation and conduct into another neighbouring ion core deeming it as a conduction electron. The absence of an electron at an ion core generates a hole. Now the band structure of graphene will be calculated using the tight binding approach.

3.2.3 Formation of graphene band structure

The Tight Binding (TB) approach is generally associated with the LCAO (Linear Combination of Atomic Orbitals) [75]. It is a standard method for solving the periodic ion potential problem met in the theory of electron transport in solids [76]. When modelling a material's band structure the tight-binding technique lies between the very accurate, very computational intensive *ab initio* methods and the fast but imprecise empirical methods [77].

The unique electronic properties of graphene arise from the quantum confinement of the conduction π-electrons [49]. Thus, the TB method will be used to determine the interaction and non-finite overlap between the π-electron wavefunctions over the entire graphene lattice space. In doing so, the dispersion relation can be attained.

The electrons associated with the in-plane σ-bonds are irrelevant to the calculation of the graphene band structure because the corresponding energy bands are too far away from the Fermi-level to contribute to the electronic transport in the material. In contrast, the π valence and conduction bands cross the Fermi-energy level as will be shown later. It will be assumed that the graphene sheet is a pure crystalline crystal free from any defects.

In the case of graphene, the TB approximation is based on the assumption that the π electrons of the neighbouring atoms of the crystal can possess similar energetic properties to that of the isolated carbon atom π electrons (i.e. the energy levels are equivalent). This assumption is based on the fact that the graphene potential is strong enough to prolong the time taken before a π electron captured by one ion can leak/tunnel to another neighbouring ion. Thus, the localized graphene π electrons are uninfluenced by the neighbouring atoms, which can be treated as a linear superposition of the free atom wavefunctions.

In general, to find the dispersion relation of any crystal one needs to solve the following Schrödinger equation:

$$\left(-\frac{\hbar^2}{2m}\nabla^2 + V(r)\right)\psi_k(r) = \mathrm{H}\psi_k(r) = E(k)\psi_k(r) \qquad 3.22$$

H is the single electron Hamiltonian of the crystal, V(**r**) is the periodic potential of the lattice, E(**k**) represents the atomic energy eigenvalue indexed according to **k**, and ψ_k(**r**) is the one-electron eigenfunction.

When Eq. 3.22 is pre-multiplied by the conjugate transpose wavefunction ψ_k^*(***r***) and then integrated over the space in which ψ_k(**r**) is defined, it is found that:

$$\int \psi_k^*(r)\mathrm{H}\psi_k(r)dr = \int \psi_k^*(r)E(k)\psi_k(r)dr = E(k)\int \psi_k^*(r)\psi_k(r)dr \qquad 3.23$$

Using bra-ket notation, Eq. 3.23 can be readily rearranged to deliver the definition of the dispersion relation for any given solid as denoted by:

$$E(k) = \frac{\langle \psi_k | H | \psi_k \rangle}{\langle \psi_k | \psi_k \rangle} \qquad 3.24$$

where

$$\langle \psi_k | H | \psi_k \rangle = \int \psi_k^*(r)\mathrm{H}\psi_k(r)dr \qquad 3.25$$

$$\langle \psi_k | \psi_k \rangle = \int \psi_k^*(r)\psi_k(r)dr \qquad 3.26$$

To simplify any further calculations the one-electron eigenfunction can be approximated by taking the product of a plane wave $e^{jk.r}$ and a modulation function u(**r**) that modulates the electron plane wave by the lattice potential period **V(r)**. This is in accord with the Bloch theorem, which states that any eigenfunction can be written as follows:

$$\psi_k(r) = e^{jk.r}u(r) \qquad 3.27$$

When analyzing more than one electron, the function u(**r**) can be approximated by $\phi_\alpha(r - R_\alpha)$, which represents the $2p_z$ atomic orbital of the isolated α atom at position $\mathbf{R_\alpha}$ from the origin [78]. Here, the α atom represents one of two carbon atoms found in the unit cell of

graphene (*i.e.* α = A or B). Therefore, the one-electron wavefunction $\psi_k(\mathbf{r})$ can now be replaced with the Bloch function $\Phi_\alpha(\mathbf{k},\mathbf{r})$, which linearly sums the effect of all the α atoms over the total number of unit cells N in the crystal [79]:

$$\Phi_\alpha(k,r) = \frac{1}{\sqrt{N}} \sum_{R_\alpha} e^{jk.R_\alpha} \phi_\alpha(r - R_\alpha) \qquad 3.28$$

To proceed with the TB calculation of the complete graphene sheet a linear combination of the two $2p_z$ orbital Bloch functions for all the A and B atoms is constructed to produce the i^{th} eigenfunction [78]:

$$\psi_i(k,r) = C_{iA}(k)\Phi_A(k,r) + C_{iB}(k)\Phi_B(k,r) = \sum_{j=1}^{n} C_{ij}(k)\Phi_j(k,r) \quad (i = 1...N) \qquad 3.29$$

$C_{ij}(k)$ is an unknown coefficient where the j^{th} atomic orbital runs from 1 to n (n is the number of orbitals per unit cell participating in the band-structure) [79]. Now that the eigenfunction has been re-defined to include the properties of the Bloch function, one can continue to calculate the dispersion relation by substituting Eq. 3.29 into Eq. 3.24 giving:

$$E_i(k) = \frac{\langle \psi_i | H | \psi_i \rangle}{\langle \psi_i | \psi_i \rangle} = \frac{\int \psi_i^* H \psi_i \, dr}{\int \psi_i^* \psi_i \, dr} = \frac{\sum_{j'=1}^{n}\sum_{j=1}^{n} C_{ij'}^* C_{ij} \int \Phi_{j'}^*(k,r) H \Phi_j(k,r) dr}{\sum_{j'=1}^{n}\sum_{j=1}^{n} C_{ij'}^* C_{ij} \int \Phi_{j'}^*(k,r) \Phi_j(k,r) dr}$$

$$= \frac{\sum_{j'=1}^{n}\sum_{j=1}^{n} C_{ij'}^* C_{ij} \langle \Phi_{j'} | H | \Phi_j \rangle}{\sum_{j'=1}^{n}\sum_{j=1}^{n} C_{ij'}^* C_{ij} \langle \Phi_{j'} | \Phi_j \rangle} \equiv \frac{\sum_{j'=1}^{n}\sum_{j=1}^{n} C_{ij'}^* C_{ij} H_{j'j}(k,r)}{\sum_{j'=1}^{n}\sum_{j=1}^{n} C_{ij'}^* C_{ij} S_{j'j}(k,r)} \qquad 3.30$$

where

$$H_{j'j}(k,r) = \langle \Phi_{j'} | H | \Phi_j \rangle \qquad 3.31$$

$$S_{j'j}(k,r) = \langle \Phi_{j'} | \Phi_j \rangle \qquad 3.32$$

The terms $H_{j'j}(k,r)$ and $S_{j'j}(k,r)$ are called the transfer and overlap integrals, respectively [14]. The $C_{ij'}^*(k)$ coefficient needs to be solved such that the energy E_i(k) is a

minimum for the eigenfunction $\psi_i(\mathbf{k},\mathbf{r})$ [79]. That is, one needs to find the value of $C^*_{ij'}(k)$ that presents a local minima in the function E_i(k). This can be done by differentiating E_i(k) with respect to $C^*_{ij'}(k)$ and equating it to zero whilst setting the other coefficient $C_{ij}(k)$ to a fixed constant.

$$\frac{\partial E_i(k)}{\partial C^*_{ij'}} = \frac{\sum_{j'=1}^{n}\sum_{j=1}^{n} C^*_{ij'} C_{ij} S_{j'j}(k) \sum_{j'=1}^{n}\sum_{j=1}^{n} C_{ij} H_{j'j}(k) - \sum_{j'=1}^{n}\sum_{j=1}^{n} C^*_{ij'} C_{ij} H_{j'j}(k) \sum_{j'=1}^{n}\sum_{j=1}^{n} C_{ij} S_{j'j}(k)}{\left(\sum_{j'=1}^{n}\sum_{j=1}^{n} C^*_{ij'} C_{ij} S_{j'j}(k) \right)^2}$$

$$= \frac{\sum_{j'=1}^{n}\sum_{j=1}^{n} C_{ij} H_{j'j}(k)}{\sum_{j'=1}^{n}\sum_{j=1}^{n} C^*_{ij'} C_{ij} S_{j'j}(k)} - \frac{\sum_{j'=1}^{n}\sum_{j=1}^{n} C^*_{ij'} C_{ij} H_{j'j}(k) \sum_{j'=1}^{n}\sum_{j=1}^{n} C_{ij} S_{j'j}(k)}{\left(\sum_{j'=1}^{n}\sum_{j=1}^{n} C^*_{ij'} C_{ij} S_{j'j}(k) \right)^2} = 0 \qquad 3.33$$

By multiplying Eq. 3.33 by $\sum_{j'=1}^{n}\sum_{j=1}^{n} C^*_{ij'} C_{ij} S_{j'j}(k)$ throughout and substituting the expression for E_i(k) of Eq. 3.30 into the second term of Eq. 3.33, the following ensues [14]:

$$\sum_{j'=1}^{n}\sum_{j=1}^{n} C_{ij} H_{j'j}(k) = E_i(k) \sum_{j'=1}^{n}\sum_{j=1}^{n} C_{ij} S_{j'j}(k) \qquad 3.34$$

Specifying $\mathbf{C_i}$ as a column vector that is of the order of *n x 1*, Eq. 3.34 can be expressed as a set of N equations of the following form:

$$HC_i = E_i(k) S C_i \qquad 3.35$$

Here, **H** and **S** are *n x n* matrices with the integrals $H_{j'j}$ and $S_{j'j}$ as entries [79]. In the case of graphene these matrices are of the order 2 x 2 since there are two $2p_z$ orbitals per unit cell participating in the band-structure. Moreover, $\mathbf{C_i}$ is a 2 x 1 column vector. Eq. 3.35 can be rewritten as $(H - E_i(k)S)C_i = 0$ [79]. If the matrix $(H - E_i(k)S)$ has the inverse $(H - E_i(k)S)^{-1}$ then this can be pre-multiplied on both sides to result in $\mathbf{C_i} = \mathbf{0}$ [79]. This

outcome implies that no eigenfunction exists. Therefore, to obtain a non-trivial solution where a wavefunction exists the matrix must have no inverse i.e. the determinant is zero:

$$\det\left[H - E_i(k)S\right] = 0 \qquad 3.36$$

Eq. 3.36 is known as the Secular equation. This equation will provide *n* different eigenvalues for E_i(k) resulting in a dispersion relation with *n* bands [79]. Since the eigenvalues E_i(k) are periodic functions in the reciprocal lattice, only the first Brillouin zone is adequate in analysing the band-structure of the crystal [14]. Further, since there are two conduction π-electrons per unit-cell being analysed there will only be two π-bands in the Brillouin zone called the bonding (π) and anti-bonding (π*) bands [14].

To solve the Secular equation for graphene the Hamiltonian (**H**) and Overlap (**S**) matrices can be resolved by evaluating each element individually. In order to accomplish this one needs to specify which neighbouring atoms will contribute towards the overlapping wavefunctions.

3.2.3.1 *Nearest-neighbour tight-binding model*

Here, the nearest-neighbour TB approximation will be derived where it is assumed that only nearest neighbour atoms have overlapping π-electron wavefunctions. Hence, given an atom A_0 as illustrated in Figure 3-5 the nearest neighbour atoms are denoted by B_{11}, B_{12} and B_{13} [80].

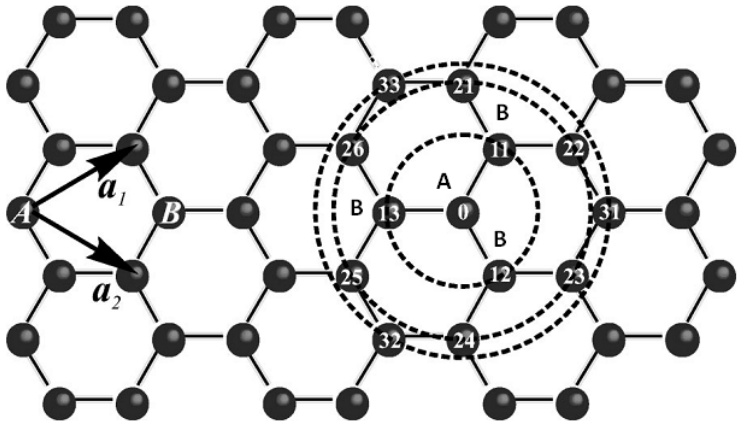

Figure 3-5: The unit cell contains two carbon atoms A and B belonging to the two sub-lattices. An atom A_0 has three nearest neighbours B_{1l} , six second-nearest neighbours A_{2l} , and three third-nearest neighbours B_{3l} [80].

For nearest-neighbour interaction the diagonal entries of the **H** matrix can be determined using Eq. 3.31 to give:

$$
\begin{aligned}
H_{AA} = H_{BB} &= \langle \Phi_A | H | \Phi_A \rangle \\
&= \frac{1}{N} \sum_{R_{A'}} \sum_{R_A} e^{jk(R_A - R_{A'})} \int \phi_A(r - R_{A'}) H \phi_A(r - R_A) dr \\
&= \frac{1}{N} \sum_{R_A = R_{A'}} \int \phi_A(r - R_{A'}) H \phi_A(r - R_A) dr \\
&+ \frac{1}{N} \sum_{R_A \neq R_{A'}} e^{jk(R_A - R_{A'})} \int \phi_A(r - R_{A'}) H \phi_A(r - R_A) dr \\
&= \frac{1}{N} \sum_{R_A = R_{A'}} \int \phi_A(r - R_{A'}) H \phi_A(r - R_A) dr + (terms \;\; further \; than \;\; R_A = R_{A'}) \\
&\approx \varepsilon_{2p}
\end{aligned}
\qquad 3.37
$$

In Eq. 3.37 R_A and $R_{A'}$ are the positions of atoms A and A', respectively [80]. Since it was assumed that ϕ_α is strongly localized, the only contributions from overlapping wave functions that need to be considered are between AA and BB [79]. The next order of contribution to H_{AA} comes from the next-nearest neighbours A_{2l}, which will be neglected for now [14]. ε_{2p} is an approximation of the $2p_z$ orbital energy and is found from fitting experimental data [80]. Note that this is not just the atomic energy value of a free atom since the Hamiltonian of Eq. 3.22 also includes the crystal potential [14]. The off-diagonal terms are given by:

$$
\begin{aligned}
H_{AB} = H^{*}_{BA} &= \langle \Phi_A | H | \Phi_B \rangle \\
&= \frac{1}{N} \sum_{R=R_A} \sum_{R=R_{B1l}} e^{jk(R_{B1l}-R_A)} \int \phi_A(r-R_A) H \phi_B(r-R_{B1l}) dr \\
&= \frac{1}{N} \Big[e^{jk(R_{B11}-R_A)} \int \phi_A(r-R_A) H \phi_B(r-R_{B11}) dr \\
&+ e^{jk(R_{B12}-R_A)} \int \phi_A(r-R_A) H \phi_B(r-R_{B12}) dr \\
&+ e^{jk(R_{B13}-R_A)} \int \phi_A(r-R_A) H \phi_B(r-R_{B13}) dr \Big] \\
&= \gamma_0 \left(e^{jk(R_{B11}-R_A)} + e^{jk(R_{B12}-R_A)} + e^{jk(R_{B13}-R_A)} \right)
\end{aligned}
\qquad 3.38
$$

where:

$$
\gamma_0 = \langle \phi_A(r-R_A) | H | \phi_B(r-R_{B1l}) \rangle \qquad 3.39
$$

The matrix element H_{BA} is obtained from H_{AB} by applying the Hermitian conjugation relation $H_{BA}=H^{*}_{AB}$, where '*' denotes the complex conjugate [14]. In Eq. 3.38 only the nearest neighbours are considered and the more distant terms are neglected [14]. Similarly, to evaluate the overlap matrix (**S**), firstly, one focuses on computing the diagonal elements. Assuming that the atomic wavefunctions are normalized (*i.e.* $\langle \Phi_A(r-R_A) | \Phi_A(r-R_A) \rangle = 1$) it can be deduced that $S_{AA}= S_{BB}= 1$ [80]. The off-diagonal terms are calculated in a similar manner to the off-diagonal elements of the Hamiltonian:

$$
\begin{aligned}
S_{AB} = S^{*}_{BA} &= \langle \Phi_A | \Phi_B \rangle \\
&= \frac{1}{N} \sum_{R=R_A} \sum_{R=R_{B1l}} e^{jk(R_{B1l}-R_A)} \int \phi_A(r-R_A) \phi_B(r-R_{B1l}) dr \\
&= \frac{1}{N} \Big[e^{jk(R_{B11}-R_A)} \int \phi_A(r-R_A) \phi_B(r-R_{B11}) dr \\
&+ e^{jk(R_{B12}-R_A)} \int \phi_A(r-R_A) \phi_B(r-R_{B12}) dr \\
&+ e^{jk(R_{B13}-R_A)} \int \phi_A(r-R_A) \phi_B(r-R_{B13}) dr \Big] \\
&= s_0 \left(e^{jk(R_{B11}-R_A)} + e^{jk(R_{B12}-R_A)} + e^{jk(R_{B13}-R_A)} \right)
\end{aligned}
\qquad 3.40
$$

where:

$$s_0 = \langle \phi_A(r - R_A) | \phi_B(r - R_{B1l}) \rangle \qquad 3.41$$

and a function *f(k)*is defined as:

$$f(k) = \left(e^{jk(R_{B11} - R_A)} + e^{jk(R_{B12} - R_A)} + e^{jk(R_{B13} - R_A)} \right) \qquad 3.42$$

Thus, having calculated all matrix elements one can now write the **H** and **S** matrices as follows:

$$H = \begin{pmatrix} \varepsilon_{2p} & \gamma_0 f(k) \\ \gamma_0 f^*(k) & \varepsilon_{2p} \end{pmatrix} \quad , \qquad S = \begin{pmatrix} 1 & s_0 f(k) \\ s_0 f^*(k) & 1 \end{pmatrix} \qquad 3.43$$

substituting these matrices into Eq. 3.36 gives:

$$\det[H - E_i(k)S] = \det \begin{bmatrix} \varepsilon_{2p} - E_i(k) & (\gamma_0 - E_i(k)s_0) f(k) \\ (\gamma_0 - E_i(k)s_0) f^*(k) & \varepsilon_{2p} - E_i(k) \end{bmatrix} = 0 \qquad 3.44$$

To find the dispersion relation is now a matter of doing a simple calculation to yield the following formula [12]:

$$\left(\varepsilon_{2p} - E_i(k)\right)^2 = \left[\left(\gamma_0 - E_i(k)s_0\right) | f(k) | \right]^2$$

$$\varepsilon_{2p} - E_i(k) = \pm \left(\gamma_0 - E_i(k)s_0\right) | f(k) |$$

$$E_i(k) = \frac{\varepsilon_{2p} \pm \gamma_0 | f(k) |}{1 \pm s_0 | f(k) |} \qquad 3.45$$

Akin to ε_{2p}, the parameters γ_0 and s_0 are found by fitting experimental or first-principle data [80]. This yields: $\varepsilon_{2p} = 0eV$, $\gamma_0 = -3.033\ eV$ and $s_0 = 0.129\ eV$ [80]. Since s_0 is small it can be neglected (as approximated by J. Slater and G. Koster [76]) producing a simplified formula [80]:

$$E_i(k) = \pm \gamma_0 | f(k) | \qquad 3.46$$

By calculating the magnitude of *f(k)*, Eq. 3.46 can now be expanded into a commonly used form that is written with respect to the *x-y* components of the **k**-space:

$$\begin{aligned} E_i(k) &= \pm\gamma_0\left|e^{jk(R_{B11}-R_A)} + e^{jk(R_{B12}-R_A)} + e^{jk(R_{B13}-R_A)}\right| \\ &= \pm\gamma_0\left|e^{jk(a_1+(R_{B13}-R_A))} + e^{jk(a_2+(R_{B13}-R_A))} + e^{jk(R_{B13}-R_A)}\right| \\ &= \pm\gamma_0\left|e^{jk(R_{B13}-R_A)}\left(1+e^{jka_1}+e^{jka_2}\right)\right| \\ &= \pm\gamma_0\left|e^{-j(\frac{a}{\sqrt{3}}k_y)}\left(1+2e^{j\frac{\sqrt{3}a}{2}k_y}\cos\left(\frac{a}{2}k_x\right)\right)\right| \\ &= \pm\gamma_0\sqrt{1+4\cos^2\left(\frac{a}{2}k_x\right)+4\cos\left(\frac{a}{2}k_x\right)\cos\left(\frac{a\sqrt{3}}{2}k_y\right)} \end{aligned} \qquad 3.47$$

Eq. 3.47 leads to the following two dispersion curves in the **k**-space:

1. $E_-(k) = \gamma_0|f(k)|$ which is referred to as the bonding π energy band (*cf.* valence band).
2. $E_+(k) = -\gamma_0|f(k)|$ which corresponds to the anti-bonding π* energy band (*cf.* conduction band).

When s_0 is not neglected in calculating Eq. 3.45 the energy dispersion relation of graphene over the entire Brillouin zone can be plotted as shown in Figure 3-6(a). It is important to note that the conduction and valence bands do actually touch each other at the six corner points of the Brillouin zone [14]. This is reinforced by taking a slice of Figure 3-6(a) at k_y=0, giving Figure 3-6(b), where the positions of the high symmetry points (K, Γ, M and K') are highlighted.

In Figure 3-6(b) the levels $E_+(k)$ and $E_-(k)$ are degenerate at the K and K' points demonstrating equivalent energy values that correspond to the Fermi energy E_F= 0 [79]. Since there are two π-electrons per unit cell, each with a different spin orientation, at T=0K both electrons occupy the lower bonding π energy band leaving the π* band empty [14].

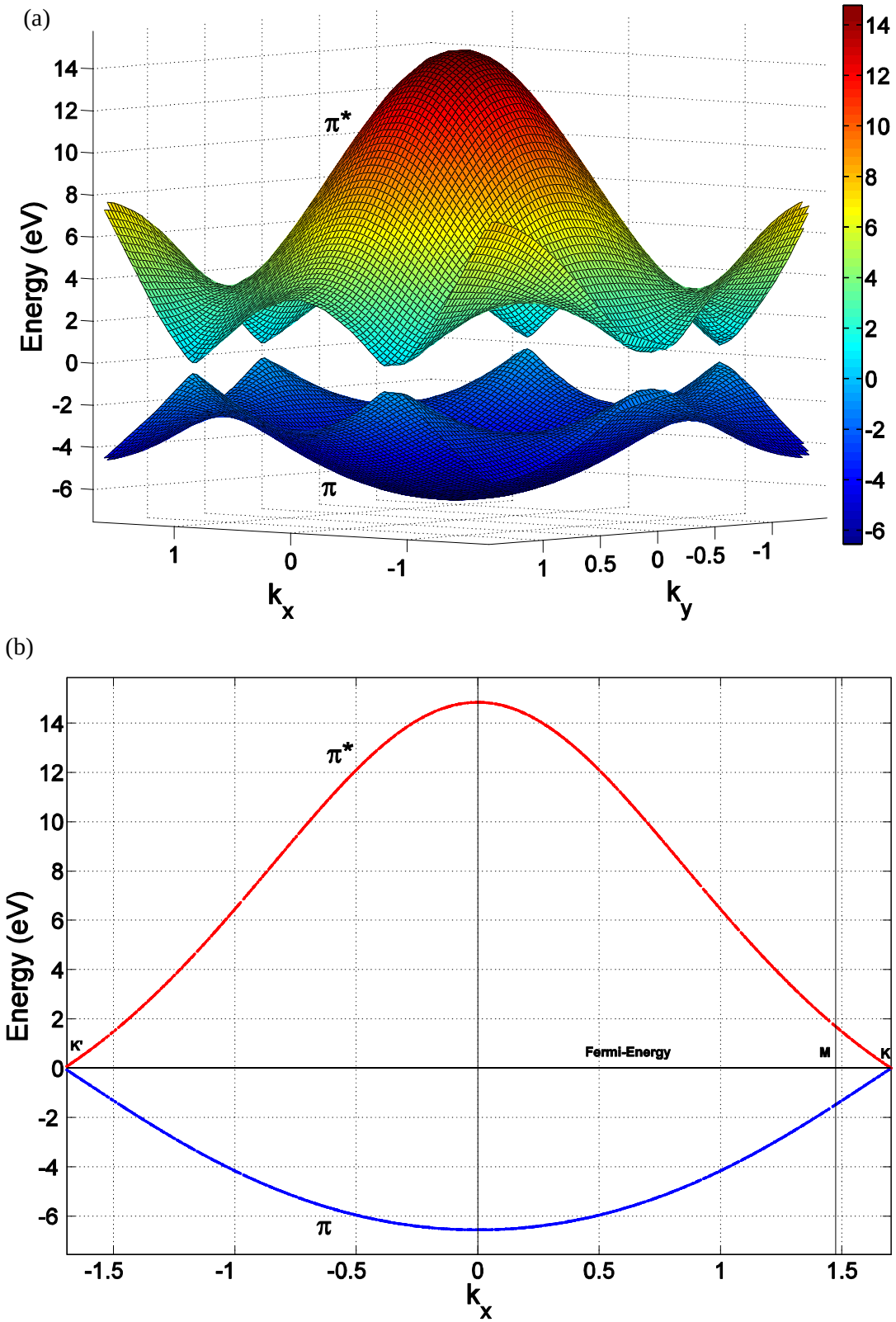

Figure 3-6: (a) The energy dispersion relation of graphene over the complete Brillouin zone. (b) Slice of (a) at k_y =0 where high symmetry points (K, Γ, M and K') are marked. Both plots are generated using MATLAB.

Hence, graphene can exhibit both semiconducting and metallic characteristics since at T = 0K its valence band is completely full and the conduction band is completely empty, yet no band-gap exists just as for a metal. Due to this unique feature, graphene is usually described as a zero band-gap semiconductor or semi-metal since the Density Of States (DOS) at the Fermi level is zero.

3.2.3.2 *Third-nearest-neighbour tight-binding model*

The nearest-neighbour TB approximation only considers the interaction between the π-electron wavefunctions with three of its neighbouring atoms. It was recently shown in [80] that there was poor agreement between the first-principle *ab initio* and nearest-neighbour TB band structures over the entire Brillouin zone. Thus, an enhancement was proposed to include up to the third-nearest-neighbour interaction when formulating the energy dispersion relation. This was achieved by considering the overlap between the π electron wavefunctions within a radius of $|R_{3l}| = 2.842$ Å [80].

To determine the third-nearest-neighbour TB dispersion one proceeds as outlined above where the elements of the Hamiltonian and Overlap matrices will be re-calculated [80]. From Figure 3-5 it can be understood that the matrix elements will have to include a summation of the effects from the first-nearest B_{1l}(l = 1, 2, 3), second-nearest A_{2l} (l = 1, 2 …6) and third-nearest neighbours B_{3l} (l = 1, 2, 3).

Again, using Eq. 3.31, the diagonal entries of the **H** matrix can be recalculated to include the third-nearest-neighbour:

$$
\begin{aligned}
H_{AA} = H_{BB} &= \langle \Phi_A | H | \Phi_A \rangle \\
&= \frac{1}{N} \sum_{R_A} \sum_{R_{A'}} e^{jk(R_{A'} - R_A)} \int \phi_A(r - R_A) H \phi_A(r - R_{A'}) dr \\
&= \frac{1}{N} \sum_{R_{A'} = R_A} \int \phi_A(r - R_A) H \phi_A(r - R_{A'}) dr \\
&+ \frac{1}{N} \sum_{R_{A'} = R_{A2l}} e^{jk(R_{A2l} - R_A)} \int \phi_A(r - R_A) H \phi_A(r - R_{A2l}) dr \\
&+ \frac{1}{N} \sum_{R_{A'} \neq R_A} e^{jk(R_{A'} - R_A)} \int \phi_A(r - R_A) H \phi_A(r - R_{A'}) dr \\
&= \varepsilon_{2p} + \gamma_1 \left(e^{-jk(a_1 - a_2)} + e^{jka_1} + e^{jka_2} + e^{jk(a_1 - a_2)} + e^{-jka_1} + e^{-jka_2} \right) \\
&= \varepsilon_{2p} + \gamma_1 u(k)
\end{aligned}
\qquad 3.48
$$

where:

$$
\gamma_1 = \langle \phi_A(r - R_A) | H | \phi_A(r - R_{A2l}) \rangle \qquad 3.49
$$

and

$$
u(k) = 2\cos(ka_1) + 2\cos(ka_2) + 2\cos(k(a_1 - a_2)) \qquad 3.50
$$

The off-diagonal terms are given by:

$$
\begin{aligned}
H_{AB} = H_{BA}^* &= \langle \Phi_A | H | \Phi_B \rangle \\
&= \frac{1}{N} \sum_{R = R_A} \sum_{R = R_{B1l}} e^{jk(R_{B1l} - R_A)} \int \phi_A(r - R_A) H \phi_B(r - R_{B1l}) dr \\
&+ \frac{1}{N} \sum_{R = R_A} \sum_{R = R_{B3l}} e^{jk(R_{B3l} - R_A)} \int \phi_A(r - R_A) H \phi_B(r - R_{B3l}) dr \\
&= \gamma_0 \left(e^{jk(R_{B11} - R_A)} + e^{jk(R_{B12} - R_A)} + e^{jk(R_{B13} - R_A)} \right) \\
&+ \gamma_2 \left(e^{jk(R_{B31} - R_A)} + e^{jk(R_{B32} - R_A)} + e^{jk(R_{B33} - R_A)} \right) \\
&= \gamma_0 f(k) + \gamma_2 m(k)
\end{aligned}
\qquad 3.51
$$

where:

$$
\gamma_2 = \langle \phi_A(r - R_A) | H | \phi_B(r - R_{B3l}) \rangle \qquad 3.52
$$

and

$$
\begin{aligned}
m(k) &= \left(e^{jk(R_{B31}-R_A)} + e^{jk(R_{B32}-R_A)} + e^{jk(R_{B33}-R_A)}\right) \\
&= \left(e^{jk\frac{2}{3}(a_1+a_2)} + e^{jk\frac{2}{3}(a_2-2a_1)} + e^{jk\frac{2}{3}(a_1-2a_2)} \right) \\
&= \left(e^{jk\frac{2}{3}(a_1+a_2)} \left(1 + e^{-jk2a_1} + e^{-jk2a_2}\right) \right) \\
&= f(2k)
\end{aligned}
\qquad 3.53
$$

The parameters γ_1 and γ_2 represent the interaction energies with the second and third-nearest neighbours, respectively [80].

Correspondingly, to evaluate the overlap matrix (**S**), the diagonal elements are first computed. Assuming that the atomic wavefunctions are normalized (*i.e.* $\langle \Phi_A(r-R_A) | \Phi_A(r-R_A) \rangle = 1$) it can be deduced that:

$$
\begin{aligned}
S_{AA} = S_{BB} &= \langle \Phi_A | \Phi_A \rangle \\
&= \frac{1}{N} \sum_{R_A} \sum_{R_{A'}} e^{jk(R_{A'}-R_A)} \int \phi_A(r-R_A)\phi_A(r-R_{A'})dr \\
&= \frac{1}{N} \sum_{R_{A'}=R_A} \int \phi_A(r-R_A)\phi_A(r-R_{A'})dr \\
&+ \frac{1}{N} \sum_{R_{A'}=R_{A2l}} e^{jk(R_{A2l}-R_A)} \int \phi_A(r-R_A)\phi_A(r-R_{A2l})dr \\
&+ \frac{1}{N} \sum_{R_{A'}\neq R_A} e^{jk(R_{A'}-R_A)} \int \phi_A(r-R_A)\phi_A(r-R_{A'})dr \\
&= 1 + s_1 \left(e^{-jk(a_1-a_2)} + e^{jka_1} + e^{jka_2} + e^{jk(a_1-a_2)} + e^{-jka_1} + e^{-jka_2} \right) \\
&= 1 + s_1 u(k)
\end{aligned}
\qquad 3.54
$$

where:

$$
s_1 = \langle \phi_A(r-R_A) | \phi_A(r-R_{A2l}) \rangle \qquad 3.55
$$

The off-diagonal terms are calculated in a similar manner to the off-diagonal elements of the Hamiltonian matrix:

$$
\begin{aligned}
S_{AB} = S_{BA}^{*} &= \left\langle \Phi_A \middle| \Phi_B \right\rangle \\
&= \frac{1}{N} \sum_{R=R_A} \sum_{R=R_{B1l}} e^{jk(R_{B1l}-R_A)} \int \phi_A(r-R_A)\phi_B(r-R_{B1l})dr \\
&+ \frac{1}{N} \sum_{R=R_A} \sum_{R=R_{B3l}} e^{jk(R_{B3l}-R_A)} \int \phi_A(r-R_A)\phi_B(r-R_{B3l})dr \\
&= s_0 \left(e^{jk(R_{B11}-R_A)} + e^{jk(R_{B12}-R_A)} + e^{jk(R_{B13}-R_A)} \right) \\
&+ s_2 \left(e^{jk(R_{B31}-R_A)} + e^{jk(R_{B32}-R_A)} + e^{jk(R_{B33}-R_A)} \right) \\
&= s_0 f(k) + s_2 f(2k)
\end{aligned}
\qquad 3.56
$$

where:

$$
s_2 = \left\langle \phi_A(r-R_A) \middle| \phi_B(r-R_{B3l}) \right\rangle \qquad 3.57
$$

Having calculated all the elements of the required matrices, **H** and **S** can now be re-written as follows:

$$
H = \begin{pmatrix} \varepsilon_{2p} + \gamma_1 u(k) & \gamma_0 f(k) + \gamma_2 f(2k) \\ \gamma_0 f^{*}(k) + \gamma_2 f^{*}(2k) & \varepsilon_{2p} + \gamma_1 u(k) \end{pmatrix},
$$

$$
S = \begin{pmatrix} 1 + s_1 u(k) & s_0 f(k) + s_2 f(2k) \\ s_0 f^{*}(k) + s_2 f^{*}(2k) & 1 + s_1 u(k) \end{pmatrix}
$$

substituting these matrices into Eq. 3.36 and using:

$$
E_i(k) = \frac{-b \pm \sqrt{b^2 - 4ac}}{2a} \qquad 3.58
$$

where:

$$
a = \left(1 + s_1 u(k)\right)^2 - s_0^2 \left| f(k) \right|^2 - s_0 s_2 g(k) - s_2^2 \left| f(2k) \right|) \qquad 3.59
$$

$$
b = 2\gamma_0 s_0 \left| f(k) \right|^2 - 2\left(\varepsilon_{2p} + \gamma_1 u(k)\right)\left(1 + s_1 u(k)\right) + \left(s_2 \gamma_0 + s_0 \gamma_2\right) g(k) + 2 s_2 \gamma_2 \left| f(2k) \right| \qquad 3.60
$$

$$
c = \left(\left(1 + s_1 u(k)\right)^2 - s_0^2 \left| f(k) \right|^2 - s_0 s_2 g(k) - s_2^2 \left| f(2k) \right|^2 \right) \qquad 3.61
$$

given that:

$$
\begin{aligned}
g(k) &= f(k)f^*(2k) + f^*(k)f(2k) \\
&= 4\cos(ka_1) + 4\cos(ka_2) + 4\cos(k(a_1 - a_2)) + 2\cos(k(a_1 + a_2)) + \\
&\quad 2\cos(k(a_1 - 2a_2)) + 2\cos(k(2a_1 - a_2))
\end{aligned}
\qquad 3.62
$$

The fitting parameters (γ's, s's and ε_{2p}) used to solve Eqs. 3.59, 3.60 and 3.61 are found in [80] by fitting the energies generated with the *ab initio* energies for all k [80]. These are listed below in Table 3-1.

ε_{2p}	γ_0	s_0	γ_1	s_1	γ_2	s_2
-0.28	-2.97	0.073	-0.073	0.018	-0.33	0.026

Table 3-1: Third-nearest-neighbour tight-binding fitting parameters (eV) [80].

By solving Eq. 3.58, a dispersion relation similar to that shown in Figure 3-6(a) is generated. The difference between the third-nearest neighbour and nearest neighbour TB approaches are further assessed by calculating graphene's band structure and plotting the results as depicted in Figure 3-7.

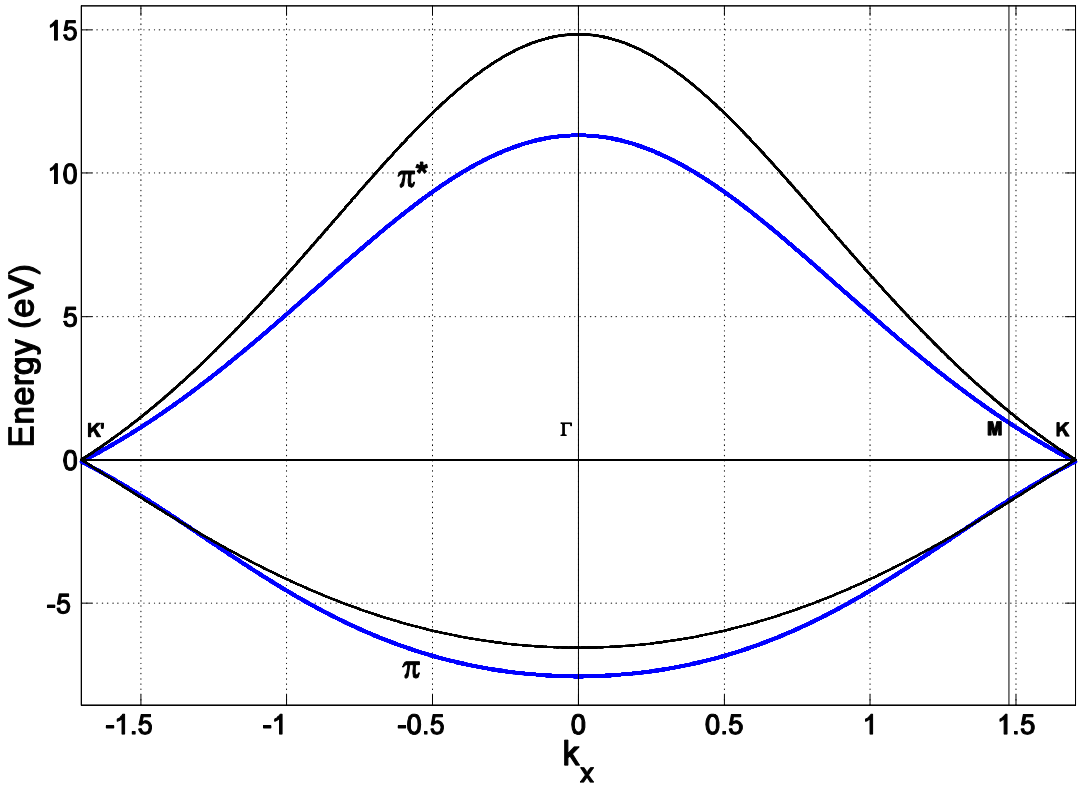

Figure 3-7: Comparison between the third-nearest neighbour (—) and nearest neighbour (—) TB graphene band structure at k_y=0.

As can be seen there is a pronounced disparity between the third-nearest neighbour and nearest neighbour TB band characteristics especially near the high-symmetry lines M and Γ. For instance, at the M points, the anti-bonding π^* energy bands differ by as much as 0.4eV.

According to [80] the agreement between the third-nearest TB electronic dispersion and the *ab initio* calculations is better than 250 meV for all k_x, offering superior fitting results than the nearest-neighbour TB approximation over the entire Brillouin zone. This is of paramount importance when calculating the transition energies and optical absorption across the complete band-structure of a nanotube with a given diameter and chirality [80]. In fact, it was established that the prediction made by the third-nearest TB model for the second transition energies of a nanotube identically matched with *ab initio* calculations, whilst the nearest-neighbour approximation offered a strong overestimation [80].

Another benefit of including more distant neighbours in the TB method will be further detailed when determining the SWCNT fundamental band-gap for different geometrical properties, which will be covered in the next chapter.

3.3 Zone-folding technique

Since a SWCNT has a single atom thickness and a small number of carbon atoms around its circumference, these two physical constraints lead to quantum confinement of the wavefunctions in both the radial and circumferential directions, respectively. As a result the electron wavelength is quantised around the circumference of the tube to satisfy the Born-von Karman boundary condition. All other wavelengths disappear by interference. The wavelength quantisation around the circumference results in a discrete set of wavevectors, **k**, which are allowed to fit around the tube as illustrated by the parallel straight blue lines in the bottom panels of Figure 3-3 [71]. However, along the nanotube axis there is no confinement producing an infinite amount of allowed k states (continuous blue lines in bottom panels of Figure 3-3) in that direction, which offers a pathway for the electron plane-waves to propagate. As will be discussed later, the intersection between the quantised wavevectors and specific points in the Brillouin zone (bottom panels of Figure 3-3) are of decisive significance in determining whether a SWCNT is semiconducting or metallic [75].

Now, if one takes the dispersion relation of graphene and imposes the periodic boundary conditions in the circumferential direction, then the band characteristics of a nanotube should emerge. This technique is called 'zone-folding' and can be applied to SWCNTs with any diameter and chirality.

Since the dispersion relation of graphene has already been calculated, now the allowed k-points generated by the newly imposed boundary conditions when the graphene sheet is rolled into a nanotube need to be identified. This necessitates the definition of the 2D Brillouin zone for a given nanotube.

3.3.1 SWCNT Brillouin zone

In the previous sections only the 2D Brillouin zone of graphene was considered. However, when analysing the band structure of a SWCNT the 2D and 1D Brillouin zones of the nanotube unit cell should be taken into account.

The nanotube unit cell presented in Figure 3-8 is the shaded rectangle bounded by the chiral vector $\mathbf{C_h}$ and the translation vector **T**. The 1D translation vector **T** is perpendicular to $\mathbf{C_h}$ and is parallel to the nanotube axis. In addition, the magnitude of **T** gives the length of the nanotube cell, which is the smallest distance along the nanotube axis before the pattern of the carbon atoms repeats itself [79].

If the vector **T** is defined as:

$$T = t_1 a_1 + t_2 a_2 \tag{3.63}$$

and

$$\begin{aligned} C_h \cdot T &= \frac{a^2}{4}(m-n)(t_1 - t_2) + \frac{3a^2}{4}(m+n)(t_1 + t_2) \\ &= t_1(2m+n) + t_2(2n+m) = 0 \end{aligned} \tag{3.64}$$

then Eq. 3.64 has an infinite number of solutions for the integer pair (t_1,t_2) [81]. Therefore, one must choose the smallest pair to attain the primitive translation vector **T** of the tube [81].

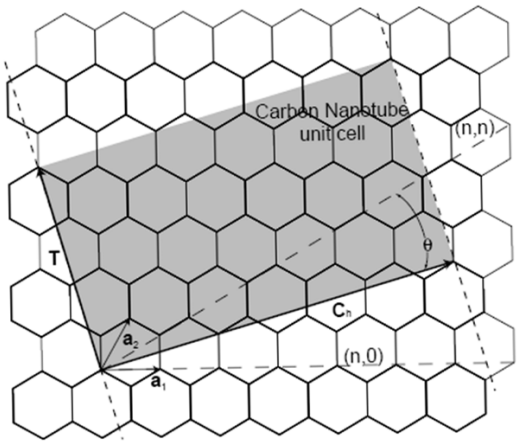

Figure 3-8: Carbon Nanotube unit cell (shaded) defined by the chiral $\mathbf{C_h}$ and translation **T** vectors. The tube emerges from rolling up the piece of graphene sheet enclosed by the shaded region. This portion can be repeated along the translation vector **T** to obtain the required length [79].

One can express the solutions for t_1 and t_2 as follows:

$$t_1 = \frac{2n+m}{d_R} \qquad t_2 = -\frac{2m+n}{d_R} \tag{3.65}$$

where

$$d_R = \gcd(2n+m, 2m+n) \tag{3.66}$$

d_R represents the greatest common devisor (gcd) of $2n+m$ and $2m+n$ [79]. Thus, the primitive translation vector **T** can be re-written as:

$$T = \frac{2n+m}{d_R}a_1 - \frac{2m+n}{d_R}a_2 \tag{3.67}$$

where the area of the carbon nanotube primitive unit cell could be define as:

$$A = C_h \times T = \frac{a^2\sqrt{3}\left(m^2+mn+n^2\right)}{d_R} \tag{3.68}$$

The number of primitive graphene unit cells in a nanotube unit cell can be determined from:

$$N = \frac{A}{a_1 \times a_2} = \frac{2\left(m^2 + mn + n^2\right)}{d_R} \qquad 3.69$$

Since a single graphene unit cell contains two carbon atoms, there are 2N carbon atoms (or $2p_z$ orbitals) in a nanotube unit cell [14].

The 2D Brillouin zone of a carbon nanotube is established by deriving the reciprocal lattice vectors from the primitive (**C_h**,**T**) pair. Using Eq. 3.14 and 3.15 and replacing **a_1**, **a_2** and **a_3** with **C_h**, **T** and the unit normal vector **($\hat{n}$),** respectively, the following is obtained:

$$K_1 = k_\perp = \frac{1}{N}(-t_2 b_1 + t_1 b_2) \qquad 3.70$$

$$K_2 = k_\parallel = \frac{1}{N}(m b_1 - n b_2) \qquad 3.71$$

In sub-section 3.2.1 it was verified that the primitive lattice vectors **a_1** and **a_2** are perpendicular to the reciprocal lattice vectors **b_2** and **b_1** respectively. Using the same argument, it can be deduced that **C_h** must be perpendicular to the second reciprocal lattice vector (**K_2**) of the nanotube. This implies that the second reciprocal lattice vector is parallel to the nanotube axis, which from now onwards will be denoted as $k_{||}$. The direction of $k_{||}$ is set by the direction of the translation vector **T** and the length is given by:

$$\left|k_\parallel\right| = \frac{2\pi}{\left|T\right|} \qquad 3.72$$

Similarly, **K_1** can be shown to be parallel to **C_h** which is perpendicular to the nanotube axis. Hence, **K_1** can be denoted as $k_\perp$ with a magnitude of:

$$\left|k_\perp\right| = \frac{2\pi}{\left|C_h\right|} \qquad 3.73$$

Just like the real space unit cell of the nanotube, the 2D Brillouin zone is also rectangular with the side lengths defined by Eq. 3.72 along the $k_{||}$ direction and Eq. 3.73 along the $k_\perp$ direction.

3.3.2 Defining the boundary conditions

The zone folding technique performs a reduction in the Brillouin zone dimensions from 2D to 1D when a SWCNT unit cell is folded into a cylinder. At the boundaries where the edges of the CNT unit cell meet, the following Bloch equation must be satisfied:

$$\psi_k(r + C_h) = e^{jk.C_h}\psi_k(r) \qquad 3.74$$

That is, the electron wavefunctions that differ by a complete lattice translation vector $\mathbf{C_h}$ along the circumference of the tube must be equivalent when scaled by the factor $e^{jk\cdot C_h}$ [75]. In addition, due to the folding, the Born-von Karman boundary condition must also be fulfilled. This is generally expressed as:

$$\psi_k(r + R) = \psi_k(r) \qquad 3.75$$

The Born-von Karman boundary condition requires that the electron wavefunctions which differ by a lattice translation vector **R** to be identical. Thus, to match Eq. 3.75 with 3.74, the following fundamental condition must be met:

$$k.C_h = 2\pi q \qquad 3.76$$

where q is an integer. To satisfy Eq. 3.76, the allowed wave vectors around the circumference have to be a multiple of $|k_\perp|$ with a total of N states in that direction [79]. On the other hand, along the tube axis there are no boundaries (assuming that the tube is infinitely long) for the wave vectors and therefore all states are allowed in that direction [79]. By expanding Eq. 3.76, this results in:

$$\begin{pmatrix} k_x \\ k_y \end{pmatrix}.(ma_1 + na_2) = k_x\frac{a}{2}(m-n) + k_y\frac{a\sqrt{3}}{2}(m+n) = 2\pi q \qquad 3.77$$

or

$$k_y = -\frac{(m-n)}{\sqrt{3}(m+n)}k_x + \frac{4\pi q}{a\sqrt{3}(m+n)} \qquad 3.78$$

Eq. 3.77 denotes a set of parallel lines that represent the allowed electron state pairs (k_x, k_y) in the 2D nanotube reciprocal space. When the electron state pairs (k_x, k_y) of Eq. 3.77 are substituted into the energy dispersion relation (Eq. 3.58) with q = 1,2…N, a set of N lines are produced, which slice the 2D bandstructure of graphene giving 1D energy bands. That is, there are N subbands associated with each q for a SWCNT [82]. If one of these slices intersects with a high symmetry K point in the Brillouin zone of graphene (where conduction and valence band touch at the Fermi-level as shown in Figure 3-6) the nanotube can be deemed metallic [79]. Otherwise, the nanotube is semiconducting with a finite band-gap. Since the allowed electron state pairs (k_x, k_y) depend on the choice of n and m, each SWCNT will have a different electronic structure as will now be illustrated.

3.4 SWCNT band structures

By imposing the allowed electron state pairs (k_x, k_y) denoted in Eq. 3.77 on the graphene band structure derived using the third nearest-neighbour TB technique (represented by Eq. 3.58) the energy dispersion is first plotted for an armchair (10,10) SWCNT. The result is demonstrated in Figure 3-9.

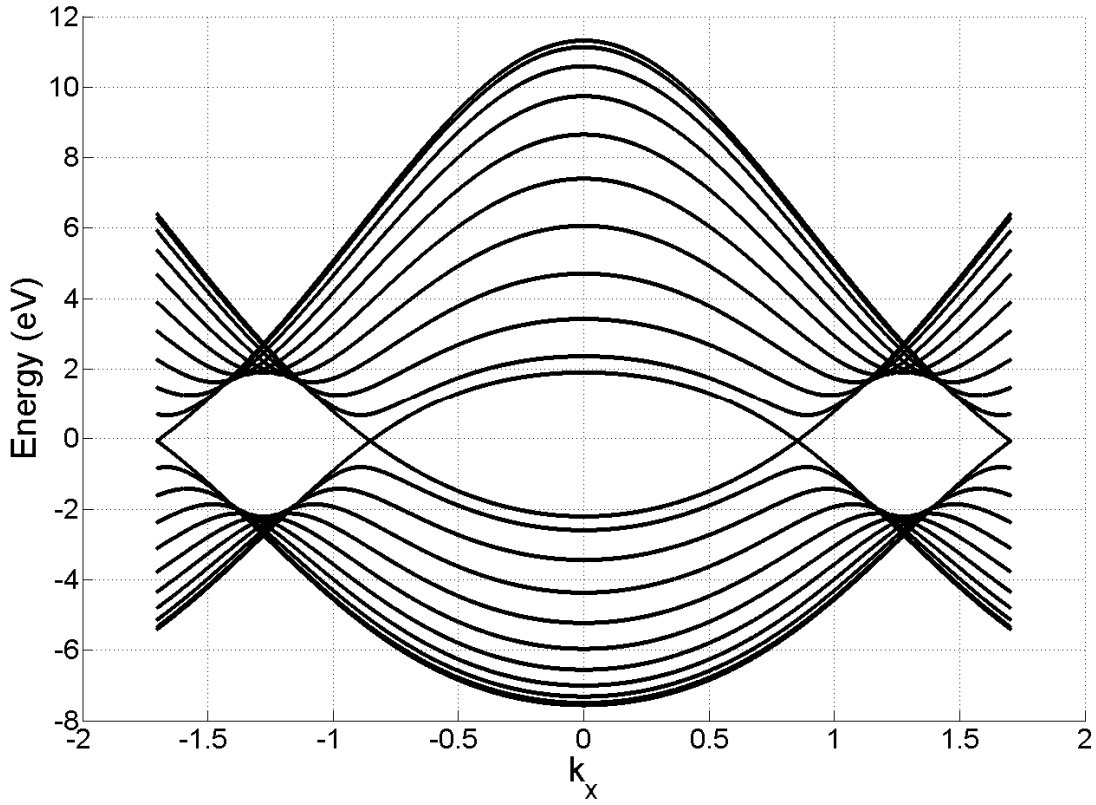

Figure 3-9: Band structure of a (10,10) carbon nanotube. Band-gap (E_{11}) is calculated to be 0 eV confirming that it is metallic.

Firstly, it can be seen from Figure 3-9 that a set of quantised subbands appear for the SWCNT band structure, which is typical of a 1D nanostructure. Secondly, as expected, the armchair tube ($m = n$) has a zero band-gap ($E_{11} = E_g = 0$eV) since the allowed state-vectors cross the corners points of the first Brillouin zone as was previously revealed in Figure 3-3(a) [50]. This confirms that the (10,10) armchair tube is metallic. On the other hand, for an *(m,n)* nanotube with the following conditions:

$$m - n \neq 3\xi \qquad or$$
$$2m + n \neq 3\xi \tag{3.79}$$

where ξ is any integer, the state-vectors miss the corner points and the nanotube is considered semiconducting [50]. Here, this is verified for two distinct nanotubes; the (19,0) zig-zag SWCNT (see Figure 3-10(a)) and the (10,9) chiral CNT (see Figure 3-10(b)).

Again, as can be clearly observed from Figure 3-10(a) and (b) that a set of quantised subbands emerge with a finite band-gap as a result of no state-vectors interacting with the

graphene Brillouin zone corners. These cases were previously portrayed in Figure 3-3(c) and (d), respectively.

Hence, from the conditions specified by Eq. 3.79 it could be reasoned that, theoretically, only 1/3rd of SWCNTs should be metallic and 2/3rd semiconducting [83]. If an *(m,n)* nanotube satisfies the condition $m - n = 3q$ and $m \neq n$ then it would be considered as a semi-metal because certain electronic states land on the corner points of the first Brillouin zone, but not all [50]. In this thesis, one shall assume all semi-metallic tubes to be metallic.

Finally, it should be noted that in both Figure 3-10(a) and (b) the nearest subbands to the Fermi level (*i.e.* the conduction and valence bands of the SWCNT) are very much aligned along the momentum axis (k_x). This re-confirms that SWCNTs are indeed direct band-gap semiconductors. Moreover, it can be seen that the conduction subband minima's and the valence subband maxima's are symmetric about the Fermi level, which has significant implications in evaluating the electron and hole effective masses. We shall return to this point in the following chapter.

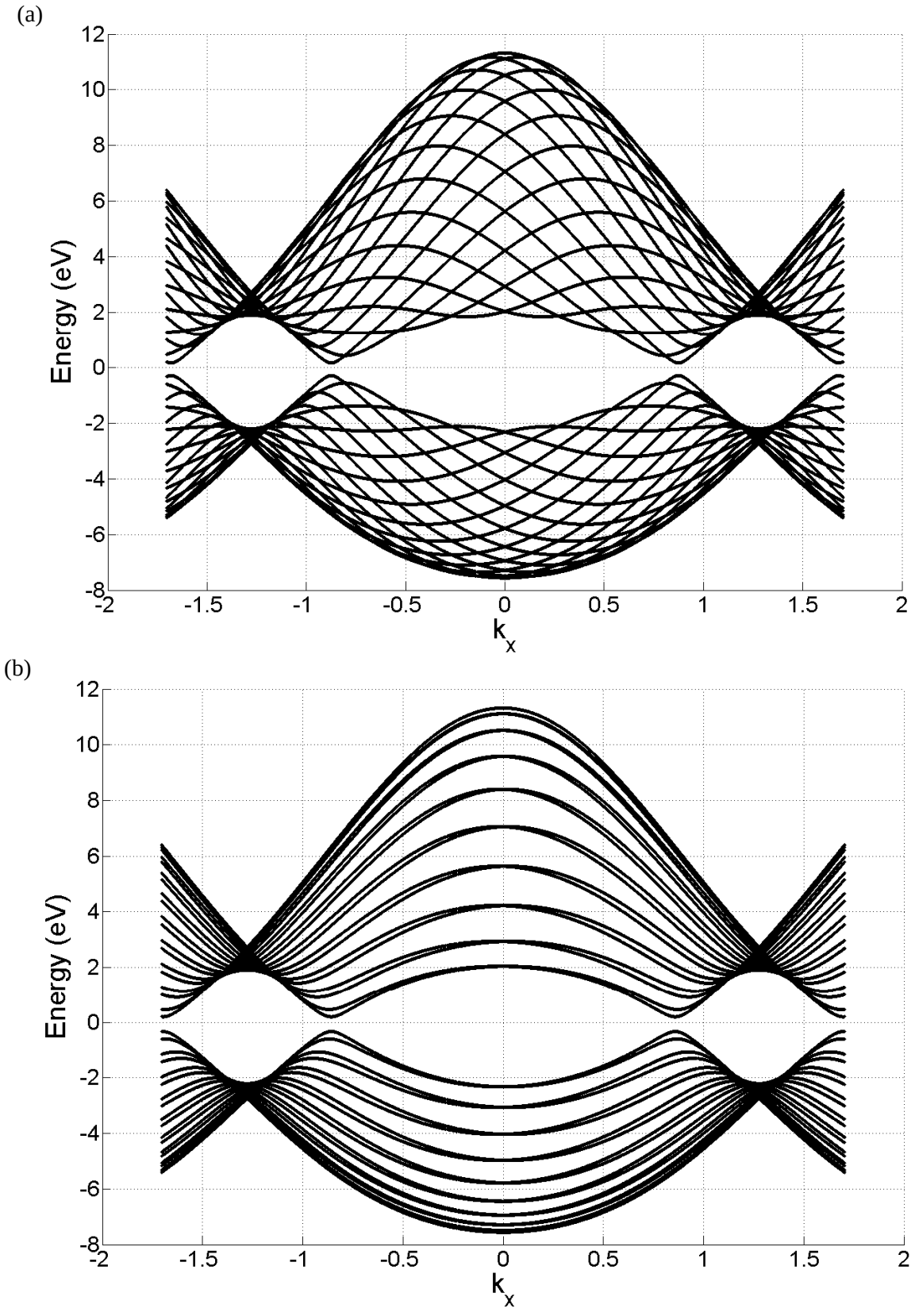

Figure 3-10: (a) Band structure of a (19,0) zig-zag carbon nanotube (E_{11}=0.452eV). (b) Band structure of a (10,9) chiral carbon nanotube (E_{11}=0.534eV).

3.5 Summary

This chapter offered a detailed overview of the chosen technique in realising the band-structure of a single-walled carbon nanotube, which will be profoundly utilised in the subsequent chapters in order to identify the related electronic and optical properties.

The basic structural features of carbon nanotubes is initially discussed where the direct and reciprocal lattice of a graphene sheet are introduced. Next, the associated electronic characteristics of graphene are derived with the development of a semi-empirical nearest-neighbour Tight-Binding (TB) model. It is confirmed that this approximation can be further improved by employing the third-nearest neighbour TB approach where a marked difference is clearly illustrated compared to the nearest-neighbour TB model over the entire first Brillouin zone. This is of utmost significance particularly when calculating higher order optical transition energies for nanotubes. Subsequently, it is demonstrated that by applying the Zone Folding (ZF) technique to the established graphene band-structure using the third-nearest neighbour TB method, this generates the SWCNT band-structure. The chapter ends with illustrative examples of SWCNT band-structures that depict either metallic or semiconducting characteristics depending on their geometrical properties. It is also confirmed that semiconducting SWCNTs do indeed possess a direct band-gap where the conduction band minima is shown to be symmetric with the valence band maxima.

The next chapter constitutes the first key contribution of this thesis where the third-nearest neighbour TB and ZF approach discussed above will be exploited in developing novel analytical models that predict the SWCNT band-gap and carrier effective mass directly from its diameter (d) and chiral angle (θ) with a runtime independent of tube size.

Chapter 4 Differentiation and Electronic Characterisation of Carbon Nanotubes

In this chapter novel analytical models are presented that predict the SWCNT band-gap and carrier effective mass directly from its diameter (d) and chiral angle (θ) with a runtime independent of tube size. These models are based on expressions that have been derived by curve-fitting the outcome generated from the third-nearest neighbour Tight-Binding (TB) method in conjunction with the Zone-Folding (ZF) technique. Notably, in resolving the SWCNT band-gap a rapid and accurate approach is established in distinguishing metallic and semiconducting nanotubes.

Herein, a brief discussion of the shortcomings associated with present-day band-gap models is initially addressed. Next, the band-structure of a distinct set of nanotubes with known geometrical properties is simulated where the corresponding band-gap characteristics are extracted. In doing so, a semi-empirical model that differentiates metallic and semiconducting nanotubes is established, which is subsequently validated against experimental data. Further, a SWCNT band-gap model is developed for semiconducting tubes, which is also verified against experimental as well as alternative theoretical values.

The final part of this chapter studies the various SWCNT carrier effective mass models in literature and proposes a new analytical approach based on fitting the energy dispersions produced using the chosen TB and ZF approach with the parabolic effective mass approximation.

4.1 Modelling the band-gap of an isolated SWCNT

In Chapter 3 it was demonstrated that the band characteristics of nanotubes with dissimilar chiral vector indices (*m*,*n*) could appreciably differ leading to diverse electronic properties. However, no quantifiable relationship between these parameters was conferred. The following work shall address this by examining the effects of two key SWCNT physical variables (namely, the diameter (*d*) and chrial angle (θ)), which could be directly measured using spectroscopic characterisation techniques, on the nanotube band-gap.

The band-gap constitutes one of the most important material dependent electronic properties and is defined as the algebraic difference in energy between the unoccupied conduction band minima and the occupied valence band maxima [19]. Generally, this gap represents the forbidden energy range where no carrier states are allowed to exist and therefore plays a dominant role in dictating the carrier transport characteristics of a material [19, 28]. For instance, as was shown in Chapter 2, this has significant implications on the saturation current of a *pn* junction photo-diode [19, 28]. Furthermore, the importance of the material band-gap on the photocurrent and photo-voltage (V_{OC}) of a PV converter was demonstrated [28].

Apart from the physical geometries, there have been experimental as well as theoretical reports that noted an observable alteration of the fundamental SWCNT band-gap with high levels of doping [84, 85]. Here, it is assumed that all SWCNTs under inspection are un-doped and exhibit complete purity with no defects. Also, there are references that have acknowledged the modification of the SWCNT band-gap under mechanical strain [86, 87]. Owing to the low magnitudes claimed for changes in the band-gap (<100 meV per 1% variation in strain [78]) it has been decided that any band-structure effects with respect to nanotube deformations could be neglected.

4.1.1 Review of current SWCNT band-gap prediction models

Earlier studies confirmed the dominant sensitivity of the CNT's band-gap to both *d* and θ, where several theoretical and analytical models have been established to simulate their electronic band-structure [14, 80, 83, 87-91]. Amongst the commonly used band models are the nearest-neighbour Tight-Binding (TB) approach with Zone-Folding (ZF) [14, 80, 83, 88,

91], the Extended Hückel Theoretical (EHT) technique [89], first-principle *ab-initio* as well as Density Functional Theory (DFT) calculations [87, 90, 91].

The TB approach has been claimed to be typically 2-3 orders of magnitude faster than the atomistic *ab initio* methods because of the single-particle approximation [77]. Yet, in terms of accuracy, it has demonstrated very good agreement with first-principles (*e.g.* <250 meV difference between the third-nearest neighbour TB and *ab initio* calculations for the graphene electronic band-structure) [80]. It has been further acknowledged that the TB method is useful in situations where the quantum mechanical effects of a system needs to be retained but the system size is too large, making rigorous *ab initio* calculations impractical [77]. This is the main reason why the TB model is a commonly used technique in analysing the electronic and optical properties of carbon nanotubes [92].

However, although very accurate, the TB model is still computationally intensive and possesses a time complexity that increases with the size of the nanotube since that influences the number of subbands N which need to be calculated. For applications that require the simultaneous simulation of millions of distinct CNT-devices the TB approach would be difficult to utilise in a timely manner.

Empirical models such as those mentioned in [93, 94] were formed by experimentally probing a small number of semiconducting SWCNTs in order to measure their geometric structure and corresponding electrical output characteristics. In turn, results were plotted and curves extrapolated to acquire the CNT band-gap [90]. Not only were these results based on undersized samples of CNTs but the measurements were found to be strongly dependent upon the characterisation technique employed [95-97]. Moreover, it has been argued that the statistical validity of measurements made using bulk sensitive probes is uncertain due to the lack of sensitivity in the characterisation of individual nanotubes present within a given sample [95, 98].

Hence, in the following we shall propose an analytical semi-empirical model based on the highly precise third-nearest neighbour TB and ZF technique with a time complexity that is independent of the size of the nanotube and simply consists of a single expression which

directly determines the band-gap of an isolated SWCNT. To the knowledge of the author, this has not been accomplished by any other work.

4.1.2 Simulating the SWCNT band-gap using the third-nearest neighbour TB and ZF technique

Previously, a discussion was imparted regarding the added benefits in terms of accuracy of using the third-nearest-neighbour TB approach over the nearest-neighbour method when calculating the graphene band-structure. It was additionally shown that the band-structure of an isolated SWCNT could be determined when applying the ZF technique. Here, this method (see MATLAB code in Appendix B) is employed to calculate the band-gap (E_g) for a set of nanotubes characterised by all possible chiralities, 0^0-30^0, and diameters ranging between 0.45nm-2.55nm. These ranges offered a total of 286 possible SWCNT chiral vector combinations of (m,n) indices. Figure 4-1 illustrates the calculated E_g for the various θ and d.

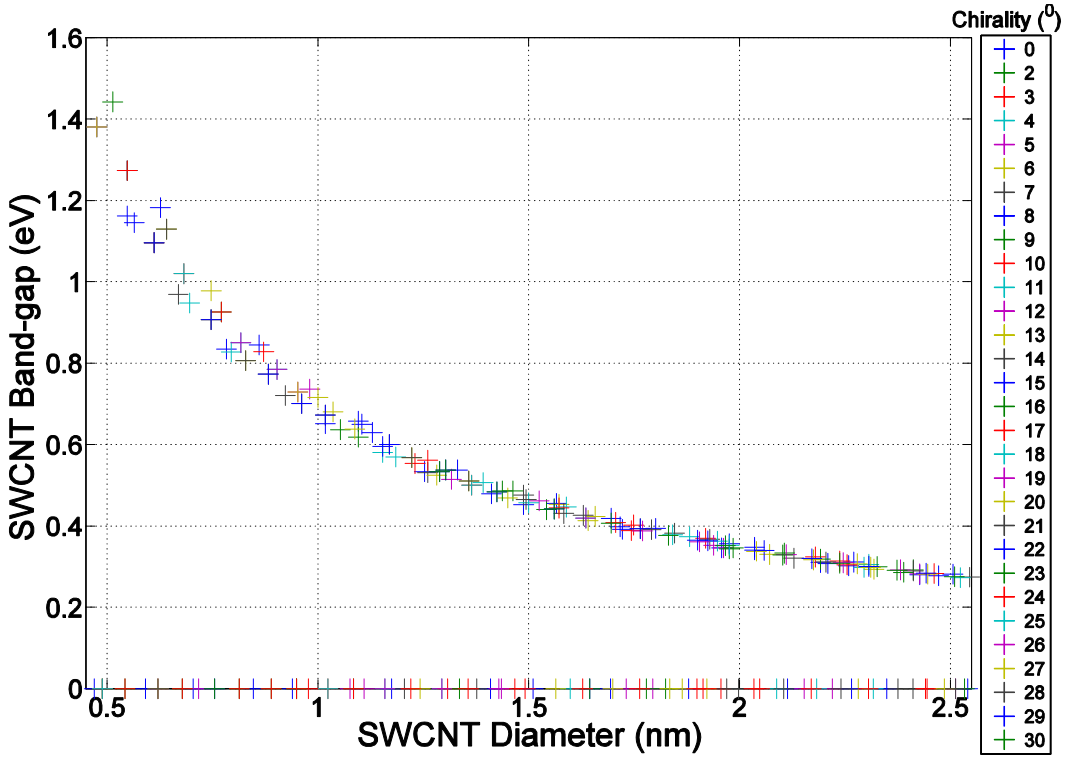

Figure 4-1: SWCNT band-gap (E_g) for different geometrical properties, d and θ. CNTs with different chirality are illustrated by separate colour shading.

Figure 4-1 clearly portrays, as expected, two distinctive nanotube types- metallic (E_g=0) and semiconducting (E_g>0), though, it is unclear how the SWCNT geometrical

properties prescribe these attributes. So, to gain a more refined perspective of this distinction a SWCNT structural parameter space is created and analysed.

4.1.3 Distinguishing metallic and semiconducting SWCNTs

The geometric variables (θ,d) that produced a zero band-gap and non-zero band-gap were separately plotted as data points, indicated by symbols + and ○ respectively, in the structural parameter space shown below in Figure 4-2.

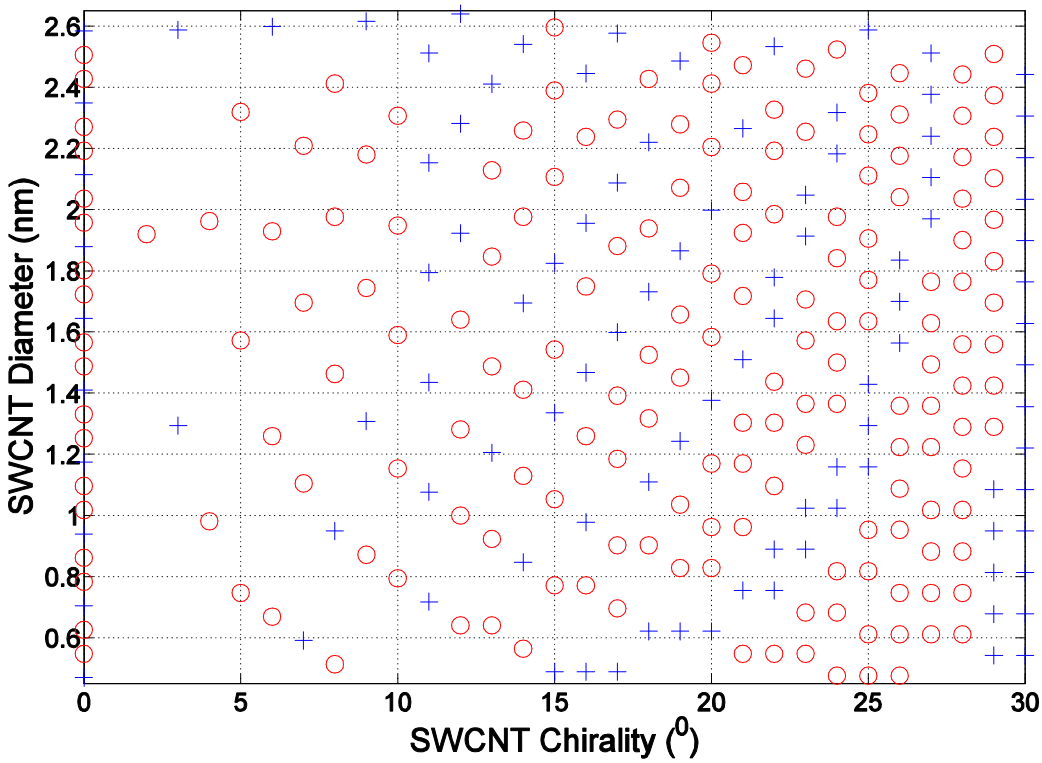

Figure 4-2: CNT structural parameter space indicating data points (θ,d) for metallic and semiconducting tubes.

From Figure 4-2 it can be firstly confirmed that all armchair tubes (θ=30^0) possess a zero band-gap. Secondly, zig-zag tubes (θ=0^0) can be observed to alternate between a zero and non-zero band-gap, which will be further discussed later. Thirdly, the zero band-gap chiral tubes (0^0<θ<30^0) could be seen to follow a pattern that shall now be uncovered.

To establish an expression that will enable us to predict the zero band-gap data points for the chiral as well as zig-zag tubes, a relationship between d and θ is initially derived as follows. By rearranging Eq. 3.7 of Chapter 3 and substituting into Eq. 3.5 gives the following:

$$d = \frac{3a_{cc}}{2\pi}\frac{n}{\sin\theta} \qquad 4.1$$

Now, assuming that the sine function of Eq. 4.1 can be approximated by a first-degree polynomial ($b\theta+c$) over the interval $0^0 \leq \theta \leq 30^0$ then it can be deduced that the diameter d is inversely proportional to $b\theta+c$. This assumption is based on the 0.6% Normalised Root-Mean-Square (NRMS) error achieved when approximating a sine function with a linear polynomial over the required interval. Hence, it is assumed that:

$$d \approx \frac{1}{b\theta+c} \qquad 4.2$$

When examining the zero band-gap data points in Figure 4-2 it could be noticed that if several distinct curves were to be fitted over the points then they would all share the same asymptote at $\theta=30^0$. Thus, b can be expressed in terms of c as $b=-c/30$, leaving us only with one unknown variable; c.

Upon close inspection of the zig-zag tubes ($\theta=0^0$) one could detect an arithmetic sequence in the tube diameters that offer a zero band-gap. These diameters include the third multiple of the smallest possible diameter. In theory, the smallest possible SWCNT diameter can be determined from Eq. 3.5 given a tube indices of *(1,0)*, providing $d_{min}=\sqrt{3}a_{cc}/\pi$. Therefore, the value of c can be expressed as a reciprocal of $3pd_{min}$, where p is a positive integer. Combining the above mentioned results allows us to form an expression for the zero band-gap data points over the tube range $0^0 \leq \theta < 30^0$:

$$D(\theta, p) = \left(\frac{\pi}{3p\sqrt{3}a_{cc}} \left(1 - \frac{\theta}{30} \right) \right)^{-1} \qquad 4.3$$

Eq. 4.3 represents the zero band-gap curves shown in Figure 4-3 where p selects the curve of interest. However, Eq. 4.3 is unable to predict armchair tubes ($\theta=30^0$) as well as zero diameter tubes. Thus, to cover all zero band-gap data points in Figure 4-2, a function can be formulated that assumes a value of zero only when *either*:

- the diameter d lies on a curve approximated by Eq. 4.3 for a given geometry,

- or, the SWCNT is an Armchair (θ=30^0) tube,
- or, the SWCNT has a null diameter (d=0nm).

Quantitatively, this can be expressed as:

$$f(\theta,d)=d(30-\theta)\prod_{p=1}^{M}(D(\theta,p)-d) \qquad 4.4$$

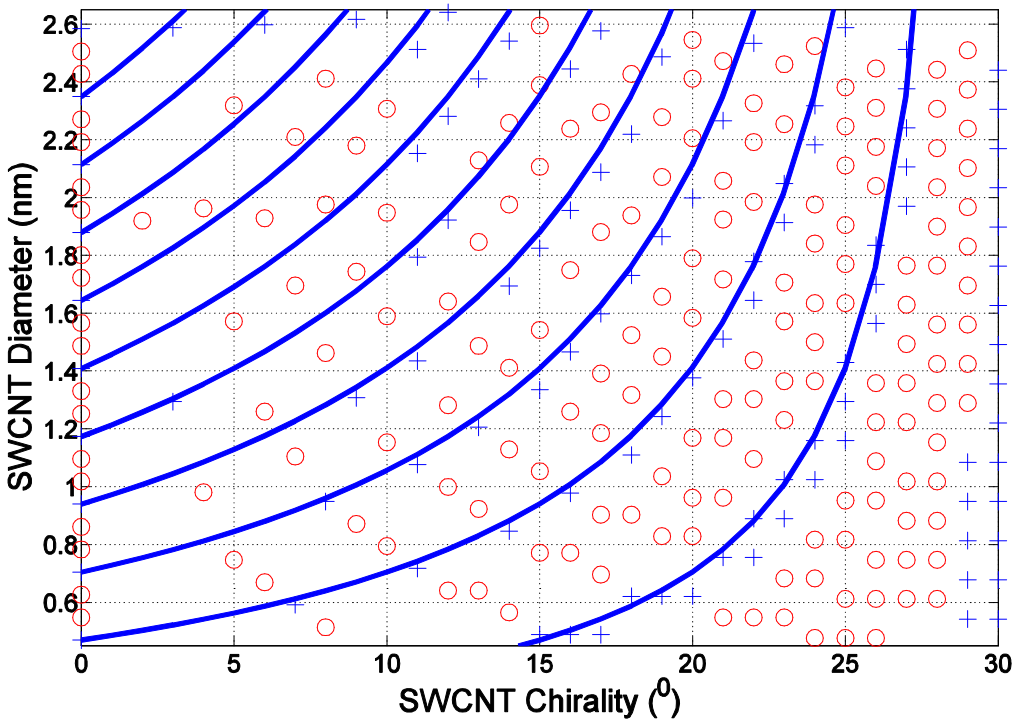

Figure 4-3: CNT structural parameter space indicating data points (θ,d) for metallic and semiconducting tubes with curves (—) representing Eq. 4.3 for p=1-10.

where M represents the total number of curves taken into consideration. $f(\theta,d)$ can be rearranged giving:

$$f(\theta,d)=d(30-\theta)\prod_{p=1}^{M}\left(1-\frac{\alpha}{p}\right)\frac{pd}{\alpha} \qquad 4.5$$

where:

$$\alpha=\frac{d\pi}{90\sqrt{3}a_{cc}}(30-\theta) \qquad 4.6$$

To solve Eq. 4.5, *M* iterations are required where each product term is evaluated individually and then multiplied by the rest of the function. This process is time consuming for simulating a design with multiple CNT-devices and hence there is a need to reduce the product term to a non-iterative form. Moreover, the accuracy of Eq. 4.5 is limited by the number of curves chosen when defining *M* since the more curves considered the higher the number of zero band-gap data points covered. One way of resolving these issues is to consider a high number of curves and taking the limit as *M* tends towards a finitely large value. To accomplish this, Eq. 4.5 is firstly multiplied and divided by the conjugate of the product term. Then, $f(\theta,d)$ is rearranged to:

$$f(\theta,d)=\frac{\alpha 90\sqrt{3}a_{cc}}{\pi}\prod_{p=1}^{M}\left(1-\frac{\alpha^2}{p^2}\right)\prod_{p=1}^{M}\left(\frac{p^2 d}{\alpha(p+\alpha)}\right) \qquad 4.7$$

As *M* tends towards a finitely large value, the first product term of Eq. 4.7 could be approximated by a $sinc(\pi\alpha)$ function and the second product term tends towards a high value. Since only the roots of $f(\theta,d)$ are of interest one could approximate Eq. 4.7 as:

$$f(\theta,d)=\left|\Re(\sin(\pi\alpha))\right| \qquad 4.8$$

where $\Re$ is a function that rounds values to the nearest integer, giving $f(\theta,d)=0$ for metallic SWCNTs and $f(\theta,d)=1$ for semiconducting tubes. Eq. 4.8 was evaluated by sourcing the geometrical properties of all the 286 distinct metallic and semiconducting SWCNTs. The results for $f(\theta,d)$ are depicted in the structural parameter space of Figure 4-4.

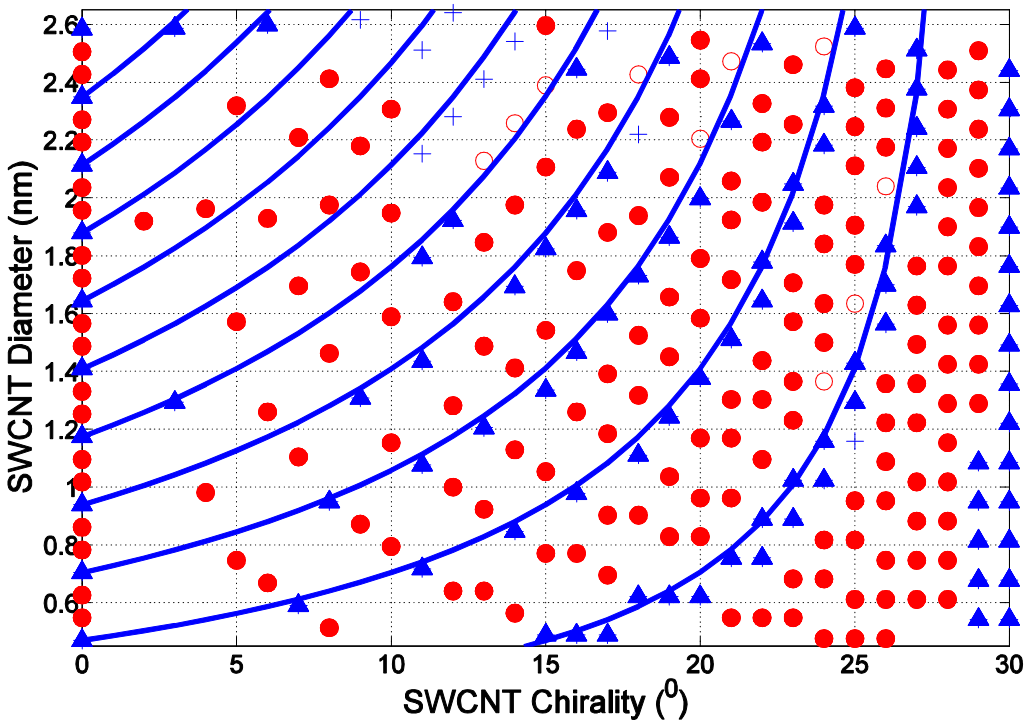

Figure 4-4: SWCNT structural parameter space indicating data points (θ,d) for metallic and semiconducting tubes. + (o) represents metallic (semiconducting) results obtained using the third-nearest-neighbour TB approach with the zone-folding technique. ▲ (●) represents metallic (semiconducting) tubes identified correctly by Eq. 4.8. ── represent Eq. 4.3 for p=1-10.

From Figure 4-4 it was found that 266 out of a total of 286 tubes are correctly assigned. That is, the formulated expression, Eq. 4.8, can correctly distinguish metallic and semiconducting tubes with 93% accuracy when compared to the third-nearest-neighbour TB approach with the ZF technique. The author believes that since the incorrectly identified tubes all lie close to the curves defined by Eq. 4.3, it is very possible that the errors arise from approximating the sine function with a first-order polynomial. Nevertheless, this still offers an 11% accuracy improvement over that obtained in [99].

To further verify Eq. 4.8, comparisons were made with respect to two references that experimentally analyzed metallic and semiconducting SWCNTs using different techniques. In [100] Scanning Tunnelling Spectroscopy (STS) was used to examine the electronic properties as a function of d and θ for a set of SWCNTs. These measurements are listed in Table 4-1 under the heading STS where the values 1 and 0 represent semiconducting and metallic tubes, respectively. In [101] Scanning Tunnelling Microscopy (STM) characterisation of the SWCNTs was undertaken and the band-gaps of 5 nanotubes were

extracted and recorded. Under the STM heading, Table 4-1 details whether these SWCNTs were found to be metallic or semiconducting.

In analysing Table 4-1 it could be initially observed that 9/12 of the SWCNTs surveyed by [100] using STS characterisation have been predicted correctly. One of the incorrectly predicted nanotubes was equally mis-represented by the third-nearest neighbour TB and ZF technique, whilst the other two could be attributed again to the approximation errors arising from Eq. 4.3. This can be confirmed by considering that those two SWCNTs (d=1.4nm, θ=5^0 and d=1.3nm, θ=24^0) are positioned very near to the curves outlined in the structural parameter space of Figure 4-3. Notably, 5/5 of the SWCNTs examined via STM measurements in [101] are correctly predicted by both the third-nearest neighbour TB + ZF technique as well as our proposed model.

***d*(nm)**	**θ(^{0})**	**STS**	**STM**	**TNN TB+ZF**	**Proposed model (Eq. 4.8)**
1.4	5	1	-	1	0
1.4	26	1	-	1	1
2.0	23	1	-	0	0
1.2	6	1	-	1	1
1.1	0	1	-	1	1
1.3	30	0	-	0	0
1.4	26	1	-	1	1
1.4	21	1	-	1	1
1.2	14	1	-	1	1
1.3	24	1	-	1	0
1.3	1	1	-	1	1
1.9	14	1	-	1	1
0.78	0	-	1	1	1
0.86	0	-	1	1	1
0.9	0	-	1	1	1
0.99	12	-	1	1	1
0.98	4	-	1	1	1

Table 4-1: Comparisons between experimentally measured SWCNTs (STS [100] and STM [101]) with various geometric structures and the Third-Nearest Neighbour (TNN) TB +ZF technique as well as the proposed model given by Eq. 4.8. 1 (0) represents a semiconducting (metallic) nanotube.

4.1.4 Calculating the band-gap of semiconducting SWCNTs

It is clear from Figure 4-1 that for all semiconducting SWCNTs, the dependence of E_g on diameter is inversely proportional. This reinforces the 1/*d* relationship derived in [14, 90, 91, 100-104]. However, all these sources differ on an additional factor that is used during the calculation of a semiconducting CNT band-gap; the overlap energy γ_0. γ_0 is a constant that has been debated to be in the range 2.45-2.90eV and no agreed value has ever emerged [103]. In [103] it was mentioned that the reason for the resulting discrepancy in γ_0 is due to the fact that chirality is neglected when interpreting the band-gap for different diameters. Thus, here, E_g has been plotted with respect to d and θ for the semiconducting nanotubes only. Subsequently, a curve-fitting technique was used to establish a relationship between E_g, d and θ. Figure 4-5 shows the resulting optimal curve (—) given by:

$$E_g = 10.2\frac{3a_{cc}}{2\pi d} = \frac{0.692}{d} \qquad 4.9$$

Eq. 4.9 confirms that E_g is proportional to *1/d* and the constant of proportionality is independent of θ. Moreover, a value of 2.44eV is calculated from Eq. 4.9 for the overlap energy constant, which is in close agreement with that derived using first-principles (γ_0 =2.5eV) in [91]. This offers a consistency check for our approach and has been highlighted in Figure 4-5 by the nearby proximity to the first-principles curve (-·-). On the other hand, the curve generated for the nearest neighbour TB and ZF method (---) with γ_0 = 2.7eV has overestimated the band-gap by as much as 0.2eV, especially, for low diameter tubes [80]. This provides further evidence to support our decision in taking account of more distant neighbours within our TB calculations.

When the semiconducting CNT band-gap values were generated using Eq. 4.9 and compared against the third-nearest-neighbour TB approach with zone folding, this yielded a NRMS error of 1.75% only.

Once more, the STS and STM measurements of [100] and [101], respectively, are used in validating Eq. 4.9. These are clearly marked in Figure 4-5. Through inspecting the experimental data points it could be verified that the measured band-gap values lie very close

to the curve proposed by Eq, 4.9. Additionally, in [101], the overlap energy was approximated as 2.45eV, which matches well with our result.

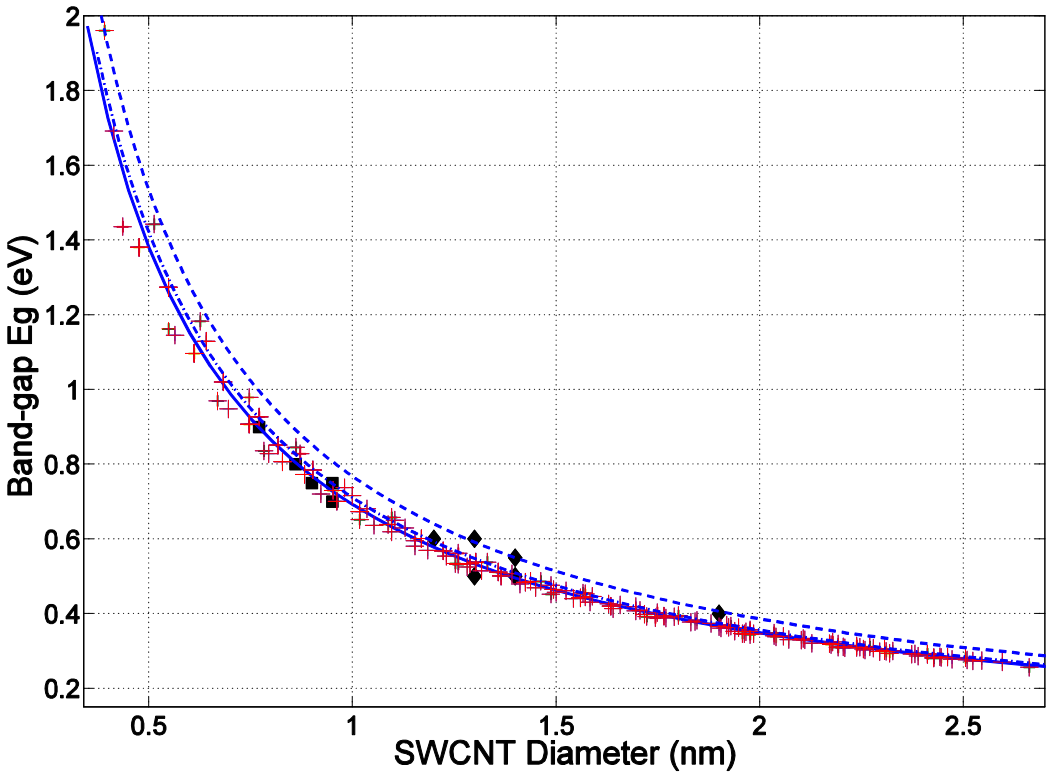

Figure 4-5: Semiconducting band-gap vs. diameter for all θ. + represents results obtained using the third-nearest-neighbour TB approach with the ZF technique. — is the fitting curve given by Eq. 4.9. -·- represents band-gap predictions made by first-principle calculations in [91]. --- corresponds to nearest-neighbour TB and ZF estimations [80]. ♦ and ■ depict experimental measurements made in [100] and [101], respectively.

Eq. 4.10 represents a simplistic model that unifies the key expressions established thus far. Given any SWCNT diameter (nm) and chirality (^{0}), Eq. 4.10 computes the SWCNT band-gap with a runtime independent of tube size and the number of subbands N. Moreover, Eq. 4.10 is more simulation efficient than the model proposed in [99], which possesses a time complexity of the order of $O(M)$.

$$Eg = \left|\Re\left(\sin\left(\pi\alpha\right)\right)\right| \frac{0.692}{d} \qquad 4.10$$

4.2 Modelling the carrier effective mass for an isolated SWCNT

The electron and hole effective masses represented by m_n and m_p, respectively, are extensively used parameters for modelling electrical transport in semiconductor devices [19, 87, 105, 106]. For example, as denoted in Chapter 2, m_n and m_p constitute one of the fundamental material-related properties that influence the saturation current of a *pn* junction diode. Generally, the effective mass dictates a crystal's carrier mobility and can therefore be utilised in characterising its electric conductivity [87].

Typically, the effective mass tensor m^* is determined by taking the reciprocal of the curvature corresponding to the band-structure of a semiconducting material along the different wave-vector (**k)** directions [87]. Formally, this is expressed as:

$$m^* = \hbar^2 \left(\frac{\partial^2 E}{\partial k^2} \right)^{-1} \qquad 4.11$$

where m^* is usually represented in terms of the electron rest mass m_0 (m_0 = 9.109 x10^{-31} kg) [87].

To-date, there has been insufficient work done on identifying the carrier effective masses for SWCNTs. Moreover, although models describing this property have been derived for achiral (zig-zag and armchair) CNTs from the nearest-neighbour TB +ZF technique, there has been no analytical model established using the third-nearest-neighbour TB +ZF approach for both achiral and chiral SWCNTs. The author believes that such a model could find widespread use in determining basic transport in CNT devices operating under equilibrium conditions without the need to perform extensive time-consuming numerical calculations [105]. Also, this may additionally enhance CNT compact models in dealing with nanotubes of various geometric structures.

In this section, our analysis is limited to semiconducting SWCNTs where only the first conduction/valence bands closest to the Fermi level are of interest since they are the dominant sub-bands participating in CNT carrier transport [106]. Furthermore, given that m^* is direction dependent, we will only evaluate the quantities associated with carriers travelling parallel to the nanotube axis (*i.e.* along the k_x axis). Again, given that some studies have

reported the deviation in carrier effective mass with high levels of doping it will be assumed that the SWCNTs under observation are un-doped [85].

4.2.1 Review of current SWCNT carrier effective mass models

One of the first studies on realising the effective mass for SWCNTs was in [107] where a selected set of 6 chiral and achiral semiconducting nanotubes were assessed. It was mentioned that the prediction of the effective mass for charge carriers required highly accurate results for the corresponding energy band dispersions, hence, *ab initio* density-functional calculations were performed [107]. Firstly, it was confirmed that the resulting SWCNT m_h and m_e identically matched due to the close symmetry between the conduction sub-band minima and valence band maxima nearest to the Fermi level [107]. Secondly, it was found that the carrier effective masses generally decreased with higher tube diameters, though, the findings seemed relatively spread and did not fall on any given trend line [107].

Following this, another research group analysed and compared the carrier effective mass of 3 zig-zag nanotubes using two different band-structure models including the EHT and the nearest neighbour TB + ZF method as well as the parabolic effective mass model (EFM) [106]. The EFM description involved using a second order polynomial fit (*e.g.* $E(k) = Ak^2+Bk+C$) to approximate the bottom of the conduction band and obtain the curvature at the minimum point. In turn, the simple relationship $m^* = 4\hbar^2/9\gamma_0 a_{cc} d$ was formulated [106]. In comparing the parabolic EFM estimation with the EHT generated first conduction band for a (13,0) nanotube it was established that very good agreement ensued up to $E \sim 200$ meV from the minimum [106]. Above this range of validity the band non-parabolicity became notably influential on the overall shape [106]. It was also noted that for SWCNT diameters lower than 1 nm the parabolic EFM approach lost its precision due to the nanotube curvature effect [87, 106].

The latest report on the development of a SWCNT carrier effective mass model considered deriving m^* from the nearest-neighbour TB energy dispersion for achiral nanotubes with diameters greater than 1 nm [105]. The outcome included a simplified expression - $m^*=4\hbar^2 E_g/3\gamma_0 a^2(2\gamma_0+E_g)$ - which was demonstrated to agree well with the aforementioned parabolic approximation [105, 106].

Here, an analytical expression shall be devised based on the parabolic EFM estimation of the third-nearest neighbour TB and ZF band dispersion that will directly ascertain the carrier effective mass of an isolated SWCNT with any chirality and diameter >1 nm. To the knowledge of the author, this has not been accomplished by any other work.

4.2.2 Simulating the SWCNT carrier effective mass using the parabolic approximation of the third-nearest neighbour TB and ZF band dispersion

Simulations are instigated by using the third-nearest-neighbour TB +ZF technique to calculate the band structure of a (13,0) nanotube. Since it is assumed that the hole effective mass is equivalent to the electron effective mass, we focus on estimating the bottom of the first conduction sub-band using the quadratic fit $E(k) = Ak^2+Bk+C$ as shown in Figure 4-6. This is automatically achieved by reducing the sum of squared residual (actual - fitted) error (commonly known as the Least Squares Estimation (LSE) technique) for the fitted curve whilst maximising the energy range (from the minimum point) within which it could be deemed valid. Subsequently, by substituting the resulting parabolic fit into Eq. 4.11 the curvature is obtained and henceforth the effective mass.

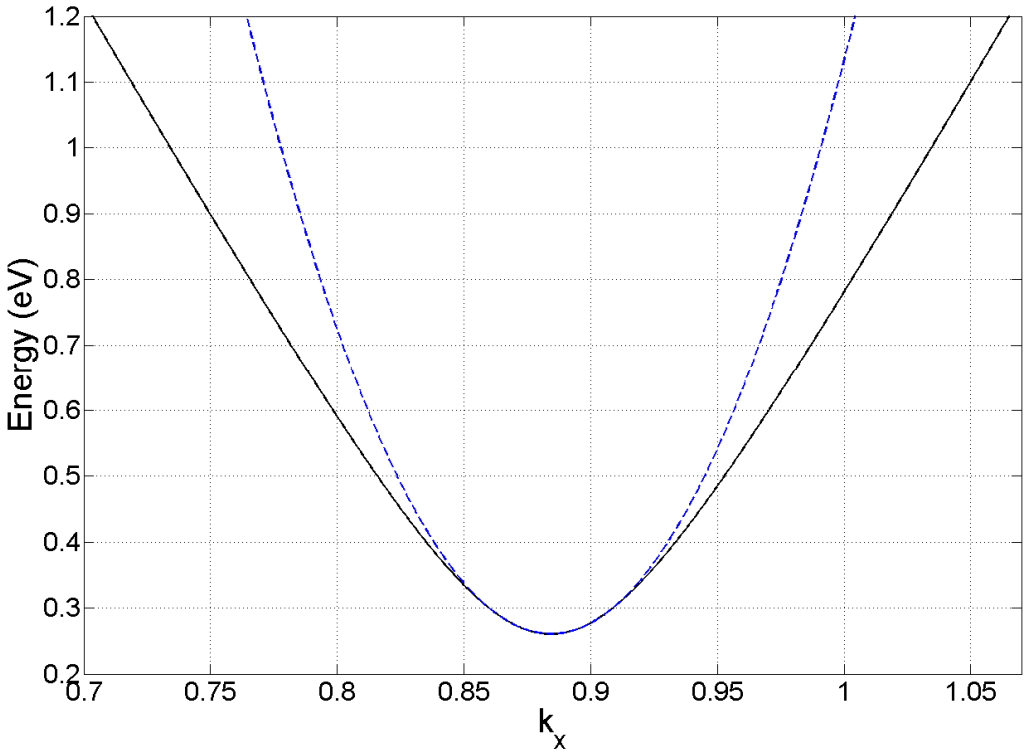

Figure 4-6: (—) *E-k* dispersion of the first conduction sub-band for a (13,0) SWCNT using the third-nearest neighbour TB +ZF technique. (---) Parabolic fit within a 52 meV validity energy range from the band minimum.

An effective mass of m^*/m_0 =0.365 was attained based on the parabolic fit of Figure 4-6. This value is moderately lower than the 0.475 and 0.542 predictions made by the models proposed in [105] and [106], respectively. This discrepancy is attributed to two factors. Firstly, because more distant neighbours are taken into account in our TB dispersion calculations, the band shape will be distinctly different from that generated by the nearest neighbour approach in [105] and [106]. Secondly, since the optimal fit of Figure 4-6 is valid over a smaller energy range compared to [106], it is expected that the curvature will be greater and therefore the effective mass to be lower.

By repeating the above computation for a group of nanotubes having diameters and chiral angles extending between 1-2.6 nm and 0^0-30^0, respectively, this offered a set of 133 dissimilar semiconducting SWCNTs. The resulting carrier effective masses have been plotted out with respect to diameter in Figure 4-7 where achiral (•) and chiral (+) tubes have been separately marked.

Figure 4-7 shows that the effective mass has a clear dependency on chiral angle and generally decreases with diameter, which is in agreement with [87, 105-107]. In comparison to *ab initio* calculations made in [107] for chiral CNTs it is also found that the data points do not fall on a simple trend line, although, this does not seem to be the case for achiral CNTs. Additionally, it is confirmed that the effective mass of chiral tubes are, in general, higher than achiral tubes with similar diameters [107].

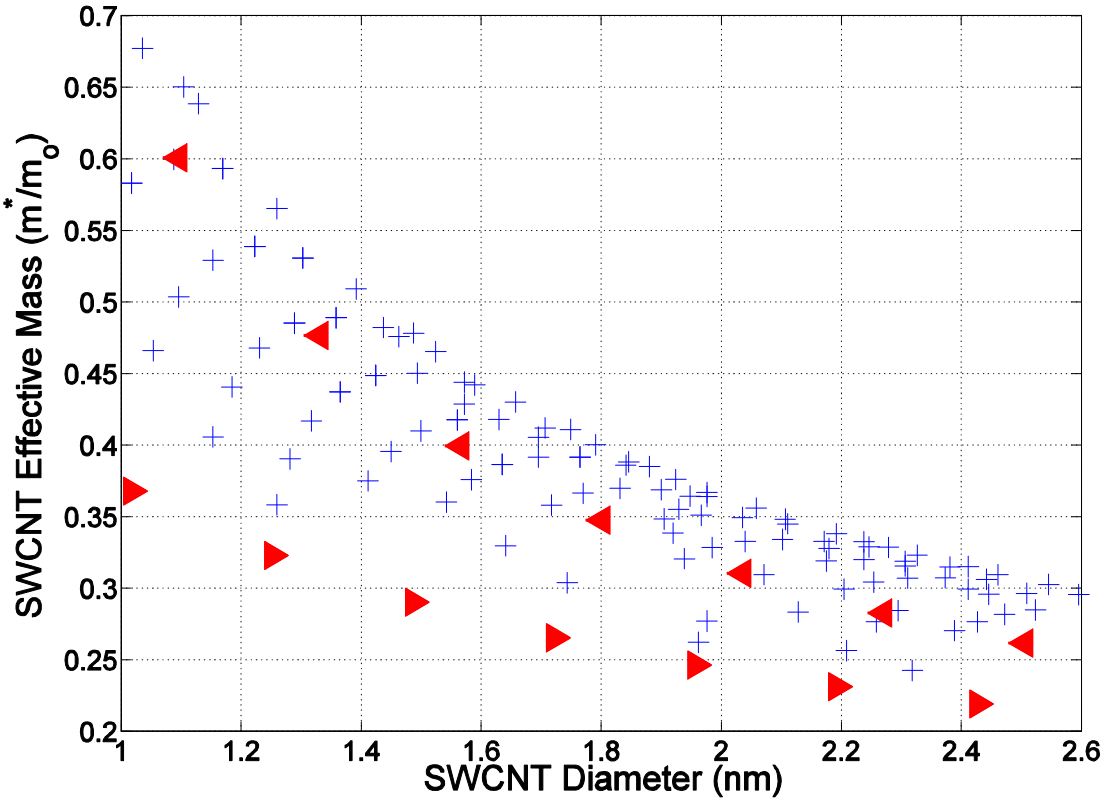

Figure 4-7: Simulated SWCNT effective mass of the lowest conduction sub-band for different geometrical properties, d and θ. + represent chiral CNTs. ▶and ◀ represent (m,0) zig-zag achiral tubes with m=3p+1 and m=3p+2, respectively.

4.2.3 Deriving an analytical model for the carrier effective mass of achiral SWCNT

It is apparent from Figure 4-7 that the carrier effective mass for achiral SWCNTs follows two trends of different slopes with respect to the diameter. This feature was similarly pointed out in [87]. The lower effective mass trend can be associated with (m,0) zig-zag tubes where m=3p+1 (p is any integer) whilst the upper effective mass trend covers zig-zag tubes with m=3p+2. These attributes could allow us to set up conditions in terms of d and θ that will enable the distinction between the observed trends.

A function such as the one derived to distinguish metallic and semiconducting tubes (Eq. 4.4) can be formulated where it assumes a value of zero if the following two conditions are satisfied:

1. It is necessary that θ is always zero.
2. The diameter of the tube must be equivalent to $d_{up} = \sqrt{3}a_{cc}(3p + 11)/\pi$ for the upper trend or $d_{low} = \sqrt{3}a_{cc}(3p + 10)/\pi$ for the lower trend.

Accordingly, two expressions can be composed as follows:

$$C_{up}(\theta,d) = \theta + \prod_{p=1}^{M}\left(d - d_{up}\right) = \theta + \prod_{p=1}^{M}\left(\pi d - \sqrt{3}a_{cc}(3p+11)\right) \qquad 4.12$$

$$C_{low}(\theta,d) = \theta + \prod_{p=1}^{M}\left(d - d_{low}\right) = \theta + \prod_{p=1}^{M}\left(\pi d - \sqrt{3}a_{cc}(3p+10)\right) \qquad 4.13$$

where M is an integer representing the number of zig-zag tubes under observation for each trend, which in our case is 7. Hence, if Eq. 4.12 or 4.13 is identically zero for a given d and θ then it can be deduced that the corresponding trend applies.

As for the slopes of the trends, one could firstly verify that the upper slope agrees well with that originated in [106] when the overlap energy constant is replaced with 2.44eV (instead of 2.7eV) to reflect the fact that more distant neighbours have been considered in our TB approach. That is:

$$m^{*} = \frac{4\hbar^{2}}{9a_{cc}\gamma_{0}d} \qquad if \quad C_{up}(\theta,d) \equiv 0 \qquad 4.14$$

Eq. 4.14 has been plotted (-·-) in Figure 4-8 where a NRMS error of 5.91% is achieved when compared to the simulated carrier effective mass of the SWCNTs belonging to the upper achiral trend.

The slope for the lower achiral trend was derived by curve-fitting the carrier effective mass data points of the SWCNTs represented by Eq. 4.13. This generated:

$$m^* = \frac{4\hbar^2}{9a_{cc}\gamma_0^2 d} + 0.12 \qquad if \quad C_{low}(\theta, d) \equiv 0 \qquad 4.15$$

where a NRMS error of 1.78% was obtained, which offers very good accuracy as depicted in Figure 4-8. Eq. 4.15 differs from Eq. 4.14 on two fronts. Firstly, the slope of the lower trend is related to the square of the overlap energy constant. Secondly, the lower trend has been translated by a factor of m^*/m_0 =0.12 that represents a horizontal asymptote for the effective mass. The implications of such a finding could possibly signify that (m,0) zig-zag tubes with m=3p+1 reach a carrier mobility limit at high diameters.

Previously proposed effective mass models such as in [106] and [105] have also been included in Figure 4-8 to validate our results. It could be seen that these models lie somewhat mid-way between the upper and lower trend lines derived in our work. This is because their methodologies fail to capture the effects of the two different zig-zag tube classes identified here. Nevertheless, good agreement can be observed for the higher diameter nanotubes.

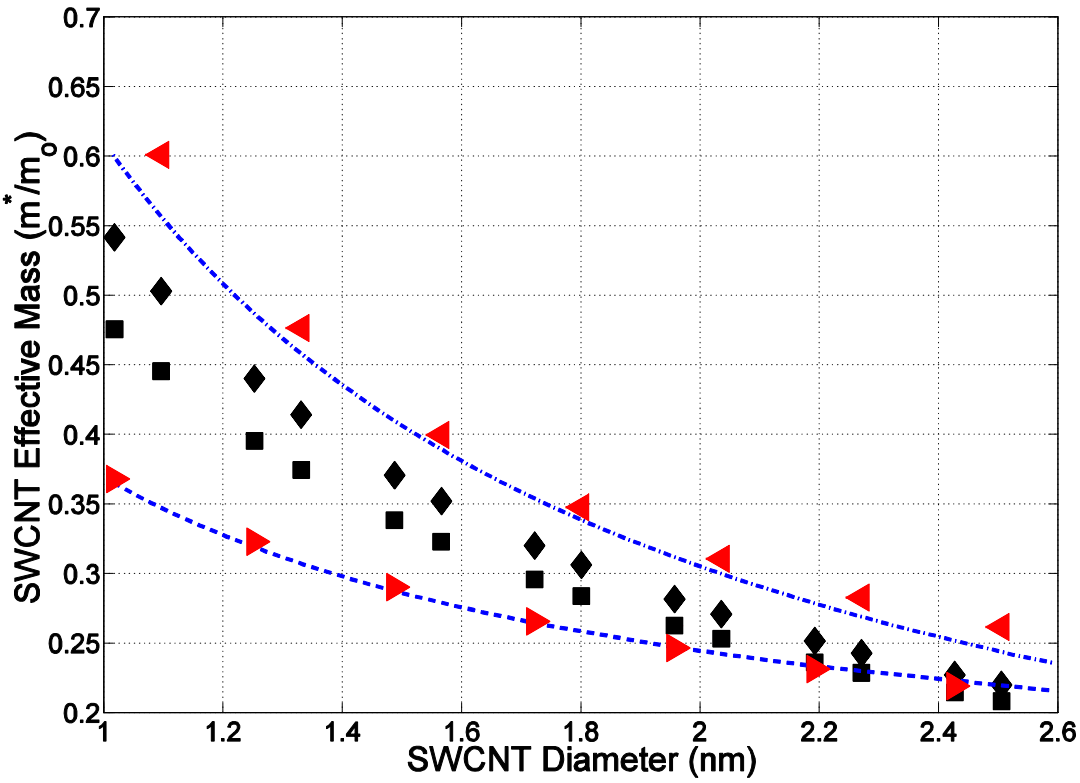

Figure 4-8: ► and ◄ represent simulated effective masses for achiral nanotubes. (-·-) is the fitted trend line given by Eq. 4.14. (---) is the fitted trend line given by Eq.4.15. ♦ and ■ depict effective mass models proposed for zig-zag tubes in [106] and [105], respectively, with γ_0= 2.7eV.

4.2.4 Deriving an analytical model for the carrier effective mass of chiral and achiral SWCNTs using a regression technique

Here, a statistical based regression technique -Response Surface Modelling (RSM) – is employed to predict the effective mass for all chiral and achiral tubes within the diameter range *d*=1-2.6 nm. The RSM method renders a first-order relationship relating the predictors *(θ,log(d))* to the response variable (log(*m**)) where:

$$\log(m^*) = \alpha\log(d) + \beta\theta + \lambda \qquad 4.16$$

Once the regression coefficients (α, β, λ) are optimised under the LSE method, an inverse-logarithmic transform is performed to yield the following model:

$$m^* = \frac{8m_0\hbar^2}{9\gamma_0^2 a_{cc}} d^{-0.7835} e^{7.4x10^{-3}\theta} \qquad 4.17$$

where γ_0 =2.44eV is the overlap energy calculated in Section 0. Eq. 4.17 (represented by ▲ in Figure 4-9) was found to predict the effective mass data points of Figure 4-9 with a NRMS error of 9.73%. This is a good approximation given that there is a nonlinear correlation between the effective mass and chiral angle.

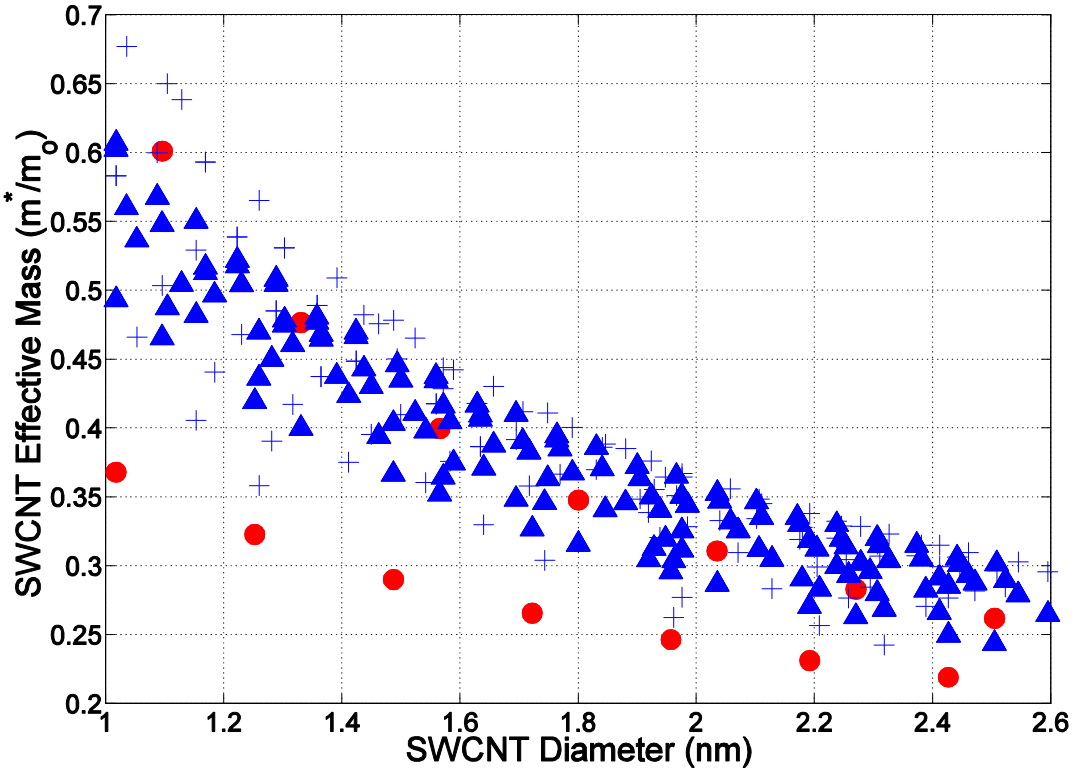

Figure 4-9: ● and + represent the simulated carrier effective mass of achiral and chiral semiconducting SWCNTs, respectively. ▲denotes the predicted effective mass by Eq. 4.17 for different SWCNT geometrical properties; *d* and *θ*.

4.3 Summary

In the first section of this chapter a novel analytical model is presented that predicts the SWCNT band-gap directly from its diameter (*d*) and chiral angle (*θ*) with a runtime independent of tube size. This model was derived from CNT band-structures created using the third-nearest-neighbour TB method in conjunction with the ZF technique. It was demonstrated that the analytical band-gap model accurately distinguishes 93% of a set of metallic and semiconducting nanotubes. Further validation was performed by comparing the

developed differentiation model against two separate sources of experimental characterisation (STS and STM) data where 14/17 tubes were correctly identified. In addition, the NRMS band-gap error recorded for semiconducting tubes was only 1.75% offering an overlap energy constant of γ_0 =2.44eV. It was further demonstrated that this value better matched first principle as well as experimental results compared to the nearest-neighbour approach, providing additional evidence to support our decision in taking account of more distant neighbours within our TB calculations.

The second section of the chapter details the derivation of novel analytical expressions based on the parabolic EFM estimation of the third-nearest neighbour TB and ZF band dispersion that directly resolve the carrier effective mass of an isolated SWCNT with any chirality and diameter >1 nm. Again, these models possess a runtime independent of the tube size. It was discovered that there exist two distinct effective mass trend lines for achiral tubes, where the corresponding slopes and geometrical structure conditions are defined. In comparison to the simulated data points, the proposed upper and lower trend models are found to predict the effective mass with an NRMS error of 5.91% and 1.78%, respectively. It was additionally shown that other previously reported effective mass models for achiral SWCNTs agree well with our expressions, especially for larger diameters. Finally, the RSM regression technique is exploited in formulating an expression for the carrier effective mass of achiral as well as chiral tubes where a low NRMS error of 9.73% is achieved. This is a good approximation given the nonlinear relation between the effective mass and chiral angle.

The subsequent chapter constitutes the second key contribution of this thesis where the novel analytical models developed in this chapter are further enhanced by adopting a statistical approach in predicting the SWCNT band-gap and carrier effective mass variation for typical uncertainties associated with the tube geometrical structure.

Chapter 5 Modelling SWCNT Band-gap and Carrier Effective Mass Variation

Synthesising SWCNTs with accurate structural control has been widely acknowledged as an exceedingly complex task culminating in the realisation of CNT devices with uncertain electronic behaviour. In this chapter, a statistical approach is applied in predicting the SWCNT band-gap and effective mass variation for typical uncertainties associated with the geometrical structure.

In the first section a brief motivation of our study is presented. Following this, a section defining realistic spreads in the geometric structure of CNTs grown using the Chemical Vapour Deposition (CVD) technique is imparted. Next, a Monte Carlo method is adopted to simulate the band-gap and carrier effective mass dispersion for a selection of structural parameter distributions. As a result, novel analytical expressions are established that separately specify the band-gap and effective mass variability (Eg_{σ}, m^*_{σ}) with respect to the CNT mean diameter (d_{μ}) and standard deviation (d_{σ}). These expressions offer insight from a theoretical perspective on the optimisation of diameter-related process parameters with the aim of suppressing band-gap and effective mass variation.

5.1 Motivation for modelling SWCNT band-gap and carrier effective mass variability

At present, the fabrication of carbon nanotubes with accurate diameter and chirality control is a serious challenge and as a result a large band-gap (*Eg*) variability is typically observed for a set of CNTs grown under identical process conditions [16, 95, 108]. Equally susceptible to structural variation is the carrier effective mass (m^*), which has a crucial influence upon the SWCNT carrier transport properties [87, 107]. Consequently, due to the unpredictability associated with these parameters, the implementation of nanotube based devices with desired performance characteristics has been problematic [16].

In an attempt to tackle this issue, researchers have proposed the adoption of statistical process optimisation techniques to optimise the CNT growth process and generate narrowly distributed geometrical characteristics around a desired mean value [54, 95, 108-113]. Progress, however, has been limited due to the incomplete understanding associated with the CNT growth mechanism [110, 114]. Further, the impact of CNT geometrical structure on the performance characteristics of various CNT Field-Effect-Transistors (FETs) has been experimentally [16, 23, 109] and theoretically [57, 106, 115-117] examined. Yet, no statistical model defining the CNT band-gap and effective mass distributions has evolved from these studies, especially with respect to semiconducting SWCNTs.

Here, a statistically supported model that predicts the CNT band-gap and effective mass distribution properties for a given structural variation is presented. The structural dispersions considered reflect typical spreads identified in CNT geometry after CVD synthesis. As an outcome of the models produced, better insight is offered on ways in which CVD process parameters such as the mean CNT diameter d_μ and standard deviation d_σ could be optimised to achieve a required band-gap or effective mass variation. Moreover, the proposed analytical methodologies could be incorporated into compact device models to accurately simulate a substantial number of dissimilar CNT-devices over a judicious time period. To the knowledge of the author this work has not been previously reported in literature.

5.2 SWCNT diameter and chiral angle distribution

The following section discusses the various SWCNT diameter and chiral angle distributions evaluated by sources employing the CVD synthesis technique. A set of probability functions that realistically replicate these spreads are subsequently defined.

5.2.1 SWCNT diameter distribution

The SWCNT structural distribution properties reported to-date differ considerably due to the utilisation of alternative synthesis techniques, growth conditions and characterisation methods [54, 95, 108, 110-113, 118-121]. Hence, since the CVD synthesis process appears to be most promising for bulk CNT production [108, 111, 112, 119], we have deliberately restricted our survey of CNT structural data to references employing the CVD technique.

The SWCNT diameter is strongly influenced by the reaction conditions set by the CVD process parameters [122]. Recently, there have been several research groups working on identifying the relationship and sensitivity between different CVD synthesis variables such as catalyst particle size [54, 110, 121], reaction temperature [113, 120], reaction pressure [108, 111, 113], hydrocarbon feeding rate [112] and the ensuing SWCNT mean diameter (d_μ) and diameter distribution (d_σ). Due to the imprecision and instability in controlling the growth conditions most of the early observations showed that the SWCNT diameter randomly spread over a wide range following no regular pattern [95]. However, recently, in [112] it was proposed that at any given CVD process condition, so long as the carbon feeding rate is fixed, there is an optimal diameter of nanoparticles that nucleate nanotubes. Any nanoparticle with too small a diameter cannot nucleate as it is ‘overfed’ with carbon feedstock and any nanocatalyst with too large a diameter is deemed to be inactive since it is ‘underfed’[112].

Thus, assuming that the process of defining the catalyst particle size can be optimised to give a narrow distribution around a specified d_μ, one could expect that as the yield of SWCNTs increases for a given batch, the spread in diameter will converge towards a Gaussian distribution. This claim can be further supported by the following experimental evidence.

In [119], High Resolution Transmission Electron Microscopy (HRTEM) images were taken of 74 randomly isolated nanotube structures grown using a CVD method. This allowed direct observation and quantitative characterisation of the SWCNT diameters with an accuracy of ±0.1 nm [119]. Figure 5-1 illustrates measurements of the SWCNT diameter distribution. As shown, more than 75% of the SWCNTs have diameters ranging between 1.2-2 nm where the best fit distribution function generated a Gaussian mean diameter d_{μ}=1.69 nm and a standard deviation d_{σ}=0.34 nm [119]. Raman scattering measurements of the same SWCNT sample set offered an average diameter of d_{μ}=1.61 nm which is in close agreement with the HRTEM fitted result, although slightly lower due to the interaction effects between different nanotubes [119].

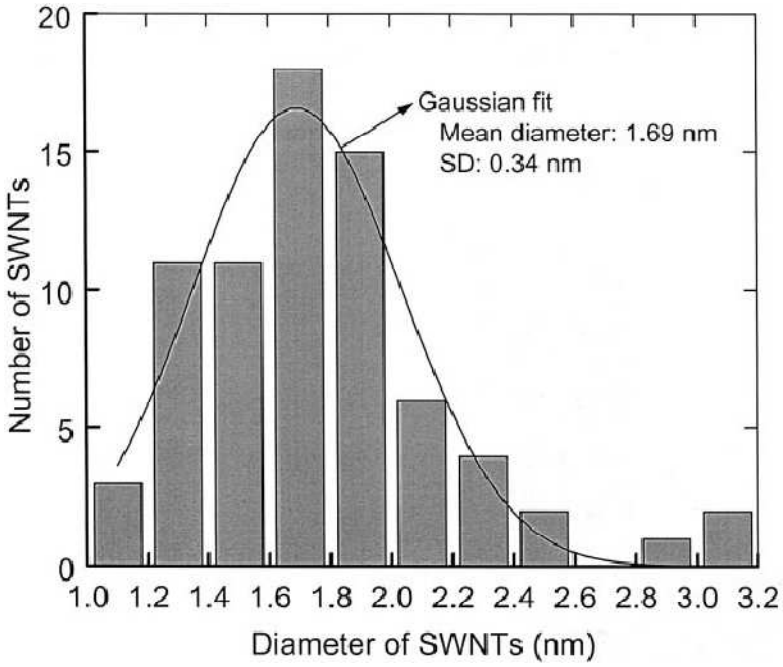

Figure 5-1: Diameter distribution of the 74 isolated SWCNTs grown using a CVD technique where the data was obtained from HRTEM images. The Gaussian fit shown offers d_{μ}=1.69 nm and d_{σ}=0.34nm [119].

Another later experiment used Atomic Force Microscopy (AFM) in combination with Scanning Electron Microscopy (SEM) imaging to characterise the diameter distribution of SWCNTs produced via the CVD approach at different growth conditions [112]. The corresponding diameter histograms are presented in Figure 5-2 where the best fit functions for the distributions are depicted by the overlapping Gaussian curves [112]. As shown in Figure 5-2 the mean of the diameter distributions were recorded as 0.93, 1.07 and 1.78 nm

with standard deviations of 0.18, 1.12 and 1.02 nm, respectively [112]. Raman spectroscopy was also used to confirm these results [112].

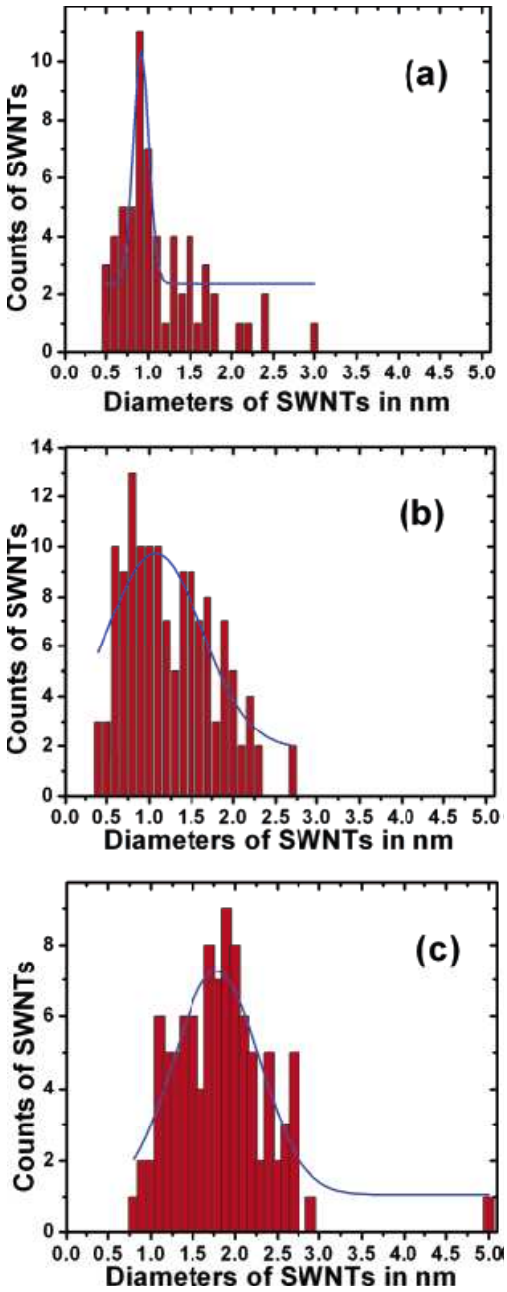

Figure 5-2: Diameter distributions of SWCNTs grown at different carbon feeding rate concentrations (a) 140 ppm; (b) 1600 ppm; (c) 14400 ppm. (—) represent Gaussian curve fits [112].

Other experimental observations that reported a Gaussian profile for their CVD grown SWCNT diameter distributions included [54, 108, 110, 111, 121]. From these results it can be assumed that mean diameters between 1.0-1.7 nm would be a suitable range to model the corresponding SWCNT electronic properties for our study.

It could be argued, however, that the diameter distributions of Figure 5-2 are not fully Gaussian, and in fact, may be truncated Gaussians. This explains the minimum and maximum cut-off observed at 0.5 and 3 nm, respectively. Also, given that in theory, catalysts with too small or too large a diameter cannot nucleate as they are overfed and underfed, respectively, this can further support the argument of having a truncated Gaussian at both ends.

One could additionally argue that a gamma distribution may provide an improved estimation of the diameter variation because it is always positive and has a wider asymmetry compared to a Normal dispersion. Nevertheless, given the small range of mean diameters considered in our study it is acknowledged that little difference will be observed compared to a Gaussian diameter distribution as has been revealed in [123].

In all the surveyed experimental reports there has been no recognised relationship between the SWCNT mean diameter and standard deviation. For instance, no correlation can be drawn from Figure 5-2 involving d_μ and d_σ as established by [112]. Whilst in [54] it was revealed that the SWCNT standard deviations broadened with higher mean diameters by roughly the same scale. Therefore, it has been decided to introduce 3 case scenarios for our simulations that appropriately scale the diameter variation with different mean values. These can be described as follows:

1. The first scenario will assume that the diameter standard deviation is *independent* of the mean diameter.
2. The second case scenario will presume that the diameter variation *scales-up* by an equivalent proportion to the percentage increase of the mean diameter.
3. The third case scenario will suppose that the diameter variation *scales-down* by a value corresponding to the percentage increase of the mean diameter.

5.2.2 SWCNT chiral angle distribution

Unlike the CNT diameter, controlling the chiral angle can be more intricate [57]. Regulating the CNT chiral angle entails the manipulation of the molecular assembly of the SWCNT [114]. This level of manipulation is unattainable using conventional CVD processes and consequently a homogeneous spread in chirality is commonly observed within a

collection of synthesised nanotubes [73, 124]. Hence, for our purposes it is reasonable to assume a uniform random distribution in the SWCNT chiral angle.

5.3 Modelling SWCNT band-gap variation

In this section the above mentioned structural distribution properties are varied and a set of Monte Carlo simulations are run to generate the corresponding band-gap dispersions, which are subsequently compared and statistically analysed. As an outcome, simplistic yet accurate models are proposed providing a relationship between the semiconducting SWCNT diameter distribution properties and the resulting band-gap variation characteristics; Eg_{μ} and Eg_{σ}.

5.3.1 Simulating and modelling the SWCNT band-gap distribution for the first case scenario

Here, the variation in CNT band-gap is determined by executing Eq. 4.10 derived in the previous chapter over a large number of samples that are randomly generated from the selected structural distributions outlined above. In order to identify an appropriate nanotube sample size for the chosen distributions the Gaussian dispersed diameter parameters are affixed to d_{μ}=1.01 nm and d_{σ}=0.2 nm and different sized nanotube sample sets are simulated within the range: 10^2-2x10^5. The mean and variability of the corresponding band-gap dispersions (Eg_{μ} and Eg_{σ}) were calculated from the sample mean and standard deviation of Eq. 5.1 and 5.2, respectively. This is because it was considered that they represent unbiased estimators of the distribution properties.

$$Eg_{\mu} = \frac{1}{N}\sum_{i=1}^{N} Eg_i \qquad 5.1$$

$$Eg_{\sigma} = \sqrt{\frac{1}{N-1}\sum_{i=1}^{N}\left(Eg_i - Eg_{\mu}\right)^2} \qquad 5.2$$

Eg_{μ} and Eg_{σ} are plotted in Figure 5-3(a) and (b), respectively, for each nanotube sample size N.

From Figure 5-3 it can be observed that the dispersion variables Eg_μ and Eg_σ converge within 0.1% and 0.3% of their ultimate true values, respectively, over the sample range 1-2x10^5 nanotubes. Hence, to gain sufficient accuracy we have chosen N=1.5x10^5 for all our simulated measurements.

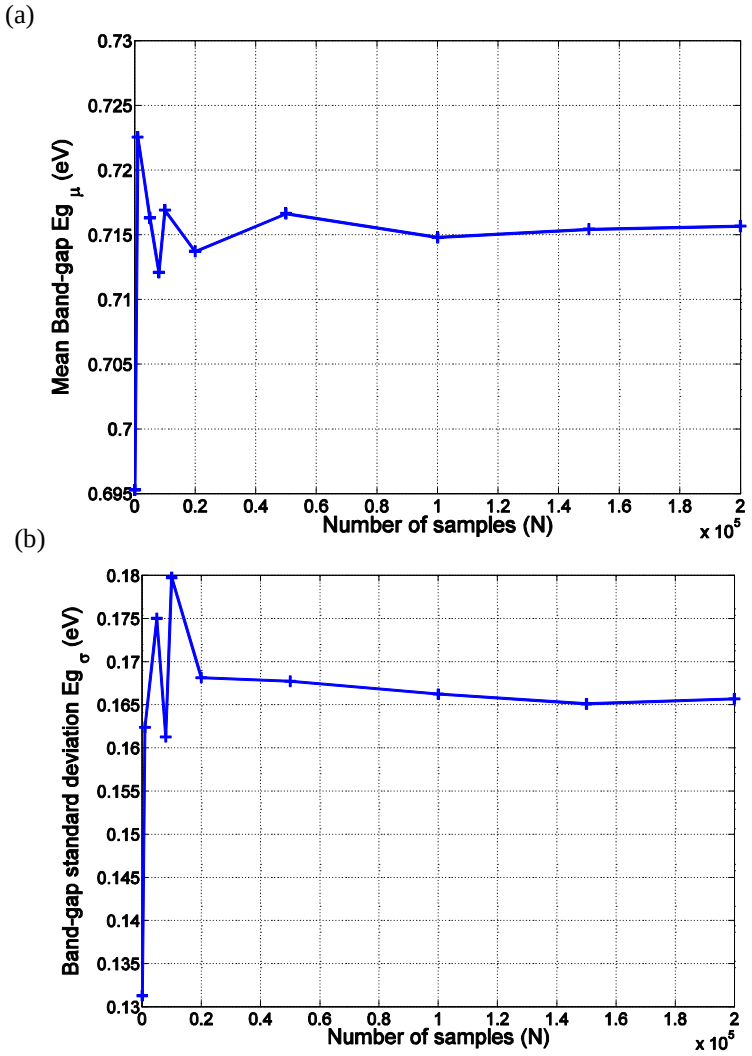

Figure 5-3: Simulated band-gap mean (a) and variability (b) as a function of distribution sample size (N) for d_μ=1.01nm and d_σ=0.2nm.

For each run of our Monte Carlo simulation the diameter distribution properties d_μ and d_σ were varied between the ranges 1.01-1.71 nm and 0.04-0.2 nm, respectively. Figure 5-4 shows a density estimation of a subset (d_μ=1.01 nm and d_σ=0.04-0.2 nm) of semiconducting SWCNT band-gap results.

It is found that the highest and lowest diameters recorded in our Monte Carlo simulations are 3.14 nm and 0.12 nm, respectively. The maximum diameter obtained was

from a diameter distribution with d_μ=1.71 nm and d_σ=0.2 nm, which is almost equivalent to the highest diameter measured in [119] (~3.0-3.2 nm, see Figure 5-1). On the other hand, the minimum diameter is too low, which was obtained from a diameter distribution with d_μ=1.01 nm and d_σ=0.2 nm. This reinforces the need to consider a truncated Gaussian or a more positively skewed function for the nanotube diameter distribution. Nevertheless, given that the lowest possible SWCNT diameter is about 0.6 nm (diameter of C_{60}) then it could be assumed that a non-truncated Gaussian would be accurate within a 2σ variation, in the worse-case, for the smallest d_μ (1.01 nm) and largest d_σ (0.2 nm) considered in our study.

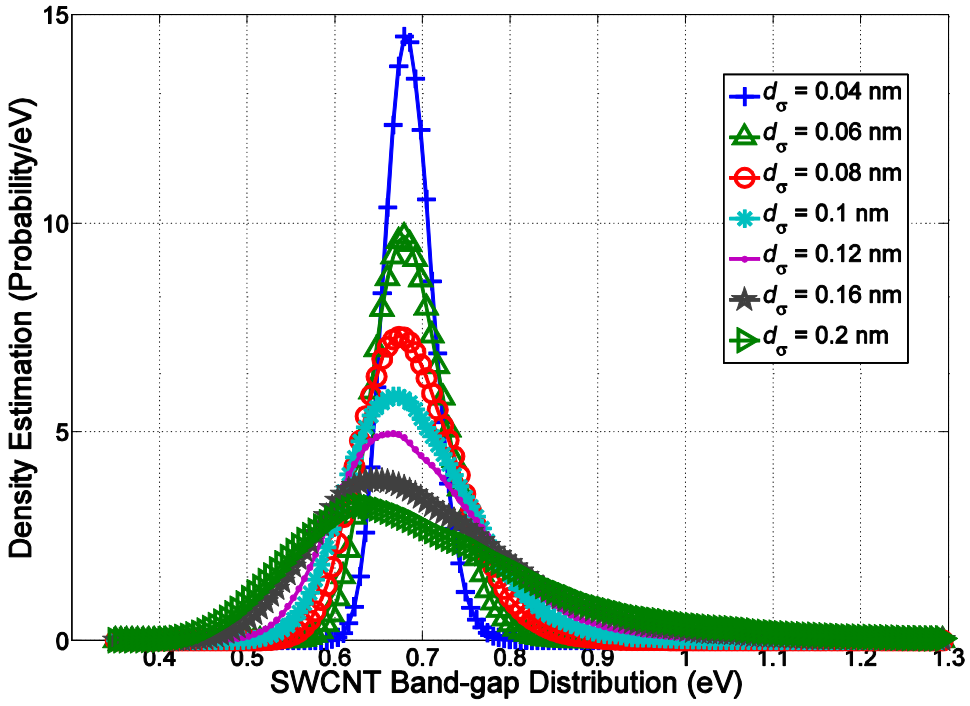

Figure 5-4: Density estimation of semiconducting nanotube band-gap values obtained from Monte Carlo simulations for a Gaussian distributed diameter with d_μ=1.01nm and d_σ=0.04-0.2nm and a randomly uniform spread in chiral angle.

When Eg_μ was plotted against d_μ for different diameter variations d_σ, as depicted by Figure 5-5, it was found that the mean band-gap shifted upwards with higher d_σ and even more so for smaller d_μ.

The Response Surface Methodology (RSM) is used here to gain a quantitative relationship between the predictor variables (d_μ, d_σ) and the response variable (Eg_μ). Given that the predictors are known, this relationship can be used to predict future values of the response. Moreover, a better understanding can be acquired on which predictors have the

greatest effect upon the response variable. Here, two relationships will be provided for each response variable; a second-order model that includes squared terms, interaction terms linear terms and constants and the second relationship will be a first-order model that only includes linear terms and constants.

The optimal curves illustrated in Figure 5-5 were created using the second-order model of the RSM regression technique that is given by Eq. 5.3.

$$\begin{aligned} Log(Eg_\mu) = \beta_0 + \beta_1 Log(d_\mu) + \beta_2 d_\sigma + ... \\ \beta_{12} d_\sigma Log(d_\mu) + ... \\ \beta_{11} \left(Log(d_\mu)\right)^2 + \beta_{22} d_\sigma^2 \end{aligned} \qquad 5.3$$

The regression coefficients of Eq. 5.3 are β_0= -0.3727, β_1= -0.9939, β_2= 0.0852, β_{12}= -0.3456, β_{11}= 0.0229 and β_{22}= 0.7070. Although Eq. 5.3 is highly accurate (NRMS error of 0.19% and a coefficient of determination R^2=1) within the mean diameter range specified in our simulation, Eq. 5.4, which represents a first-order model, can also provide a reasonable approximation of the response especially for large mean diameters.

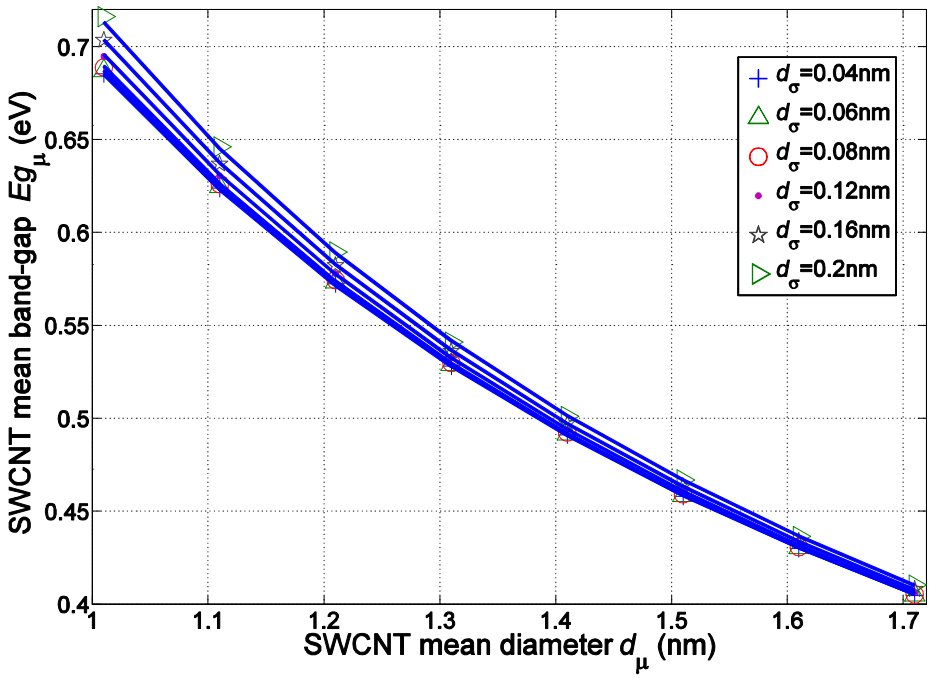

Figure 5-5: SWCNT band-gap distribution mean (Eg_μ) vs. mean diameter (d_μ). Data sets with different diameter standard-deviations (d_σ) have been marked by a distinct symbol. — represents the fitted curve given by Eq. 5.3.

$$Eg_{\mu} = \frac{0.692}{d_{\mu}} \qquad 5.4$$

For 1.01 nm $\leq d_{\mu} \leq$ 1.71 nm the NRMS error of Eq. 5.4 in predicting the actual mean band-gap is 2.7% and has an R^2 value of 0.992.

Next, the data points of the band-gap standard-deviation (Eg_{σ}) were plotted against the diameter standard-deviation (d_{σ}) for different sets of d_{μ} as shown in Figure 5-6. Again, the curves of best fit were generated by employing the second-order RSM model giving the following expression:

$$\begin{aligned} Log(Eg_{\sigma}) = \gamma_0 + \gamma_1 Log(d_{\sigma}) + \gamma_2 Log(d_{\mu}) + ... \\ \gamma_{12} Log(d_{\sigma}) Log(d_{\mu}) + ... \\ \gamma_{11} \left(Log(d_{\sigma})\right)^2 + \gamma_{22} \left(Log(d_{\mu})\right)^2 \end{aligned} \qquad 5.5$$

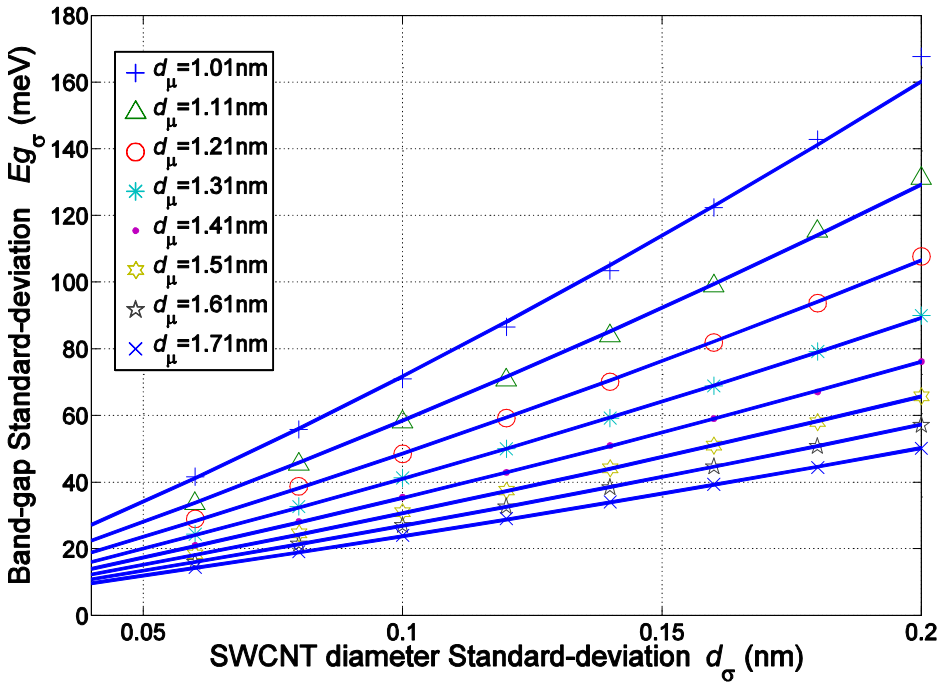

Figure 5-6: Band-gap standard-deviation (Eg_{σ}) vs. diameter standard deviation (d_{σ}). Data sets with different mean diameters (d_{μ}) have been marked by a distinct symbol. — represents the fitted curve given by Eq. 5.5 for each d_{μ}.

where the regression coefficients are γ_0= 0.2883, γ_1= 1.4036,γ_2= -2.5146, γ_{12}= -0.1460, γ_{11}= 0.0624 and γ_{22}= 0.1515. The NRMS error of Eq. 5.5 in predicting the data points was evaluated as 0.66% (R^2 value of 0.999). Additionally, the first-order approximation was

generated, given by Eq. 5.6, which possesses a NRMS error of 4% and an R^2 value of 0.981 within the ranges specified for d_μ and d_σ.

$$Eg_\sigma = \frac{0.8}{d_\mu^{2.2}} d_\sigma \qquad 5.6$$

Equation 5.6 acknowledges a linear relationship between Eg_σ and d_σ. More interestingly, it indicates that the band-gap variation can be significantly reduced by defining catalyst particle sizes with a higher mean diameter. Notably, it seems apparent that Eq. 5.6 is almost identical to the derivative of Eq. 5.4. This hypothesis is tested by an illustrative plot (see Figure 5-7) comparing the actual simulated results of Eg_σ with the predicted values generated by the absolute of the derivative of Eq. 5.4. Data points calculated using Eq. 5.6 are also included for comparison.

Figure 5-7 portrays the derivative of Eq. 5.4 diverging away from the simulated results with higher band-gap variations (*i.e.* low mean diameters and high diameter variability) rendering a NRMS error of 7.1% and an R^2 value of 0.961 over the considered diameter range. On the other hand, it can be seen that Eq. 5.6 better predicts the band-gap standard deviation for larger variations given its nearby proximity to the simulated data, which is represented here by the one-to-one correspondence linear line (---).

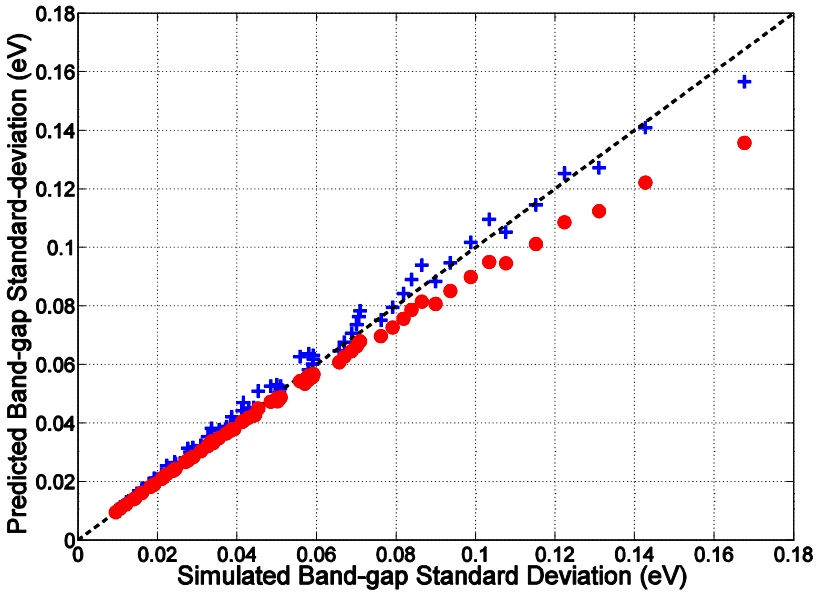

Figure 5-7: Comparison plot between the simulated band-gap standard-deviation and the corresponding predictions calculated from Eq. 5.6 (+) and the derivative of Eq. 5.4 (●).

5.3.2 *Simulating and modelling the SWCNT band-gap distribution for the second case scenario*

The band-gap distribution properties (Eg_{μ}, Eg_{σ}.) were again computed in a similar manner to that outlined above but with the diameter variation scaled-up with an increase in mean diameter as denoted by Eq. 5.7:

$$d_{\sigma\_up} = \frac{d_{\mu}}{1.01} d_{\sigma} \qquad 5.7$$

where d_{μ} =1.01 nm is the lowest mean diameter considered in our analysis. It is firstly confirmed that Eg_{μ} may still be accurately described by Eq. 5.4, which was indeed the case. Subsequently, the band-gap standard-deviation (Eg_{σ}) was plotted against the scaled-up diameter standard-deviation (d_{σ_up}) for different sets of d_{μ} as shown in Figure 5-8.

It was found that the band-gap variation could also be expressed by Eq. 5.5 with regression coefficients γ_0= 0.6238, γ_1= 1.69, γ_2= -2.693, γ_{12}= -0.23286, γ_{11}= 0.12057 and γ_{22}= 0.14838. This model has a small NRMS error of 0.39% (R^2 =0.999). A first-order approximation of the variability is given by Eq. 5.8 where the NRMS error is 4.1% (R^2 = 0.972).

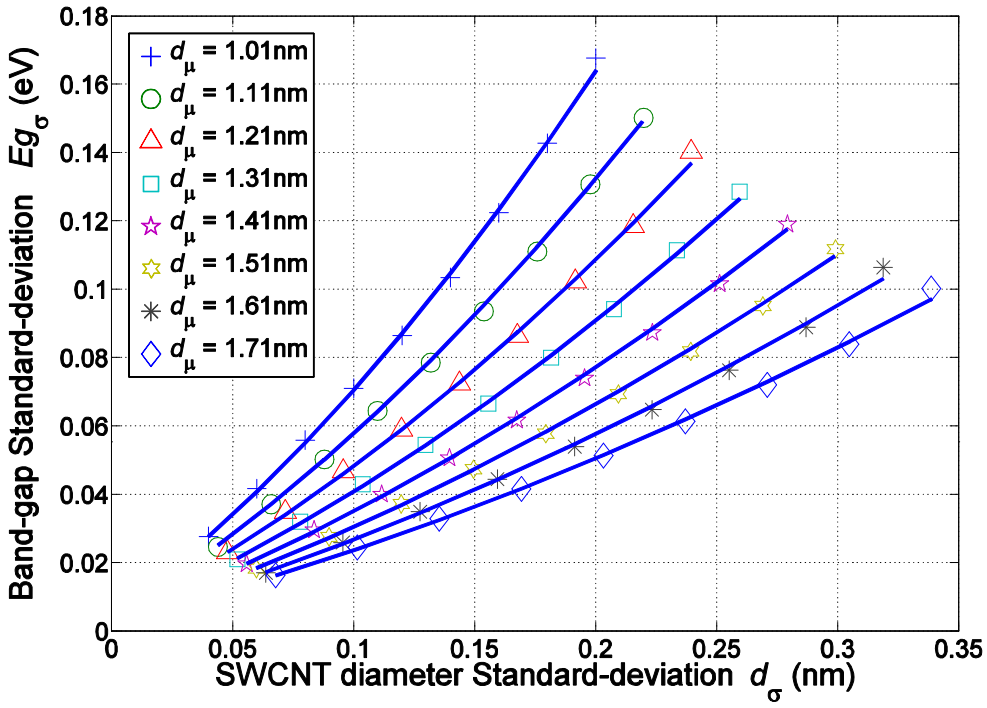

Figure 5-8: Band-gap standard-deviation (Eg_{σ}) vs. scaled-up diameter standard deviation (d_{σ_up}). — represents the fitted curve given by Eq. 5.5 for each d_{μ} with new regression coefficients.

$$Eg_{\sigma\_up} = \frac{0.75}{d_{\mu}^{2}} d_{\sigma\_up} \qquad 5.8$$

The close resemblance between Eq. 5.8 and Eq. 5.6 suggests that variation in CNT band-gap may not significantly depend on the scaling of the underlying diameter distribution with the mean diameter over the ranges considered in our simulation. Eq. 5.8 also reinforces the inverse-square relationship between the mean diameter and band-gap variability that was hypothesised in the pervious sub-section to originate from the derivative of Eq. 5.4.

5.3.3 Simulating and modelling the SWCNT band-gap distribution for the third case scenario

Again, here, the band-gap distributions are re-simulated with the diameter variation scaled-down with increases in mean diameter as denoted by:

$$d_{\sigma\_down} = \left(1 - \frac{d_{\mu} - 1.01}{1.01}\right) d_{\sigma} \qquad 5.9$$

After once more confirming that Eg_{μ} can be accurately described by Eq. 5.4, the band-gap standard-deviation (Eg_{σ}) is plotted against the scaled-down diameter standard-deviation (d_{σ_down}) for different sets of d_{μ} as depicted in Figure 5-9. An important point to note here is that from Figure 5-9 it can be clearly observed that the band-gap variability is intensely inhibited for high mean diameters.

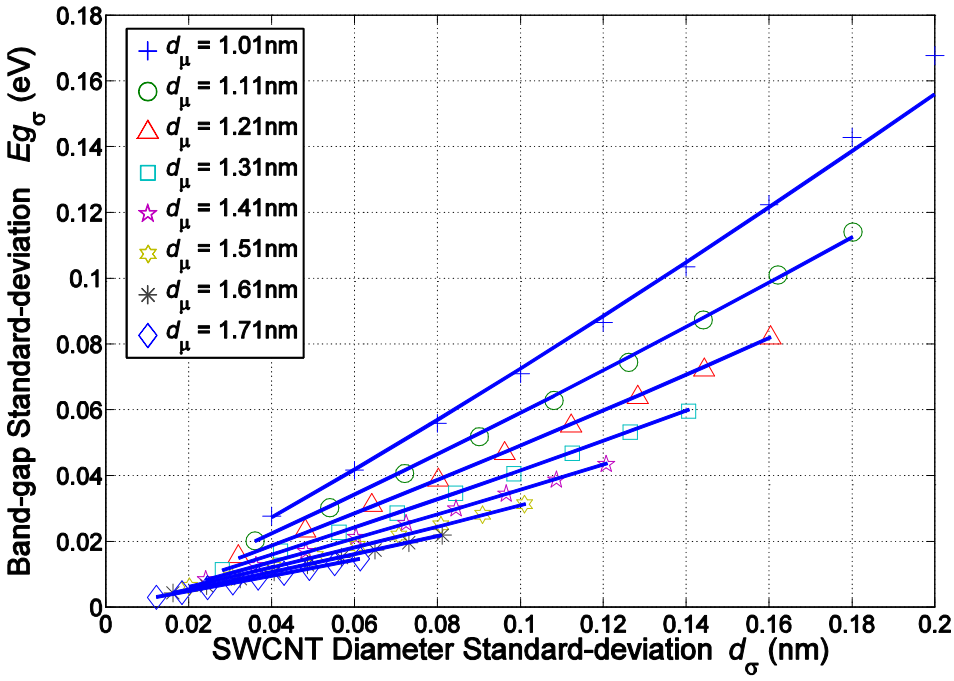

Figure 5-9: Band-gap standard-deviation (Eg_σ) vs. scaled down diameter standard deviation (d_{σ_down}). — represents the fitted curve given by Eq. 5.5 for each d_μ with new regression coefficients.

It was discovered that the band-gap variation could, as well, be articulated by Eq. 5.5 with regression coefficients γ_0= 0.034, γ_1= 1.2027, γ_2= -2.3641, γ_{12}= -0.0764, γ_{11}= 0.0249 and γ_{22}= 0.1931. This model offered an NRMS error of 0.57% and an R^2 value of 0.998. A first-order approximation was defined for the variability given by the RSM method, which generates the following:

$$Eg_{\sigma\_down} = \frac{0.74}{d_\mu^{2.1}} d_{\sigma\_down} \qquad 5.10$$

where the NRMS error is only 2.76% and R^2 = 0.990. The close similarity between Eq. 5.10, 5.8 and 5.6 further strengthens the argument that the band-gap variability is not significantly reliant on the scaling of the underlying diameter distribution with mean diameter. Hence, according to our results, CNT synthesis processes have to be optimised in minimising d_σ as well as increasing d_μ in order to suppress band-gap variation. This is independent of how the diameter dispersion scales with the mean diameter.

Coincidently, the proposition of increasing d_μ in order to reduce band-gap variation leads to the reduction of Eg_μ, which in turn yields CNT devices with improved performance characteristics such as lower contact resistances [109, 125, 126].

5.4 Modelling SWCNT carrier effective mass variation

In this section the formerly defined structural distributions are employed in determining the SWCNT carrier effective mass dispersions by running another Monte Carlo simulation. As in the previous section, the same ranges for d_μ and d_σ are adopted as well as the different scaling scenarios for the diameter variation. The final outcome consists of a set of proposed models that attempt to relate the semiconducting SWCNT diameter distribution properties with the resulting effective mass variation characteristics; m^*_μ and m^*_σ.

5.4.1 Simulating and modelling the SWCNT carrier effective mass distribution for the first case scenario

The variation in CNT carrier effective mass was determined by executing Eq. 4.17 over a sample size of N=1.5x10^5 nanotubes. This is because it was found that the dispersion variables, m^*_μ and m^*_σ, converge again within the sample range 1-2x10^5 nanotubes when setting the Gaussian dispersed diameter parameters to d_μ=1.01nm and d_σ=0.2nm and simulating sample sets of progressively larger sizes.

For each run of our Monte Carlo simulation the diameter distribution properties d_μ and d_σ were varied between the ranges 1.01-1.71nm and 0.04-0.2nm, respectively. Figure 5-10(a) represents a subset of the CNT effective mass results showing a more positively skewed distribution with higher diameter variations. The effective mass sample mean (m^*_μ) was evaluated for each d_μ and d_σ as depicted in Figure 5-10 (b). Akin to the mean band-gap results, it is observed that m^*_μ is somewhat shifted upwards with respect to the diameter variation, especially at lower mean diameters. The curves shown are given by:

$$\begin{aligned} Log(m^*_\mu / m_0) = \beta_0 + \beta_1 Log(d_\mu) + \beta_2 d_\sigma + ... \\ \beta_{12} d_\sigma Log(d_\mu) + ... \\ \beta_{11}\left(Log(d_\mu)\right)^2 + \beta_{22} d_\sigma^2 \end{aligned} \qquad 5.11$$

where the regression coefficients are β_0= -0.5823, β_1= -0.7804, β_2= 0.0538, β_{12}= -0.2359, β_{11}= 0.0176 and β_{22}= 0.5039. This model offers an NRMS error of 0.2% and an R^2 value of 1. A first-order expression is also proposed for the mean carrier effective mass, given by the RSM generated Eq. 5.12, which provides a slightly higher NRMS error of 3.0% and an R^2 value of 0.979. Eq. 5.12 indicates that the mean carrier effective mass is approximately inversely

proportional to the mean diameter, which closely agrees with the underlying expression (Eq. 4.17) formulated in the prior chapter.

$$m_{\mu}^{*} = \frac{0.56 m_0}{d_{\mu}^{0.8}} \qquad 5.12$$

(a)

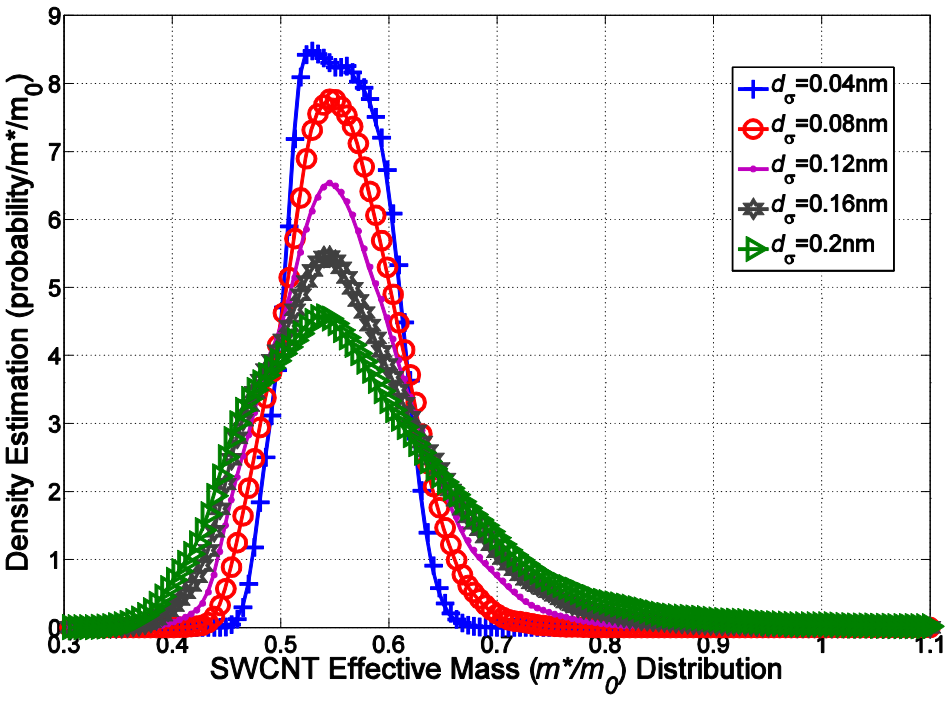

(b)

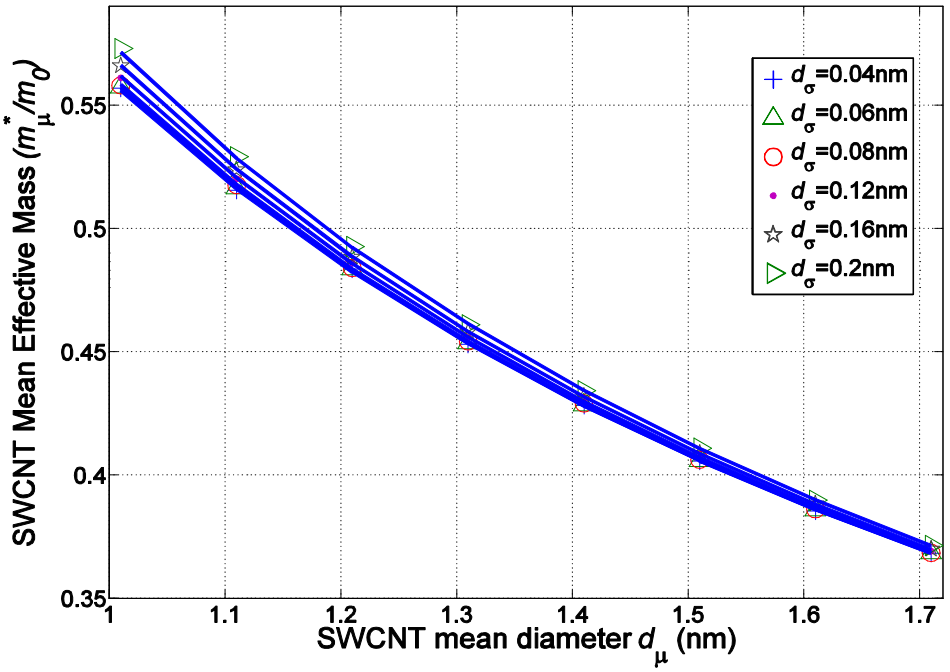

Figure 5-10: (a) Density estimation of effective mass obtained from Monte Carlo simulations for a Normally dispersed diameter with d_{μ}=1.01 nm and d_{σ}=0.04-0.2 nm. (b) SWCNT effective mass distribution mean (m^*_{μ}/m_0) vs. mean diameter (d_{μ}). Data sets with different d_{σ} have been marked by a distinct symbol. — represents the fitted curve given by Eq. 5.11.

Next, a plot was created as shown in Figure 5-11 to ascertain the variation in effective mass (m^*_σ) with respect to the diameter standard-deviation for each d_μ. The fitted curves illustrated are expressed by the second-order Eq. 5.13 with regression coefficients γ_0= -3.4453, γ_1= 5.6367, γ_2= -0.8807, γ_{12}= -5.276, γ_{11}= 2.8868 and γ_{22}= 0.2781. The first-order Eq. 5.13 was estimated to predict the effective mass variation data points with an NRMS error of 0.48% only and an R^2 value of 0.999.

$$Log(m^*_\sigma / m_0) = \gamma_0 + \gamma_1 d_\sigma + \gamma_2 Log(d_\mu) + \ldots \\ \gamma_{12} d_\sigma Log(d_\mu) + \ldots \\ \gamma_{11} d_\sigma^2 + \gamma_{22} \left(Log(d_\mu)\right)^2 \qquad 5.13$$

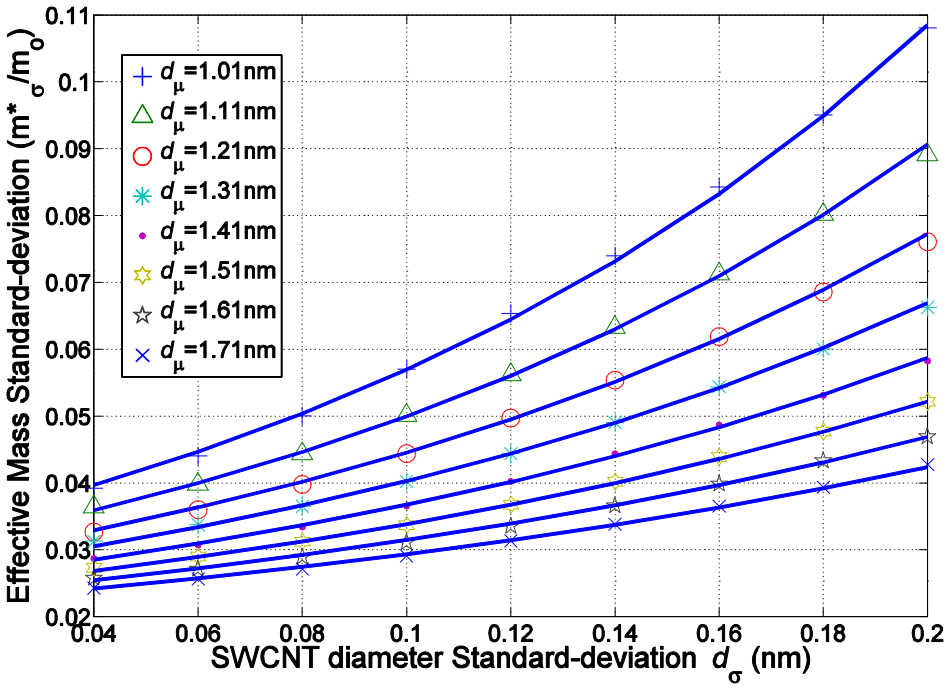

Figure 5-11: Effective mass standard-deviation (m^*_σ/m_0) vs. diameter standard deviation (d_σ). Data sets with different mean diameters (d_μ) have been marked by a distinct symbol. — represents the fitted curve given by Eq. 5.13 with new regression coefficients.

Once again, Eq. 5.14 is proposed as more concise first-order model of the effective mass variability to that of Eq. 5.13. This comes with an extended NRMS error of 3.22% and an R^2 value of 0.974.

$$m_{\sigma}^{*} = \frac{0.037 m_0}{d_{\mu}^{1.36}} e^{4.78 d_{\sigma}} \qquad 5.14$$

Unlike the band-gap variability, Eq. 5.14 indicates that the effective mass variation increases exponentially with diameter fluctuation. This has significant implications as it hints that the carrier effective mass is critically sensitive to any diameter variability. It is also observed that there is a reduction in m^*_{σ} with higher mean diameters, although not as much as with the band-gap variation.

5.4.2 Simulating and modelling the SWCNT carrier effective mass distribution for the second case scenario

For the second case scenario the scaled-up diameter standard deviation is varied according to Eq. 5.7 whilst simulating the effective mass dispersions. The carrier effective mass standard-deviation (m^*_{σ}/m_0) was plotted against the scaled-up diameter standard-deviation (d_{σ_up}) for different sets of d_{μ} as shown in Figure 5-12.

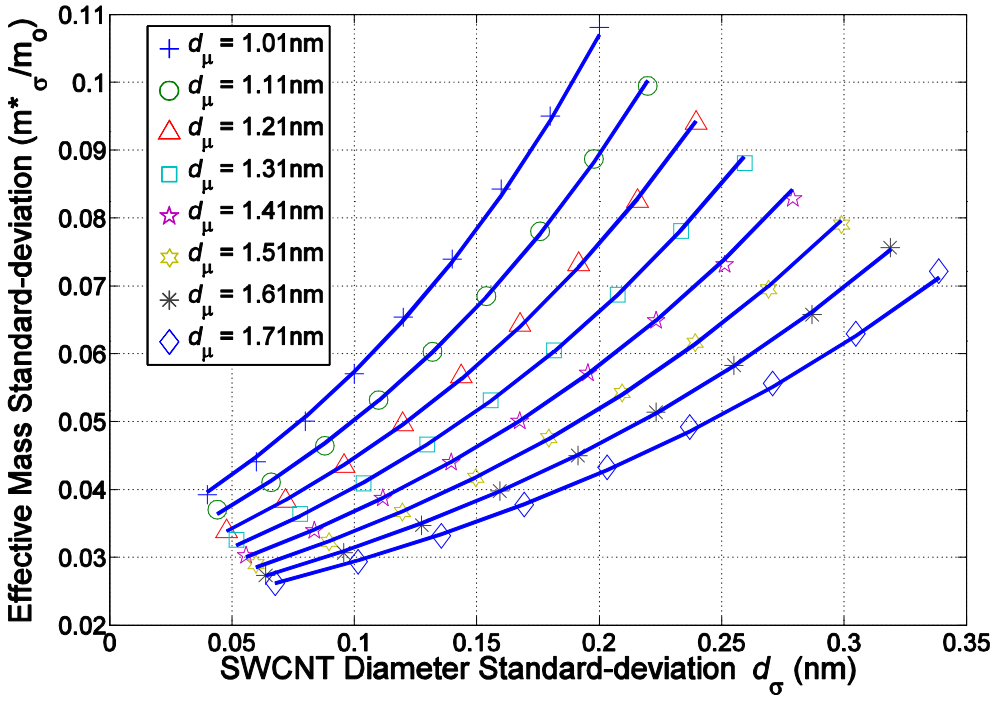

Figure 5-12: Effective mass standard-deviation (m^*_{σ}) vs. scaled-up diameter standard deviation (d_{σ_up}). — represents the fitted curve given by Eq. 5.13 for each d_{μ} with new regression coefficients.

The second-order RSM generated fitted curves were best expressed by Eq. 5.13 with the following regression coefficients; γ_0= -3.4648, γ_1= 6.1740, γ_2= -0.9780, γ_{12}= -4.8975, γ_{11}=

0.3743 and γ_{22}= 0.3650. A small NRMS error of 0.52% (R^2 =1) was evaluated for this model. Additionally, a the first-order expression of the variability can be given by Eq. 5.15 where the NRMS error amounts to 4.4% and an R^2 value of 0.966.

$$m^*_{\sigma\_up} = \frac{0.0386 m_0}{d_\mu^{1.5}} e^{4.6 d_{\sigma\_up}} \qquad 5.15$$

Again, close agreement is identified between Eq. 5.15 and Eq. 5.14, although the reduction in $m^*_{\sigma\_up}$ with higher mean diameters seems to be more pronounced. That said, the carrier effective mass variation does not appear to be significantly dependent on the scaling of the underlying diameter distribution with the mean diameter over the considered ranges in our simulation. Eq. 5.15 further reinforces the exponential relationship between the diameter standard-deviation and effective mass variability.

5.4.3 Simulating and modelling the SWCNT carrier effective mass distribution for the third case scenario

Finally, in the third case scenario the effective mass dispersions are simulated for scaled-down diameter variations specified by Eq. 5.9. Figure 5-13 is a plot representing the effective mass standard-deviation (m^*_σ/m_0) against the scaled-down diameter variability (d_{σ_down}) for different sets of d_μ.

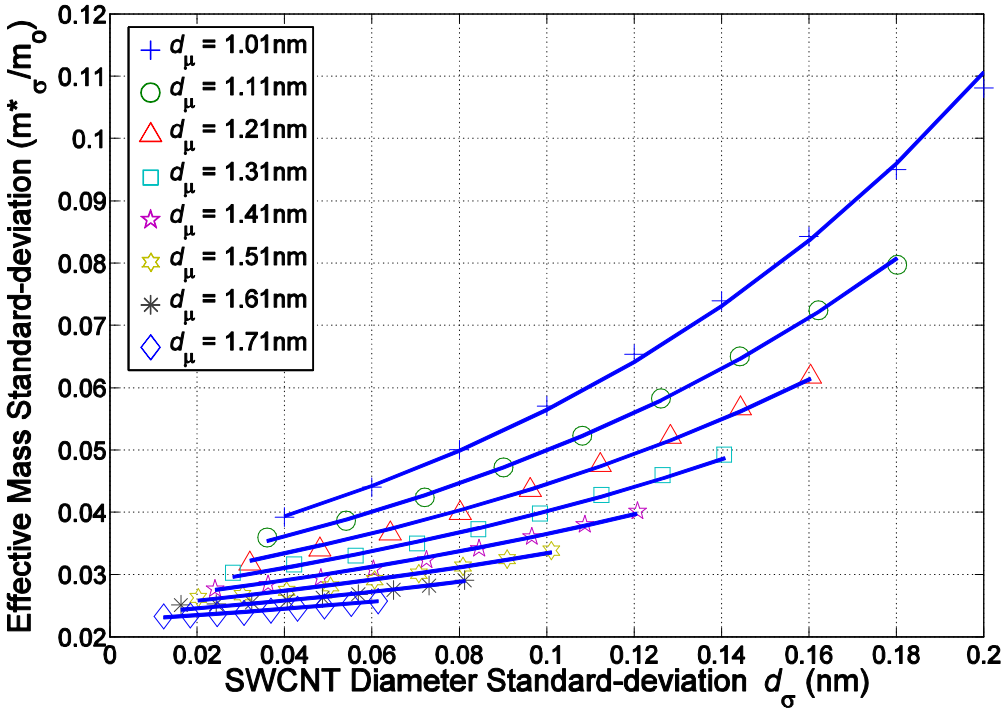

Figure 5-13: Effective mass standard-deviation (m^*_σ) vs. scaled-down diameter standard deviation (d_{σ_down}). — represents the fitted curve given by Eq. 5.13 for each d_μ with new regression coefficients.

Once more, the best fit curves shown in Figure 5-13 can be conveyed by the second-order Eq. 5.13 with the following regression coefficients; γ_0= -3.4511, γ_1= 5.4529, γ_2= -0.6515, γ_{12}= -6.6908, γ_{11}= 4.4829 and γ_{22}= 0.0362. This provided an NRMS error of 0.6% and an R^2 of 0.999. Moreover, a first-order expression is posed for the effective mass variability (denoted by Eq. 5.16) where the NRMS error is only 3.81% and R^2 = 0.965.

$$m^*_{\sigma\_down} = \frac{0.0343 m_0}{d_\mu} e^{5.0 d_{\sigma\_down}} \qquad 5.16$$

Eq. 5.16 signifies that the carrier effective mass variation is directly inversely related to the mean diameter, which is of lower intensity compared to the other case scenarios. This implies that the effective mass variability may possibly depend on the scaling of the underlying diameter distribution. Apart from this, close agreement between all three first-order expressions is visible including the exponential relationship between the diameter standard-deviation and effective mass variability.

5.5 Summary

Due to the lack of accurate control over SWCNT synthesis a statistical approach is applied in predicting the SWCNT band-gap and carrier effective mass variation for typical uncertainties associated with their structural properties.

By defining realistic spreads for the geometric structure of CNTs grown using the CVD method and in exploiting the band-gap and effective mass models developed in the previous chapter, a set of extensive Monte Carlo simulations are run in order to realise the corresponding distributions. In turn, the RSM regression technique is employed to established novel simulation-efficient and accurate models that predict the variation in CNT band-gap and effective mass for different structural dispersions. Furthermore, the generated models are compared and analysed for 3 distinct case scenarios including:

- The diameter variation is *independent* of the mean diameter
- The diameter variation *scales-up* with the mean diameter
- The diameter variation *scales-down* with the mean diameter

The implications of our work advocate that CNT synthesis processes have to be optimised in minimising the diameter variability (d_σ) as well as increase the mean diameter (d_μ) to suppress band-gap and carrier effective mass variations. Specifically, it is demonstrated that under all three case scenarios the band-gap variability is always directly proportional to the diameter variation and is almost inversely related to the square of the mean diameter. However, an observable change is observed for the carrier effective mass variation amongst the three scaling scenarios particularly in the inverse relationship with the mean diameter. Also, given that the effective mass variation increases exponentially with diameter variability we stress on this critical sensitivity.

Chapter 6 Modelling SWCNT Optical Absorption Properties

The essential function of a solar cell is the generation of mobile excess carriers by absorption of optical light [28]. The core focus of this chapter is to address the process of photo-current generation in a SWCNT and model the corresponding optical absorption properties under laser illumination.

The first section offers a background on existing studies related to the analysis of SWCNT photo-absorption. Next, the third-nearest neighbour tight-binding and zone-folding approximation of the SWCNT band-structure is employed in deriving the optical Transition Rate (TR) from first order perturbation theory. The subsequent section describes how the TR is utilised in formulating the photo-generated current and quantum efficiency spectral responses for an intrinsic nanotube exposed to a given laser illumination. Additionally, a comparison is made against experiential and theoretical data where a discussion is presented on the accuracy of the adopted novel approach.

6.1 SWCNT photo-absorption background

Since optical absorption is a fundamental property of any bulk semiconducting material, it can be well described by the semiconductors' electronic band-structure. Normally when a photon is absorbed in a direct-gap semiconductor, electron transitions occur vertically in the band-structure, between an occupied energy band and an un-occupied band with a similar wave vector k to ensure conservation of energy and momentum [127]. Consequently, this generates free electron-hole (e-h) pairs that contribute to the photo-generated current.

In Chapter 2, experimental evidence was presented claiming that the photo-current produced by SWCNTs was consistent with the resonant band-to-band excitation model of e-h pairs. However, there have been well-justified arguments to indicate otherwise, demonstrating that this may not provide a completely accurate picture of the photo-absorption process within a CNT [60].

It has been accepted that electron-hole interactions of low-dimensional structures promote the formation of excitons -strongly bound electron-hole states - which better correspond to the observed optical excitations in [23, 60, 128]. Indeed, in [60] it was experimentally confirmed that upon close inspection of the SWCNT photo-current spectral features, the optical transitions were well matched with excitonic transitions rather than their inter-band counterpart. In fact, when the photo-current spectrum was compared to the calculated inter-band absorption continuum an energy shift was detected by a quantity known as the exciton binding energy [128]. The binding energy represents energy required for an exciton to disassociate into an e-h pair and has been measured to vary depending on factors such as the tube diameter, light polarisation as well as the dielectric properties of the surrounding environment [23, 128]. On the other hand, a more recent controversial experiment reported evidence of photo-current generation from e-h pair excitation across the nanotube sub-bands, particularly the second sub-band, further reinforcing the inter-band transition theory [26].

Unfortunately, modelling the excitonic absorption spectra of a SWCNT would entail the consideration of many-body interactions amongst the confined carriers, which still remains unclear and has proven to be a difficult undertaking [92]. Thus, several studies have resorted to using a single-particle approximation that, although inaccurate, has offered good insight when comparing the optical absorption of SWCNTs with different chiralities [92, 127, 129, 130]. This is because in general, the excitionic absorption follows a similar oscillatory strength with that found for uncorrelated e-h pairs [92]. Hence, the authors acknowledge that using the band-to-band transition model for our study would provide a good first approximation of the CNTs excitonic absorption properties. This is in line with the approximation made in [92].

From a theoretical perspective, the most accurate description of the CNT band-to-band optical absorption spectra can be realised through *ab initio* methods where the imaginary part of the dielectric response function is calculated over a range of photon energies. However, as this is a computationally intensive approach, *ab initio* techniques are infeasible in assessing a large number of nanotubes with varying sizes and incident illumination conditions [131]. Hence, most analytical studies have chosen to derive the optical absorption spectra by means of the tight-binding approximation, which has demonstrated good agreement with experimental observations for a selection of nanotubes [92, 130].

Here, by employing the third-nearest neighbour TB and ZF approximation of the SWCNT band-structure (derived in Chapter 3) the optical Transition Rate (TR) is calculated over all wave vectors *k* within the Brillouin zone. Importantly, this assumes that the incident light is always polarised parallel to the nanotube axis and that the dielectric function can be well described by vacuum conditions. Additionally, it is assumed that no photon-assisted tunnelling occurs in our model, implying that there should be no response below the CNT band-gap [64].

Whilst the same methodology has been carried out in [92] using the nearest-neighbour TB band-structure, we consider more distant neighbours in our generated band-structure due to the enhanced accuracy in evaluating higher order optical transitions as discussed in Chapter 3 [80]. The SWCNT photo-current and Quantum Efficiency (QE) spectra's are subsequently deduced for various nanotubes where experimental as well as theoretical validation is conducted. To the knowledge of the author this methodology in calculating the SWCNT photo-current and QE spectra has not surfaced in prior literature.

6.2 Theory of calculating SWCNT optical transition properties

In this section, the photon-electron interaction for a SWCNT will be described. The optically allowed transitions between the bonding (π) and anti-bonding (π^*) bands will be derived from Fermi's Golden Rule. The concepts pertaining to the optical matrix element as well as the dipole selection rules will be introduced here and used in formulating the electronic transition rate spectra for a nanotube according to its diameter and chiral angle parameters.

6.2.1 Electronic Transition Rate

In order to calculate the optical absorption properties of any crystal, the transition rate (probability of transition per unit time from a filled energy state with wavefunction $\psi_v(k)$ and energy $E_v(k)$ to an empty energy band represented by $E_c(k)$ and wavefunction $\psi_c(k)$) is required [28]. This may be approximated by Fermi's golden rule, which is expressed as:

$$TR(E_p,k)=\frac{2\pi}{\hbar}\left|\langle\psi_c(k)|H'|\psi_v(k)\rangle\right|^2\delta\left(E_c(k)-E_v(k)-E_p\right) \qquad 6.1$$

where $TR(E_p,k)$ denotes the transition rate as a function of the photon energy (E_p) and the wave vector k [28]. The term within the bra-ket is a matrix that describes the interaction between the two wavefunctions, $\psi_v(k)$and $\psi_c(k)$, under an assumed perturbation conveyed by the Hamiltonian H'. In this case, the perturbation H' describes the effect of an incident light field on the transition of an electron from the valence to the conduction band of the exposed semiconductor [28]. The delta function in Eq. 6.1 is included to ensure conservation of energy [28].

Considering a steady-state incident electromagnetic field with intensity I and polarisation unit vector $\boldsymbol{P}$, the perturbation H' can be estimated by the dipole approximation as:

$$H'=j\frac{q\hbar^2}{m_0E_p}\sqrt{\frac{I}{\varepsilon c}}P\cdot\nabla \qquad 6.2$$

where ∇ is called the momentum operator, ε is ascribed as the vacuum dielectric permittivity and c is the speed of light. Therefore, the TR can be rewritten as:

$$TR(E_p,k)=\frac{2\pi q^2\hbar^3 I}{\varepsilon c m_0^2E_p^2}\left|M(k)\right|^2\delta\left(E_c(k)-E_v(k)-E_p\right) \qquad 6.3$$

with

$$M(k)=P\cdot D(k) \qquad 6.4$$

and

$$D(k) = \langle \psi_c(k) | \nabla | \psi_v(k) \rangle \qquad 6.5$$

where *M(k)* is referred to as the optical matrix element that describes the strength of the optical transition and *D(k)* is the transition dipole vector [92]. We shall now proceed with deriving the dipole vector.

6.2.2 Transition dipole vector for Graphene

To calculate *D(k)* the TB approximation is used as in [92]. As previously shown in Chapter 3, the eigenfunction can be expressed as a linear combination of the two $2p_z$ orbital Bloch functions for the A and B atoms in the graphene unit cell. That is:

$$\psi_i(k,r) = \sum_{A,B} C_{ij}(k)\Phi_j(k,r) = \sum_{A,B} C_{ij}(k)\frac{1}{\sqrt{N}}\sum_{R_j} e^{jk\cdot R_j}\phi_j(r-R_j) \qquad 6.6$$

where (i=*c*,*v*) and (j=A,B). The unknown coefficients $C_{ij}(k)$ are found by solving the equation $HC_i = E_i(k)SC_i$ previously defined in Chapter 3 where the Hamiltonian and Overlap matrices were deduced for the nearest-neighbour approximation [92]. This offers two simultaneous equations:

$$C_{iA}(\varepsilon_{2p} - E_i(k)) + C_{iB} f(k)(\gamma_0 - E_i(k)s_0) = 0 \qquad 6.7$$

$$C_{iA} f^*(k)(\gamma_0 - E_i(k)s_0) + C_{iB}(\varepsilon_{2p} - E_i(k)) = 0 \qquad 6.8$$

Substituting the energy eigenvalues ($E_v(k) = \gamma_0|f(k)|$, $E_c(k) = -\gamma_0|f(k)|$) established earlier into Eq. 6.7 and Eq. 6.8 as well as assuming that $\varepsilon_{2p}= 0$ and $s_0 = 0$, the following solutions for C_{ij} are obtained:

$$C_{vA} = C_{vB}\frac{f(k)}{|f(k)|},\quad C_{vB} = C_{vA}\frac{f^*(k)}{|f(k)|},\quad C_{cA} = -C_{cB}\frac{f(k)}{|f(k)|},\quad C_{cB} = -C_{cA}\frac{f^*(k)}{|f(k)|} \qquad 6.9$$

f(k) was derived in Chapter 3, which can be re-defined as:

$$f(k) = \sum_{l=1}^{3} e^{jk\cdot b_l} \qquad 6.10$$

In Eq. 6.10, $\boldsymbol{b_l}$ represents the vectors from carbon atom A to the three nearest-neighbour B atoms [92].

Before inserting the Bloch wavefunction of Eq. 6.6 into Eq. 6.5, first, one needs to define which optical transitions are allowed in the crystal according to the dipole selection rules. Primarily, the dipole selection rule prohibits any optical transitions to occur at the same carbon atom, that is, within a $2p_z$ orbital and itself (*i.e.* $\left\langle \phi_{j'}(r-R_{j'})\middle|\nabla\middle|\phi_j(r-R_j)\right\rangle = 0$) [127]. However, transitions are permitted between $2p_z$ orbital's of adjacent carbon atoms, which includes carbon atoms A and it's 3 nearest-neighbours B_{11}, B_{12} and B_{13} only. Therefore:

$$D(k) = C_{cA'}C_{vB}\left\langle \Phi_{A'}(k,r)\middle|\nabla\middle|\Phi_B(k,r)\right\rangle + C_{cB'}C_{vA}\left\langle \Phi_{B'}(k,r)\middle|\nabla\middle|\Phi_A(k,r)\right\rangle \qquad 6.11$$

Expanding further:

$$\begin{aligned} D(k) = {} & \frac{C_{cA'}C_{vB}}{N}\sum_{R_{A'}}\sum_{l=1}^{3} e^{jk\cdot b_l}\int \phi_{A'}(r-R_{A'})\nabla\phi_B(r-R_{B1l})dr \\ & + \frac{C_{cB'}C_{vA}}{N}\sum_{R_A}\sum_{l=1}^{3} e^{-jk\cdot b_l}\int \phi_{B'}(r-R_{B1l'})\nabla\phi_A(r-R_A)dr \end{aligned} \qquad 6.12$$

Applying the definition stated in [127] for the constant dipole matrix element between the two nearest-neighbour carbon atoms separated by $\boldsymbol{b_l}$:

$$\left\langle \phi_{B'}(r-R_{Bl'})\middle|\nabla\middle|\phi_A(r-R_A)\right\rangle = -\left\langle \phi_{A'}(r-R_{A'})\middle|\nabla\middle|\phi_B(r-R_{Bl})\right\rangle = \frac{M_c b_l}{|b_l|} \qquad 6.13$$

where M_c can be obtained by approximating the $2p_z$ orbital, which, according to a number of sources has been estimated as unity (M_c=1) [73, 92, 127]. By substituting Eq. 6.13 into Eq. 6.12, *D(k)* can be shortened to:

$$D(k) = \frac{M_c}{a_{cc}}\left[C_{cA'}C_{vB}\sum_{l=1}^{3} e^{jk\cdot b_l} b_l - C_{cB'}C_{vA}\sum_{l=1}^{3} e^{-jk\cdot b_l} b_l \right] \qquad 6.14$$

D(k) can be further simplified using the results yielded for the C_{ij} coefficients above as well as the fact that the addition of $exp(jk.b_l)$ and its complex conjugate is always real:

$$D(k) = \frac{2\sqrt{3}M_c}{a|f(k)|}\mathrm{Re}\left[f^*(k)\sum_{l=1}^{3} e^{jk\cdot b_l} b_l \right] \qquad 6.15$$

Eq. 6.15 represents the transition dipole vector for graphene, which can be inserted into Eq. 6.3 to determine the transition rate for a given photon energy and wave vector after performing the dot product with the incident field polarization vector.

6.2.3 Optical Transition Rate for an isolated SWCNT

In this work, it is assumed that light is polarized parallel to the nanotube axis at all times (*i.e. P* = (*0,0,1*)) and therefore, only the *z* component of the optical matrix element, *M(k)*, is of interest [92]. The motive behind this assumption stems from the experimental as well as theoretical results confirming that photo-absorption is maximised when the electric field of the incident light is polarized parallel to the nanotube axis [46, 59, 67]. Moreover, this assumption would greatly simplify our calculations [92].

By supposing that the graphene wavefunctions remain unaltered when rolling up a nanotube, Eq. 6.15 can be used to determine the SWCNT transition dipole vector with the $\boldsymbol{b_l}$ vectors replaced by distances that are expressed as a function of the tube chiral (*m,n*) vector [92]. This was derived in [92] for the *z* component of the optical matrix element $M_z(k)$ yielding the following:

$$M_z(k) = \frac{M_c}{2\sqrt{U}|f(k)|}\left[(m-n)\cos(k\cdot(a_1-a_2)) - (2m+n)\cos(k\cdot a_1) + (m+2n)\cos(k\cdot a_2)\right] \qquad 6.16$$

where $U = m^2+mn+n^2$ and a_1 and a_2 are the two graphene basis vectors introduced in Chapter 3 [92]. Once again, by imposing the periodic boundary conditions in the circumferential direction, the allowed wave vectors that can be assumed in Eq. 6.16 are constrained [92]. Thereafter, Eq. 6.16 is inserted into Eq. 6.3 where all possible contributions of the allowed *k* vectors in the Brillouin zone are taken into consideration by summing numerically over *k* [92, 127]. Consequently, for a given vertically polarized incident photon energy, the total optical transition rate within the primitive unit cell area (*A*) of an isolated (*m,n*) SWCNT is:

$$TR(E_p) = \frac{8\pi q^2 \hbar^3 I}{A\varepsilon c m_0^2 E_p^2} \sum_k \left|M_z(k)\right|^2 \delta\left(E_c(k) - E_v(k) - E_p\right) \qquad 6.17$$

where $E_c(k)$ and $E_v(k)$ are determined by resolving the SWCNT band-structure from the third-nearest neighbour TB and ZF approach (see Chapter 3). Further, Eq. 6.17 has been modified to take account of the 4 degenerate pairs of electron-hole excitations associated with the doubly degenerate valence and conduction bands (since there are two equivalent dispersions at the K and K' points in the Brillouin zone) in addition to the spin degeneracy [60, 127].

6.3 Simulating the SWCNT photo-current and quantum efficiency spectra

The SWCNT optical TR spectra was simulated (see Matlab code in Appendix C) by computing Eq. 6.17 over a nanotube diameter range of 0.8-2.6 nm with chiral angles distributed between 0^0-30^0. These ranges offered 154 distinct chiral vector combinations (*m,n*) of semiconducting nanotubes. This simulation was repeated for 2 different laser illumination intensities; 15 W/cm^2 and 20 W/cm^2 each with photon energies ranging between 0-4eV.

6.3.1 Evaluating SWCNT photo-current spectra

By considering every SWCNT to be illuminated over a 1 μm length (L), the corresponding total photo-current spectra I_p was calculated using Eq. 6.18, where T represents the translation vector along the nanotube axis (see derivation in Chapter 3). Eq. 6.18 enables us to impose a linear scaling of the current with length, since, as the illumination region is increased, a longer section of the nanotube is available for band-to-band transitions [64].

$$I_p(E_p) = q\frac{L}{|T|}TR(E_p) \qquad 6.18$$

Figure 6-1 illustrates a selected subset of photo-current spectra generated for a (*10,0*), (*14,0*), (*17,0*) and a (*19,18*) SWCNT, which are all exposed to an illumination intensity of 15 W/cm^2.

It is clear from Figure 6-1 that a series of distinct narrow photo-current peaks within tens of Pico-amps arise for each nanotube. These correspond to the vertical band-to-band transitions from the valence to conduction sub-bands with the same index number [92]. This can be verified by considering the onset of the peaks, which take place at approximately multiple values of the SWCNT direct band-gap (*e.g.* E_{11} = 0.54eV and E_{22} = 0.975eV for the (*17,0*) CNT). The presence of these resonances in our photoresponses *qualitatively* agree with previous experimental [59, 60, 128] and theoretical [64, 67, 92, 132, 133] findings. Figure 6-1 also reveals that higher bands have lower photo-current peaks as a consequence of the inverse square relation with the photon energy E_p^{-2}, further reinforcing the photo-current decays obtained in [92, 132, 133].

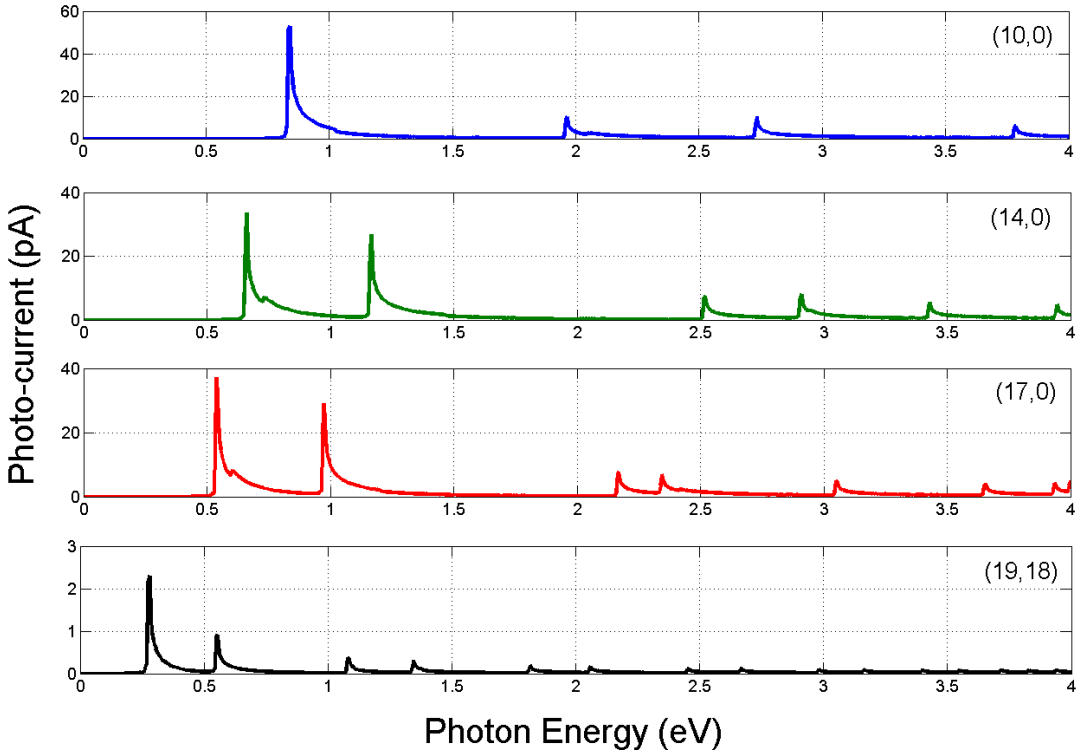

Figure 6-1: Photo-current for a 1 μm long (*10,0*), (*14,0*), (*17,0*) and (*19,18*) SWCNT under an incident illumination intensity of 15W/cm^2.

Unlike some reported photo-current spectra, we do not detect a side-band feature immediately following the photo-current peaks, which have been reasoned to emanate from exciton-phonon coupling clearly observed in experimental measurements [60]. Various experimental results have additionally demonstrated that the peaks feature a Lorentzian resonance as opposed to the narrow, sharp peaks shown here [60, 84]. In [84] it was argued

that this discrepancy occurs because of the excitonic nature of optical absorption in SWCNTs.

Crucially, Figure 6-1 indicates that the optical absorption strongly depends on nanotube chirality, which corroborates with experiments carried out in [134, 135] as well as theoretical calculations performed in [132, 133, 136]. Specifically, for the plotted nanotubes, it is found that the magnitude of the photo-current peak is observably higher with smaller tube diameters [132, 133].

To compare the positions of the absorption peaks in Figure 6-1 with those produced using the Nearest Neighbour (NN) TB model in [132], Table 6-1 is created. Table 6-1 shows the energy values of the absorption peaks calculated using both models for a (*10,0*), (*14,0*) and (*17,0*) nanotube. It is immediately recognized from the table that the absorption peak energies of the proposed model are, in general, lower than those generated in [132], especially for the higher order inter-band transitions. This is to be expected since the inclusion of more distant neighbours in the TB calculation has been previously shown in [80] to be overestimated by the nearest-neighbour approximation (see Chapter 3, Figure 3-7).

	(*10,0*)		**(*14,0*)**		**(*17,0*)**	
	NN TB model [132]	Proposed model	NN TB model [132]	Proposed model	NN TB model [132]	Proposed model
E_{11} **(eV)**	0.886	0.842	0.693	0.661	0.556	0.541
E_{22} **(eV)**	1.909	1.965	1.240	1.165	1.034	0.975
E_{33} **(eV)**	3.091	2.735	2.750	2.515	2.250	2.169

Table 6-1: Comparison between absorption peak energy values calculated in [132] using the NN TB approach and the proposed model, which employs the third-NN TB technique.

In order to ascertain the accuracy of the photo-current magnitude generated by our model a comparison was carried out against experimental data published in [34]. A ~1 nm diameter SWCNT was exposed to a laser illumination source over a 1 μm length with a variable output power and a fixed photon energy of 0.8 eV [34]. The recorded photo-current results at a zero bias voltage (V_{DS}=0) are depicted in Figure 6-2, where, as expected, a linear dependence with optical power density ensues. Correspondingly, our model generated photo-current is plotted under the same conditions for two zig-zag nanotubes, (*13,0*) and (*14,0*), both having roughly a similar diameter of 1 nm. As can be inferred from Figure 6-2, the

modelled results offer a very close match to the experimental data affirming the linear dependency with optical power [26, 34, 59]. It is also suspected that the reason our model is consistently yielding slightly higher photo-current may possibly be due to the fact that in [34] the utilised laser source was circularly polarised, which, as stated, contributes to lower photo-absorption.

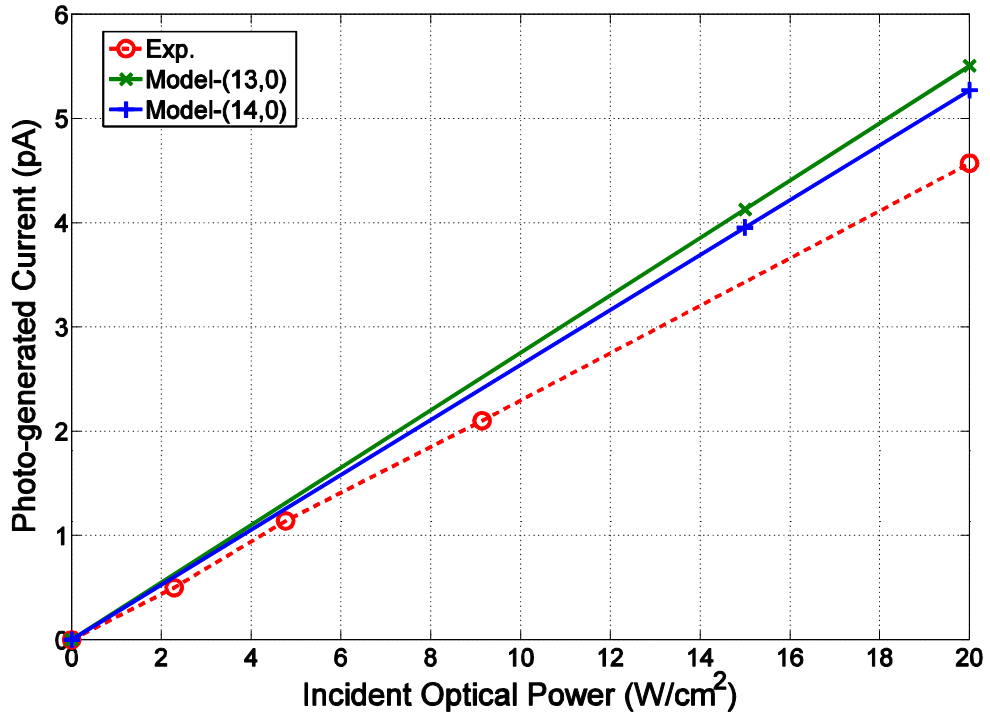

Figure 6-2: Comparison between experimental [34] and calculated photo-current dependence on incident optical power for a (13,0) and (14,0) (d~1 nm) SWCNT at E_p = 0.8eV.

6.3.2 Evaluating SWCNT quantum efficiency spectra

The Quantum Efficiency (QE) of a SWCNT is an essential parameter to address as it provides an introspective on the number of e-h pairs created and delivered to the external circuit per incoming photon [28]. Before calculating this quantity the following assumptions are made:

- No reflection losses ($R(E_p)$=0) are experienced by the analysed SWCNTs
- All generated e-h pairs are perfectly separated and transported to the contacts
- The SWCNTs are ideally interfaced with the contacts enabling no collection losses

In employing the photo-current results acquired in the previous section, the SWCNT QE is derived from the well established expression [59, 132]:

$$QE(E_p) = (I_p(E_p)/q)/(P_{op}/E_p) \qquad 6.19$$

where P_{op} is the optical power of the incident light delivered to the SWCNT [132]. Figure 6-3 depicts a subset of 154 simulated SWCNT QE spectral responses. This subset consists of a (*10,0*), (*14,0*) and (*17,0*) zig-zag nanotube, which are compared to previously reported theoretical and experimentally derived data values [59, 132].

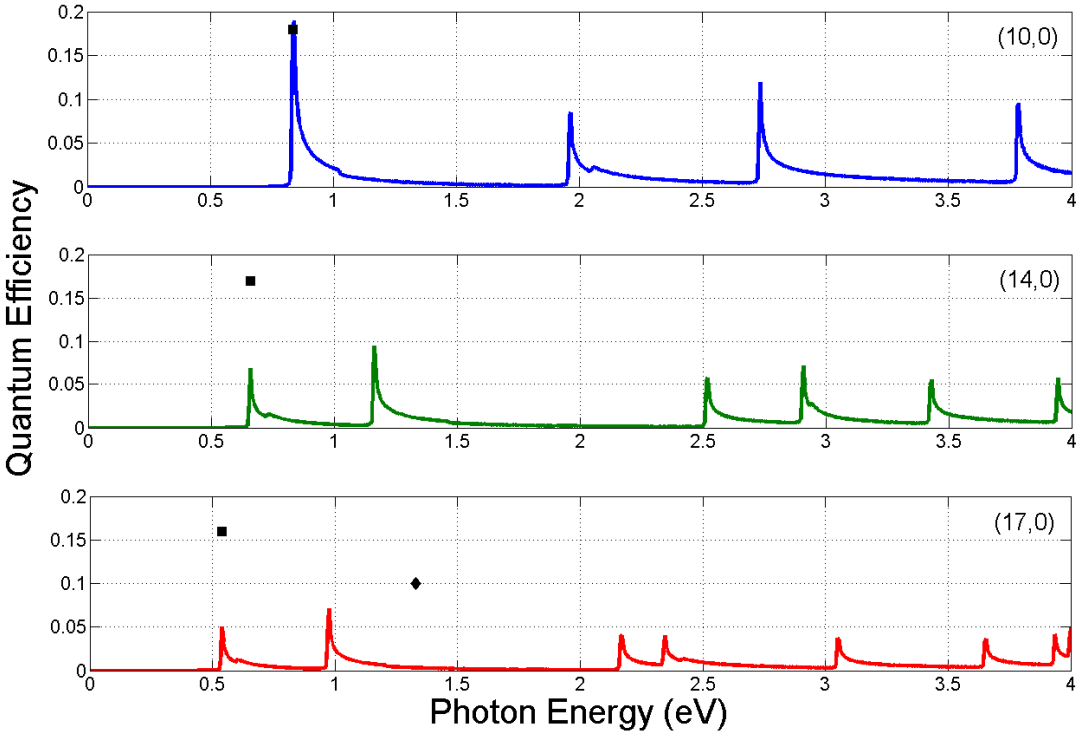

Figure 6-3: Quantum efficiency spectra for a (*10,0*), (*14,0*) and (*17,0*) nanotube. ■ represent corresponding theoretical QE values obtained in [132] using the nearest neighbour TB approximation. ♦ is associated with an experimental result acquired from [59].

Initially it can be identified from Figure 6-3 that the QE spectra also consists of multiple sharp peaks corresponding to the resonant band-to-band transitions associated with each nanotube. In contrast to the photo-current spectra, the relative heights of these peaks are significantly different, following no pre-defined characteristic. For instance, with the (*14,0*) and (*17,0*) tubes it is clearly distinguishable that the QE peaks due to the second interband transitions (E_{22}) are observably higher than their first peak. However, one would expect the heights of the QE peaks to decrease with photon energy given the E_p^{-1} relation in Eq. 6.19. In

[64] it was reasoned that this photo-response is a result of different sub-bands having different carrier effective masses. Indeed, it was found that the effective masses of the E_{22} bands to be much higher (lower curvature) than the E_{11} bands for the (*14,0*) and (*17,0*) nanotubes.

This implies that the QE is very much sensitive to the CNT carrier effective mass, which as discussed in Chapter 4 is strongly dependent on CNT diameter and chirality. In fact, if the QE values of the first interband transitions are compared for zig-zag nanotubes, it is observed that a general decline in QE with diameter ensues, as expected, since the effective mass for E_{11} also decreases with diameter (see Chapter 4). This result has not been identified in previous literature.

That said, there lies an inconsistency in this finding that encourages us to believe that the carrier effective mass is *not the only factor* dictating the quantum efficiency peak values. The inconsistency arises from the first interband transition QE results (also seen in Figure 6-3) demonstrating that (m,0) zig-zag tubes where $m=3p+1$ (p is any integer) have higher peaks compared to zig-zag tubes with $m=3p+2$. Previously it was shown that $m=3p+1$ zig-zag tubes in fact have lower carrier effective masses compared to $m=3p+2$ zig-zag CNTs, which does not fit with our conviction that higher effective masses lead to higher QE values.

Nevertheless, the implications of the above QE results suggest that photons with energies corresponding to the second interband or higher transitions may possibly have a higher probability in being absorbed and converted to an e-h pair compared with photons matching E_{11}. This aligns well with the experimentally supported theory related to highly efficient optical absorption into the CNT's second electronic subband, although, it does not rule out E_{11} in providing a sizable photo-current response [23, 26, 60].

Figure 6-3 portrays the QE magnitude to vary up to 0.19 for the first subband transition of the (*10,0*) SWCNT, which is in agreement with the 0.18 value obtained using the theoretical self-consistent non-equilibrium Green's function in [132]. On the other hand, a notable mismatch is recognized for the (*14,0*) and (*17,0*) CNTs, where the simulated QE magnitudes at E_{11} are 0.07 and 0.05, respectively. These are almost a third of the values reported in [132]. Additionally, for the (*17,0*) nanotube, a comparison of our model generated

maximum QE (0.07 at E_{22} = 1eV) is made against an experimentally calculated QE (0.1 at E_{22} = 1.3eV) for a SWCNT with a similar diameter ~1.3 nm [59]. Despite the 0.3 eV difference between the second interband transition energies, which again is attributed to the excitonic nature of optical absorption in CNTs, it can be established that the quantum efficiency values are relatively close.

Most importantly, it is found that the overall maximum quantum efficiency is strongly dependent upon the SWCNT chirality and diameter, as expected. This is further illustrated in Figure 6-4.

According to our simulated results it is clear from Figure 6-4 that the highest quantum efficiencies occur chiefly for zig-zag SWCNTs (chirality = 0^0) with low diameters due to the higher carrier effective mass. The maximum value attained is exhibited by the (*10,0*) tube, which was previously discussed. Other nanotubes experience very little photo-absorption with quantum efficiencies in the order of 0.02 or lower. These findings have not been revealed in prior literature and offer an insight on the optimal SWCNT structural properties needed for photo-detection and photovoltaic purposes.

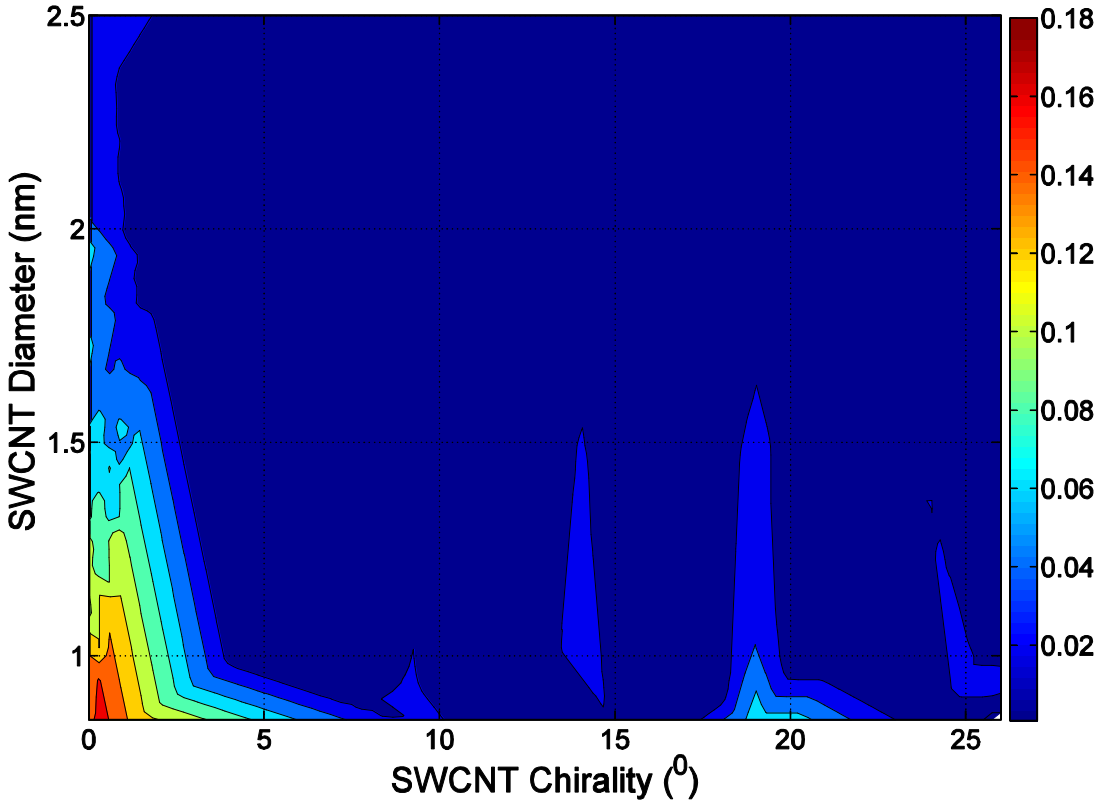

Figure 6-4: Calculated maximum quantum efficiency (indicated by the contour colour bar) as a function of SWCNT chirality (^{0}) and diameter (nm).

6.4 Summary

By employing the third-nearest neighbour TB and ZF approximation of the intrinsic SWCNT band-structure (derived in Chapter 3) the optical Transition Rate (TR) was calculated for 154 distinct nanotubes under 2 different laser illumination intensities with photon energies ranging between 0-4eV. Notably, it is assumed that the incident light is always polarised parallel to the nanotube axis and that the dielectric properties can be described by vacuum conditions.

The SWCNT optical TR is initially utilised in formulating the photo-current spectral response where a series of distinct narrow peaks within tens of pico-amps ensue. This is shown to be due to the resonant band-to-band transitions associated with the SWCNT sub-bands, which *qualitatively* agree with previous experimental [59, 60, 128] and theoretical [64, 67, 92, 132, 133] findings. Additionally, it is revealed that the optical absorption strongly depends on nanotube chirality with higher photo-current peaks arising for smaller diameter tubes [132, 133]. The modelled photo-current is also confirmed to possess a linear

dependence on the incident optical power, closely matching experimental results obtained in [34].

The Quantum Efficiency (QE) spectra is later derived from the SWCNT photo-current where it is discovered that the peak values are highly sensitive to the carrier effective masses of the corresponding band transitions. In fact, when comparing the QE height values of the first interband transitions for the zig-zag nanotubes, a general decline in QE is observed with respect to diameter since the effective masses for E_{11} also decrease with diameter (see Chapter 4). However, the observation that (m,0) zig-zag tubes with m=3p+1 (low effective mass) having higher QE peaks compared to zig-zag tubes with m=3p+2 (high effective mass) encourages us to believe that the carrier effective mass is *not the only factor* dictating the quantum efficiency peak values. Next, a comparison of the generated QE spectra of three nanotubes is made against theoretical and experimental data, the outcome of which demonstrated some agreement although not entirely.

Crucially, it is found that the overall maximum quantum efficiencies (~0.05-0.18) occur chiefly for zig-zag SWCNTs (chirality = 0^0) with low diameters. Other nanotubes are found to experience very little photo-absorption, offering quantum efficiencies in the order of 0.02 or lower. These findings have not been revealed in prior literature and offer an insight on the optimal SWCNT structural properties required for photo-detection and photovoltaic purposes.

The following chapter embodies the final key contribution of this thesis where the novel approach established in this chapter to simulate the nanotube QE will be adopted in evaluating the performance metrics of isolated CNTs as well as multi-CNT PV devices under solar radiation. This will enable us to uncover the optimised CNT geometric structures for PV conversion.

Chapter 7 Performance Evaluation of SWCNT based Photovoltaic Devices

This chapter aims to evaluate the ideal performance of SWCNT based solar cells under solar light radiation. Specifically, we shall endeavour to employ the quantum efficiency model created in the former chapter to analyse the Photovoltaic (PV) conversion efficiency for a set of distinct semiconducting nanotube devices.

In the first section a framework of assumptions will be defined for calculating the ultimate conversion efficiency of an isolated SWCNT PV represented by the ideal equivalent circuit model introduced in Chapter 2. The subsequent section will discuss the resulting short-circuit current, open-circuit voltage, saturation current, fill factor and conversion efficiency when exposed to both the AM0 and AM1.5 solar spectrum. Next, an equivelent circuit-level model is developed for a multi-bandgap SWCNT PV device based on the proposed hypothetical solar cell defined at the end of Chapter 2. Simulations are carried out to identify the optimal geometrical structures needed and corresponding conversion efficiencies for each multi-CNT PV device. In the final section our findings are summarised where a discussion on the implications of our results is reported.

7.1 Background in modelling SWCNT based photovoltaic devices

In prior literature there have been two main theoretical approaches that have been employed in modelling CNT based PV devices in order to ascertain their performance [67, 132].

The first is a technique recently published by [67], which involved the development of an electromagnetic (EM) scattering model for a PV device based on a periodic array of SWCNTs [67]. Each nanotube, excited by a classical EM light wave, was effectively modelled as a lossy dielectric cylinder with a frequency-dependent complex permittivity [67]. Although this method offered good insight on the variation of absorbed optical power by the CNTs due to different nanotube geometrical properties as well as various scattering effects from the device structure, the related *I-V* characteristics could not be evaluated.

The second technique was originally devised by [64, 132], where the electronic transport characteristics of an illuminated single nanotube *pn* junction under bias was calculated using a self-consistent Non-Equilibrium Green's Function (NEGF) formalism [132]. This method assumed a fixed incident light field on the SWCNT and neglected all scattering effects from the surrounding structure [67].

Generally, the NEGF simulation computes the Poisson equation (*i.e.* the potential profile) of a device and the transport equation (*i.e.* the electron density) iteratively until they converged to a self-consistent value [132]. This possesses a large time complexity that is further augmented by the fact that the device must be resolved into principle real-space layers, which in the case of a nanotube comprises of a set of atomic CNT rings [132]. More importantly, the results of the NEGF simulation in [132] discovered that the *I-V* characteristics of various CNT PV devices can be well approximated by the following expression:

$$I(V) = I_{sat}(e^{qV/k_BT} - 1) - I_{sc} \qquad 7.1$$

where:

$$I_{sat} \sim e^{-E_g/k_BT} \qquad 7.2$$

This identically matches with the formula stated in Chapter 2 for describing the steady-state *J-V* characteristics of the ideal PV equivalent circuit model. Notably, the work of [132] was followed by a report confirming the accuracy of the NEGF method in modelling the electron-photon coupling effect as well as the CNT quantum transport mechanism whilst analysing the photoconductivity of a Schottky-Barrier CNT FET [136]. Moreover, during an experimental investigation of a CNT diode PV device in [25], the measured *I-V* characteristics were found to fit well with Eq. 2.7 and 7.2 for a range of illumination intensities. In turn, this was used to evaluate the conversion efficiency [25].

To obtain an accurate theoretical description of a CNT based PV device, ideally, both the EM and quantum mechanical NEGF approaches should be coupled together and solved self-consistently [67]. However, this entails significant added simulation complexity. Thus, it has been decided to make a number of assumptions and adopt the ideal PV equivalent circuit model (*i.e.* Eq. 2.7 and 7.2) as the foundation of our CNT based PV device analysis. Henceforth, the following sub-section is dedicated to outlining these core assumptions.

7.1.1 SWCNT PV device assumptions

Since this study will take advantage of previously derived photo-absorption models for a given SWCNT, we briefly reiterate some of the assumptions made earlier, including:

- The incident light will always be polarised parallel to the nanotube-axis and no light reflection is allowed to occur (*i.e.* R=0). Additionally, the surrounding medium in which light travels will possess a dielectric constant described by vacuum conditions.
- Scattering effects from nearby structures (*e.g.* source/drain electrodes) are ignored.
- All optical absorption in the SWCNT is associated with band-to-band transitions, which directly result in e-h pair formation. Thus, any excitonic effects are neglected as it is beyond the scope of this study (see Chapter 6 for related argument). Moreover, the effects of photon-assisted tunnelling are discarded.
- The steady-state short-circuit current (I_{sc}) will only be determined from the incident illumination intensity and Quantum Efficiency (QE) spectra of the

nanotube [136]. It is also assumed that I_{sc} is independent of the doping density in agreement with experimental results in [34].

- It will be assumed that the QE peak energies are not shifted due to the presence of an internal electric field caused by the Stark effect [23]. As of yet, experiments investigating this effect particularly for well-defined single CNT samples have not been conducted [23].

As it has already been declared, the ideal equivalent PV circuit model will be exploited towards modelling the *I-V* characteristics of our CNT PV devices, which implies that the following assumptions apply:

- All photo-generated e-h pairs are perfectly separated and transported ballistically to the corresponding nanotube electrodes. That is, generated electrons and holes are swept to the *n*-type and *p*-type terminals, respectively, by the built-in potential [64].
- Although it has been claimed that the mean-free path of CNT charge carriers is 1 μm according to [23], it will be assumed that all photo-generated carriers are collected within this length [16]. Therefore all tube lengths (L) will be considered 1 μm.
- The absence of non-radiative recombination ($R_{sh} = \infty$) is supposed given we are only interested in predicting the upper limit of the SWCNT conversion efficiency.
- We assume that the SWCNT experiences no contact resistance ($R_s = 0$).
- The open-circuit voltage will be taken to equal the SWCNT band-gap ($V_{OC}=E_g$). This has been experimentally confirmed in [26] under an ambient temperature of T=60K [26]. Therefore, we assume that the SWCNT PV device is operating at T=60K.
- We presuppose that the forward-bias dark current is independent of the doping level as well as the SB characteristics. In reality, this is not the case, but since this study is only a first estimate we shall overlook this effect.

7.2 Isolated SWCNT PV device simulation and results

In this section the performance of a single SWCNT based *pn* junction solar cell is evaluated. Figure 7-1 depicts the PV device where the nanotube diameter d and chirality θ are allowed to vary over the ranges 0.8-2.7nm and $0\text{-}30^0$, respectively. As can be seen from Figure 7-1, the nanotube edges are terminated by a drain and source contact, across which a bias V is applied. It is important to note that the incident z-polarised light, represented by the AM0/1.5 spectrum, is only exposed over the window area: Lxd.

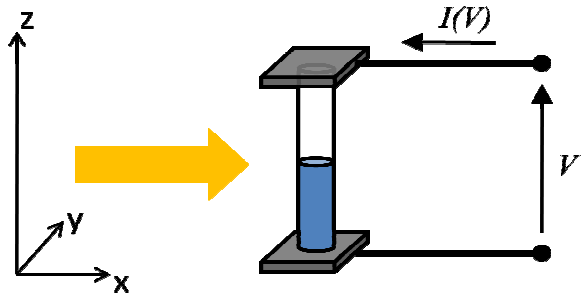

Figure 7-1: Isolated SWCNT based *pn* junction PV device.

The *I(V)* characteristic of the device is modelled using Eq. 7.1, which consists of two components; the short-circuit current (I_{sc}) and the forward-bias dark current [132]. We shall now proceed by first solving I_{sc} under the various mentioned conditions and assumptions.

7.2.1 Simulating the isolated SWCNT PV device short-circuit current

The short-circuit current of Eq. 7.1 can be calculated from the nanotube quantum efficiency $QE(E_p)$ and incident solar flux spectrum $\phi_s(E_p)$ by integrating the product over all photon energies E_p [28]:

$$I_{sc} = qA\int_0^\infty QE(E_p)\phi_s(E_p)dE_p \qquad 7.3$$

where A is the nanotube surface area. Here, the QE model derived in Chapter 6 is employed in computing Eq. 7.3 for 154 distinct semiconducting nanotubes over the specified geometrical structure range. This was carried out using the AM0 as well as AM1.5 spectrum data taken from [27]. A sub-set of the simulated results is shown in Figure 7-2 where I_{sc} is depicted across the photon energy range 0-4.4 eV.

Above the CNT band-gap, Figure 7-2 demonstrates a common feature amongst all nanotubes that can be described as short-circuit current steps. The onset of these steps clearly take place at photon energies matching the resonant band-to-band transitions of the corresponding nanotube. A comparable experimental observation was also recently reported whilst measuring the I-V characteristics of a SWCNT *pn* junction photodiode in [26]. It was similarly advocated that the current steps occurred at intervals approximately equal to the nanotube band-gap [26]. It could be additionally inferred that since I_{sc} is dependent on the QE magnitude, then the carrier effective mass of each interband transition must play a contributing factor in defining the height of each step. This finding has not been detected in prior literature.

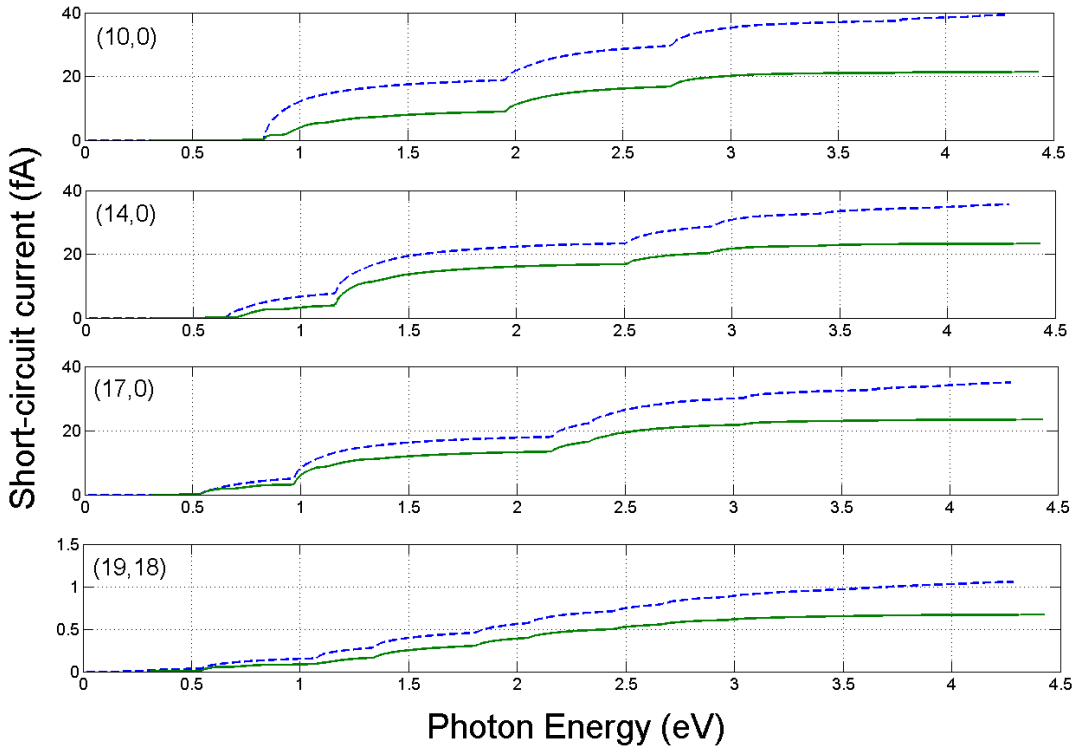

Figure 7-2: Short-circuit current (I_{sc}) vs. photon energy for a (10,0), (14,0), (17,0) and (19,18) SWCNT. --- (—) represent simulated results under AM0 (AM1.5) conditions taken from [27].

Notably, as can be seen for all CNTs in Figure 7-2, the total short-circuit current over the entire AM1.5 photon spectrum is roughly 50-70% of the respective AM0 value. This is reasonable given that the AM1.5 spectrum has a total power density (897.8 W/m^2) which is

two-thirds of the corresponding AM0 estimate figure (1360.2 W/m^2) over the same photon energy range.

Next, a plot of the short-circuit current under the AM1.5 spectrum is produced as a function of semiconducting nanotube diameter and chirality. Figure 7-3 visibly illustrates zig-zag SWCNTs having an appreciably higher I_{sc} compared to chiral nanotubes, which is as much as 11 times greater. This is understandable knowing that the highest quantum efficiencies only occur for zig-zag CNTs. We can therefore acknowledge that chiral nanotubes are unsuitable for PV conversion and shall now only focus on investigating zig-zag nanotubes.

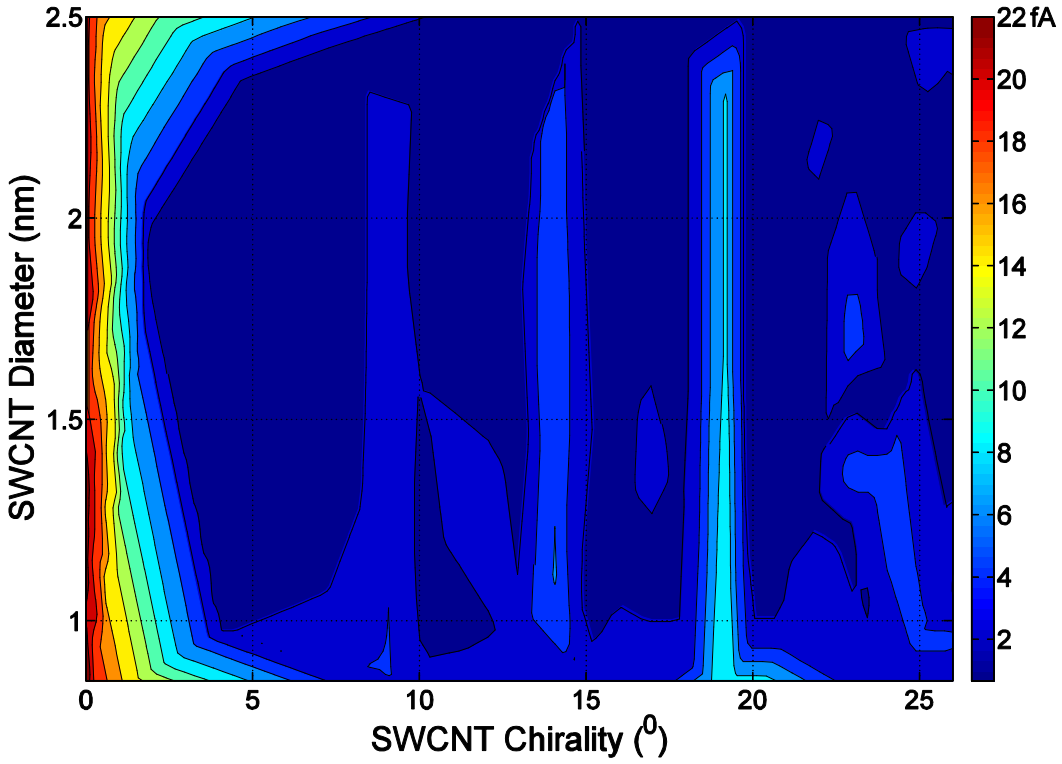

Figure 7-3: Simulated short-circuit current variation (under an AM1.5 spectrum) over the SWCNT structural parameter space. The contour colour bar represents the magnitude of I_{sc}.

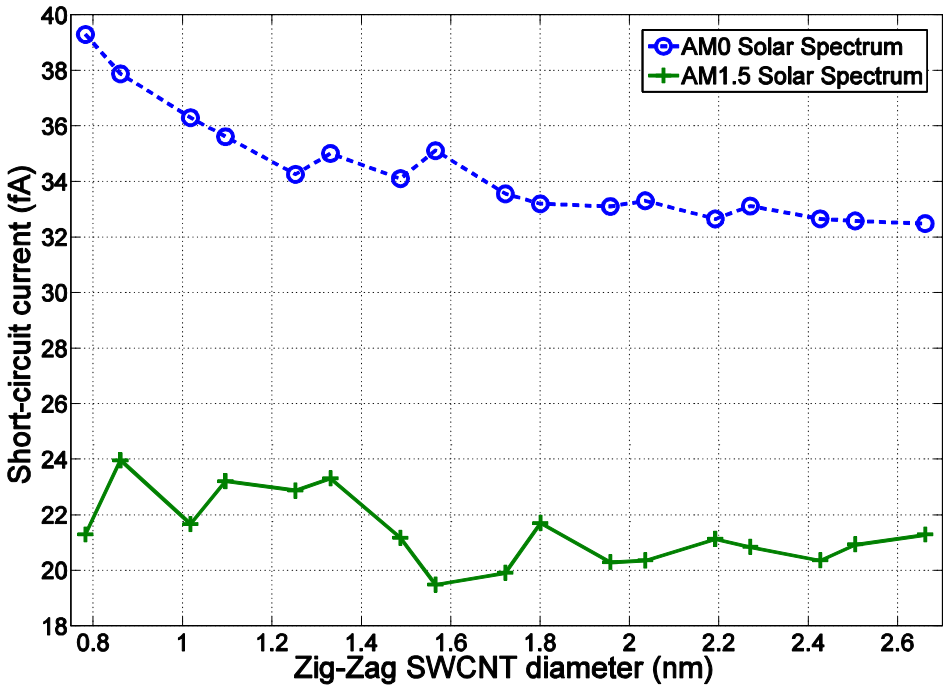

Figure 7-4: Simulated short-circuit current vs. zig-zag SWCNT diameter.

Figure 7-4 is formed to gain a better insight on the relationship between I_{sc} and diameter for semiconducting zig-zag nanotubes. It portrays a slight decay in short-circuit current with respect to the zig-zag nanotube diameter. This decline is more pronounced for the AM0 spectrum (of about ~8 fA) compared to the AM1.5 spectrum where I_{sc} seems to fluctuate about a decreasing value. The implications of such an outcome could imply that the diameter of the CNT is not as vital as the tube chirality in maximising photo-absorption. However, this cannot be confirmed until the other equally significant performance parameters of our PV device are analysed.

7.2.2 Simulating the isolated SWCNT PV device open-circuit voltage

As previously established, one should primarily focus on studying zig-zag nanotubes. Thus, the associated open-circuit voltages shall now be calculated taking into account the assumptions made in sub-section 7.1.1. Since it is presumed that the open-circuit voltage is equivalent to the CNT band-gap (V_{oc}=E_g) under a temperature condition of T=60K [26], then, all that needs to be done is to examine the band-gap for the zig-zag nanotubes of interest.

Using the third-nearest neighbour tight-binding method in conjunction with the zone-folding technique as reported in [80], the SWCNT band-gap is evaluated and plotted with respect to the zig-zag tube diameter as revealed in Figure 7-5.

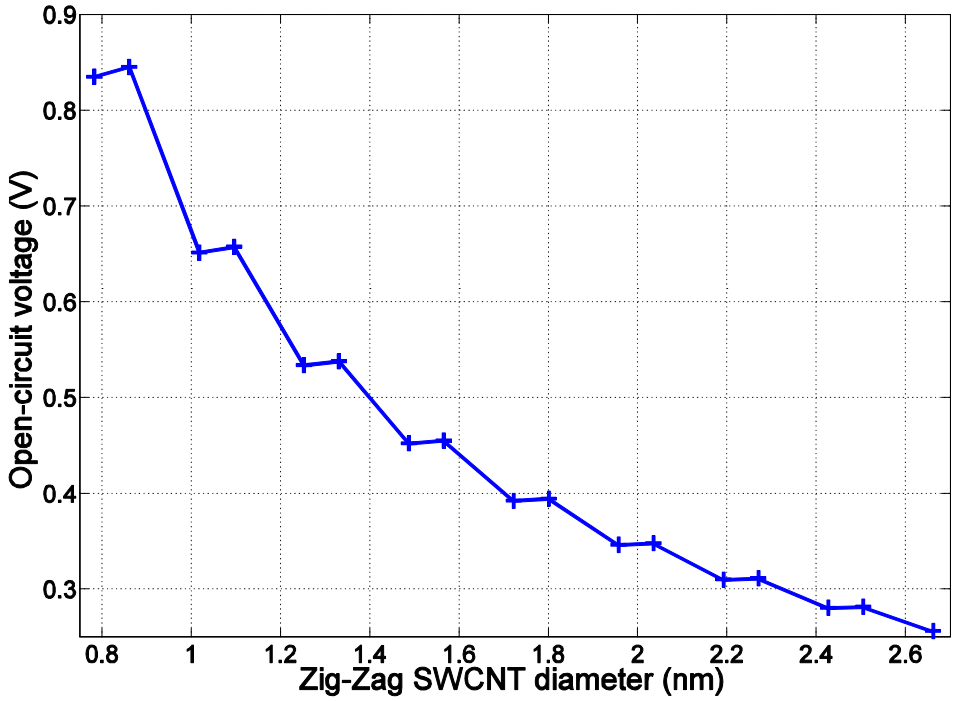

Figure 7-5: Simulated open-circuit voltage (V_{oc}=E_g) vs. zig-zag CNT diameter.

The dependence of V_{oc} on d is consistent with our previously derived relationship V_{oc}=E_g=0.692/d. Moreover, this relation aligns well with the experimentally measured result V_{oc}~0.66/d in [26]. Evidently, smaller diameter tubes will be needed in order to maximise the open-circuit voltage for a SWCNT PV device.

7.2.3 Simulating the isolated SWCNT PV device saturation current and fill factor

According to Eq. 7.2, the saturation-current (I_{sat}) decreases exponentially with the SWCNT band-gap [132]. In our scenario, it could be further reasoned that I_{sat} decreases exponentially with the open-circuit voltage since V_{oc}=E_g. By rearranging the open-circuit voltage formula defined in Chapter 2, I_{sat} can be expressed as follows:

$$I_{sat} = I_{sc}(e^{qV_{oc}/k_BT} - 1)^{-1} \qquad 7.4$$

In this case, the saturation-current is a function of both the SWCNT open-circuit voltage (band-gap) and the short-circuit current I_{sc}. Under a T=60K condition, Eq. 7.4 can be instantly solved using the V_{oc} and I_{sc} results previously derived for the zig-zag SWCNTs. Figure 7-6 illustrates a logarithmic plot of the saturation-current with respect to the zig-zag SWCNT diameter.

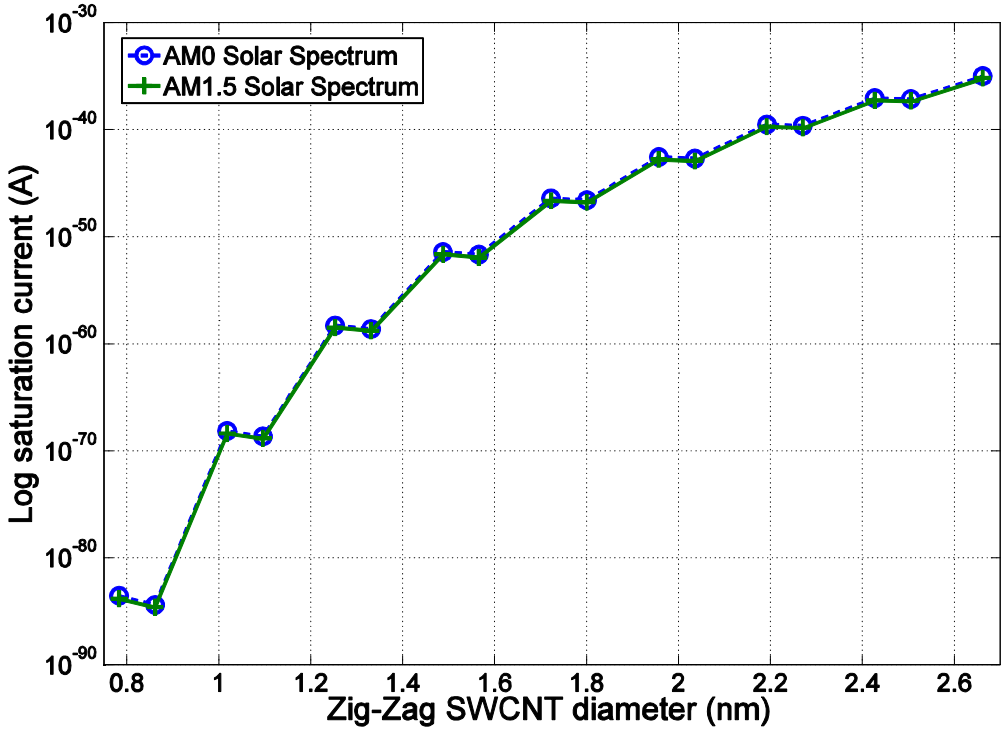

Figure 7-6: Logarithmic plot of saturation-current vs. zig-zag SWCNT diameter under both the AM0 and AM1.5 solar spectrum.

It is evident from Figure 7-6 that the saturation-current rises exponentially with the zig-zag SWCNT diameter, which is a direct consequence of the V_{oc} (E_g) reduction. As expected, a negligible difference is identified between the saturation-currents under the AM0 and AM1.5 solar spectrum suggesting that the short-circuit current affects I_{sat} to a much lesser extent compared to V_{oc} (E_g). From the results of Figure 7-6 it could be affirmed that smaller diameter tubes are better suited to minimising the saturation-current for a SWCNT based PV device.

By substituting the derived I_{sc} and I_{sat} parameters into Eq. 7.1, the *I-V* characteristics are generated for the different diameter zig-zag SWCNT PV devices as shown in Figure 7-7. The *I-V* curves demonstrate ideal characteristics for all nanotubes where V_{oc} is considerably reduced with diameter (see arrow) and I_{sc} is weakly diminished. Notably, the *I-V* curves are

seen to arise in pairs, which represent (*m*,0) nanotubes with successive *m* indices that possess almost identical V_{oc} values.

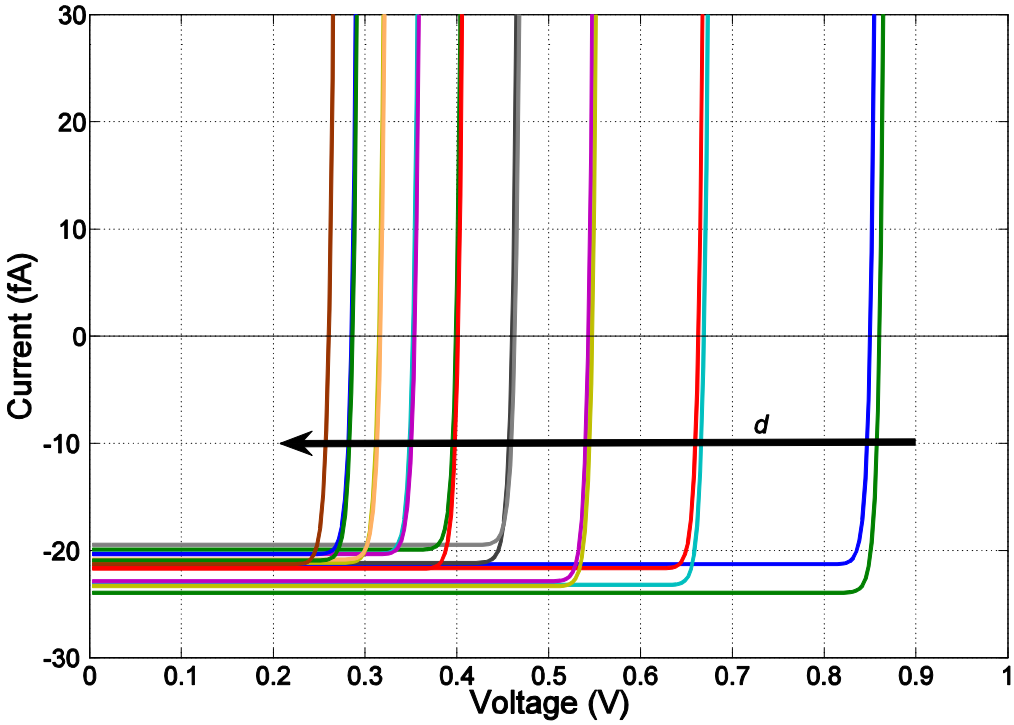

Figure 7-7: *I-V* characteristics of different diameter zig-zag SWCNT based PV devices under the AM1.5 solar spectrum.

The corresponding Fill Factor (FF) of the above CNTs can be evaluated using the expression:

$$FF = \frac{P_m}{I_{sc}V_{OC}} \qquad 7.5$$

where P_m is the maximum operating power point obtained by solving $dP/dV = 0$ inside the 4th quadrant. The variation in fill factor is portrayed in Figure 7-8 with respect to the SWCNT diameter where it is observed that the FF ranges within 0.963-0.9, which is excessively high as a result of the ideal assumptions made. Nevertheless, this is comparable with the predicted value of FF>0.8 claimed in [34] that was also calculated using the ideal equivalent PV circuit model.

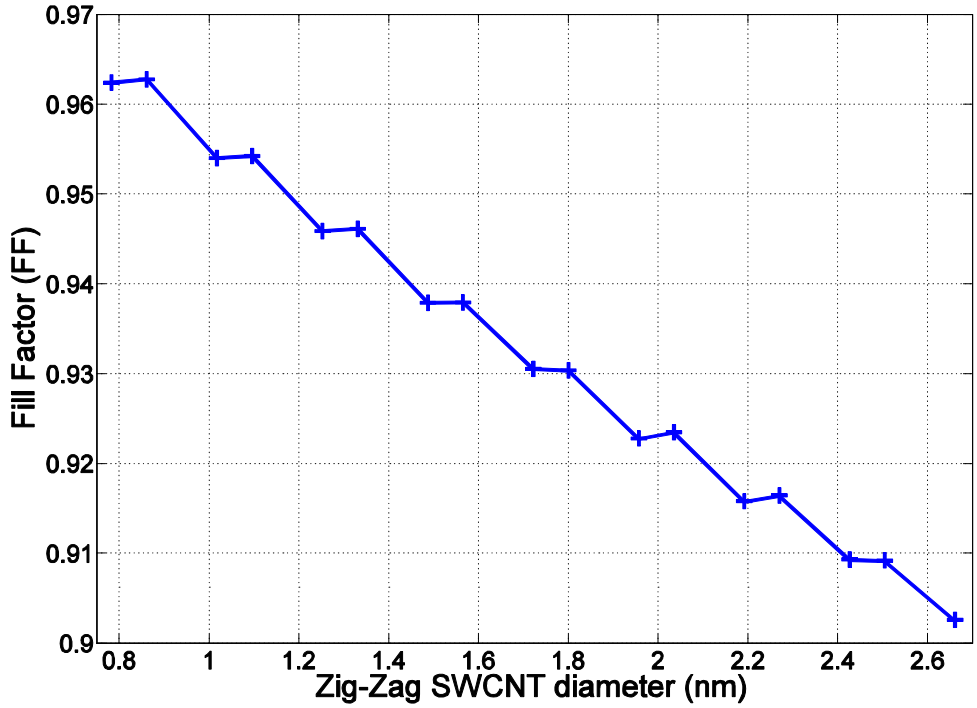

Figure 7-8: Simulated Fill Factor vs. zig-zag SWCNT diameter.

The plot additionally exhibits an approximate 0.03 decline in fill factor for every 1 nm increase in CNT diameter. This again indicates that smaller diameter tubes are more appropriate for PV conversion due to the superior FF.

7.2.4 Simulating the isolated SWCNT PV device conversion efficiency

The PV power conversion efficiency of the examined zig-zag SWCNTs can be identified using the familiar equation:

$$\eta = FF\frac{I_{sc}V_{OC}}{P_{in}} \qquad 7.6$$

where P_{in} is the incident solar power exposed over the specified window area. Figure 7-9 displays the corresponding conversion efficiency as a function of the nanotube diameter under both the AM0 and AM1.5 spectrum. As can be seen, irrespective of the incident solar spectrum, the efficiency drops dramatically from ~2.5% for a sub-1 nm CNT to <0.5% for nanotubes greater than 1.8 nm. This is in good agreement with recommendations made in [34] where it was argued that SWCNTs having diameters around 0.8 nm would offer significant improvements in PV conversion efficiency due to the larger band-gap [46]. Moreover, it was estimated that ideal efficiencies can be as high as 5% based on actual absorbed power, which is relatively comparable to our simulated results [34]. Similarly, our

conversion efficiencies are found to be appreciably high considering that the modelled QE's are as low as 0.18. Again, this can be attributed to the idealistic assumptions made in our study, which have caused the reporting of a 7x enhancement in our performance value at *d*=1 nm compared to the experimentally measured result in [34] (see Figure 7-9).

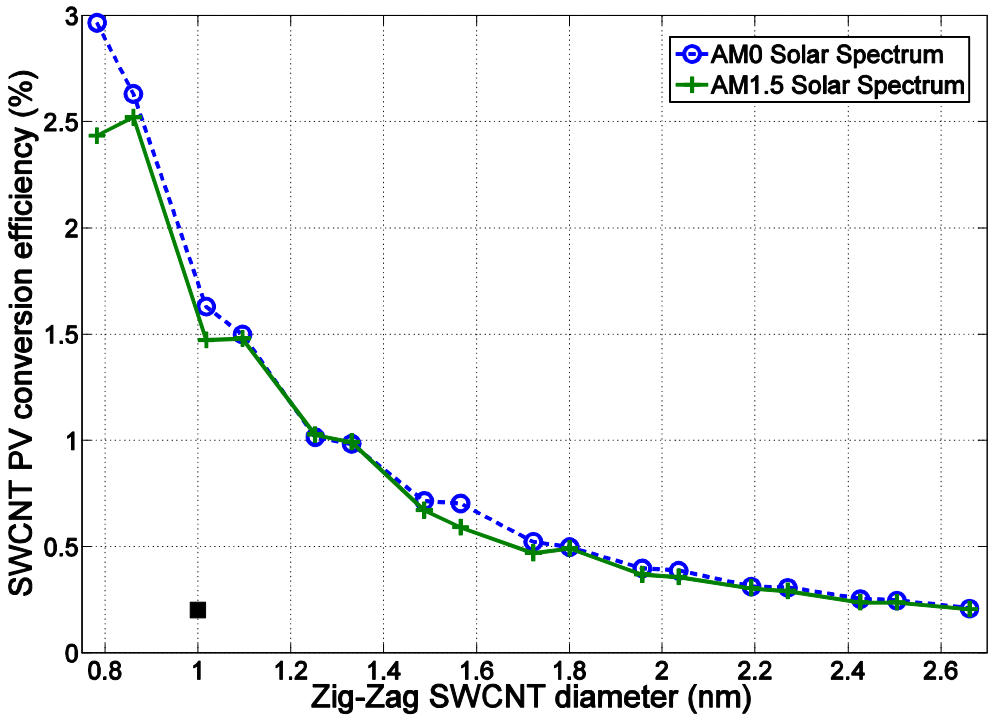

Figure 7-9: Simulated PV conversion efficiency vs. zig-zag SWCNT diameter for the AM0 and AM1.5 solar spectrum. ■ represents the conversion efficiency value experimentally measured by [34].

7.3 Proposed multi-SWCNT PV device simulation and results

In Chapter 2 it was advocated that much needed improvements in SWCNT PV performance may be achieved by employing a network of dissimilar nanotubes where the diversity in band-gap characteristics could lead to higher responsivity. In this section an attempt is made to validate this proposition by simulating and analysing the hypothetical multi-CNT PV device formerly proposed. However, before doing so, first an equivalent circuit model needs to be developed.

7.3.1 Multi-SWCNT PV equivalent circuit model

Earlier it was shown that the hypothetical multi-CNT PV device comprised a large number of vertically aligned semiconducting SWCNTs with distinct structural geometries bridging a common drain and source metal electrode. It was presumed that all SWCNT *pn* junctions are ideally doped and exhibit ultimate rectification behaviour. Hence, the device could be considered as a concatenation of isolated SWCNTs each acting as an ideal PV source. A representative equivalent circuit can be modelled as shown below:

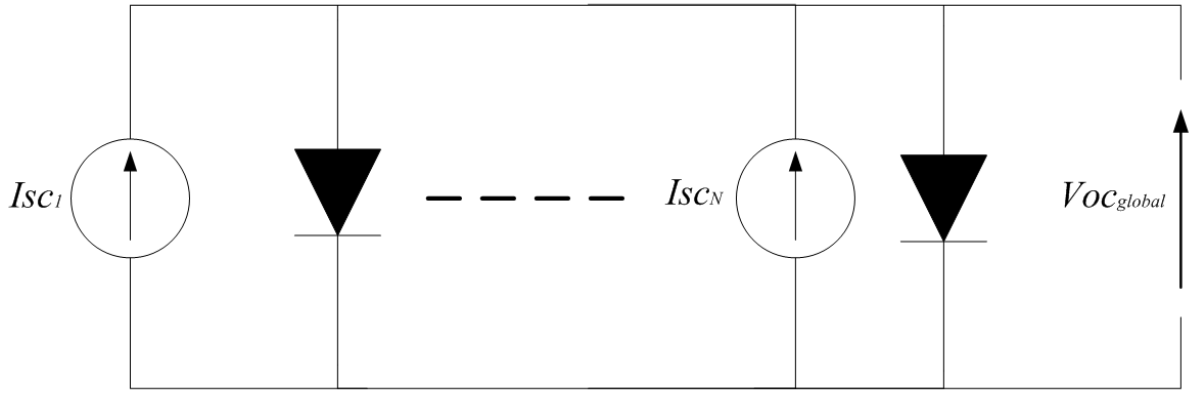

Figure 7-10: Ideal equivalent circuit model of proposed multi-SWCNT PV device.

Figure 7-10 presents a tandem set of *N* ideal equivalent SWCNT PV circuit models connected in parallel feeding a common output terminal. In principle, when this device is subjected to illumination the tubes will absorb photons of various wavelengths according to the multi band-gap distribution. In turn, photogenerated electron-hole pairs in each semiconducting tube will be effectively separated by a built-in potential produced at their respective *pn* junctions. As a consequence, the generated short-circuit current of the individual SWCNTs (I_{scn}) will contribute towards the global cell short-circuit current $I_{scglobal}$ in accord with Eq. 7.7.

$$I_{sc_{global}} = \sum_{n=1}^{N} I_{sc_n} \qquad 7.7$$

Furthermore, when the semiconducting tubes are generating power they will bias each other affecting their respective saturation-currents. This biasing can be taken into account by considering that the minimum open-circuit voltage of all the SWCNTs appears across the unloaded output terminals of the global cell ($V_{ocglobal}$) as articulated by Eq. 7.8. This is

because, in general, when a string of power sources are connected in parallel, the potential across the combination is dictated by the smallest bias [36]. Since the SWCNT PVs are ordered, with that possessing the highest band-gap (V_{oc}) nearest to the light source and the lowest located at the furthest end, then the final SWCNT PV will impose its open-circuit voltage (V_{ocN}) upon the global open-circuit voltage.

$$V_{oc_{global}} = Min\ (V_{oc_n}) = V_{oc_N} \qquad 7.8$$

On top of the assumptions made in sub-section 7.1.1, one final critical conjecture relating to the incident light experienced by each SWCNT within the device is included. Given that most of the power absorbed by a CNT takes place at photon energies corresponding to the band-to-band transitions, it could be assumed that the solar spectrum interacting with a given SWCNT is equivalent to that witnessed by the preceding nanotube less any power absorbed precisely at the inter-band transition energies of the latter tube. That is, if the incident solar spectrum of nanotube *n* can be represented by $\phi_n(E_p)$, then:

$$\phi_n(E_p) \approx \phi_{n-1}(E_p) - \phi_{n-1}(E_p)\sum_i \delta_{n-1}(E_{ii}) \qquad 7.9$$

where $\delta_{n-1}(E_{ii})$ denotes a delta function (with a 0.1 eV width) positioned at the inter-band transition energies E_{ii} of the preceding tube *n-1*. This simplification assumes, firstly, that once it has interacted with a nanotube, the solar spectrum power is fully absorbed at the corresponding E_{ii} energies. Secondly, it is presumed that the spectrum power at photon energies outside the tubes' inter-band transition energies remains unaltered.

7.3.2 Simulating the multi-SWCNT PV device conversion efficiency

The circuit model of Figure 7-10 was first simulated with only two zig-zag SWCNTs (N=2). Eq. 7.7 and 7.8 were used in calculating the new conversion efficiency of the solar cell device for each combination of (m,0) nanotubes.

Table 7-1 reveals the conversion efficiency results under an (a) AM0 (b) AM1.5 solar spectrum with respect to the zig-zag CNT indices: *m*. The row based *m* index represents the zig-zag SWCNT located nearest to the light source and the column based index denotes the nanotube at the rear of the first.

(a)

m	10	11	13	14	16	17	19	20
10	4.5078	5.3457	4.1947	4.2281	3.3000	3.4429	2.7731	2.5039
11	-	4.1167	3.6192	3.7258	2.9818	3.0459	2.5305	2.4607
13	-	-	2.5695	3.0306	2.4482	2.4744	2.0910	2.1075
14	-	-	-	2.3508	2.1444	2.2635	1.8538	1.9469
16	-	-	-	-	1.5911	1.9352	1.5936	1.5548
17	-	-	-	-	-	1.5503	1.5064	1.5399
19	-	-	-	-	-	-	1.1668	1.3839
20	-	-	-	-	-	-	-	1.1415

(b)

m	10	11	13	14	16	17	19	20
10	4.0175	4.9904	3.7129	3.9014	3.0479	3.1964	2.4712	2.1881
11	-	4.1305	3.4257	3.6964	2.9876	3.0494	2.4508	2.3504
13	-	-	2.3651	2.8980	2.3655	2.3955	1.9524	1.8651
14	-	-	-	2.2698	2.1287	2.2684	1.8046	1.7952
16	-	-	-	-	1.5741	1.9253	1.5603	1.4293
17	-	-	-	-	-	1.5047	1.4572	1.4162
19	-	-	-	-	-	-	1.0796	1.2311
20	-	-	-	-	-	-	-	1.0028

Table 7-1: Conversion efficiency (%) for a PV device containing two (*m*,0) zig-zag SWCNTs under an (a) AM0 and (b) AM1.5 solar spectrum illumination.

In Table 7-1 (a) and (b) it is observed that the maximum conversion efficiencies (highlighted) occur with a (10,0) nanotube followed by an (11,0) SWCNT. This is a sensible result given that these particular CNTs offer the largest open-circuit voltages (see Figure 7-5) whilst the combined short-circuit current is relatively high compared to that produced by a (10,0) followed by another (10,0) nanotube due to the lack of photo-absorption experienced by the shadowed tube. Hence, the prescribed interaction caused by the CNT upon the transmitted solar radiation has evidently taken effect. Most importantly, we note a near doubling of conversion efficiency compared to the isolated SWCNT case, which provides a very good indication that multiple CNTs within a PV device significantly enhance performance. However, this is only true if the tubes are chosen to precisely match the optimised geometrical structures stated above, because, as can be seen in Table 7-1, the efficiency noticeably deteriorates for other geometries.

The above simulation is repeated for N=3-7 considering all possible zig-zag CNT combinations. Figure 7-11 depicts the maximum resulting conversion efficiency and the corresponding CNT indices. It could firstly be seen that the multi-SWCNT PV efficiency increases linearly at a rate of 1.5% per N nanotubes within the PV cell under both the AM0 and AM1.5 solar spectrum. Despite the fact that $V_{ocglobal}$ is maintained at a high 0.84V throughout, the increase in power efficiency can be attributed to the linear rise in $I_{scglobal}$ with the number of CNTs.

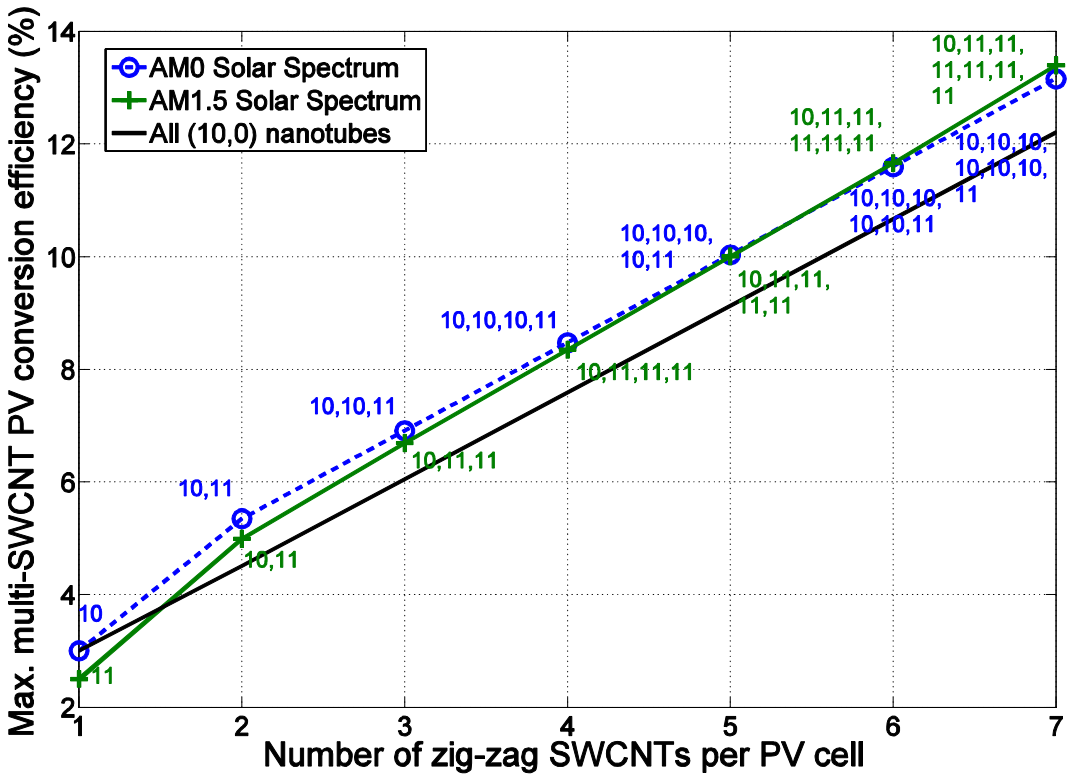

Figure 7-11: Simulated maximum conversion efficiency for each tandem SWCNT PV cell where N=1-7. Corresponding zig-zag tube indices are adjacent to the efficiency value. Also included is the efficiency curve for an all (10,0) nanotube tandem cell under an AM0 solar illumination.

Figure 7-11 demonstrates that the (10,0) and (11,0) are the most favoured nanotubes for solar absorption mainly because they exhibit by far the largest band-gap and hence the optimal $V_{ocglobal}$. Additionally, these specific geometries reappear multiple times within the same PV cell because they still generate a sizable photo-current, even if preceded by the exact same nanotube, due to the absorption of photons with energies that lie just outside the corresponding inter-band transitions. This is a limitation caused by our model since it assumes that power is only absorbed at the band-to-band transition energies and not at nearby energies as well. Interestingly, the (11,0) nanotube appears more frequently for the AM1.5

spectrum over the (10,0) CNT since the (11,0) nanotube generates a marginally higher short-circuit current compared to the (10,0) CNT under an AM1.5 illumination (refer to Figure 7-4). This does not occur at the expense of a lower $V_{ocglobal}$ since both the (10,0) and (11,0) nanotubes almost have the same open-circuit voltage.

The efficiency curve for an all (10,0) nanotube tandem PV cell under AM0 illumination is also incorporated in Figure 7-11 for comparison. It is observed that the all (10,0) nanotube trend line increases at rate matching the optimal curve produced by the combination of (10,0) and (11,0) nanotubes exposed to AM0 illumination. The only difference is a minor constant downshift in conversion efficiency which is in the order of 1%. The implications of this finding suggests that having multiple band-gap CNTs in a PV cell does not provide a substantial benefit over CNTs that exhibit the same band-gap which is maximised.

Thus, according to our study the inclusion of more semiconducting SWCNTs with *specific geometrical structures* does act favourably upon the ideal performance of a CNT based PV device. However, our model demonstrates that it is not essential to adopt a multi-band-gap CNT regime in order to optimise conversion efficiency so long as the band-gap of the nanotubes is maximised (diameter is minimised).

7.4 Summary

In this chapter the ideal performance of various SWCNT based solar cells was evaluated under solar light radiation. A number of assumptions are initially defined where the ideal PV equivalent circuit model is selected as the foundation of our CNT based PV device analysis.

The quantum efficiency model created in the previous chapter is employed to calculate the generated short-circuit current (I_{sc}) of 154 distinct semiconducting SWCNT solar cells under the AM0/1.5 solar spectrum. The outcome of this demonstrated that current steps occurred at intervals matching the resonant band-to-band transitions energies of the corresponding nanotube, which is in agreement with experimental measurements made in [26]. Additionally, it was deduced that since the short-circuit current is dependent on the QE magnitude, then the carrier effective mass of each interband transition must play a contributing factor in defining the height of each current step. This finding has not been

detected in prior literature. Having further analysed the short-circuit current with respect to the nanotube diameter and chirality it was illustrated that zig-zag SWCNTs have an appreciably higher I_{sc} compared to chiral nanotubes, implying that chiral CNTs are unsuitable for PV conversion. It was also discovered that I_{sc} experiences a slight decline with respect to the zig-zag nanotube diameter, although, not appreciably.

By focusing the remainder of our study on zig-zag tubes, the associated open-circuit voltage, saturation-current and fill factor were simulated. Assuming that $V_{oc}=E_g$, the dependence of V_{oc} on d is shown to be consistent with our previously derived relationship $V_{oc}=E_g=0.692/d$. Further, the saturation-current is revealed to rise exponentially with the zig-zag SWCNT diameter, which is a direct consequence of the V_{oc} (E_g) decline. Conversely, the FF is observed to reduce with diameter, possessing values in the range: 0.963-0.9, which is excessively high as a result of the ideal assumptions made. Nevertheless, this is comparable with the predicted value of FF>0.8 claimed in [34].

Irrespective of the incident solar spectrum, the power conversion efficiency of the analysed zig-zag SWCNT PV devices is found to drop dramatically from ~2.5% for a sub-1 nm CNT to <0.5% for nanotubes greater than 1.8 nm. This is in good agreement with recommendations made in [34] where it was argued that SWCNTs having diameters around 0.8 nm would offer significant improvements in PV conversion efficiency due to the larger band-gap [46]. That said, our conversion efficiency are found to be appreciably high considering that the modelled QE's are as low as 0.18. This can be attributed to the idealistic assumptions made in our study that have caused the reporting of a 7x enhancement in our performance at d=1 nm compared to the experimentally measured result in [34] (see Figure 7-9).

In the final section of the chapter an equivalent circuit model is established for the hypothetical multi-bandgap SWCNT PV device defined at the end of Chapter 2 (shown in Figure 2-22). This is exploited towards analysing the power conversion efficiency with respect to different combinations of (m,0) nanotubes within the solar cell. It is demonstrated that the multi-SWCNT PV efficiency increases linearly with the number of nanotubes (N) per PV cell.

Thus, according to our study the inclusion of more semiconducting SWCNTs with *specific geometrical structures* does act favourably upon the ideal performance of a CNT based PV device. However, our models demonstrate that it is not essential to adopt a multi-band-gap CNT regime in order to optimise conversion efficiency so long as the band-gap of the nanotubes is maximised (diameter is minimised).

Chapter 8 Conclusion and Future Work

The overall aim of this thesis was to numerically analyse the effects of CNT diameter and chirality variation upon the resulting band-gap, carrier effective mass and optical absorption properties. In addition, these parameters were to be exploited towards identifying the conversion efficiency of an isolated and conceptually originated multi-band-gap SWCNT PV device. To meet this aim, a quantum mechanical approach was adopted whereby the SWCNT band-gap, carrier effective mass, photo-current and quantum efficiency spectral responses were extracted. During this process, simulation-efficient and accurate models were created for the band-gap and carrier effective mass. Furthermore, attempts were made in statistically modelling their variation with respect to typical uncertainties in the geometric distributions. A novel technique was subsequently developed in calculating the optical absorption properties of CNTs, which were utilised in combination with an equivalent PV circuit model to evaluate the performance metrics of isolated CNT based PV devices under solar radiation. A proposed set of mulit-band-gap CNT PV devices were also analysed where the optimal CNT structures for PV conversion are identified.

This chapter presents a summary of the work accomplished in this thesis and offers recommendations for future work. Specifically, this chapter is divided into two sections; Conclusions and key contributions and Future work.

8.1 Conclusions and key contributions

In Chapter 1 the main objective of this thesis was clearly stated as follows:

"The primary aim of this thesis is to develop novel computational methodologies that characterise the electronic and optical properties of SWCNTs with respect to their geometrical structure variability. Further, the methodologies created will be utilised in identifying the theoretical limiting performance achieved by an isolated and tandem SWCNT based solar cell. The chief outcome of this analysis will be to define the optimal nanotube geometrical properties that deliver the highest conversion efficiencies within the confines of the assumptions made. Ultimately, this study should supplement experimental efforts in the evaluation of nano-structured solar cells."

In Chapter 2 a comprehensive discussion was initially introduced pertaining to the operation of present-day bulk solar cells. The associated technology limitations as well as potential solutions were additionally covered. Subsequently, an up-to-date literature review of Carbon Nanotube (CNT) based devices and photodiodes was imparted, highlighting their strengths and shortcomings. The chapter was finalised with the proposal of a conceptual multi-band-gap SWCNT Photovoltaic (PV) device upon which we further examine in Chapter 7. In order to achieve the thesis objective, the author firstly examined the effects of the CNT diameter and chirality variation upon the corresponding band-gap, electronic transport and optical absorption properties, which are all extracted directly from the nanotube band-structure.

Chapter 3 presents a detailed account of the chosen technique employed in realising the SWCNT band-structure for various geometrical structures. It was decided that the tube band-structure would be best reproduced by utilising the semi-empirical third nearest-neighbour Tight-Binding (TB) model in conjunction with the Zone Folding (ZF) method established in [80]. This is because, according to [80], the agreement between the third-nearest TB electronic dispersion and *ab initio* calculations is better than 250 meV for all wavevectors k within the first Brillouin zone. This is of paramount importance when evaluating the transition energies and optical absorption across the entire nanotube band-structure [80]. It is further confirmed from the simulation of arbitrary SWCNT band-structures that a nanotube can indeed exhibit either metallic or semiconducting characteristics depending on its geometrical properties. At the end of the chapter it is verified that semiconducting SWCNTs

do indeed possess a direct band-gap where the conduction band minima is depicted to be symmetric with the valence band maxima.

In Chapter 4, a novel analytical model is presented that predicts the SWCNT band-gap directly from its diameter (d) and chiral angle (θ) with a runtime independent of tube size [99, 123]. This model was derived from the simulated band-structures of 286 distinct nanotubes. It is demonstrated that the proposed analytical band-gap model accurately distinguishes 93% of a set of metallic and semiconducting CNTs. Additional validation was performed by comparing the developed differentiation model against two separate sources of experimental characterisation data (STS and STM) where 14 out of 17 tubes were correctly identified. In addition, the NRMS band-gap error recorded for semiconducting tubes was only 1.75% offering an overlap energy constant of γ_0 =2.44eV. It is revealed that this value better matched first principle as well as experimental results compared to the nearest-neighbour approach, providing further evidence to support our decision in taking account of more distant neighbours within our TB calculations.

The second part of the chapter covered the derivation of novel analytical expressions based on the parabolic EFM estimation of the simulated band dispersions. This proposed model directly resolved the carrier effective mass of an isolated SWCNT with any chirality and diameter >1 nm and possesses a runtime independent of the tube size [123]. It is discovered that there exist two distinct effective mass trend lines for achiral semiconducting tubes, where the geometrical structure conditions and slopes are defined. In comparison to the simulated data points, the proposed trend models are found to predict the effective mass with an NRMS error of 5.91% and 1.78%, respectively. Additionally, it was shown that other previously reported effective mass models for achiral SWCNTs agree well with our expressions, especially for larger diameters. Finally, the RSM regression technique is employed to formulate an expression for the carrier effective mass of achiral as well as chiral tubes where a low NRMS error of 9.73% is achieved. This is a good approximation given the nonlinear relationship between the effective mass and chiral angle.

Since synthesising SWCNTs with accurate structural control has been widely acknowledged as an exceedingly complex task culminating in the realisation of CNT devices with uncertain electronic behaviour, in Chapter 5, a statistical approach is applied in

predicting the SWCNT band-gap and effective mass variation for typical uncertainties associated with the tube structure [123].

By defining realistic spreads for the geometric structure of CNTs grown using the CVD method and in exploiting the band-gap and effective mass models developed in Chapter 4, a set of extensive Monte Carlo simulations are executed in order to realise the associated distributions. In turn, the RSM regression technique is utilised in establishing novel simulation-efficient and accurate models that predict the variation in CNT band-gap and effective mass for different structural dispersions. Furthermore, the generated models are compared and analysed for 3 distinct case scenarios including:

- The diameter variation is *independent* of the mean diameter
- The diameter variation *scales-up* with the mean diameter
- The diameter variation *scales-down* with the mean diameter

The implications of our Monte Carlo results advocate that CNT synthesis processes have to be optimised in minimising the diameter variability (d_σ) as well as increase the mean diameter (d_μ) to suppress band-gap and carrier effective mass variations. Specifically, it is demonstrated that under all three case scenarios the band-gap variability is always directly proportional to the diameter variation and is almost inversely related to the square of the mean diameter. However, for the carrier effective mass variation an observable change amongst the three scaling scenarios is observed in the inverse relationship with the mean diameter. Also, given that the effective mass variation increases exponentially with diameter variability we stress on this critical sensitivity.

In our aim towards building a SWCNT PV device model, in Chapter 6, we first address the process of photo-current generation in a SWCNT and adopt a novel approach in realising the related optical absorption properties under laser illumination. This approach is based on calculating the optical Transition Rate (TR) using the third-nearest neighbour TB and ZF approximation of the CNT band-structure. Notably, it is assumed that the incident light is always polarised parallel to the nanotube axis and that the dielectric properties can be described by vacuum conditions.

The SWCNT optical TR is initially employed in formulating the photo-current spectral response where a series of distinct narrow peaks within tens of pico-amps ensue. It is shown that this is due to the resonant band-to-band transitions associated with the SWCNT sub-bands, which *qualitatively* agree with previous experimental [59, 60, 128] and theoretical [64, 67, 92, 132, 133] findings. Additionally, it is revealed that the optical absorption strongly depends on nanotube chirality with higher photo-current peaks arising for smaller diameter tubes [132, 133]. The modelled photo-current is also confirmed to possess a linear dependence on the incident optical power, closely matching experimental results obtained in [34]. Next, the Quantum Efficiency (QE) spectra is derived from the SWCNT photo-current where it is discovered that the peak values are highly sensitive to the carrier effective masses of the corresponding band transitions. In fact, when comparing the QE height values of the first interband transitions for the zig-zag nanotubes, it is observed that the QE generally declines with diameter since the effective masses for E_{11} also decrease with diameter (see Chapter 4). However, the observation that (m,0) zig-zag tubes with m=3p+1 (low effective mass) having higher QE peaks compared to zig-zag tubes with m=3p+2 (high effective mass) encourages us to believe that the carrier effective mass is *not the only factor* dictating the quantum efficiency peak values. Later, the generated QE spectra of three nanotubes are compared against theoretical and experimental data, the outcome of which demonstrated some agreement although not entirely. Crucially, it is found that the overall maximum quantum efficiencies (~0.05-0.18) occur chiefly for zig-zag SWCNTs (chirality = 0^0) with low diameters. Other nanotubes are found to experience very little photo-absorption, offering quantum efficiencies in the order of 0.02 or lower. These findings have not been discovered in prior literature and offer an insight on the optimal SWCNT structural properties required for photo-detection and photovoltaic purposes.

The objective of this thesis is ultimately tackled in Chapter 7 where the PV conversion efficiency is analysed for a set of distinct semiconducting nanotube devices under solar light radiation.

Initially, a framework of assumptions is outlined, where the ideal PV equivalent circuit model is selected as the foundation of our CNT based solar cell analysis. The quantum efficiency model created in the previous chapter is taken advantage of in generating the short-circuit current (I_{sc}) of 154 distinct semiconducting SWCNT solar cells when exposed to the

AM0 and AM1.5 solar spectrum. The outcome of this demonstrated that current steps occurred at intervals matching the resonant band-to-band transitions energies of the associated nanotube, which is in agreement with experimental measurements made in [26]. Additionally, it is deduced that since the short-circuit current is dependent on the QE magnitude, then the carrier effective mass of each interband transition must play a contributing factor in defining the height of each current step. This finding has not been detected in prior literature. Having further analysed the short-circuit current with respect to the nanotube diameter and chirality it was illustrated that zig-zag SWCNTs have an appreciably higher I_{sc} compared to chiral nanotubes, implying that chiral CNTs are unsuitable for PV conversion. It was also discovered that I_{sc} experiences a slight decline with respect to the zig-zag nanotube diameter, although, not appreciably.

By focusing the remainder of our study on zig-zag tubes, the related open-circuit voltage, saturation-current and fill factor are simulated. Assuming that $V_{oc}=E_g$, the dependence of V_{oc} on d is shown to be consistent with our previously derived relationship $V_{oc}=E_g=0.692/d$ (see Chapter 4). Further, the saturation-current is shown to rise exponentially with the zig-zag SWCNT diameter, which is a direct consequence of the V_{oc} (E_g) decline. Conversely, the FF is observed to reduce with diameter, possessing values in the range: 0.963-0.9, which is excessively high as a result of the ideal assumptions made. Nevertheless, this is comparable with the predicted value of FF>0.8 claimed in [34].

Irrespective of the incident solar spectrum, the power conversion efficiency of the analysed zig-zag SWCNT PV devices is found to drop dramatically from ~2.5% for a sub-1 nm CNT to <0.5% for nanotubes greater than 1.8 nm. This is in good agreement with recommendations made in [34] where it was argued that SWCNTs having diameters around 0.8 nm would offer significant improvements in PV conversion efficiency due to the larger band-gap [46]. That said, it is found that our conversion efficiencies are appreciably high considering that the modelled QE's are as low as 0.18. This can be attributed to the idealistic assumptions made in our study that have caused the reporting of a 7x enhancement in our performance at d=1 nm compared to the experimentally measured result in [34].

In the final section of the chapter an equivalent circuit model is established for the hypothetical multi-bandgap SWCNT PV device defined at the end of Chapter 2. This is

exploited towards analysing the power conversion efficiency with respect to different combinations of (m,0) nanotubes within the solar cell. It is demonstrated that the multi-SWCNT PV efficiency increases linearly with the number of nanotubes (N) per PV cell.

Thus, according to our study the inclusion of more semiconducting SWCNTs with *specific geometrical structures* does act favourably upon the ideal performance of a CNT based PV device. However, our models demonstrate that it is not essential to adopt a multi-band-gap CNT regime in order to optimise conversion efficiency so long as the band-gap of the nanotubes is maximised (diameter is minimised).

In conclusion, considering the assumptions made in this study it can be reasoned that *low-diameter zig-zag* SWCNTs may yield competitive PV conversion efficiency compared to other nanotechnology based solar cells. However, given that the quantum efficiencies calculated are in the order of <0.2, we maintain our reservations on whether it could outperform bulk PV materials. Notably, the challenge of synthesising SWCNTs with precise geometries would be beyond the reach of present-day fabrication technology, thus, deeming the proposed device unattainable. Nevertheless, the models presented in this thesis should provide a good starting point for further investigating the feasibility of a SWCNT PV device.

The key contributions of this work have resulted in the publications listed in Appendix D and could be articulated in the following points:

- A simulation-efficient and accurate analytical model has been created to distinguish metallic and semiconducting nanotubes and predict the band-gap of semiconducting CNTs. Moreover, a separate analytical model that approximates the semiconducting CNT's carrier effective mass is developed [99] [123].

- The variation in CNT band-gap and carrier effective mass is statistically modelled for typical uncertainties in the geometrical structure. This offered a valuable insight on the optimisation of diameter related process parameters towards suppressing electronic variability [123].

- A novel approach is adopted in calculating the photo-generated current and quantum efficiency spectral responses of CNT with various tube geometries. It is found that the overall maximum quantum efficiencies occur chiefly for zig-zag SWCNTs with low diameters.

- The established quantum efficiency model is combined with an equivalent PV circuit model to evaluate the performance metrics of isolated CNTs as well as multi-CNT PV devices under solar radiation. This revealed the optimal CNT structures for PV conversion.

The analytical models developed in this work may facilitate the experimental research of CNTs in a number of ways. First, the band-gap variation models proposed in Chapter 5 could potentially be utilised in defining the mean diameter and standard-deviation of the catalyst nano-particles needed in order to synthesis CNTs with a required band-gap variation. Secondly, the photo-current and quantum efficiency models proposed in Chapter 6 could be employed in characterising the diameter and chirality of CNTs by comparing them with the measured photo-absorption spectra. Thirdly, researchers looking to realise a CNT photovoltaic device may consider adopting structural geometries matching those advocated in Chapter 7 in order to achieve optimal conversion efficiencies.

8.2 Future work

Suggestions for future work mainly rest upon refining the CNT models developed whilst carrying out substantial experimental validation.

8.2.1 SWCNT model refinements

From a CNT modelling perspective, several refinements to the existing methodologies can be made. For instance, given that the CNT band-gap and carrier effective mass models produced here are dependent upon the realisation of the nanotube band-structure using the third nearest-neighbour TB approximation, it would be interesting to include more distant neighbours for future work. This may provide better accuracy especially in handling the

curvature effect of low diameter CNTs where the σ-π rehybridization becomes more prominent.

An *ab initio* approach could also be adopted in modelling the CNT optical absorption spectra where excitonic effects are considered. This should offer an enhanced representation of the SWCNT photo-current spectra with respect to different geometrical structures, light polarisation angles as well as various dielectric properties of the surrounding environment. Moreover, with the atomistic *ab initio* technique the effects resulting from topological or substitutional defects can be included. Although, this comes at a high computational cost.

The equivalent PV circuit model used in this thesis can be further refined to incorporate e-h pair recombinations, collection losses due to doping imperfections and contact resistances. In addition, it would be beneficial to take account of the wave scattering effects and radiative coupling between the SWCNTs in the proposed tandem PV device. This may entail a quantum mechanical treatment of individual CNTs which is coupled with classical electromagnetic scattering models in order to assist the design and optimisation of SWCNT based solar cells.

8.2.2 Experimental validation

Unfortunately, in this thesis, no experimental work was carried out, which meant that the author could only rely on the little data previously published by other groups to provide some form of credibility to the CNT models developed. For example, it would be valuable to use different characterisation techniques (*e.g.* resonant Raman spectroscopy, STS or STM) to identify the SWCNT diameter and chirality distributions of a CVD processed batch and ascertain the corresponding band-gap dispersion. This would provide crucial evidence in supporting the established band-gap variation models.

So far, studies on the photo-current responses of SWCNTs have been limited. Therefore, it would be very helpful to perform photo-absorption measurements on various SWCNT samples and compare them with the spectral responses simulated by our approach. This would further clarify whether a band-to-band transition model may be used to reasonably approximate the optical excitations. Importantly, these experimental measurements can further provide an improved insight on the corresponding quantum

efficiencies and the optimal CNT structural properties needed for photo-detection and photovoltaic purposes.

The most ideal, but most challenging experimental validation, would be to fabricate an isolated zig-zag CNT based PV device with electrostatic doping (as in [34]) in the first instance and then a multi-SWCNT device that could be inserted inside a solar simulator. The short-circuit current, open-circuit voltage, fill factor and conversion efficiency measurements may then be directly compared with the results originated in this study.

Appendix A: Solving Non-ideal PV Equivalent Circuit Model using the Newton-Raphson Approximation

The Newton-Raphson technique is a root-finding routine that consists of extending the tangent line of a function $f(x_i)$ at the current point x_i until it crosses zero and then setting the next guess x_{i+1} to the abscissa of that zero-crossing [35]. Algebraically, the method is derived from the Taylor series expansion and is specified by the following formula [35]:

$$x_{i+1} = x_i - \frac{f(x_i)}{f'(x_i)} \qquad \text{A.1}$$

where $f'(x_i)$ is the first derivative of $f(x_i)$ [35]. Eq. A.1 is calculated iteratively until the absolute difference between two successive values of a given iteration converges to zero.

In the case of solving for the non-ideal PV circuit model of Chapter 2, the implicit function 2.22 ($f(J_i(V),V)=0$) is considered and the root of interest is defined as the output current density $J_{i+1}(V)$ for a given voltage. Therefore, the Newton-Raphson formula can be re-stated as follows:

$$J_{i+1}(V) = J_i(V) - \frac{f(J_i(V),V)}{\frac{\partial f(J_i(V),V)}{\partial J}} \qquad \text{A.2}$$

This algorithm was evaluated using the PV cell example given in Chapter 2 (J_{sc} = 50mA/cm^2, J_{sat} = 0.5 nA/cm^2, n = 1 and T =300K) where R_s=0 and R_{sh}=∞. The output current density was generated over the voltage range -0.2V—0.6V by setting the initial guess value

to $J_0(V)=J_{sc}$ and executing Eq. A.2 until the condition $|J_{i+1}(V)-J_i(V)|<10^{-15}$ was satisfied. When the outcome was compared to the ideal circuit model *J-V* characteristic, the resulting Normalised Root-Mean-Square (NRMS) error was calculated to be 0.00052%, which is sufficiently accurate for our purpose.

Appendix B: Matlab Code for Solving SWCNT Band Structure

```
function min_band_gap = sim_nanotube_bandstructure(d, theta_degrees)

format long

a_0 = 0.142*sqrt(3);     % working in nm
theta = theta_degree*pi/180; %convert degrees into rad
number_of_samples = 2000;

e_2p = -0.28;       %Define 3rd nearest-neighbour TB coefficients
L_0 = -2.97;
s_0 = 0.073;
L_1 = -0.073;
s_1 = 0.018;
L_2 = -0.33;
s_2 = 0.026;

term1 =((sqrt(3)/tan(theta))-1);

%convert geometrical structure into tube indices
if isinf(term1)
    m=0;
    n= round((pi*d)/a_0);
else
    n = round((pi*d)/(a_0*sqrt(1+0.25*(term1^2)+ 0.5*term1)));
    m = round((n/2)*term1);
end

% setup translation vector T
d_R = gcd((2*m+n),(2*n+m));
N = 2*((m^2)+ m*n + (n^2))/d_R; %Number of primitive graphene unit cells
per CNT unit cell
t_1 = (2*n+m)/d_R;
t_2 = -(2*m+n)/d_R;

if isinf(N)|isnan(N)
   return;

end

% initialize variables
```

```
band_gaps = zeros(1,N);
k_x = zeros(number_of_samples,N);
k_y = zeros(number_of_samples,N);
E_k_pos = zeros(number_of_samples,N);
E_k_neg = zeros(number_of_samples,N);

%3rd nearest-neighbour TB + ZF technique for calculating CNT band-structure
for sample = 1:number_of_samples

    %compute bands along kx-axis
    k_x(sample,1) = ((4*pi)/(3*a_0))*(sample/number_of_samples);    %
allowable electron states along kx

    for q=1:N

            %compute bands along ky-axis
            k_y(sample,q) = -((m-n)/((m+n)*sqrt(3)))*k_x(sample,1)+
(4*pi*q)/(a_0*sqrt(3)*(m+n));      % allowable electron states along ky

            f_k =
(2*cos((a_0*k_y(sample,q))/(2*sqrt(3)))*cos((a_0*k_x(sample,q))/2)+cos((a_0
*k_y(sample,q))/sqrt(3))) + ...

i*(2*sin((a_0*k_y(sample,q))/(2*sqrt(3)))*cos((a_0*k_x(sample,q))/2)-
sin((a_0*k_y(sample,q))/sqrt(3)));
            u_k =
4*cos((a_0*k_x(sample,q))/2)*cos((a_0*sqrt(3)*k_y(sample,q))/2)+2*cos(a_0*k
_x(sample,q));
            f_2k = cos((2*a_0*k_y(sample,q))/sqrt(3)) +
2*cos(a_0*k_x(sample,q))*cos((a_0*k_y(sample,q))/sqrt(3)) + ...
                i*(sin((2*a_0*k_y(sample,q))/sqrt(3))-
2*sin((a_0*k_y(sample,q))/sqrt(3))*cos(a_0*k_x(sample,q)));
            g_k = 2*u_k + 2*cos(sqrt(3)*a_0*k_y(sample,q)) +
4*cos((3*a_0*k_x(sample,q))/2)*cos((a_0*sqrt(3)*k_y(sample,q))/2);

            a = ((1 + s_1*u_k)^2) - (s_0^2)*(abs(f_k)^2) - s_0*s_2*g_k -
(s_2^2)*(abs(f_2k)^2);
            b = 2*L_0*s_0*(abs(f_k)^2) - 2*(e_2p+L_1*u_k)*(1 + s_1*u_k) +
s_2*L_0*g_k + s_0*L_2*g_k + 2*s_2*L_2*(abs(f_2k)^2);
            c = ((e_2p+ L_1*u_k)^2) - (L_0^2)*(abs(f_k)^2) - L_0*L_2*g_k -
(L_2^2)*(abs(f_2k)^2);

            E_k_pos(sample,q) = (-b+sqrt((b^2)-(4*a*c)))/(2*a);
            E_k_neg(sample,q) = (-b-sqrt((b^2)-(4*a*c)))/(2*a);

    end

end

%band-gap calculation
band_gaps = min(E_k_pos)-max(E_k_neg);
min_band_gap = min(band_gaps)

if min_band_gap <= 0.01

    min_band_gap = 0
end
```

Appendix C: Matlab Code for Solving SWCNT Photo-current and Quantum Efficiency Spectral Response

```
function [photocurrent_1,quantum_efficiency] =
calc_nanotube_photocurrent_QE_spectra(theta_degree,d,tube_length,
field_strength,photon_energies)

%Initialize constants
planks_constant = 6.582e-16;
electron_charge = 1.60217646e-19;
rest_mass_electron = 9.109e-31;
speed_of_light= 299792458;
dielectric_constant = 1;                % dielectric constant of CNT = 1
permittivity_free_space = 8.8542e-12;
refractive_index = 1;
k_B=8.6172343e-5;

% Initialize variables
number_of_photon_samples = length(photon_energies);
number_of_samples = 2000;
photocurrent_1 = zeros(number_of_photon_samples,1);
photocurrent_2 = zeros(number_of_photon_samples,1);
Power_generated = zeros(number_of_photon_samples,1);
quantum_efficiency = zeros(number_of_photon_samples,1);
max_conversion_efficiency = zeros(number_of_photon_samples,1);
max_photocurrent = 0;
incident_power_total=0;
generation_rate = 0;
V_oc=0;
saturation_current = 0;

band_gaps = zeros(1,N);
k_x = zeros(number_of_samples,1);
k_y = zeros(number_of_samples,N);
E_k_pos = zeros(number_of_samples,N);
E_k_neg = zeros(number_of_samples,N);
optical_matrix_element = zeros(number_of_samples,N);
```

```
%Initialize CNT constants
a_0 = 0.142*sqrt(3);    % working in nm

theta = theta_degree*pi/180;    %convert degrees into rad

%3rd nearest-neighbour Tight-Binding coefficients
e_2p = -0.28;
L_0 = -2.97;
s_0 = 0.073;
L_1 = -0.073;
s_1 = 0.018;
L_2 = -0.33;
s_2 = 0.026;

M_c = 1;                                % constant dipole matrix element
delta_accuracy = 0.5e-12;

term1 =((sqrt(3)/tan(theta))-1);

%convert geometrical structure into tube indices
if isinf(term1)
    m=0;
    n= round((pi*d)/a_0);
else
    n = round((pi*d)/(a_0*sqrt(1+0.25*(term1^2)+ 0.5*term1)));
    m = round((n/2)*term1);
end

% setup translation vector T
d_R = gcd((2*n+m),(2*m+n));
N = 2*((m^2)+ m*n + (n^2))/d_R;
A_CNT = sqrt(3)*(pi^2)*((d*1e-9)^2)/d_R;
T_mag = sqrt(3)*pi*(d*1e-9)/d_R;

if isinf(N)|isnan(N)
   return;

end

 %3rd nearest-neighbour Tight-Binding technique for calculating CNT band-
structure
    for sample = 1:number_of_samples

        %compute bands along kx-axis
        k_x(sample,1) = ((4*pi)/(3*a_0))*(sample/number_of_samples);

        for q=1:N

            %compute bands along ky-axis
            k_y(sample,q) = -((m-n)/((m+n)*sqrt(3)))*k_x(sample,1)+
(4*pi*q)/(a_0*sqrt(3)*(m+n));   %allowable electron states along ky


            f_k =
(2*cos((a_0*k_y(sample,q))/(2*sqrt(3)))*cos((a_0*k_x(sample,1))/2)+cos((a_0
*k_y(sample,q))/sqrt(3))) +
```

```
i*(2*sin((a_0*k_y(sample,q))/(2*sqrt(3)))*cos((a_0*k_x(sample,1))/2)-
sin((a_0*k_y(sample,q))/sqrt(3)));
            u_k =
4*cos((a_0*k_x(sample,1))/2)*cos((a_0*sqrt(3)*k_y(sample,q))/2)+2*cos(a_0*k
_x(sample,1));
            f_2k = cos((2*a_0*k_y(sample,q))/sqrt(3)) +
2*cos(a_0*k_x(sample,1))*cos((a_0*k_y(sample,q))/sqrt(3)) +
i*(sin((2*a_0*k_y(sample,q))/sqrt(3))-
2*sin((a_0*k_y(sample,q))/sqrt(3))*cos(a_0*k_x(sample,1)));
            g_k = 2*u_k + 2*cos(sqrt(3)*a_0*k_y(sample,q)) +
4*cos((3*a_0*k_x(sample,1))/2)*cos((a_0*sqrt(3)*k_y(sample,q))/2);

            a = ((1 + s_1*u_k)^2) - (s_0^2)*(abs(f_k)^2) - s_0*s_2*g_k -
(s_2^2)*(abs(f_2k)^2);
            b = 2*L_0*s_0*(abs(f_k)^2) - 2*(e_2p+L_1*u_k)*(1 + s_1*u_k) +
s_2*L_0*g_k + s_0*L_2*g_k + 2*s_2*L_2*(abs(f_2k)^2);
            c = ((e_2p+ L_1*u_k)^2) - (L_0^2)*(abs(f_k)^2) - L_0*L_2*g_k -
(L_2^2)*(abs(f_2k)^2);

            E_k_pos(sample,q) = (-b+sqrt((b^2)-(4*a*c)))/(2*a);
            E_k_neg(sample,q) = (-b-sqrt((b^2)-(4*a*c)))/(2*a);

           %calculate Dipole vector
            Dipole_vector_kz = M_c*((m-n)*cos(a_0*k_x(sample,1))-
(2*m+n)*cos((sqrt(3)*a_0*k_y(sample,q)/2)+(a_0*k_x(sample,1)/2))+(m+2*n)*co
s((sqrt(3)*a_0*k_y(sample,q)/2)-
(a_0*k_x(sample,1)/2)))/(2*abs(f_k)*sqrt(m^2 +n^2 + m*n));
            optical_matrix_element(sample,q) = abs(Dipole_vector_kz)^2;

        end
    end

%band-gap calculation
band_gaps = min(E_k_pos)-max(E_k_neg);
[min_band_gaps,min_band_gaps_index] = sort(band_gaps);

if min_band_gaps(1,1) <= 0.01

    minimum_band_gap = 0;
    return;

else
    minimum_band_gap = min_band_gaps(1,1);
    V_oc = minimum_band_gap;

end

%Calculate TR & photo-current and QE spectral response
for counter = 1:number_of_photon_samples

    sum_optical_strength = 0;

    for sample = 1:number_of_samples

        for q= 1:N

            %find conduction and valance band energies and subtract photon-
energy
```

```
            delta_var = abs(E_k_pos(sample,q)-E_k_neg(sample,q)-
photon_energies(counter,1));

            if (delta_var<=0.1)

                %compute delta function
                delta_function =
2*(planks_constant)*(sin(delta_var*delta_accuracy/(2*planks_constant))^2)/(
(delta_accuracy)*(pi)*((delta_var)^2));
            else

                delta_function = 0;
            end
            % sum optical strength for all k in CNT band-structure
            sum_optical_strength = sum_optical_strength +
(optical_matrix_element(sample,q)*delta_function);

        end

    end

    %Calculate Transition Rate for given photon-energy
    TR =
(8*pi*(electron_charge^2)*(field_strength(counter,1))*(planks_constant^3)*(
sum_optical_strength))/((A_CNT)*(rest_mass_electron^2)*(photon_energies(cou
nter,1))*(speed_of_light)*(dielectric_constant)*(permittivity_free_space)*(
refractive_index));

    %Calculate photo-current for given photon-energy
    photocurrent_1(counter,1)=TR*electron_charge*((tube_length*1e-
9)/T_mag);

    %Calculate quantum-efficiency for given photon-energy

quantum_efficiency(counter,1)=(photocurrent_1(counter,1)/electron_charge)/(
(field_strength(counter,1)*d*tube_length*1e-18)/electron_charge);

end
```

Appendix D: Publications

The following lists papers published during the course of this research as well as papers in preparation for submission:

1. K. El Shabrawy, K. Maharatna, D. M Bagnall, B. M Al-Hashimi, “A new analytical model for predicting SWCNT band-gap from geometrical properties”, ICICDT 2008, IEEE International Conference on, Grenoble, France, pp. 211-214, June 2008. *Best Student Paper Award (Silver).*

2. K. El Shabrawy, K. Maharatna, D. M Bagnall, B. M Al-Hashimi, “Modeling SWCNT Band-gap and Effective Mass Variation using a Monte Carlo Approach”, IEEE Transactions on Nanotechnology, vol. 9, issue 2, July 2009.

3. K. El Shabrawy, K. Maharatna, B. M Al-Hashimi, “Exploiting SWCNT structural variability towards the development of a photovoltaic device”, ISIC 2009, Singapore, pp. 248-251, December 2009.

4. K. Maharatna, K. El Shabrawy, B. M Al-Hashimi, “Chapter 8: Energy Harvesting for Bio-Sensing Using Carbon Nanotubes” Nano-Bio-Sensing edited by Sandr Carrara, Springer Science + Business Media, 2011.

5. K. El Shabrawy, K. Maharatna, D. M Bagnall, B. M Al-Hashimi, “Modeling SWCNT based Photovoltaics: A First Approximation”. *In preparation for IEEE Transactions on Nanotechnology.*

References

1. *IEA Key World Energy Statisitics 2009*. 2009, International Energy Agency.
2. MacKay, D., *Sustainable Energy-without the hot air*. 2008: UIT Cambridge.
3. *Global Trends in Sustainable Energy Investment 2009*. 2009, United Nations Environment Programme (UNEP).
4. Tsakalakos, L., *Nanostructures for photovoltaics.* Material Science and Engineering R, 2008. **62**: p. 175-189.
5. *Renewables Global Status Report: 2009 Update*. 2009, REN21 Renewable Energy Policy Network for the 21st Century.
6. Green, M.A., *Third generation photovoltaics: solar cells for 2020 and beyond.* Physica E: Low-dimensional Systems and Nanostructures, 2002. **14**(1-2): p. 67-70.
7. *Highest Silicon Solar Cell Efficiency Ever Reached*, in *ScienceDaily (http://www.sciencedaily.com/releases/2008/10/081023100536.htm)*. 2008.
8. W. Shockley and H. Queisser, *Detailed Balance Limit of Efficiency of p-n Junction Solar Cells.* Journal of Applied Physics, 1961. **32**(3): p. 510-519.
9. A. Goetzberger and C. Hebling, *Photovoltaic materials, past, present, future.* Solar Energy Materials & Solar Cells, 2000. **62**(1): p. 1-19.
10. T. Markvart and L. Castaner, *Practical Handbook of Photovoltaics Fundamentals and Applications*. 2003: Elsevier Limited.
11. Sze, S.M., *Semiconductor Devices, Physics and Technology*. 2002, USA: John Wiley & Sons Inc.
12. A. Marti and G. Araujo, *Limiting efficiencies for photovoltaic energy conversion in multigap systems.* Solar Energy Materials & Solar Cells, 1996. **43**: p. 203-222.
13. USDE, *PV Efficiencies*, in *Wikipedia (http://en.wikipedia.org/wiki/File:PVeff(rev110707)d.png#file)*. 2009, United States Department of Energy.
14. R. Saito, M. S. Dresselhaus, and G. Dresselhaus, *Physical Properties of Carbon Nanotubes*. 1998: Imperial College Press.
15. S. Iijima, *Helical microtubules of graphitic carbon.* Nature, 1991. **354**: p. 56-58.
16. P. McEuen, M. Fuhrer, and H. Park, *Single-Walled Carbon Nanotube Electronics.* IEEE Transactions on Nanotechnology, 2002. **1**(1): p. 78-85.
17. P. Avouris, et al., *Carbon Nanotube Electronics.* Proceedings of the IEEE, 2003. **91**(11): p. 1772-1784.
18. N. Sinha and J.T.-W. Yeow, *Carbon Nanotubes for Biomedical Applications.* IEEE Transactions on Nanobioscience, June 2005. **4**(2).

19. S. M. Sze and K.K. Ng, *Physics of Semiconductor devices*. 3rd ed. 2007: John Wiley & Sons, Inc.
20. H. Zhu, et al., *Applications of carbon materials in photovoltaic solar cells.* Solar Energy Materials & Solar Cells, 2009. **93**: p. 1461-1470.
21. E Kymakis, et al., *Effective mobility and photocurrent in carbon nanotube-polymer composite photovoltaic cells.* Nanotechnology, 2007. **18**(435702): p. 1-6.
22. A. Nieuwoudt and Y. Massoud, *On the Impact of Process Variations for Carbon Nanotube Bundles for VLSI Interconnect.* IEEE Transactions on Electron Devices, 2007. **54**(3): p. 446-455.
23. P. Avouris, M. Freitag, and V. Perebeinos, *Carbon-nanotube photonics and optoelectronics.* Nature photonics, 2008. **2**: p. 341-350.
24. P. Ong, W. Euler, and I. Levitsky, *Hybrid solar cells based on single-walled carbon nanotubes/Si heterojunctions.* Nanotechnology, 2010. **21**(105203): p. 1-7.
25. J. U. Lee, P. P. Gipp, and C.M. Heller, *Carbon nanotube p-n junction diodes.* Appl. Phys. Lett., 2004. **85**(1): p. 145-147.
26. N. Gabor, et al., *Extremely Efficient Multiple Electron-Hole Pair Generation in Carbon Nanotube Photodiodes* Science, 2009. **325**: p. 1367-1371.
27. *Standard G173-03 Tables for Reference Solar spectral Irradiances: Terrestrial Global 37 degree South Facing Tilt & Direct Normal + Circumsolar*. http://rredc.nrel.gov/solar/spectra/am1.5/ 1999 [cited.
28. Nelson, J., *The Physics of Solar Cells*, ed. I.C. Press. 2003, London.
29. Henry, C.H., *Limiting efficencies of ideal single and multiple energy gap terrestrial solar cells.* Journal of Applied Physics, 1980. **51**(8): p. 4494-4500.
30. G. L. Araújo and A. Marti, *Absolute limiting efficiencies for photovoltaic energy conversion.* Solar Energy Materials and Solar Cells, 1994. **33**(2): p. 213-240.
31. S. R. Wenham, et al., *Applied Photovoltaics*. 2007, UK: Earthscan.
32. P. Kittidachachan, T. Markvart, and D. Bagnall, *Optimisation, Design and Fabrication of high Efficiency p-n Junction Solar Cell*, in *PG Conference*. 2003, Electronic and Computer Science, University of Southampton: Southampton.
33. Mazhari, B., *An improved solar cell circuit model for organic solar cells.* Solar Energy Materials & Solar Cells 2006. **90**: p. 1021-1033.
34. Lee, J.U., *Photovoltaic effect in ideal carbon nanotube diodes.* Appl. Phys. Lett., 2005. **87**.
35. W. H. Press, et al., *Numerical Recipes in C: The Art of Scientific Computing*. 1992: Cambridge University Press.
36. I. Dharmadasa, *Third generation multi-layer tandem solar cells for achieving high conversion efficiencies* Solar Energy Materials and Solar Cells, 2005. **85**(2): p. 293-300.
37. G. Konstantatos and E. Sargent, *Nanostructured materials for photon detection.* Nature nanotechnology, 2010. **78**: p. 1-9.
38. Brabec, C.J., *Organic photovoltaics: technology and market.* Solar Energy Materials & Solar Cells, 2004. **83**(2-3): p. 273-292.
39. B. O'Regan and M. Gratzel, *A low-cost, high-efficiency solar cell based on dye-sensitized colloidal TiO_2 films.* Nature, 1991. **353**: p. 737-739.
40. K. Barnham, et al., *Quantum well solar cells.* Physica E, 2002. **14**: p. 27-36.
41. J.C. Rimada, et al., *Conversion efficiency enhancement of AlGaAs quantum well solar cells.* Microelectronics Journal, 2007. **38**: p. 513-518.
42. J. Baxter and E. Aydil, *Nanowire-based dye-sensitized solar cells.* Applied Physics Letters, 2005. **86**(053114): p. 1-3.

43. M. Law, et al., *Nanowire dye-sensitized solar cells.* Nature Materials, 2005. **4**: p. 455-459.
44. Tsakalakos, L., et al., *Silicon nanowire solar cells.* Applied Physics Letters, 2007. **91**.
45. L. Hu and G. Chen, *Analysis of Optical Absorption in Silicon Nanowire Arrays for Photovoltaic Applications.* Nano Letters, 2007. **7**(11): p. 3249-3252.
46. K. El Shabrawy, K. Maharatna, and B.M. Al-Hashimi, *Exploiting SWCNT Structural Variability Towards the Development of a Photovoltaic Device*, in *International Symposium on Integrated Circuits (ISIC).* 2009, IEEE: Singapore.
47. Z. Yang, et al., *Experimental Observation of an Extremely Dark Material Made By a Low-Density Nanotube Array.* Nano Letters, 2008. **8**(2): p. 446-451.
48. A. Luque, A. Marti, and A. Nozik, *Solar Cells Based on Quantum Dots: Multiple Exciton Generation and Intermediate Bands.* MRS Bulletin, 2007. **32**: p. 236-241.
49. Terrones, M., *Science and Technology of the Twenty-First Century: Synthesis, Properties, and Applications of Carbon Nanotubes.* Annual Review of Materials Research, 2003. **33(1)**: p. 419-501.
50. Dai, H., *Carbon nanotubes: opportunities and challenges.* Surface Science 2002: p. 218-241.
51. Klinke, C., *Analysis of Catalytic Growth of Carbon Nanotubes*, in *Institut de physique des nanostructures, Section De Physique*. 2003, École Polythechnique Federale De Lausanne: Lausanne.
52. K. B. Teo, et al., *Catalytic Synthesis of Carbon Nanotubes and Nanofibers.* Encyclopidia of Nanoscience and Nanotechnology, 2003.
53. S.B. Sinnott, et al., *Model of carbon nanotube growth through chemical vapor deposition.* Chemical Physics Letters, 1999. **315**: p. 25-30.
54. C. L. Cheung, et al., *Diameter-Controlled Synthesis of Carbon Nanotubes.* J. Phys. Chem. B, 2002. **106**: p. 2429-2433.
55. R. Martel, et al., *Single and multi-wall carbon nanotube field-effect transistors.* Appl. Phys. Lett., 1998. **73** (17): p. 2447-2449.
56. C. Zhou, et al., *Modulated Chemical Doping of Individual Carbon Nanotubes.* Science, 2000. **290**: p. 1552-1555.
57. A. Hazeghi, T. Krishnamohan, and H.-S.P. Wong, *Schottky-Barrier Carbon Nanotube Field-Effect Transistor Modeling.* IEEE Transactions on Electron Devices, 2007. **54**(3): p. 439-445.
58. Y. Zhang and S. Iijima, *Elastic Response of Carbon Nanotube Bundles to Visible Light.* Phys. Rev. Lett., 1999. **82**(17): p. 3472-3475.
59. M. Freitag, et al., *Photoconductivity of Single Carbon Nanotubes.* Nano Letters, 2003. **3**(8): p. 1067-1071.
60. X. Qiu, et al., *Photoconductivity Spectra of Single-Carbon Nanotubes: Implications on the Nature of Their Excited States.* Nano Letters, 2005. **5**(4): p. 749-752.
61. J. Arranz-Andres and W. Blau, *Enhanced device performance using different carbon nanotube types in polymer photovoltaic devices.* Carbon, 2008. **46**: p. 2067-2075.
62. C. Chen, et al., *Nanowelded Carbon-Nanotube_based Solar Microcells.* Small, 2008. **4**(9): p. 1313-1318.
63. Derek A. Stewart and F. Léonard, *Energy Conversion Efficiency in Nanotube Optoelectronics.* Nano Letters, 2005. **5** (2): p. 219 -222.
64. D. A. Stewart and F. Léonard, *Photocurrents in Nanotube Junctions.* Phys. Rev. Lett., 2004. **93**(10).
65. M. Anantram and F. Léonard, *Physics of carbon nanotube electronic devices.* Reports on Progress in Physics, 2006. **69**(3): p. 507-561.

66. K. Mizunoa, et al., *A black body absorber from vertically aligned single-walled carbon nanotubes.* PNAS, 2009. **106**(15): p. 6044-6047.
67. C. Chen, et al., *Assessment of Optical Absorption in Carbon Nanotube Photovoltaic Device by Electromagnetic Theory.* IEEE Transactions on Nanotechnology, 2009. **8**(3): p. 303-314.
68. M. Bissett and J. Shapter, *Photocurrent Response from Vertically Aligned Single-Walled Carbon Nanotube Arrays.* J. Phys. Chem. C, 2010. **114** (14): p. 6778–6783.
69. Z. Poh, et al., *Fabrication and electrochemical behavior of vertically-aligned carbon nanotube electrodes covalently attached to p-type silicon via a thioester linkage.* Materials Letters 2009. **63**: p. 757-760.
70. M.S. Dresselhaus and H. Dai, *Carbon Nanotubes: Continued Innovations and Challenges.* MRS BULLETIN, 2004: p. 237-243.
71. M. S. Dresselhaus, G. Dresselhaus, and P. Avouris, *Carbon Nanotubes: Synthesis, Structure, Properties and Applications.* April 20, 2001: Springer.
72. D. Qian, et al., *Mechanics of carbon nanotubes.* Appl Mech Rev., November 2002. **55**(6).
73. C. Thomsen, S. Reich, and J. Maultzsch, *Carbon Nanotubes: Basic Concepts and Physical Properties.* 2004: Wiley-VCH.
74. J. R. Hook and H.E. Hall, *Solid state Physics*. June 1995: Wiley.
75. Kittel, C., *Introduction to Solid State Physics*, ed. t. Edition. 1986: Wiley.
76. Slater, J.C. and G.F. Koster, *Simplified LCAO Method for the Periodic Potential Problem.* Physical Review, 1954. **94**(6): p. 1498.
77. C. M. Goringe, D. R. Bowler, and E. Hernández, *Tight-binding modelling of materials* Rep. Prog. Phys., 1997. **60**.
78. Minot, E.D., *Tuning the band structure of carbon nanotubes*. 2004, Cornell University.
79. Hauptmann, J.R., *Spin-Transport in Carbon Nanotubes*, in *Faculty of Science*. 2003, University of Copenhagen.
80. S. Reich, et al., *Tight-binding description of graphene.* Physical Review B, 2002. **66**(3): p. 035412.
81. Y. Kawazoe, T. Kondow, and K. Ohno, *Clusters and Nanomaterials: Theory and experiment*

2001: Springer.

82. H. Hsu and L.E. Reichl, *Modelling graphene layers and single-walled carbon nanotubes with regularized δ-function potentials.* PHYSICAL REVIEW B, 2005. **72**: p. 155413
83. N. Hamada, S. Sawada, and A. Oshiyama, *New one-dimensional conductors: Graphitic microtubules* Phys. Rev. Lett., 1992. **68**: p. 1579 - 1581.
84. Lee, J., *Band-gap renormalization in carbon nanotubes:Origin of the ideal diode behavior in carbon nanotube p-n junction.* Phys. Rev. B, 2007. **75**(075409): p. 1-5.
85. C. Spataru and F. Leonard, *Tunable Band Gaps and Excitons in Doped Semiconducting Carbon Nanotubes Made Possible by Acoustic Plasmons.* Phys. Rev. Lett., 2010. **104**(17).
86. E. D. Minot, et al., *Tuning Carbon Nanotube Band Gaps with Strain.* Physical Review Letters, 2003. **90**(15): p. 156401.
87. S. Sreekala, et al., *Effect of strain on the band gap and effective mass of zigzag single-wall carbon nanotubes: First-principles density-functional calculations.* Physical Review B (Condensed Matter and Materials Physics), 2008. **77**(15): p. 155434.
88. R. Saito, et al., *Electronic structure of chiral graphene tubules.* Applied Physics Letters 1992. **60**(18): p. 2204-2206.

89. D. Kienle, J.I. Cerda, and A.W. Ghosh, *Extended Hückel theory for bandstructure, chemistry and transport : I. Carbon Nanotubes.* J. Appl. Phys., 2006. **100**: p. 043714.
90. O. Gülseren, T. Yildirim, and S. Ciraci, *Systematic ab initio study of curvature effects in carbon nanotubes.* Physical Review B, 2002. **65**: p. 153405.
91. J. W. Mintmire and C.T. White, *Electronic and Structural properties of Carbon nanotubes.* Carbon, 1995. **33** (7): p. 893-902
92. E. Malic, et al., *Analytical approach to optical absorption in carbon nanotubes.* Physical Review B (Condensed Matter and Materials Physics), 2006. **74**(19): p. 195431.
93. Teri Wang Odom, et al., *Atomic structure and electronic properties of single-walled carbon nanotubes.* Nature, 1998. **391**: p. 62-64.
94. Jeroen W. G. Wildoer, et al., *Electronic Structure of atomically resolved carbon nanotubes.* Nature, 1998. **391**: p. 59-62.
95. X. Liu, et al., *Detailed analysis of the mean diameter and diameter distribution of single-wall carbon nanotubes from their optical response.* Physical Review B, 2002. **66**(4).
96. S. Reich, C. Thomsen, and P. Ordejon, *Electronic band structure of isolated and bundled carbon nanotubes.* Physical Review B, 2002. **65**(15): p. 155411.
97. Yuta Sato, et al., *Chiral-Angle Distribution for Separated Single-Walled Carbon Nanotubes.* Nano Letters, 2008. **8**(10).
98. Albert G. Nasibulin, H.J. Peter V. Pikhitsa, and E.I. Kauppinen, *Correlation between catalyst particle and single-walled carbon nanotube diameters.* Carbon, 2005. **43**: p. 2251-2257.
99. K. El Shabrawy, et al., *A new analytical model for predicting SWCNT band-gap from geometrical properties*, in *ICICDT*. 2008: Grenoble, France.
100. J. W. G. Wildoer, et al., *Electronic Structure of atomically resolved carbon nanotubes.* Nature, 1998. **391**: p. 59-62.
101. T. W. Odom, et al., *Atomic structure and electronic properties of single-walled carbon nanotubes.* Nature, 1998. **391**: p. 62-64.
102. M. S. Dresselhaus, R. Saito, and A. Jorio. *Semiconducting Carbon Nanotubes*. in *International Conference on the Physics of Semiconductors - ICPS-27*. 2005
103. J. W. Ding, X. H. Yan, and J.X. Cao, *Analytical relation of band gaps to both chirality and diameter of single-wall carbon nanotubes.* Physical Review B, 2002. **66**: p. 073401.
104. C. L. Kane and E.J. Mele, *Size, Shape, and Low Energy Electronic Structure of Carbon Nanotubes.* Physical Review Letters, 1997. **78**(10): p. 1932 - 1935.
105. D. Akinwande, Y. Nishi, and H.-S.P. Wong, *An Analytical Derivation of the Density of States, Effective Mass, and Carrier Density for Achiral Carbon Nanotubes.* IEEE Transactions on Electron Devices, 2008. **55**(1): p. 289-297.
106. S. O. Koswatta, et al., *Dependence of DC Characteristics of CNT MOSFETs on Bandstructure Models.* IEEE Transactions on Nanotechnology, 2006. **5**(4): p. 368-372.
107. G. L. Zhao, D. Bagayoko, and L. Yang, *Effective masses of charge carriers in selected symmorphic and nonsymmorphic carbon nanotubes.* Phys. Rev. B, 2004. **69**: p. 245416
108. D. Selbmann, et al., *A parametric study of the synthesis and purification of single-walled carbon nanotubes using the high-pressure carbon monoxide process.* Applied Physics A: Materials Science & Processing, 2008. **90**(4): p. 637-643.
109. Y. Tseng, et al., *Effect of Diameter Variation in a Large Set of Carbon Nanotube Transistor.* Nano Letters, 2006. **6**(7): p. 1364-1368.

110. A. G. Nasibulin, et al., *Correlation between catalyst particle and single-walled carbon nanotube diameters.* Carbon, 2005. **43**: p. 2251-2257.
111. T. Hiraoka, et al., *Control on the diameter of single-walled carbon nanotubes by changing the pressure in floating catalyst CVD.* Carbon, 2006. **44**: p. 1853-1859.
112. C. Lu and J. Liu, *Controlling the Diameter of Carbon Nanotubes in Chemical Vapor Deposition Method by Carbon Feeding.* J. Phys. Chem. B, 2006. **110**: p. 20254-20257.
113. P. Nikolaev, et al., *Gas-phase catalytic growth of single-walled carbon nanotubes from carbon monoxide.* Chemical Physics Letters, 1999. **313**: p. 91-97.
114. O. Zhou, et al., *Materials Science of Carbon Nanotubes: Fabrication, Integration, and Properties of Macroscopic Structures of Carbon Nanotubes.* Accounts of Chemical Research, 2002. **35**(12): p. 1045-1053.
115. J. Guo, S. Datta, and M. Lundstrom, *A Numerical Study of Scaling Issues for Schottky-Barrier Carbon Nanotube Transistor.* IEEE Transactions on Electron Devices, 2004. **51**(2): p. 172-177.
116. A. Raychowdhury, S. Mukhopadhyay, and K. Roy, *Modeling of Ballistic Carbon Nanotube Field Effect Transistors for Efficient Circuit Simulation*, in *International Conference on Computer Aided Design (ICCAD'03)*. 2003.
117. J. Deng and H.-S.P. Wong, *A Compact SPICE Model for Carbon-Nanotube Field-Effect Transistors Including Nonidealities and Its Application-Part II: Full Device Model and Circuit Performance Benchmarking.* IEEE Transactions on Electron Devices, 2007. **54**(12): p. 3195-3205.
118. S. Bandow, et al., *Effect of the Growth Temperature on the Diameter Distribution and Chirality of Single-Wall Carbon Nanotubes.* Physical Review Letters, 1998. **80**(17): p. 3779-3782.
119. H.M. Cheng, et al., *Bulk morphology and diameter distribution of single-walled carbon nanotubes synthesized by catalytic decomposition of hydrocarbons.* Chemical Physics Letters, 1998. **289**: p. 602-610.
120. Y. Yao, et al., *Temperature-mediated growth of single-walled carbon-nanotube intramolecular junction.* Nature materials, 2007. **6**: p. 283 - 286.
121. G. Jeong, et al., *Effect of nanoparticle density on narrow diameter distribution of carbon nanotubes and particle evolution during chemical vapor deposition growth.* Journal of Applied Physics 2005. **98**: p. 124311.
122. Pavel Nikolaev, et al., *Gas-phase catalytic growth of single-walled carbon nanotubes from carbon monoxide.* Chemical Physics Letters, 1999. **313**: p. 91-97.
123. K. El Shabrawy, et al., *Modeling SWCNT Band-gap and Effective Mass Variation using a Monte Carlo Approach.* IEEE Transactions on Nanotechnology, 2009.
124. Y. Sato, et al., *Chiral-Angle Distribution for Separated Single-Walled Carbon Nanotubes.* Nano Letters, 2008. **8**(10): p. 3151–3154.
125. X. Zhou, et al., *Band Structure, Phonon Scattering, and the Performance Limit of Single-Walled Carbon Nanotube Transistors.* Physical Review Letters, 2005. **95**: p. 146805
126. V. Perebeinos, J. Tersoff, and P. Avouris, *Electron-Phonon Interaction and Transport in Semiconducting Carbon Nanotubes.* Physical Review Letters, 2005. **94**: p. 086802.
127. A. Gruneis, et al., *Inhomogeneous optical absorption around the K point in graphite and carbon nanotubes.* Phys. Rev. B, 2003. **67**(16): p. 165402-1-7.
128. J. Lee, P. Codella, and M. Pietrzykowski, *Direct probe of excitonic and continuum transitions in the photocurrent spectroscopy of individual carbon nanotube p-n diodes.* Applied Physics Letters, 2007. **90**(053103): p. 1-3.

129. J. Jiang, et al., *Optical aborption matrix elements in single-wall carbon nanotubes.* Carbon, 2004. **42**: p. 3169-3176.
130. R. Saito, et al., *Optical absorption of graphite and single-wall carbon nanotubes.* Appl. Phys. A, 2004. **78**: p. 11099-1105.
131. V. Perebeinos, J. Tersoff, and P. Avouris, *Scaling of Excitons in Carbon Nanotubes.* Phys. Rev. Lett., 2004. **92**(25): p. 257402-1-4.
132. D. A. Stewart and F. Léonard, *Energy Conversion Efficiency in Nanotube Optoelectronics.* Nano Letters, 2005. **5** (2): p. 219 -222.
133. V. Popov and L. Henrard, *Comparative study of the optical properties of single-walled carbon nanotubes within orthogonal and nonorthogonal tight-binding models.* Phys. Rev. B, 2004. **70**(11).
134. S. M. Bachilo, et al., *Structure-Assigned Optical Spectra of Single-Walled Carbon Nanotubes.* Science, 2002. **298**: p. 2361-2365.
135. H. Kataura, et al., *Optical properties of single-wall carbon nanotubes.* Synthetic Metals, 1999. **103**: p. 2555-2558.
136. J. Guo, M. A. Alam, and Y. Yoon, *Theoretical investigation on photoconductivity of single intrinsic carbon nanotubes.* Appl. Phys. Lett., 2006. **88**(133111): p. 1-3.